

The copyright of this thesis vests in the author. No quotation from it or information derived from it is to be published without full acknowledgement of the source. The thesis is to be used for private study or non-commercial research purposes only.

Published by the University of Cape Town (UCT) in terms of the non-exclusive license granted to UCT by the author.

**Issues in the processing and analysis of functional NIRS
imaging and a contrast with fMRI findings in a study of
sensorimotor deactivation and connectivity**

by
Frances Robertson

Thesis presented for the Degree of

Doctor of Philosophy

in the Department of Human Biology

UNIVERSITY OF CAPE TOWN

February 2012

Acknowledgements

I would like to thank both my supervisors for their constant support and approachability, and their patience with my cautious progress. I am particularly grateful to my principal supervisor Prof. Ernesta Meintjes for the extensive MR physics knowledge and fMRI expertise that she was able to provide, and to my co-supervisor Prof. Tania Douglas for her consistently rapid and practical feedback.

I am thankful to Prof. Dan Stein of the Department of Psychiatry for the opportunity to work with the DYNOT system and his continued interest and support. A great many thanks go to Dr Annerine Roos, my co-explorer of NIRS, for her tireless efforts running the DYNOT system and willing assistance which increased the efficiency and accuracy of optode placement for each subject.

I am grateful to Dr Laurie Rauch from the Sports Science Institute of South Africa for the loan of the Biopac equipment for physiological recordings with NIRS, to Dr Bruce Spottiswoode for modifying the fMRI pulse sequence to log physiological data, and to the radiographers at the Cape Universities Brain Imaging Centre: Marie-Louise, Naomi and Fran for running the MRI scanner and for their patience when trying to get an acceptable ECG trace. Thanks also go to Nicolette Hamman for her assistance with task administration during the fMRI scans.

I would also like to thank my friends and colleagues in the Department of Biomedical Engineering, in particular Dr Aaron Hess for interesting and helpful discussions.

Most importantly I thank all the volunteers who took part in my experiments and the National Research Foundation of South Africa for financial support.

Finally, I owe a great many thanks to my supportive family: to Jeremy for his understanding support and excellent coffee, to Adam for allowing his mother to burn the midnight oil without too much interruption, to my dear sisters who do any favour I ask, and my wonderful parents who have faith in my abilities despite absence of any evidence.

Issues in the processing and analysis of functional NIRS imaging and a contrast with fMRI findings in a study of sensorimotor deactivation and connectivity

Frances Robertson

February 2012

Abstract

The first part of this thesis examines issues in the processing and analysis of continuous wave functional near infrared spectroscopy (fNIRS) of the brain using the DYNOT system. In the second part, the same sensorimotor experiment is carried out using functional magnetic resonance imaging (fMRI) and near infrared spectroscopy in eleven of the same subjects, to establish whether similar results can be obtained at the group level with each modality.

Various techniques for motion artefact removal in fNIRS are compared. Imaging channels with negligible distance between source and detector are used to detect subject motion, and in data sets containing deliberate motion artefacts, independent component analysis and multiple-channel regression are found to improve the signal-to-noise ratio.

In an initial NIRS motor experiment, some inconsistency between oxyhaemoglobin and deoxyhaemoglobin responses is found. The same analysis on task-free data results in a few false positive voxels, which are eliminated with correction for multiple comparisons. The effect of smoothing, high pass filtering and prewhitening on the false positive rate in group analyses of null data is investigated. Although no false positives are found in random effects analyses, in fixed effects analyses the number of false positives increases with increased smoothing, and is eliminated with prewhitening and correction for multiple comparisons.

Using fMRI and NIRS in two separate sessions, a sensorimotor task is conducted, consisting of motor and noxious cold stimulation in a conventional alternating block design, followed by longer blocks of motor and cold stimulation and resting fixation to allow for the assessment of steady-state inter-regional connectivity during each task condition. Group level analyses are performed on the fMRI, NIRS and simultaneously recorded physiological data, to examine cardiorespiratory changes, neuronal activation, deactivation and connectivity in cortical sensorimotor regions with each task condition.

NIRS responses are more consistently found in oxyhaemoglobin than in deoxyhaemoglobin. Group laterality effects from the NIRS and fMRI experiments are in agreement, with a larger contralateral response to left hand tapping, but to a right hand cold stimulus; and greater ipsilateral deactivation to a noxious cold stimulus applied to the left, rather than the right hand. However, ipsilateral deactivation to unilateral tapping is found at the group level in fMRI but not in NIRS data. Interhemispheric connectivity between primary sensorimotor regions is found in all conditions in fMRI data, but using NIRS only at rest and only in oxyhaemoglobin. No significant change in connectivity between activated and deactivated sensorimotor regions with task condition is found between regions of interest in either NIRS or fMRI data.

List of Abbreviations

- ABP** Arterial blood pressure
- ACC** Anterior cingulate cortex
- ALFF** Amplitude of low frequency fluctuations
- AR(p)** Autoregressive model (order p)
- ASL** Arterial spin labelling
- AUC** Area under curve
- BA** Brodmann area
- BCI** Brain-computer interface
- BOLD** Blood oxygenation level dependent
- DeoxyHb** Deoxyhaemoglobin
- CBF** Cerebral blood flow
- CBV** Cerebral blood volume
- CNR** Contrast-to-noise ratio
- CMRO₂** Cerebral metabolic rate of oxygen consumption
- CSF** Cerebrospinal fluid
- CV** Coefficient of variation
- CW** Continuous wave
- DICOM** Digital imaging and communications in medicine
- DPF** Differential pathlength factor
- DMN** Default mode network

DOI/DOT Diffuse optical imaging/ diffuse optical tomography

EPI Echo planar imaging

FDR False discovery rate

FEM Finite element method

FIX Experimental fixation condition

fMRI Functional magnetic resonance imaging

FRE Fiducial registration error

FWE Family-wise error

FWHM Full width half maximum

GLM General linear model

Hb Haemoglobin

HPF High pass filter

HR Heart rate

HRF Haemodynamic response function

HRV Heart rate variability

IBI Interbeat interval

ICA Independent component analysis

IFG Inferior frontal gyrus

IPL Inferior parietal lobule

ITG Inferior temporal gyrus

LCOLD Experimental condition in which subjects received a cold stimulus to the left hand.

LF Low frequency (0.04 - 0.12 Hz)

LPA Left pre-auricular point

LPF Low pass filter

LTAP Experimental condition in which subjects tapped the fingers of the left hand.

M1 Primary motor cortex

MNI Montreal Neurological Institute

MTG Middle temporal gyrus

PCL Paracentral lobule

PET Positron emission tomography

PFC Prefrontal cortex

PMC Premotor cortex

PMU Physiological monitoring unit

PSD Power spectral density

NIRS/fNIRS Near infrared spectroscopy/ functional near infrared spectroscopy

OxyHb Oxyhaemoglobin

PCA Principal component analysis

RCOLD Experimental condition in which subjects received a cold stimulus to the right hand.

RETROICOR Retrospective image correction (for physiological motion effects)

RFT Random field theory

ROC Receiver operating characteristic

ROI Region of interest

RPA Right pre-auricular point

RLS Recursive least squares

RSA Respiratory sinus arrhythmia

RTAP Experimental condition in which subjects tapped the fingers of the right hand.

S1 Primary somatosensory cortex (BA 123)

S2 Secondary somatosensory cortex

SDNN Standard deviation of the interbeat interval

SE Spin echo

SM1 Primary sensorimotor cortex

SMA Supplementary motor area

SNR Signal-to-noise ratio

SPL Superior parietal lobule

SPM Statistical parametric mapping

STG Superior temporal gyrus

SSFP Steady-state free precession

TCD Transcranial Doppler

TotHb Total haemoglobin

TE Echo time

TMS Transcranial magnetic stimulation

TR Repetition time

TRE Total registration error

VLF Very low frequency (0.01 - 0.04 Hz)

University of Cape Town

Contents

1	Introduction	1
I	Processing and analysis of brain imaging data: unresolved issues for NIRS	5
2	Functional brain imaging: fMRI and NIRS	7
2.1	Functional MRI: the Blood Oxygen Level Dependent (BOLD) signal	8
2.2	Noise sources in fMRI	9
2.2.1	Scanner noise	9
2.2.2	Cardiac pulsation	10
2.2.3	Respiration-induced signal changes	10
2.2.4	Aliasing of systemic noise	11
2.3	Analysis of fMRI data	12
2.4	Near infrared spectroscopy (NIRS): Oxyhaemoglobin, deoxyhaemoglobin and cerebral blood volume (CBV)	13
2.4.1	Continuous wave, frequency domain and time domain NIRS	14
2.4.2	Depth resolution of NIRS	14
2.4.3	Vessel sensitivity	15
2.5	Diffuse optical imaging	15
2.5.1	Modelling light transport	16
2.5.2	Solving the forward problem	16
2.5.3	Image reconstruction	16
2.5.4	Incorporating a priori information	17
2.5.5	The DYNOT (dynamic optical tomography) system	17
2.6	Noise removal in functional NIRS	17
2.6.1	Systemic interference	18

2.6.2	Motion artefact	19
2.7	Optode placement and intersubject registration	19
2.8	Analysis of fNIRS data	20
2.8.1	Model-based vs model-free analysis	21
2.8.2	Temporal autocorrelation	22
2.8.3	Multiple comparison correction	24
2.8.4	Group-level comparisons	24
2.9	Conclusion	25
3	A comparison of methods for motion artefact removal in fNIRS	27
3.1	Methods	28
3.1.1	Data acquisition	28
3.1.2	Motion artefact detection using co-located channels	29
3.1.3	Motion artefact removal	29
3.1.3.1	Two-input RLS adaptive filter	30
3.1.3.2	Wavelet-based filter	31
3.1.3.3	Two-channel multiple regression	32
3.1.3.4	Multiple regression with all 30 channels	32
3.1.3.5	Independent component analysis	32
3.1.3.6	Calculation of SNR change after filtering	33
3.2	Results	34
3.2.1	Motion artefact detection in datasets with deliberate motion	34
3.2.1.1	Dependence on type of motion	35
3.2.1.2	Threshold selection and motion classification	35
3.2.1.3	Motion artefact on measurement channels	36
3.2.2	Motion artefact removal	38
3.2.2.1	Application of filtering methods to data sets containing known motion	38
3.2.2.2	Application of filtering methods to data set containing unknown motion	40
3.2.2.3	Correlation of signals with source and detector references	41
3.3	Discussion	42
3.4	Summary	44

4	Investigation of NIRS-DOT data analysis in a motor execution and observation task and on null data	45
4.1	A motor execution and observation task in single subjects using NIRS	45
4.1.1	Methods	47
4.1.2	Results	54
4.1.3	Discussion	57
4.2	The effect of preprocessing on false positives in group analyses	61
4.2.1	Methods	61
4.2.2	Results	62
4.2.3	Discussion	66
4.3	Summary and conclusions	67
II	Group level comparisons of fNIRS and fMRI in sensory and motor tasks	69
5	Experiment description and physiological data analysis	71
5.1	An investigation of systemic and cerebral responses to motor and noxious thermal stimulation	72
5.1.1	Task	72
5.1.2	Subjects	72
5.1.3	Functional imaging	73
5.1.3.1	Functional MRI	73
5.1.3.2	NIRS	74
5.2	Physiological responses to sensorimotor stimulation	74
5.2.1	Methods	74
5.2.1.1	Synchronising physiological recordings with fMRI data	74
5.2.1.2	Processing of ECG and pulse oximeter data	79
5.2.1.3	Analysis of physiological data	81
5.2.2	Results	83
5.2.2.1	Short blocks: task-related physiological changes	83
5.2.2.2	Long blocks: task-related physiological changes	83
5.2.2.3	Physiological changes during the cold pressor test	88
5.2.3	Conclusions	89
6	Registration of NIRS and MRI data	91
6.1	Background	91

6.1.1	Landmark-based registration	91
6.1.2	Surface-based registration	92
6.2	Methods	93
6.2.1	Head shape data	93
6.2.2	Evaluation of registration accuracy	94
6.2.3	Landmark registration	94
6.2.4	Surface registration	94
6.2.5	Simulated surface registration: the effect of fiducial and surface point error	95
6.3	Results	95
6.3.1	Landmark registration	95
6.3.2	Initial landmark-based registration followed by surface registration	98
6.3.3	Conclusions	98
7	Ipsilateral activations and deactivations in unilateral motor tasks	103
7.1	Introduction	103
7.1.1	BOLD deactivations	104
7.1.2	Transcallosal inhibitory and uncrossed descending pathway hypotheses	105
7.1.3	Factors affecting ipsilateral activation and deactivation	105
7.2	Methods	106
7.2.1	Subjects and task	106
7.2.2	Image preprocessing and quality control	106
7.2.3	Analysis	107
7.3	Results	110
7.3.1	Motor task activation	110
7.3.2	Motor task deactivation	110
7.3.3	Differences between left and right tapping	112
7.3.4	Activation asymmetry: effect of tapping hand and hemisphere of activation	117
7.3.5	Intersubject variability of activation and deactivation	120
	7.3.5.1 Individual ipsilateral activation in fMRI and NIRS	122
	7.3.5.2 Individual ipsilateral deactivation in fMRI and NIRS	124
7.3.6	Intersubject correlations between activation and deactivation	125
7.4	Discussion	125
7.5	Summary	129

8	Activation and deactivation to a noxious thermal stimulus	131
8.1	Introduction	132
8.1.1	Activations and deactivations to different types of sensory stimulation	132
8.1.2	Lateralisation of somatosensory processing	133
8.2	Methods	134
8.3	Results	134
8.3.1	Areas activated by a cold stimulus applied to each hand	134
8.3.2	Regions deactivated by a cold stimulus applied to each hand	136
8.3.3	Difference between left and right hand cold stimulus	138
8.3.4	Investigation of activation asymmetry: effect of stimulus side and hemisphere of activation	142
8.3.4.1	Intersubject correlations	147
8.3.4.2	Between subject variability of activation and deactivation in fMRI and NIRS	149
8.4	Discussion	150
8.4.1	Activation of contralateral and ipsilateral somatosensory areas (S1 and S2)	150
8.4.2	Deactivation in response to cold stimulation	151
8.4.3	Pathways for ipsilateral deactivation	151
8.4.4	Lateral asymmetry of activations and deactivations	152
8.4.5	Relation between activations and deactivations	153
8.5	Summary	153
9	Task-related changes in brain functional connectivity	155
9.1	Introduction	155
9.1.1	Functional connectivity in the default-mode network	156
9.1.2	The effect of task performance on connectivity	157
9.1.3	NIRS functional connectivity	158
9.2	Methods	159
9.2.1	Subjects and task	159
9.2.2	Physiological noise removal	159
9.2.3	Region of interest definition	160
9.2.4	Connectivity analysis	160
9.2.5	Power spectral density analysis	161
9.3	Results	161
9.3.1	Steady-state and resting functional connectivity	161
9.3.2	Effect of TAP and COLD conditions	166

9.3.3	Relation of connectivity to activation and deactivation	175
9.3.4	Power spectral density analysis	176
9.4	Discussion	177
9.4.1	Spurious correlations, the global signal and physiological noise	177
9.4.2	The effect of different TRs	178
9.4.3	Steady-state connectivity in task conditions	179
9.4.4	Discrepancies between fMRI and NIRS	179
9.4.5	Considerations for NIRS	180
9.4.6	Change in connectivity with task	181
9.4.6.1	Interhemispheric SM1 connectivity	181
9.4.6.2	Connectivity to precuneus	182
9.4.6.3	Relation to deactivation	183
9.4.7	Task design and variation between runs	183
9.4.8	Power spectrum changes	184
9.5	Summary	185
10	Conclusions	187
	Bibliography	192

List of Figures

2.1	Absorption spectra of deoxyhaemoglobin (<i>HHb</i>), oxyhaemoglobin (<i>O₂Hb</i>) and water.	13
2.2	Banana shape of photon density path from source to detector.	15
3.1	Location of NIRS optodes. Each numbered optode location consists of both a source and detector fibre.	28
3.2	RLS noise cancellation diagram.	30
3.3	Sensitivity from ROC curve for each co-located channel, restricting 1-specificity to 0.01 (16 false positives).	34
3.4	Subject 2: (a) motion events and channels with (b) good and (c,d) bad motion discrimination.	35
3.5	Amplitude of motion artefact in each co-located channel for each motion type	36
3.6	Data set 3 motion detection	36
3.7	Relative amplitude of motion artefact for each data set.	37
3.8	Example of a motion reference (co-located) channel and dependent measurement channels.	38
3.9	Example of a measurement channel with the detected signal in its source and detector reference.	39
3.10	Map of SNR change in dB for subject 1 after RLS adaptive filter of order 10.	40
3.11	Sample results from RLS filtering for a channel with decreased SNR after filtering (S25 D18), and a channel with increased SNR (S19 D18).	41
4.1	FEM model generator utility in NAVI.	48
4.2	DOT/MRI overlay displayed by NAVI.	50
4.3	Model evidence for different haemodynamic basis sets	55
4.4	Area of overlap between significant oxyHb and deoxyHb clusters for the L_TAP contrast	56
4.5	False positives for 10 s blocks without AR1 correction.	64
4.6	False positives for oxyHb with a block length of 20 s.	66
5.1	Task design.	73
5.2	Number of samples in PMU log file vs length of scan showing linear relationship.	77

5.3	Mean IBI in the Short_Blocks runs during NIRS and MRI scanning.	85
5.4	Mean IBI in the Long_Blocks runs during NIRS and MRI scanning.	86
5.5	Mean IBI and SDNN for first and second runs during fMRI and NIRS for 8 subjects.	87
5.6	Mean IBI in 50s intervals, pre- and during cold pressor test.	89
6.1	Simulated landmark and surface point data extracted from a subject's MRI	95
6.2	Map error and fiducial registration error for increasing number of fiducials	96
6.3	Mean FRE and map error for each landmark after least-squares affine registration.	97
6.4	The 36 predefined optode positions offered in NAVI software.	101
7.1	Diagnostic plots of data quality.	108
7.2	Functional MRI statistical map of LTAP > RTAP (orange) and RTAP > LTAP (blue) thresholded at $p < 0.001$ FDR.	114
7.3	Thresholded oxyHb map of LTAP > RTAP (orange) and RTAP > LTAP (blue) transformed into MNI space and overlaid on a template brain MRI.	115
7.4	Thresholded deoxyHb map of LTAP > RTAP (orange) and RTAP > LTAP (blue) transformed into MNI space and overlaid on a template brain MRI.	116
7.5	Mean parameter estimates for ROIs used in two-way ANOVA	119
7.6	Mean parameter estimates for oxyHb and deoxyHb in sensorimotor area, used in two-way ANOVA	120
7.7	Correlation across subjects between mean β parameter estimates to RTAP in contralateral and ipsilateral ROIs for oxyHb and deoxyHb.	128
8.1	BOLD activation (orange) and deactivation (blue) for RCOLD vs FIX thresholded at $p < 0.001$. 137	
8.2	BOLD activation (orange) and deactivation (blue) for LCOLD vs FIX thresholded at $p < 0.001$. 138	
8.3	Thresholded NIRS maps of RCOLD > FIX (orange) and RCOLD < FIX (blue) transformed into MNI space and overlaid on a template brain MRI.	140
8.4	Thresholded NIRS maps of LCOLD > FIX (orange) and LCOLD < FIX (blue) transformed into MNI space and overlaid on a template brain MRI.	141
8.5	Mean BOLD effect for right cold (RCOLD) and left cold (LCOLD) conditions in contralateral and ipsilateral ROIs	145
8.6	Mean NIRS parameter estimates for oxyHb and deoxyHb in sensorimotor area, used in two-way ANOVA	146
8.7	Correlation across subjects between mean β parameter estimates for RCOLD in contralateral and ipsilateral ROIs for oxyHb and deoxyHb.	148
9.1	Unthresholded t-maps of BOLD signal connectivity to left M1 during the REST1 condition for 1100 ms and 2200 ms TRs, with and without physiological noise removal.	165

9.2	Pearson correlation between left and right M1 ROIs for each subject in each condition measured with NIRS.	167
9.3	Brain regions showing significantly greater connectivity to the precuneus ROI in the TAP vs REST condition.	170
9.4	Mean and standard deviation across subjects of connectivity z-score between left and right M1 ROIs in each condition.	172
9.5	Mean and standard deviation across subjects of connectivity z-score between left and right S1 ROIs in each condition.	173
9.6	Connectivity z-scores between left and right M1 ROIs for each condition, averaged over 14 subjects	175
9.7	Connectivity z-scores between left and right S1 ROIs for each condition, averaged over 14 subjects	176
9.8	Correlation across subjects between ipsilateral deactivation to RTAP and L-R M1 connectivity during the 120 s TAP condition (fMRI).	177

University of Cape Town

List of Tables

3.1	Motion event detection using all channels using a threshold $T=2$	37
3.2	Median change in SNR in dB using RLS adaptive filtering, averaged over all channels for 3 different data sets	39
3.3	Median SNR change in dB over all channels using each filtering method	40
3.4	Median SNR change in dB over all channels using each filtering method for data set 4 (n=879)	41
3.5	Value for two-channel and all-channel regression and percentage of channels where the largest regression coefficient is from neither source nor detector	42
4.1	Channel diagnostics after bandpass filtering between 0.01 and 0.15 Hz.	49
4.2	Boundaries of the head in various images used by NAVI	51
4.3	Actual head dimensions and calculated DOT voxel size.	51
4.4	Calculation of the DOT offset with respect to the MRI in X, Y and Z directions.	52
4.5	Calculation of the required translation to align DOT and MRI images	52
4.6	Number of significant voxels in each cluster for each contrast $p < 0.05$ FDR corrected.	56
4.7	Number of significant voxels in each cluster for each contrast tested on null (baseline) data.	57
4.8	OxyHb: False positive voxels in a fixed effects group analysis of null data from 10 subjects	62
4.9	DeoxyHb: False positive voxels in a fixed effects group analysis of null data from 10 subjects	63
4.10	OxyHb: False positive voxels in fixed effects analysis of null data from 17 subjects	64
4.11	DeoxyHb: False positive voxels in fixed effects analysis of null data from 17 subjects	65
5.1	Summary of useable data obtained for study session.	73
5.2	Time difference between length of fMRI run and physiological recording	75
5.3	Apparent sampling rates based on length of log file.	76
5.4	Number of samples in PMU log file for various scan lengths and TRs.	78
5.5	Average sampling rate and offset for each log file calculated by linear regression of samples-per-file vs scan length.	79
5.6	Outcome of semi-automatic processing of pulse oximeter and ECG data.	82

5.7	Results of two way repeated measures ANOVA with factors COND (task condition) and RUN for heart rate during NIRS and MRI Short_Blocks runs.	83
5.8	Significant Newman-Keuls post-hoc tests for differences between mean IBI in each NIRS Short_Blocks run.	84
5.9	Results of two way repeated measures ANOVA with factors COND (task condition) and RUN for heart rate during NIRS and MRI Long_Blocks runs.	84
5.10	Results of two way repeated measures ANOVA with factors COND (task condition) and RUN for heart rate variability during NIRS and MRI Long_Blocks runs.	84
5.11	Number of subjects whose heart rate increased, decreased or remained the same in TAP and COLD compared to REST in the first run.	88
5.12	Results of one way repeated measures ANOVA with 4 levels of factor “Cold” for heart rate during NIRS and MRI.	88
5.13	Number of subjects showing an increase, decrease or no change in heart rate during the stages of the cold pressor test.	89
6.1	Mean FRE and median map error over all landmark points for all registrations using $n - 1$ fiducials	98
6.2	Map, fiducial and residual error after registration: initial landmark-based, optimisation using surface alignment, and projection to head surface.	99
7.1	Positive BOLD responses to unilateral finger tapping of each hand.	111
7.2	NIRS activation (oxyHb increase and deoxyHb decrease) to unilateral finger tapping of each hand.	112
7.3	Negative BOLD responses to unilateral finger tapping of each hand	113
7.4	Regions activated for LTAP > RTAP and RTAP > LTAP	114
7.5	Regions activated for LTAP > RTAP and RTAP > LTAP	115
7.6	Results of two way ANOVA with factors hemisphere and hand for selected ROIs.	118
7.7	Results of two way ANOVA with factors hemisphere and hand for selected NIRS ROIs.	119
7.8	Test for dominant response to one hand in contralateral and ipsilateral hemispheres.	121
7.9	Results of multi-subject conjunction analysis.	121
7.10	Summary of individual subject BOLD responses in SM1 region for each contrast.	122
7.11	Activations for individual subjects for the LTAP > FIX and RTAP > FIX contrasts.	123
7.12	Summary of individual subject activations and deactivations in SM1 region for each contrast.	124
7.13	Pearson correlation between ipsilaterally activated or deactivated ROIs and contralaterally activated ROIs for RTAP.	126
7.14	Pearson correlation between ipsilaterally activated or deactivated ROIs and contralaterally activated ROIs for LTAP.	127

8.1	BOLD activation for RCOLD > FIX and LCOLD>FIX	135
8.2	NIRS activation (oxyHb increase and deoxyHb decrease) to unilateral cold stimulus applied to each hand.	136
8.3	BOLD activation for RCOLD < FIX and LCOLD < FIX.	137
8.4	NIRS deactivation (oxyHb decrease and deoxyHb increase) to unilateral cold stimulus applied to each hand.	139
8.5	BOLD activation for LCOLD > RCOLD and RCOLD < LCOLD	139
8.6	Number of voxels activated for LCOLD > RCOLD and RCOLD > LCOLD.	142
8.7	Results of two way ANOVA with factors hemisphere and hand for selected fMRI ROIs.	143
8.8	Results of two way ANOVA with factors hemisphere and hand for selected NIRS ROIs.	145
8.9	Test for dominant response to a cold stimulus applied to one hand in contralateral and ipsilateral hemispheres.	146
8.10	Pearson correlation between ipsilaterally deactivated ROIs and contralaterally activated ROIs for RCOLD.	147
8.11	Pearson correlation between ipsilaterally deactivated ROIs and contralaterally activated ROIs for LCOLD.	148
8.12	Summary of individual subject activations and deactivations in SM1 region for each contrast.	150
9.1	Brain regions showing connectivity to the left M1 ROI.	162
9.2	Brain regions showing connectivity to the right M1 (deactivation) ROI.	163
9.3	Areas that show greater connectivity to left M1 than right M1 and to right M1 than left M1 (p<0.05 FDR)	164
9.4	T-statistics and p values for one sample t-tests on mean ROI connectivity z-score across subjects for M1 and S1 ROIs in fMRI.	166
9.5	T-statistics and p values for one sample t-tests on mean ROI connectivity z-score across subjects for M1 ROIs in NIRS.	166
9.6	Areas that show greater BOLD signal connectivity with the left M1 ROI during TAP than REST in the 1100 ms TR data (p<0.05 FDR)	168
9.7	Areas that show greater BOLD signal connectivity with the left M1 ROI during TAP than REST in the 1100 ms TR data with physiological correction (p<0.05 FDR)	169
9.8	Areas that show greater BOLD signal connectivity with the left M1 ROI during TAP than REST.	170
9.9	Areas that show greater BOLD signal connectivity with the precuneus during TAP than REST (p<0.05 FDR).	171
9.10	Number of subjects showing increases or decreases in connectivity with condition.	173

9.11	Number of voxels in each hemisphere showing changed connectivity to the ROI in the same hemisphere at $p < 0.01$ FDR, with and without physiological noise correction.	174
9.12	Number of voxels in each hemisphere showing changed connectivity to the ROI in the opposite hemisphere at $p < 0.01$ FDR, with physiological noise correction applied.	174
9.13	Number of subjects showing increases or decreases in connectivity with condition.	175

University of Cape Town

Chapter 1

Introduction

Near infrared spectroscopy (NIRS) is rapidly gaining popularity for functional brain imaging. It is portable, easily tolerated and well-suited to studies of patients or children, and its relative inexpensiveness makes it an ideal tool for neuroimaging research, particularly in developing countries, where more expensive imaging techniques such as functional magnetic resonance imaging (fMRI) are often not available.

NIRS offers advantages over fMRI in that it measures concentration changes in both oxygenated and deoxygenated haemoglobin, and has finer temporal resolution. However, there are certain disadvantages and limitations to the use of NIRS. These are well-known to imaging experts, but may not be to researchers using an off-the-shelf imaging system to address neuroscientific questions, who may therefore fail to design and analyse experiments appropriately or to interpret their data correctly. Some of these limitations include the fact that NIR light only penetrates the adult skull sufficiently to sample cortical areas; the diffuse nature of light propagation in tissue makes localisation difficult, resolution poor and measured signals noisy; the measurement of brain signals through the skull and scalp introduces systemic interference into the measured responses; the consistent placement of optodes between subjects and sessions is difficult; and variations in anatomy, skull thickness, skin colour and the presence of hair may alter the measurable signal. In addition, some of the same considerations that apply to the analysis of fMRI data apply equally to the analysis of fNIRS.

The ability to reconstruct images in three dimensions from NIRS data, as in diffuse optical tomography (DOT), holds much appeal, as the depth localisation of functional responses is improved. However, these images are still subject to noise and systemic variation, and in the solution of the inverse problem the location of activation is biased towards more superficial regions.

Although several early studies have established the correspondence between oxyhaemoglobin (oxyHb) and deoxyhaemoglobin (deoxyHb) signals measured with NIRS and the BOLD signal measured with fMRI in individual subjects [1, 2, 3], a question of relevance to NIRS researchers is whether similar conclusions would be drawn from the same population and task, measured with NIRS or fMRI [4]. Two studies have recently directly or indirectly addressed this question for NIRS [4, 5], but no such investigation has been done for images reconstructed using DOT techniques.

In this thesis we use the DYNOT (DYnamic Optical Tomography) system, a commercially-available NIRS imaging system by NIRx Medical Technologies, NY, to examine selected topics of current relevance in neuroimaging of the sensorimotor system using fNIRS/DOT. Because facilities for simultaneous imaging were not available, we perform the same experiment twice, in 11 of the same subjects, once using fNIRS and once using fMRI performed on a 3T Siemens Allegra scanner, in order to determine whether broadly similar results can be obtained at the group level using each technique.

First, ipsilateral activation and laterality effects to motor and noxious cold stimulation are investigated in a conventional neuroimaging block design. These have previously been studied using fMRI with some conflicting results, but not previously using NIRS imaging. Second, in a novel task, we investigate the modulation of interhemispheric functional connectivity in the sensorimotor system to motor and noxious cold stimulation. Because systemic interference is known to affect NIRS data, and may alter the spontaneous haemodynamic fluctuations used to assess connectivity in both fMRI and NIRS, physiological recordings of pulse or ECG and respiration were performed simultaneously with each scan.

Although strictly DOT refers to 3D imaging using NIRS measurements, throughout this thesis we use the terms NIRS or NIRS imaging to refer to DOT images reconstructed from multichannel NIRS measurements.

Thesis outline

This thesis consists of two parts. Part I relates primarily to NIRS, although a description of fMRI techniques is included to highlight similarities and differences between the two modalities. Part II describes a sensorimotor experiment with several components, which was conducted twice, once with fMRI and once with NIRS.

In chapter 2, the principles behind neuroimaging with functional MRI and NIRS are described, with particular emphasis on sources of noise, which may be shared, or specific to one modality. Various factors that affect the preprocessing and analysis of NIRS data are discussed, to introduce the options from amongst which a prospective NIRS researcher might have to select.

Chapter 3, which has been previously published in [6], considers and compares several different methods for the removal of artefacts in NIRS data caused by motion. The signal from imaging channels with negligible distance between the source and detector is used as an indicator of head motion, instead of using an additional sensor. Results are evaluated using NIRS data sets containing deliberate head motion.

The investigation of a motor execution and observation task using NIRS in single subjects is described in chapter 4. Adaptations required to analyse DOT images with a software package intended for fMRI data are described. Results of the investigation are discussed in terms of the consistency of oxyhaemoglobin (oxyHb) and deoxyhaemoglobin (deoxyHb) responses, and the impact of data quality. The final section of this chapter presents an investigation of the effect of different preprocessing parameters and design block length on the rate of false positive results in group analyses.

Chapter 5, the first in part II, describes the subjects, task and imaging for a sensorimotor experiment assessing autonomic and cerebral responses to a finger tapping task and to noxious cold stimulation. The task consists of two runs of motor and cold stimulation in a 12 s alternating block design, as conventionally used in fMRI

experiments. This is followed by two runs of motor and cold stimulation and resting fixation with longer block length to allow for the assessment of steady-state inter-regional connectivity during each task condition. The results of the analysis of physiological data are then presented. Chapter 6 describes an attempt to register the locations of NIRS probes to individual subjects' MRIs and evaluate the registration accuracy using markers. Because of poor results, an alternative approximate registration method is adopted.

In chapter 7, activations and deactivations to left and right hand motor tasks, particularly in ipsilateral primary motor cortex (M1), are investigated in our group of right-handed subjects using both functional MRI and NIRS. The effect of tapping hand: dominant or non-dominant, on the degree of ipsilateral and contralateral activation is investigated using region of interest (ROI) analyses and voxelwise statistics, and the relationship across subjects between the magnitude of ipsilateral responses and contralateral responses in motor regions is examined in both modalities. The group results from analysis of BOLD fMRI data and the NIRS oxyHb parameter are found to be in broad agreement. In chapter 8 activations and deactivations to a noxious cold stimulus are investigated in a similar manner.

Chapter 9 describes the measurement of interhemispheric connectivity at rest between primary sensorimotor areas that are activated and deactivated by the tasks. The modulation of inter-regional connectivity by task condition is investigated using both fMRI and NIRS. Simultaneous changes in systemic variables are accounted for using the RETROICOR algorithm [7], and regression of heart rate, heart rate variability and respiration variation signals.

Finally, in chapter 10 a synopsis of the most important findings of this theses is presented, the limitations are discussed and recommendations made for future studies using NIRS/ DOT.

Part I

Processing and analysis of brain imaging
data: unresolved issues for NIRS

Chapter 2

Functional brain imaging: fMRI and NIRS

Although the first use of fMRI for studying the haemodynamics associated with brain function [8, 9, 10, 11] does not significantly pre-date the use of NIRS [12], the enormous interest in fMRI has led to huge growth in the field, resulting in the development of advanced and rigorous techniques for processing, analysis and interpretation of fMRI data. There are several software packages for the analysis of fMRI data, many of which are freely available, and although the methods used by these programs differ in minor ways, there is to a large extent standardisation of generally accepted analysis techniques.

Functional NIRS on the other hand has developed somewhat less rapidly and there has been less standardisation of preprocessing, artefact rejection, and statistical analysis; and intersubject registration and comparison is an ongoing problem which is just starting to be addressed. This is possibly due to the variation in instrumentation used by different research groups, where for example the number of measurement channels may vary between 1 and 128 or more, making registration and multiple comparison correction either more or less relevant.

Some of the issues affecting the processing and analysis of brain imaging data that have been resolved or standardised for MRI differ widely in published NIRS studies. These include

- identification and rejection or filtering of artefacts, for example due to motion
- registration to anatomical locations and between subjects
- analysis of the task-related response, which may be model-based or model-free
- accounting for temporal autocorrelation
- identification of and compensation for systemic effects (physiological noise)
- correction for multiple comparisons

- group-level comparisons

Both fNIRS and fMRI measure the evoked haemodynamic response to functional stimulation, however, the different biophysical principles behind the methods means that there are some considerations unique to one or other of the techniques. The physical principles behind the imaging techniques are described in sections 2.1, 2.4 and 2.5. Sections 2.2 and 2.6 contain a description of the types of noise present and preprocessing required for fMRI and NIRS respectively. Intersubject registration and the analysis of fNIRS data is dealt with in sections 2.7 and 2.8.

2.1 Functional MRI: the Blood Oxygen Level Dependent (BOLD) signal

The usual measurement parameter in fMRI is the BOLD signal, which, broadly speaking, depends, as its name suggests, on the oxygenation state of blood. However, the oxygenation state in turn depends on flow, volume and oxygen consumption, and, although models exist that attempt to elucidate this relationship [13], the exact contribution of each of these to the BOLD signal is not yet entirely clear.

Although the mechanism by which neuronal demand increases blood flow is not known, the increased BOLD signal in response to neuronal activity results from an oversupply of oxygenated blood to the area. Because oxygenated haemoglobin (oxyhaemoglobin) has different magnetic properties from deoxyhaemoglobin, this changes the transverse relaxation rate ($T2^*$) of intra- and extravascular protons. The relative decrease in paramagnetic deoxyhaemoglobin resulting from an increase in regional cerebral blood flow thus causes an increase in BOLD signal. BOLD percentage signal change is thought to increase linearly with echo time (TE) in grey matter and blood vessels [14], where the maximum BOLD contrast (“active” versus “rest”) occurs at a TE equal to the resting $T2^*$ of grey matter.

Because the BOLD signal is sensitive to the concentration of deoxyhaemoglobin [15], signal changes occur mostly because of haemodynamic changes in the veins, rather than in arteries, although a T1-related flow component may also occur, due to the inflow of unsaturated spins into the imaging slice. Contributions to the BOLD signal come from the macrovasculature (large arteries and veins), microvasculature (arterioles, venules and capillaries) and extravascular tissue.

BOLD vessel sensitivity depends on the field strength, echo time (TE) and the pulse sequence used [16, 17]. The more commonly used gradient echo (GE) BOLD is sensitive to inhomogeneities of all sizes, and therefore represents both intravascular and extravascular signal contributions from small vessels as well as draining veins. At low field strengths the veins contribute most to the BOLD signal, but at high field strengths larger contributions from the capillaries and extravascular tissue is observed [16]. However, there remains a significant extravascular contribution from tissue water surrounding larger veins.

Spin echo (SE) BOLD is less commonly used, but is considered to have greater specificity, since it is sensitive to small compartments, such as red blood cells and capillaries. This makes SE BOLD sensitive to intravascular protons in vessels of all sizes, and extravascular signal surrounding small vessels such as capillaries, which

are closer to the site of neuronal demand than are draining veins. In spite of the fact that SE BOLD is more spatially specific, and less subject to signal dropout, it is also less sensitive to functional BOLD signal changes, since these arise from the same inhomogeneities that can be refocused using a spin echo pulse. At higher field strengths the T2 and T2* of blood decreases faster than that of grey matter, so at long TE (>70 ms) the sensitivity of both GE and SE BOLD towards extravascular signal increases. However, high field strengths also increase physiological noise and signal dropout.

For fMRI a scanner with high-performance gradients and uniform field density is required. The Siemens Allegra 3T scanner used in this study is a head-only scanner designed for brain research, and has a maximum gradient strength of 40 mT/m and slew rate of 400 T/m/s. The relatively high field strength offers good signal-to-noise ratio and BOLD contrast, and although physiological noise is increased at 3T relative to 1.5 T, susceptibility-based distortions are minimised by ultra-short echo-spacing.

2.2 Noise sources in fMRI

There are many different sources of signal fluctuation in BOLD imaging, some of which have complex effects on the image time series. Noise sources include

- scanner instabilities
- thermal noise
- subject motion
- changes in B0 field homogeneity due to the shifting of organs on respiration
- motion of blood vessels and CSF caused by respiration and cardiac pulsation
- cardiac-related flow changes, causing inflow effects (fresh spins) resulting in T1-dependent signal increases
- cardiac and respiration related changes in spin density caused by blood volume changes
- changes in T2* relaxation due to changes in blood oxygenation state, which may be caused by changes in flow, volume or oxygenation due to cardiac pulsation, respiration, or ongoing metabolic activity

2.2.1 Scanner noise

Low frequency drift below 0.015 Hz in the fMRI T2* signal has been investigated previously, and has been found to be greater in regions with large spatial intensity gradients in both cadavers and non-homogeneous phantoms as much as in healthy volunteers. Less drift occurs in a homogeneous phantom, suggesting that the cause of the drift is slight changes in the local magnetic field due to scanner instabilities, which causes a more prominent partial volume effect in areas with large spatial changes in intensity [18].

2.2.2 Cardiac pulsation

Cardiac pulsation, respiration and brain motion can cause fluctuations in signal intensity and phase [19]. The traditional idea has been that cardiac pulsation should affect mainly the arterial compartment due to propagation of the pulse pressure wave, and that respiration is apparent mainly in the veins due to blood volume changes [20]. Because of the dampening of periodic pressure changes along the circulatory system, cardiac pulsation should not be expected in small vessels and capillaries. However, the veins in the head do exhibit pulsatile blood flow because of the fixed cranial volume and compression from pulsating brain tissue. For this reason cardiac-related BOLD signal changes also occur around the venous sinuses [21].

It has been suggested that cardiac noise in a BOLD time series is due to an interaction of steady-state free precession (SSFP) effects and field changes from cardiac and respiratory movement in regions where the T2 relaxation times are much longer than the repetition time (TR), especially in CSF. If this were the only source of cardiac noise it should not be significant in BOLD-weighted voxel time series with a long TR, and undersampling should not cause aliasing of the cardiac signal [22, 23]. However, even when crusher gradients are applied to eliminate SSFP in the CSF, cardiac pulsations are still present in arteries, veins and grey matter, and hence must be at least in part due to genuine T2* effects or vessel motion [24].

Cardiac-induced noise has been found to be dominant near large vessels [25], including veins, arteries and CSF [21, 26, 20] and in the midbrain [27], but has also been found in grey matter [20, 27]. Dagle et al. [21] found strong cardiac-related BOLD signal variation in almost 30% of brain voxels, but especially near large vessels and CSF. This affected medial areas of the brain, the anterior temporal lobes and insula, and the anterior interhemispheric fissure in the medial frontal lobes, as well as the sigmoid transverse and superior sagittal sinus regions.

2.2.3 Respiration-induced signal changes

Respiration can affect the fMRI BOLD signal in several ways. It may produce motion of the head or brain parenchyma, as well as changes in static magnetic field homogeneity due to moving organs in the chest. This leads to susceptibility changes, particularly at the base of the brain, which decreases with increasing distance from the chest [28, 29, 19]. The resulting distortion in the phase encoding direction becomes greater at higher field strengths [30, 31] and varies in space as well as time [32], making respiration-related variation dependent on local image properties, rather than being simply additive [30].

Several strategies have been used to attempt to correct for respiration-induced susceptibility changes. These include K-space correction of phase variation [33], real time B0 shimming [31], changing the resonance frequency in real time to match the respiration-induced offset [34], and global [35], 1D [32] and 2D navigator correction [36].

As well as affecting the static magnetic field, respiration also has purely physiological effects on cerebral haemodynamics, which therefore also affect imaging modalities other than fMRI. Changes in arterial blood pressure (ABP) and hence cerebral blood flow are also caused both by mechanical consequences of respiration and by the effects of the autonomic nervous system. By the first mechanism, a change in intra-thoracic

pressure on inspiration or expiration causes changes in central venous pressure. On inspiration, the decreased intra-thoracic pressure causes increased venous return to the heart along the steeper pressure gradient. This increases cardiac output through increased cardiac contractility, and hence affects ABP.

Secondly, the phenomenon known as respiratory sinus arrhythmia (RSA), thought to be mediated by the arterial baroreceptor reflex, causes slowing down of the heart on expiration, and acceleration of heart rate during inspiration, thereby modifying cardiac output and ABP. This is achieved through the activation or inhibition of the parasympathetic nervous system which exerts its influence on the heart through the vagus nerve [37].

A further mechanism by which respiration affects cerebral blood flow is through variations in end-tidal carbon dioxide pressure (end-tidal $p\text{CO}_2$), since arterial CO_2 causes cerebral vasodilation [20]. This causes slow oscillations in BOLD signal which may be confused with the correlated fluctuations exhibited by functionally connected networks during the resting state [38].

In fact, both physiological and magnetic field effects of respiration have been found in functional MRI [20]. Respiratory-induced noise has been found to be prominent in the cerebral veins [26, 20, 25], as well as in CSF [25, 39], and at the edges of the brain [25]. Because most sources of physiological noise have multiple different effects on the fMRI signal, the signal characteristics may vary between tissue types and brain regions [27].

2.2.4 Aliasing of systemic noise

Some effort has been made to disassociate correlated slow fluctuations in the BOLD signal, which are used to examine resting state connectivity, from physiological noise. Using a short TR, Cordes et al. [26] found that connectivity resulted mostly from correlations below <0.1 Hz, and not at respiratory and cardiac frequencies. Using independent component analysis (ICA) decomposition Beckmann et al. [40] also found that low-frequency patterns appeared primarily in grey matter, while separate blood vessel networks were found with slightly higher peak frequencies. However, the low sampling rate of fMRI image acquisition (about 2 s for whole brain acquisition) means that the temporal variation of BOLD signal caused by cardiac and respiratory cycles is aliased into the low frequency range [41]. Some resting state correlation arises due to this aliased noise [26]. Lowe et al. [42] observed that increasing the TR introduced spurious correlations, which was attributed to the increasing contribution from aliased cardiac and respiratory noise.

Undersampling of the cardiac rate can therefore confound measures of functional connectivity, particularly when heart rate changes due to the task or pharmacological manipulations [23, 43].

Many techniques have been used to reduce the effect of physiologically-induced noise in fMRI time series. These include the use of fixed bandwidth finite impulse response band-reject digital filters [44] to eliminate signal at the cardiac and respiratory frequencies, Fourier series fitting in the image domain [7], adaptive filtering [45], and regressing the signals from the time series during analysis [25]. The latter three methods require simultaneous recordings of physiological variables.

To overcome the problem of physiological noise in functional connectivity studies, one must either take simultaneous measurements of heart beat and respiration to regress out of the time series, or critically sample these signals to prevent aliasing. It is difficult to estimate cardiac and respiratory noise directly from

the fMRI data, however, the spatial patterns of physiological noise have been found to be rather consistent over time [46], and ICA has been used to find subject-specific spatial patterns of physiological noise, allowing the temporal noise signal to be estimated in subsequent scans [27]. It has been shown that ICA techniques are reasonably good at separating respiratory and cardiac noise sources from grey matter fluctuations, even when these signals are aliased to lower frequencies [47, 40]. Alternatively, a global pattern of variation can be removed from the time series by subtraction or partial correlation of the average brain time course [48]. There is some evidence that the preprocessing strategy chosen can have an effect on subsequent measures of connectivity [49].

Using faster sampling rates it has been shown that low frequency correlations still exist when physiological noise is regressed out or critically sampled [42, 26, 50]. However, the cardiac cycle is not completely regular: there are differences in the length of the diastolic period that contribute to variation in the time interval between beats [21]. Cardiac variability at respiratory and lower frequencies is a potentially important source of low frequency noise.

Certain sources of “noise”, namely those originating from the subject, may be common to both fMRI and fNIRS time series. However, even these common sources of noise may manifest differently in each of the imaging techniques due to their different physical principles.

2.3 Analysis of fMRI data

In the design of fMRI experiments, the most commonly used paradigm is the ‘block’ design, also sometimes called a box-car design, in which a series of trials of one condition is presented in a continuous block with duration ranging from 10 s to a minute. Repeated blocks of two or more different conditions are presented in an alternating manner, and the BOLD signal measured during blocks of one condition is then compared with that from blocks of another condition. This design enables differences in regional brain activity to be detected with good statistical power. By contrast, in an event-related paradigm, individual trials of different types are presented in random order. Because the BOLD response to repeated events sums linearly, the signal contribution from individual trials of one type can be extracted and directly compared to the contribution from trials of a different condition [51].

The most common approach to fMRI data analysis is a mass-univariate approach in which the haemodynamic response is estimated at each voxel, independently of all other voxels, to produce a statistical parametric map (SPM). This approach is offered by the SPM fMRI analysis software, as well as many other widely available software packages.

The generation of a statistical map involves the detection of voxels in which a haemodynamic response is present. This may be done either making no assumption about the form of the haemodynamic response, for example averaging the signal over time, or by detecting signal that correlates with a specified haemodynamic response function. The former, model-free, method may be less powerful than extracting activity corresponding to the known characteristics of the haemodynamic response function. However, the model-based method is less sensitive if the modelled haemodynamic response does not match the shape of the actual response.

2.4. NEAR INFRARED SPECTROSCOPY (NIRS): OXYHAEMOGLOBIN, DEOXYHAEMOGLOBIN AND CEREBRAL BLOOD VOLUME (CBV)

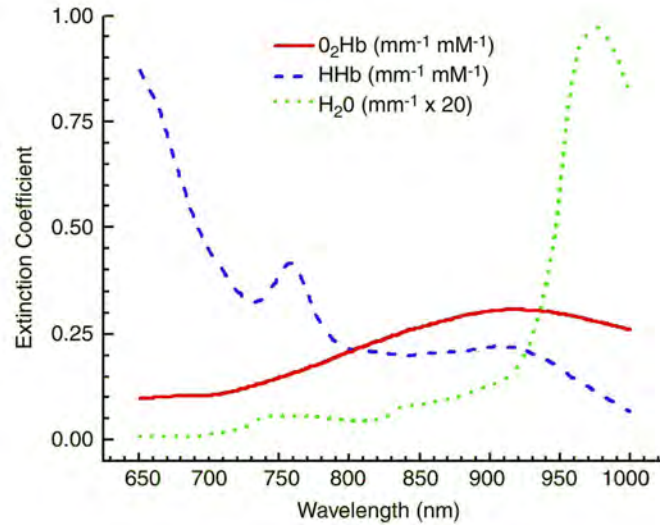


Figure 2.1: Absorption spectra of deoxyhaemoglobin (*HHb*), oxyhaemoglobin (*O₂Hb*) and water.

Most often, fMRI experiments are repeated for several subjects from a population, and group level analysis is required to combine the results across multiple subjects. In the early days of fMRI, fixed effects analyses were often performed, in which it is assumed that the response and its variance is the same across all runs, sessions and subjects and that variation between subjects is not of interest. A more appropriate method in most cases is a random effects analysis, which assumes that the measurements are a random sample from a larger population. Unlike fixed effects analysis, random effects analysis allows inference to be made about the population from which the sample is drawn, by considering the effect size relative to the between-subject variance [51].

2.4 Near infrared spectroscopy (NIRS): Oxyhaemoglobin, deoxyhaemoglobin and cerebral blood volume (CBV)

Near infrared spectroscopy (NIRS) [52] makes use of the fact that changes in haemoglobin concentration in tissue affect the absorption of infrared light by the tissue. Near infrared light sources placed on the scalp emit light at two or more wavelengths between 650 nm and 850 nm, in the region where limited absorption by haemoglobin and water allows light to penetrate tissue sufficiently. The absorption spectra of oxy- and deoxyhaemoglobin and water are shown in figure 2.1. NIRS studies of the brain usually use a wavelength on each side of the isobestic point of haemoglobin at 800 nm [53].

Detectors a few centimetres away from the source measure the light that is transmitted through the skin, scalp and skull. The light attenuation, which is proportional to the distance that the light travels and the absorption of the molecules in the medium, is converted to concentrations of oxyhaemoglobin (oxyHb) and deoxyhaemoglobin (deoxyHb), using the modified Beer Lambert law in equation 2.1:

$$\Delta A = \log\left[\frac{I_0}{I}\right] = \sum_i a_i \cdot \Delta c_i \cdot DPF \cdot d \quad (2.1)$$

where ΔA is the change in attenuation (optical density), I_0 is the emitted light intensity, I is the intensity of light transmitted through the medium, a_i is the specific extinction coefficient of each absorbing compound i (in micromolar per cm), Δc_i is the change in concentration of each absorbing compound (in micromolar), and d is the distance of the path between source and detector. DPF is a differential pathlength factor which accounts for the increased distance travelled through biological tissue because of the large amount of scatter. The additional amount of light lost to scatter is unknown, so using continuous wave NIRS it is not possible to calculate absolute chromophore concentrations, but by assuming constant light attenuation due to scatter, changes in oxyhaemoglobin and deoxyhaemoglobin concentration may be calculated.

The DPF depends on tissue type, optode geometry and wavelength and can therefore vary between subjects and systems [54]. An incorrect DPF causes incorrect estimates of oxy- and deoxyhaemoglobin concentrations, and introduces crosstalk between the two measurements [55].

2.4.1 Continuous wave, frequency domain and time domain NIRS

Continuous wave (CW) NIRS instruments have a source that either emits light at constant intensity, or is modulated at a low frequency (a few kHz) in order to exploit phase-locked signal detection. These instruments only provide information about the intensity of the light transmitted through the medium. In frequency and time domain instruments, the light source is intensity modulated between 50 and 500 MHz, or pulsed with a duration of a few picoseconds, which makes it possible to measure respectively the phase or the temporal delay of the light propagation, as well as its intensity. In addition to allowing the measurement of the optical path length and hence the DPF, this enables absolute absorption and scattering properties of the tissue to be estimated [53].

In contrast with frequency and time domain methods, CW NIRS has poor depth resolution, poor ability to separate the effects of absorption and scatter, and it only allows the calculation of relative and not absolute chromophore concentrations. Despite these limitations, CW systems are the most frequently used for functional brain imaging, perhaps due to their relatively better SNR, faster sampling rates, lower cost, and greater ease of use.

2.4.2 Depth resolution of NIRS

The penetration depth of near infrared light depends on the separation distance between the light source and detector: it is often assumed to be about half the source-detector distance [53]. However, the adult head is not a homogeneous medium, and in reality the low-scattering cerebrospinal fluid layer and the highly scattering skull have a large effect on the NIRS signal at source-detector separations greater than 3 cm, and the penetration depth does not increase with separation distances greater than this [56, 57]. A separation distance of 3 cm has been suggested to be sufficient to sample cortical tissue (at approximately 1 cm depth)

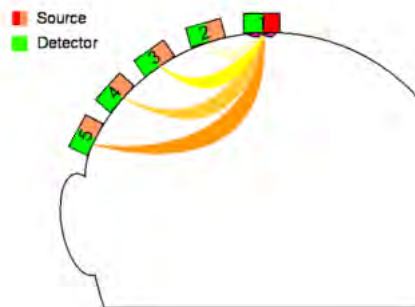


Figure 2.2: Banana shape of photon density path from source to detector.

[58, 53]. One confound in CW NIRS imaging is the contribution of signal from superficial tissues, which cannot be fully characterised or compensated for. At small source detector separation distances, signal contribution is entirely from superficial tissue such as skin, whereas at larger distances, although the signal is smaller due to increasing light attenuation by absorption and scattering, it is more heavily weighted towards deeper tissue. However, a signal contribution from superficial tissue is possible even at optimum separation distances, as intensity measurements are much more sensitive to surface than to deeper tissues. This is because of the ‘banana’ shape of the volume of tissue interrogated, which is narrow near the source and detector and very broad in the middle [53] (figure 2.2).

2.4.3 Vessel sensitivity

Because it measures changes in both oxygenated and deoxygenated haemoglobin, NIRS is sensitive to both arterial and venous blood. However, because of the high probability of photon absorption in larger vessels, the technique has a theoretically greater sensitivity to small vessels and capillaries. The total haemoglobin (totHb) signal can be used as an indicator of cerebral blood volume (CBV), based on the assumption of a constant haematocrit.

2.5 Diffuse optical imaging

Concentration changes measured with NIRS can be mapped spatially with low resolution using tomographic or topographic techniques. Because of the diffuse nature of light in biological tissue more than 1 mm from the source, these techniques are known as diffuse optical imaging, topography or tomography (DOI, DOT). Topographic imaging, in which a two dimensional image is created from non-overlapping measurements at a single source-detector separation, has been used far more often than tomography, but has limited lateral resolution and no depth separation.

Using high-density DOT grids, measurements at different source–detector separation distances provide information about different depths, and overlapping measurements provide superior resolution and localisation [59, 60]. High-density probes are not always practical, however, depending on the area of interest, and the subject’s hair colour and thickness [61]. In the case where multiple overlapping sets of sources and detectors are used, three dimensional reconstruction of the superficial internal optical properties of the head is possible. A full tomographic data set can be acquired rapidly enough for the optical properties to remain approximately stationary, and fast reconstruction algorithms allow for three dimensional functional imaging of the brain [62]. When multichannel measurements are used for tomographic reconstruction an estimate of the DPF is not required [63].

Image reconstruction from diffuse optical measurements is an inverse problem, which is ill-posed and underdetermined because the large amount of scatter makes each measurement sensitive to the whole imaged volume. Solving the inverse problem involves first solving the forward problem: a model of light propagation in tissue must be used to predict the distribution of light in the imaged area. This allows the measurements to be predicted from the model, and generates a sensitivity matrix which relates the surface measurements to the internal optical properties of the medium. The image is reconstructed by inverting the sensitivity matrix to solve the inverse problem. However, because of its ill-posed nature, some form of regularisation is required [53].

2.5.1 Modelling light transport

For diffuse optical imaging, the diffusion equation derived from the radiative transport equation, is commonly used. This assumes that light propagation is isotropic, which is usually true in tissue but the assumption does not hold near the source, near the surface, near internal boundaries, in anisotropic tissues such as skin and muscle, and in regions where absorption is greater than scatter, such as CSF.

2.5.2 Solving the forward problem

The forward problem $y = F(x)$ involves calculating simulated data y , given a forward operator F and knowledge of the internal optical properties x . The forward problem may be solved analytically using Green’s functions; statistically, using techniques such as the Monte Carlo method; or numerically, using methods such as finite element (FEM) modelling. Solutions to Green’s function only exist for simple objects. Monte Carlo methods are commonly used in diffuse optical imaging, however, a finite element mesh can be used to model complex geometries with inhomogeneous optical properties.

2.5.3 Image reconstruction

To reconstruct an image the inverse problem $x = F^{-1}(y)$ must be solved to determine the internal optical properties x , given data y . This problem can be linearised by reconstructing the difference between two similar states, where the actual optical properties x are close to an initial estimate x_0 and the measured data y are close to the simulated measurements y_0 . The Born approximation linearises the problem to $\Delta y = J\Delta x$

by neglecting higher order terms of the Taylor expansion of $x = F^{-1}(y)$, while the Rytov approximation linearises the change in log intensity [53].

Image reconstruction then involves inverting the matrix J using truncated singular value decomposition or Tikhonov regularisation to minimise the effect of noise and modelling errors.

2.5.4 Incorporating a priori information

The quality of the image reconstruction can be improved by using prior information, for example by incorporating anatomical information into the forward model, or by considering temporal information from auxiliary physiological signals such as the heart rate, respiration and vasomotion. If physiological changes occur on a shorter time scale than the image acquisition, the optical properties change during image acquisition. The Kalman filter has been used to improve image reconstruction by modelling these physiological changes [64].

2.5.5 The DYNOT (dynamic optical tomography) system

The DYNOT (NIRx Medical Technologies, New York) continuous wave imaging system used in this study uses time-division multiplexing of 30 sources and parallel detection by 30 detectors. Frequency modulated light from laser diodes is coupled to an optical switch which sequentially directs light at wavelengths of 760 nm and 830 nm to each illumination fibre. Light collection occurs simultaneously at the 30 detectors, each of which uses a lock-in amplifier to allow separation of the signals at different wavelengths. The detector gain is individually adjustable for each channel, offering a wide dynamic range (90 dB) in detection sensitivity [65], which allows for tomographic imaging. Complete tomographic data sets can be acquired at a sampling rate of 1.8 Hz. This ability to perform rapid three-dimensional measurements suggests a possible equivalency with fMRI, at least for imaging haemodynamic activity in the cerebral cortex. It is therefore particularly relevant to compare NIR images from the DYNOT system to similar data acquired using fMRI.

2.6 Noise removal in functional NIRS

There are multiple sources of noise and artefact in functional NIRS, which have distinct statistical properties. These include [66, 67]: instrument noise, such as electronic (Johnson-Nyquist) noise and shot noise, which follows a Poisson distribution; low frequency drift, which may be introduced by small instabilities in the laser diode light sources; measurement noise, which is assumed to be Gaussian random white noise; and finally noise introduced by the human subject, which includes motion artefact and “global” oscillations from systemic sources (pulse, respiration, blood pressure Mayer waves and other low frequency oscillations). Since photons reflected from brain tissue must travel through the skin, skull and dura before reaching a detector on the scalp surface, there is also interference in the NIRS signal arising from fluctuations in the superficial layers of the scalp.

Preprocessing is an essential requirement for functional NIRS data. As much noise as possible should be removed or regressed from the time series to enable better detection of task-related changes and to enhance the

quality of tomographic image reconstructions. Routine preprocessing for functional NIRS data primarily involves fixed-bandwidth high and low pass filtering before signals are converted to oxy- and deoxyhaemoglobin concentrations. Commonly used high pass cutoff frequencies range from 0.004 to 0.1 Hz and low pass from 0.1 Hz to 0.8 Hz [68]. Whereas this filtering is effective in eliminating much of the low frequency instrument noise and white measurement noise as well as physiological noise which falls outside of the filter pass-band, some of the noise originating from the human subject may remain. A significant amount of postprocessing is almost invariably needed to allow functional activation to be detected in the presence of possible subject movement, heart beat and respiration effects, and other physiological variation [67].

2.6.1 Systemic interference

Because light spreads as it penetrates deeper into the tissue, NIRS measurements are much more sensitive to absorption changes in the superficial layers of the scalp than those in the cerebral cortex. This means that NIRS-measured signals include contributions from systemic processes such as cardiac pulsation, respiration, and blood pressure changes, which manifest as haemodynamic changes in the scalp and underlying cerebral tissue. This physiological “noise” can obstruct the detection of smaller functional responses, although it may also contain interesting information about vascular physiology, such as vasomotion or autonomic regulation [69].

Removal of superficial and global signals has been addressed using linear regression [2, 70, 60, 68] and least mean square adaptive filtering [71, 72] to separate physiological variation detected in short-separation channels from the deeper brain signal. Eigenvector-based spatial filtering [73] and independent component analysis (ICA) [74] have been used for similar purposes. Adaptive filtering and regression of auxiliary physiological measurements have also been used to remove contributions from cardiac pulsation and respiration [75, 76].

Although is not common practice to measure physiological signals simultaneously with NIRS brain signals during motor tasks, it is difficult to interpret measured haemodynamic changes as localised task-related activity if changes in the global systemic or brain resting state are occurring at the same time [77]. Some studies have included a measure of heart rate [78, 79, 80], but only rarely blood pressure, respiratory motion or skin flux [81]. Heart rate measurements have rarely been used to investigate the influence of systemic changes on changes in cerebral haemodynamics [81] even though NIRS data may contain physiological contributions from breathing, heart rate, and Mayer waves of arterial pressure.

A few investigators have simultaneously monitored mean blood pressure, heart rate and scalp blood flow, and found significant changes in these variables during motor [82] and anagram-solving tasks [83, 84], which in some cases correspond to cerebral haemodynamic changes measured with NIRS. This can result in apparent activation of a control region which is not expected to be activated by a particular task [83]. In particular, stressful tasks may elicit an emotional response which produces changes in blood pressure and may cause changes in scalp blood flow that are picked up as task-related changes in oxyHb and deoxyHb as measured by NIRS. The effect of systemic changes should therefore be considered in NIRS analysis [83, 84, 77]. Simultaneous blood pressure changes, manifesting haemodynamically both outside and within the brain, have been shown to confound detection of functional responses using NIRS [85].

Franceschini et al. [82] attempted to correct for the systemic contribution by subtracting the haemoglobin concentration changes at a location outside the region of interest from haemoglobin concentration changes measured at all other locations. This produced a more localised oxyHb response, comparable to that of deoxyHb, without changing the deoxyHb response.

Physiological fluctuations may be separated from the evoked haemodynamic response using simultaneously acquired physiological data and regression or adaptive filtering, or using blind source separation techniques such as Principal Component Analysis and Independent Component Analysis [86]. However, these techniques are not universally used, despite significant systemic effects during tasks involving some degree of physical exertion [87].

2.6.2 Motion artefact

One important form of subject-introduced noise is motion artefact, which may affect the measured signal in several ways. First, the uncoupling of the source or detector from the skin may result in sudden increases or decreases in the measured light attenuation. Second, gravitational effects may result in changes in blood flow or volume in parts of the head. Effort is made when designing NIR instruments to address the first problem: probes are fitted firmly to the head using a cap or frame to minimise the effects of motion, and optical fibres are placed at right angles to the scalp surface. However, motion artefacts cannot always be eliminated entirely. This is a particular concern in studies on patients or children - populations for which NIRS imaging is otherwise well suited, given its portability, cost-effectiveness, and ease of use compared to other brain imaging techniques.

Many NIRS studies concentrate on identifying motion artefact in the time series, and then removing the affected blocks or events from the analysis. Not many studies also attempt to clean the signal of motion artefact, and few evaluate the efficacy of their artefact removal procedures. Among the methods used to filter motion artefact are adaptive filtering, Wiener filtering [88], and principal component analysis (PCA) [89, 90, 91]. The former two require some knowledge about the expected signal variation caused by motion, whereas the latter assumes that the principal components accounting for the largest variance in the data set correspond to motion artefact. All methods require that the artefact be uncorrelated with any signal of interest.

Body-movement artefacts are larger and occur more rapidly than genuine haemodynamic changes, and are more irregular than system noise [92]. Most motion detection methods have relied on detecting changes between successive samples that are larger than a specified threshold value [93, 94], and eliminating these blocks from the analysis. In a departure from this strategy, Sato et al. [92] introduced a wavelet-based method for detecting body-movement artefacts in optical topography, producing good motion-detection results.

2.7 Optode placement and intersubject registration

In functional MRI it is a simple matter to ensure the area of interest is being imaged, and intersubject registration is achieved by transforming brain images from all subjects to fit a template brain in a stereotac-

tic co-ordinate system for comparison. Because anatomical information is not available in NIRS, accurate positioning of optodes over an area of interest is a challenge, and it is less straightforward to register data, both between sessions and subjects, and to anatomical images so that the NIRS signal can be localised to a particular region of cerebral cortex.

Ideally optodes should be positioned stereotactically using a neuronavigation device before data acquisition [95, 96], but most often in NIRS studies, the optodes are positioned using the International 10-20 system for electrode placement [97]. The relationship of the 10-20 positions on the head surface to underlying cortical anatomy in stereotactic co-ordinates have been described probabilistically [98]. In some studies where there is a typical expected response, in primary motor cortex for example, if no signal change is observed the optodes can be repositioned until the expected signal is observed [99, 100, 101, 102, 103].

To confirm after the fact that the intended brain regions were interrogated by NIRS, fiducial markers at optode locations are often used, with high resolution T1-weighted 3D MRI images [104, 105, 79, 106, 107, 108, 80, 2]. Alternatively, optode surface locations in fNIRS may be measured in 3D with a magnetic digitiser and registered to individual subjects' MRIs using landmarks visible in both modalities [63], or alignment of head surfaces [109]. These techniques require an MRI of each subject, thereby negating the cost advantage of NIRS, although if surface-based alignment is used only one MRI is required for each subject, instead of having to acquire an MRI image for each NIRS session.

Digitised optode surface locations in fNIRS also may be transformed directly to MNI space so that an anatomical MRI of each subject is not necessary. This was first done using the 10-20 electrode locations and knowledge of their probabilistic MNI co-ordinates [110]. Based on this, several groups are beginning to register optode locations directly to an atlas or brain template, bypassing the need for individual MRIs [111, 112, 113, 114, 115]. Virtual registration to MNI space using knowledge of the deformation of the optode holder may also be performed [116], if optodes are placed in a reproducible manner. This technique eliminates the need for digitisation of 3D co-ordinates, but it is not yet widely used [81].

In DOT, the forward problem may be solved once optode registration has been performed using knowledge of individual [111] or atlas [111, 114] anatomy.

Most of these registration techniques do not, however, ensure accurate optode positioning before data acquisition, although they may justify rejection of data [81]. Recently a method has been proposed to locate the appropriate 10-20 positions for optode placement given the MNI co-ordinates of a target region of interest, using a physical model of the ICBM152 template [115]. Although registration efforts are sometimes not reported, effort should be made to report the registration technique, and the degree of misalignment between intended and actual channel locations [87].

2.8 Analysis of fNIRS data

In functional MRI, the spatial proximity of measurements is often used in the analysis of image time series, and the evoked response is represented by a combination of basis functions. By contrast, until recently information from neighbouring measurements was not often used in the analysis of NIRS data, and traditional time-series

analysis methods such as linear deconvolution have been used to retain information about the haemodynamic response, after band pass filtering to remove artefacts in the signal [69].

Unresolved issues affecting the analysis of fNIRS data include

- the specification of an appropriate haemodynamic model in the analysis of the task-related response
- selection of a method to account for temporal correlation
- correction for multiple comparisons over several measurement channels or image voxels
- comparisons at the group-level, which are complicated by vascular, anatomical and probe positioning differences between subjects

2.8.1 Model-based vs model-free analysis

The conventional approach to NIRS analysis has been model-free, consisting of block designs in which Hb concentrations during a task period and a control period are averaged together, and tested for significant differences using either a parametric [117, 104, 118, 119, 120, 121, 122] or non-parametric [123, 124] statistical test. This still appears to be the most widely used format for NIRS experiments, with event-related designs used far more rarely. Until recently, the most frequent approach to NIRS analysis has been a linear deconvolution, or event-related averaging which does not assume a fixed form for the response function, therefore avoiding the possibility of misspecification and different response functions for different subjects, brain regions and haemoglobin species [69]. The alternative, model-based, approach as is used in an SPM-type analysis in functional MRI, consists of fitting a haemodynamic response function (HRF) to the data using the general linear model (GLM) (e.g. [125, 126, 127]).

The good temporal correlation between the BOLD fMRI signal and the deoxyHb signal measured with NIRS and between oxyHb and ASL-measured blood flow [3], justifies the use of the GLM with an appropriate haemodynamic response function for NIRS [128], and since the BOLD response is closely related to deoxyhaemoglobin, there is justification for the use of the same HRF for deoxyhaemoglobin as for fMRI [3, 128, 69]. However, because of the different timing of the deoxyHb and oxyHb responses, it is not certain that the convolution of the paradigm with a single canonical haemodynamic response function for both haemoglobin species is most fitting [128, 69]. The basis functions most often chosen to model NIRS responses include a Gaussian function and its temporal derivatives [129] or a combination of gamma functions, as is often used for fMRI analysis [63]. Using a canonical basis set incorporating the temporal and dispersion derivatives of the canonical HRF is a common way to improve flexibility of model-based analysis. Although there is a strong correlation between the canonical HRF and deoxyHb, the weaker correlation between the canonical HRF and oxyHb/totHb is increased by including the temporal and dispersion derivatives in the specification of the HRF, and increased further if the HRF is approximated with multiple gamma functions [63]. A constrained parameter estimation approach has been proposed with NIRS in order to produce realistic HRFs using the basis set consisting of the canonical HRF and its derivatives [130]. Hu et al. [131] and Abdelnour et al. [132] have used an adaptive GLM to monitor haemodynamics in real time. In this method, the parameter

estimate of the canonical response function used is allowed to vary with time, so although a form for the haemodynamic response function is assumed, it acts as a prior rather than a strict constraint on the shape of the response as in the static general linear model approach.

The GLM method has the advantages of imposing a priori assumptions on the model, temporal smoothness for example, and reducing the number of unknowns, which improves the response detection efficiency and simplifies subsequent statistical tests [69]. And in spite of the limitations, GLM-based analyses of NIR data have successfully been used [125, 129, 128, 127] with a single haemodynamic response function (HRF) for both Hb species specified by a Gaussian kernel [125, 129, 127] or combination of gamma functions [132].

Plichta et al. [129] compared a GLM model-based analysis (of a rapid event-related design) with a model free analysis, using a Gaussian HRF with derivatives for both oxyHb and deoxyHb to analyse responses to visual stimulus with parametrically varying contrast. The magnitude of response estimates were similar with both approaches, although compared to the event-related averages the model was found to peak about 0.5 s too early. In control regions, however, the model-based method was found to produce far fewer false positives [129, 77]. This is especially true for oxyHb, which is more affected by systemic physiology. These results [129, 77] suggest that the SPM model-based approach may be more rigorous than traditional analysis methods for NIRS have been. The reason for this may simply be that the model-based approach includes a serial correlation correction whereas averaging often remains uncorrected.

Publicly available packages for NIRS analysis include HomER [69] in which the individual haemodynamic response is calculated using ordinary least-squared linear deconvolution and no canonical haemodynamic response is assumed, and the functional optical signal analysis (fOSA) [133] and NIRS-SPM [63] toolboxes which use SPM methods for NIRS data in the same way as is done for fMRI.

Wavelet-based methods have also been used for response detection [134] and estimation [135, 136, 137].

2.8.2 Temporal autocorrelation

The General Linear Model (GLM) used for neuroimaging time-series data, as in SPM, assumes that the errors are zero mean, have constant variance, and are independent and normally distributed. The assumption of normality and independence is primarily to obtain accurate p values to determine the statistical significance of effects, while the remaining assumptions ensure that the estimates of the regression coefficients are unbiased and have the minimum possible variance. However, it is known that the noise in brain haemodynamics as measured with fMRI and with NIRS is not random, or white; instead the power spectrum is dominated by low frequencies and varies according to $1/\text{frequency}$ [138]. The sources of this low frequency noise include low-frequency drift from hardware imperfections, oscillations due to respiration and cardiac pulsation, spontaneous vasomotion and residual movement artefacts [25]. When noise is not white the errors are correlated and the assumption of normality and independence is violated. The temporal correlation does not bias the estimates of regression coefficients, but estimates of their variance are biased, which inflates significance and can lead to increased type I error rates.

Most fMRI analysis packages offer methods to detect the serial autocorrelations in the residuals of a linear model using a one-lag autoregression, AR(1), and use the estimated autocorrelation to whiten the residuals

in a second analysis [139]. However, although recommended, these methods are not universally used [140]. Although the autocorrelation model is less of a concern in a random effects group analysis [141], it has been shown that the problem of non-white noise and the method used for correction can affect the results of a second-level analysis [142]. This is thought to occur if within-subject variance is larger than between-subjects variance, when the reverse is usually assumed to be true. Therefore random effects analysis may also be affected by non-white noise, although less than fixed effects analysis [140].

There are two possible reasons for false positives occurring in NIRS data. One is the occurrence of task-related systemic changes which modulate scalp blood flow, affecting the transcranial measurements of cerebral Hb changes, as suggested in [77]. The other is that systemic biorhythms and ongoing vasomotor fluctuations, both intra- and extra-cerebral, result in autocorrelation in the Hb time series which inflates t-values and hence false positives when parametric statistics are used for analysis. This issue is well-known in fMRI analysis where the usual approaches are to precolour [143] or prewhiten [139, 144] the time series in order to apply parametric statistical tests. Precolouring uses a low pass filter to impose a known correlation structure on the time series; the standard deviation and degrees of freedom can then be adjusted accordingly. In the prewhitening method the intrinsic autocorrelation is estimated from the data, usually using an autoregressive (AR) model, and used to whiten the data. These approaches have only recently started to be used for NIRS data [125, 129, 128, 133, 77, 63].

Whitening serially correlated data, as used in SPM for fMRI, is the more statistically efficient approach to parameter estimation [145], particularly for event-related designs [146] and is the one that is usually used in NIRS GLM analyses [147, 129, 133]. However, differences between the assumed and the actual autocorrelations may bias parameter estimates [145], which is likely to be a greater problem in NIRS than in fMRI because the smaller number of channels and lower SNR of the unsmoothed time series reduces the precision of autocorrelation estimation [63]. Also in the SPM method spatial homogeneity of autocorrelation is assumed, which may not be the case with NIRS data which is often sparsely spatially sampled.

Ye et al. [63] compared the precolouring and prewhitening methods for NIRS data and found no significant difference between the methods in deoxyHb t-statistics averaged over an activated region. In the control region the t-statistics resulting from the prewhitening method were more variable those using the precolouring method. When prewhitening was performed after an anti-aliasing filter and downsampling a significant difference was found between deoxyHb t-statistics in activated and non-activated regions using either method, but for oxyHb there was only a significant difference between activated and deactivated regions when the precolouring method was used. They conclude that precolouring is more appropriate for NIRS data than prewhitening. This effect appears to be minimised when a low pass anti-aliasing filter is used prior to whitening as this improves the SNR of the time series used to derive the estimated autocorrelation. However, the reason that low pass filtering appears less effective for oxyHb than for deoxyHb may be that an AR1 model is insufficient to model the oscillatory behaviour of this haemoglobin species, rather than an issue of low SNR.

Because smoothing is usually required for NIRS data and is often performed as a preprocessing step, which is not usually done for fMRI, it may be advantageous to use precolouring to estimate temporal autocorrelation, since a large degree of smoothing swamps any intrinsic temporal correlation, and the known, imposed

autocorrelation can be used instead of a possibly inaccurate estimate of the intrinsic correlation.

2.8.3 Multiple comparison correction

In multichannel NIRS, multiple hypothesis tests are made simultaneously, which increases the risk of Type I error (false positives). This is an issue that is well-known in fMRI where multiple comparison correction is required for tests performed at each voxel. Because of the increasing availability of NIRS instruments with 30 or more measurement channels, there is an increasing number of multichannel NIRS studies, as well as topographic or tomographic imaging studies, necessitating correction for multiple comparisons. The most frequently used method in NIRS is still Bonferroni correction e.g. [78, 119, 61], where to test n comparisons at a significance level of α the individual tests should be tested at α/n . However, although this provides strong control against Type I error it is conservative and comes at the expense of reduced power, especially in neuroimaging data [148].

The random field theory (RFT) method [149] used for PET and fMRI requires data to be smoothed. In an SPM analysis for fMRI it is assumed that after smoothing with a Gaussian kernel the residuals are dense samples on a homogeneous Gaussian random field. Because there is a comparatively large distance between channels and a small number of measurements this is not feasible for channel-wise NIRS [148, 63], although it may be possible when tomographic images are reconstructed from NIRS data. A recent development is NIRS-SPM [63] that uses Sun's tube formula [150] to calculate the p-value required to reject the null hypothesis as the excursion probability of an inhomogeneous Gaussian random field resulting from interpolated estimates between NIRS measurements, which are sparse and irregularly distributed. This also allows super-resolution localisation on two dimensional activation images for oxyHb, deoxyHb and totHb.

Another approach to the multiple comparison problem which is frequently used in neuroimaging is the false discovery rate (FDR) method [151], which controls the expected proportion of false positive detections among the channels found to be significant. Singh et al. [148] found that the FDR method provided a better balance between specificity and power than Bonferroni in simulated and real NIRS data. When activation is widespread, the FDR method is more sensitive than Bonferroni correction and if there is no significant activation the family-wise error (FWE) is as strongly controlled as with Bonferroni correction. In this method the p values for N tests are arranged in ascending order, $P(1) \leq P(2) \leq P(3) \dots \leq P(N)$ corresponding to null hypotheses, $H_1, H_2, H_3, \dots, H_N$. The largest k is found such that

$$P(k) \leq \frac{k}{N} \alpha$$

Then the null hypotheses $H_i = 1..k$, for which $P(i)$ is less than or equal to $P(k)$ may be rejected.

2.8.4 Group-level comparisons

Ciftci et al. [61] compared classical and Bayesian inference methods and were able to identify group-level activations in oxyHb using Bayesian, random or mixed-effects analysis. However they found large intersubject

variation in deoxyHb and failed to find any activation at the group level for deoxyHb. They recommend the use of mixed/random effects at the group level because the within-subject variance is much smaller than between-subject variance. Conjunction analysis across subjects is a possible way to avoid the problem of false positives in fixed effects analyses [61].

The comparison of results both in multichannel NIRS and DOI across multiple subjects is complicated by vascular and anatomical differences between individuals and differences in the positioning of the NIRS probe which can introduce partial-volume and path-length differences [69]. To overcome this difficulty in DOI, Abdelnour et al. [152] have proposed a random effects model for simultaneously reconstructing images from multiple subjects to estimate group-level statistics. Because of the ill-posed nature of the diffuse optical image reconstruction inverse problem, the solutions to individual image reconstructions may differ between subjects even if the brain activity did not differ. This leads to a decrease in statistical power when individually-constructed brain images are averaged across subjects in the conventional way. However, if no solution to the inverse problem can be found that matches all the data from all the subjects, the hypothesis that two groups of subjects are identical can be rejected. If a solution does exist, this does not allow precise conclusions about how the two groups may differ, but it does eliminate the possibility that differences are due to systematic anatomical or probe differences [152]. With small random displacements of the probe and differences in subject anatomy they show more localised estimation using the simultaneous group reconstruction method with a fixed, random or mixed effects model than by reconstructing images for each subject individually.

Large inter-individual variability in NIRS response has been observed during finger-tapping, with detectable oxyHb increases found in 90% of participants and deoxyHb decreases only in 76% [153]. Weaker significance has also been found for group and individual level NIRS responses to visual stimulation [154] and cognitive tasks [4] than for simultaneously recorded fMRI. In a comparison of the variability of fMRI and NIRS, the intersubject variability in response amplitude during a visual task was found to be almost twice as great for NIRS than fMRI, even with careful optode positioning. However, the within-subject variability of response amplitude was not significantly different between the two methods [5].

2.9 Conclusion

Although fNIRS and fMRI measure a similar functional response, the different biophysical principles behind the techniques mean that there are different considerations for the preprocessing and analysis of NIRS data than for fMRI. Preprocessing issues that have been described in this chapter include the removal of systemic interference and motion artefact, optode placement and intersubject registration. The analysis of NIRS data requires consideration of the type of analysis: model-based or model-free, the selection of a haemodynamic response function if appropriate, a method to deal with temporal autocorrelation, correction for multiple comparisons and factors that affect group-level comparisons.

Standards for the processing and analysis of NIRS data are beginning to be established, and several software packages for NIRS data exist, including HomER [69], fOSA [133] and NIRS-SPM [63]. However, these packages deal with channel-wise NIRS data. NIR data that has been reconstructed into tomographic images

as in DOT is less frequently used, and it may be possible to adapt and use software intended for fMRI data for the analysis of these images.

University of Cape Town

Chapter 3

A comparison of methods for motion artefact removal in functional near infrared spectroscopy

Although functional NIRS is reportedly less sensitive to head motion than other brain imaging methods, motion can still have a significant effect on the signal time course. If not removed, these artefacts can confound the detection of activation-related changes. It is therefore desirable to have an indicator of head motion which can be used to remove artefact from the NIRS signal. Adaptive motion artefact removal algorithms for NIRS, as well as EEG, ECG and photoplethysmography generally use an additional sensor to measure motion, such as an accelerometer [155, 156]. However, when the optodes on the imaging system house both light source and detector, for each source, the detector on the same optode should measure little or no physiological signal, because photon penetration depth is dependent on source detector separation. Signal variations at this optode may provide a representation of signal fluctuations caused by changes in optode coupling to the head.

This chapter evaluates the use of these redundant imaging channels with a negligible source-detector separation to identify artefacts resulting from changes in optode coupling due to motion. The detected signals from these channels where the source and detector are co-located, are then used to filter motion artefacts from the functional NIRS time series. Several different methods are compared: recursive least square (RLS) adaptive filtering, wavelet-based filtering, independent component analysis (ICA), and multiple linear regression. These methods have previously been used to remove artefacts of various origins from functional MRI [45], EEG [157, 158, 159], photoplethysmography [155] or ECG [156] time series.

The methods used in this study are detailed in section 3.1. Section 3.1.1 describes the data acquisition, section 3.1.2 describes the procedure used to detect signal variations due to motion on the co-located channels, and section 3.1.3 describes the different techniques used to remove motion artefact from the measurement channels, as well as the method used to evaluate the change in SNR after filtering.

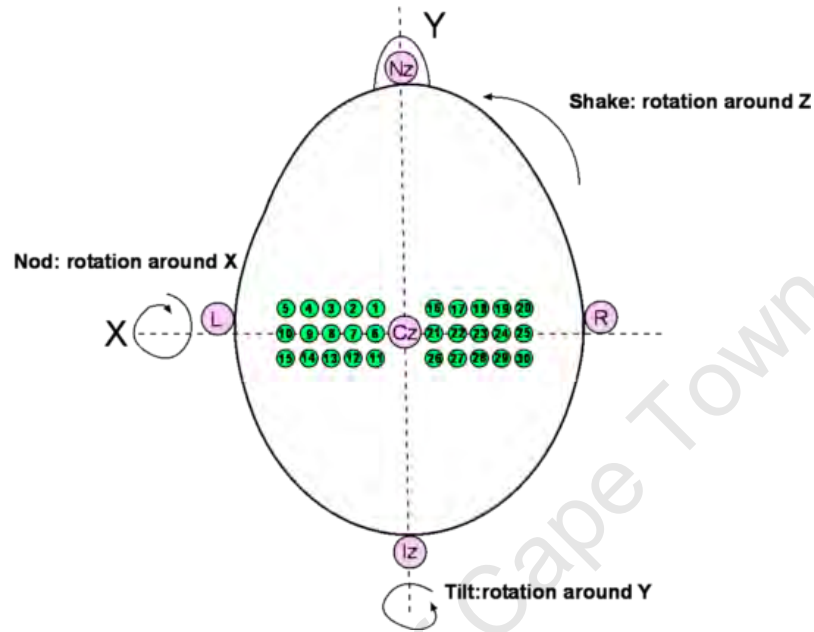


Figure 3.1: Location of NIRS optodes. Each numbered optode location consists of both a source and detector fibre.

Results are presented in section 3.2. The results of applying the motion detection procedure to a dataset containing known motion are presented in section 3.2.1. Section 3.2.2 presents the change in SNR that results from applying each filtering technique to datasets containing known and unknown motion. Finally, the results are compared and discussed.

3.1 Methods

3.1.1 Data acquisition

Data containing known motion and periods without motion were collected from three subjects using the DYNOT imaging system (NIRx Medical Technologies, New York). NIRS data was obtained simultaneously at wavelengths of 760 and 830 nm, with a sampling rate of 1.8 Hz. Fifteen source-detector pairs were placed over each of the left and right motor cortices, as illustrated in figure 3.1, using Cz from the 10-20 system for EEG electrode placement as a reference point for consistent positioning between subjects. To produce motion-related signal variations, subjects were instructed to shake, tilt or nod their heads slightly at a demonstrated speed.

A fourth data set was recorded from another subject who did not perform deliberate movements. Instead, this subject performed a left-hand sequential finger tapping task in 30 second blocks, alternating with 30 seconds of rest, repeated six times. In this subject all 30 optodes were placed over the right motor cortex to facilitate the detection of activation-induced haemodynamic changes.

3.1.2 Motion artefact detection using co-located channels

Motion artefacts are usually characterised by rapid signal changes manifesting as sharp spikes, generally much larger in magnitude than absorption-related changes, which either return immediately to pre-movement values or result in a dc signal change. Algorithms to detect motion rely on these characteristics to distinguish artefact from other signal changes. The use of a co-located channel for motion artefact detection presents an advantage, since apart from instrument noise, there should be very little other signal change on these channels, allowing artefacts to be detected easily.

Each of the 30 numbered optodes in figure 3.1 contains both a source and detector. Since each detector measures signal from every source, each detector will measure signal from the source at the same optode location. Measurement channels where detector n measures signal from source n are referred to as co-located. Because each dataset provides measurements from 30 co-located source detector pairs at two different wavelengths, 60 channels were examined for motion artefact. To detect rapid deviations in the detected signal from the co-located channel, the difference between each sample and the previous one was calculated. If the only signal variation is due to random noise, these differences should be centered about zero; outliers in this difference series can be attributed to motion. Outliers were calculated as values greater than T times the interquartile range above and below the upper and lower quartiles respectively.

To examine the differing predictive value of channels at different locations and wavelengths, receiver operating characteristic (ROC) curves were generated for all channels by increasing the threshold T at which outliers were defined along a scale where T ranges from -10 to 10, and plotting the hit rate (detection of motion events: sensitivity) against the false positive rate (1-specificity). The area under the ROC curve (AUC) is used as an index of each channel's reliability in detecting motion events, where larger values for AUC represent better discrimination between motion and non-motion.

3.1.3 Motion artefact removal

The results of motion detection using the co-located channels suggest that it should be possible to use these channels to remove motion artefact from the other channels which contain correlated artefacts. Five different methods are evaluated on the same data sets.

The data was first band pass filtered between 0.01 and 0.3 Hz to remove some of the random noise from the measurement channels and to suppress aliased cardiac noise and remove low frequency drift. After band pass filtering, excessively noisy channels were excluded from the analysis. Noisy channels result from poor optode coupling or source-detector separations that are too large for any signal to be registered at the detector. Channels with a coefficient of variation (CV) greater than 10% were rejected, where $CV = \sigma/\mu$ and σ is the signal standard deviation during a period while the subject was at rest, and μ is the mean signal level. The log-normalised optical density time series for each wavelength was then calculated.

The signal measured at each channel was considered as a combination of true signal, noise resulting from motion of the source fibre, and noise resulting from motion of the detector fibre. Motion of the source and detector were approximated using the co-located channel measurements for the relevant source and detector,

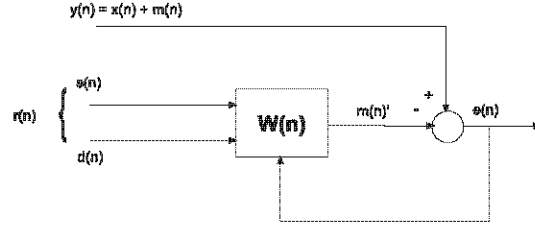


Figure 3.2: $y(n)$ is the measured signal assumed to contain true signal $x(n)$ plus noise $m(n)$ due to motion, $r(n)$; the motion noise reference is the concatenation of the estimates of the source motion $s(n)$ and detector motion $d(n)$; $e(n)$ is the difference between the measured signal and the filtered noise reference $m(n)'$.

which are expected to be correlated in some way with the motion artefact. For example, the signal measured from source 1 detector 5 was filtered using the signal from source 1 detector 1 as an estimate of source motion, and source 5 detector 5 as an estimate of motion of the detector. All processing was done in Matlab[®] (2007b, The MathWorks, Natick, MA, USA).

3.1.3.1 Two-input RLS adaptive filter

Figure 3.2 illustrates the recursive least squares (RLS) noise cancellation algorithm [160] adapted for the multichannel case [161, 162] with two noise reference inputs representing source and detector motion.

Equation 3.1 is the recursive algorithm for updating the filter weights

$$w(n+1) = w(n) + e(n)K(n) \quad (3.1)$$

where $e(n)$ is the estimated error: the difference between the measured signal $y(n)$ and the filtered noise reference $r(n)$, calculated as in 3.2, and $K(n)$ is the gain, calculated according to 3.3 and 3.4.

$$e(n) = y(n) - w^T(n)r(n) \quad (3.2)$$

$$K(n) = \frac{P(n).r(n)}{\lambda + r^T(n)P(n)r(n)} \quad (3.3)$$

$$P(n+1) = \lambda^{-1}P(n) - \lambda^{-1}K(n)r^T(n)P(n) \quad (3.4)$$

Here $y(n)$ is the measured signal, assumed to contain the signal of interest x with some noise m due to motion. λ is the forgetting factor which weights how sensitive the filter is to previous samples. $P(n)$ is the scaled covariance matrix of the weight vector $w(n)$. The reference signal $r(n)$ is formed by concatenating M samples of $s(n)$ and $d(n)$, the estimates of the source and detector motion, as follows:

$$r(n) = [s(n), s(n-1), \dots, s(n-M+1), d(n), d(n-1), \dots, d(n-M+1)]^T$$

where M is the length of the filter.

3.1.3.2 Wavelet-based filter

The wavelet transform [163, 164] expresses a time series as a combination of shifted and scaled mother wavelets. The wavelet transform W of a time series $f(t)$ using the mother wavelet $\psi(t)$ is a function of time τ and scale s .

$$W(\tau, s) = \frac{1}{\sqrt{|s|}} \int f(t) \overline{\psi\left(\frac{t-\tau}{s}\right)} dt \quad (3.5)$$

In the discrete case the mother wavelet is scaled and translated discretely in powers of two. The wavelet basis functions are related to the mother wavelet by 3.6, where the mother wavelet is scaled by $s = 2^{-j}$ and translated by $\tau = k2^{-j}$.

$$\psi_{j,k}(t) = 2^{-j/2} \psi(2^{-j}t - k) \quad (3.6)$$

The wavelet coefficients are

$$C_{j,k} = \sum_t f(t) 2^{-j/2} \psi(2^{-j}t - k) \quad (3.7)$$

The wavelet transform thus provides a time-scale decomposition of a signal in a limited number of wavelet coefficients, where high frequencies are well localised in time and low frequencies are poorly localised in time, but have high frequency resolution. Wavelet shrinkage denoising is an effective method for reducing Gaussian noise in a signal [165, 166].

The wavelet transform is good at localising rapid signal changes [92], and is able to separate signal into different frequency components at different times, allowing frequency components related to motion at specific times to be removed, rather than filtering a particular frequency from the entire time series.

To identify motion artefact the discrete wavelet transform was applied to the co-located channels representing the source and detector noise references. The decomposition was performed to 10 levels using a symlet 8 wavelet, which is not shifted in time and thus suited for localising high frequency artefacts [157]. At each level j , a threshold was calculated according to the following rule

$$T = 3\hat{\sigma}_j^2 \sqrt{2\log(N)} \quad (3.8)$$

where N is the length of the signal.

The estimate of the variance σ^2 at each scale j is

$$\hat{\sigma}_j^2 = \text{median}(|C_{j,k}|) / 0.6745 \quad (3.9)$$

The same process was applied to the signal for each source-detector combination. Wavelet coefficients larger than the threshold T in both the signal and in either its source or detector reference were shrunk to 10

percent of their initial value; thus only large wavelet coefficients that did not appear in either the source or detector reference signals were retained.

3.1.3.3 Two-channel multiple regression

The simplest technique for motion removal was to subtract a best-fit linear combination of the source and detector noise references from each signal. This was done using least squares multiple linear regression of the form

$$y = aX + R \quad (3.10)$$

where

$$y = \begin{pmatrix} y_1 \\ \vdots \\ y_n \end{pmatrix}$$

is the time series of measurements from a single channel and

$$X = \begin{pmatrix} 1 & x_{s,1} & x_{d,1} \\ \vdots & \vdots & \vdots \\ 1 & x_{s,n} & x_{d,n} \end{pmatrix}$$

where x_s is the signal from the co-located source reference and x_d is the signal from the detector reference. The regression coefficient vector a is calculated from $(X^T X)^{-1} X^T y$. The filtered signal is the remaining signal R once a linear combination of source and detector signal $\hat{y} = aX$ has been subtracted from the measured signal y .

3.1.3.4 Multiple regression with all 30 channels

To attempt to improve on this result, a best-fit regression on all the co-located channels, not only the source and detector involved in the measurement, was also performed. This involved fitting the 30 co-located channels to the measured signal and then subtracting the best fit. The rationale for attempting this was that if the motion characteristics of a particular co-located channel do not appear in the signal, the regression coefficient for that co-located channel would be expected to be zero, and it would therefore not be subtracted from the signal. This procedure also allowed us to examine which co-located channels contributed most to the signal variation measured at each channel.

3.1.3.5 Independent component analysis

ICA is a signal processing technique which attempts to decompose a linear mixture of signals into source signals that are maximally statistically independent, using transformations that minimise the Gaussianity of

the signal mixture. The FastICA algorithm [167, 168] achieves this through negentropy minimization. If X is a set of measured signals then the entry $a_{i,j}$ in the mixing matrix A specifies the contribution of source s_j in S to measured signal x_i .

$$x = As \quad (3.11)$$

Unmixing the signals to find the sources s involves finding the unmixing matrix A^{-1} . Because the components are statistically independent, the motion artefact can be expected to be separated from signals of physiological interest and to appear in a small number of components. Once identified, these artefactual components can be removed, and the cleaned signal matrix X' reconstructed using $x' = As'$.

The difficulty, however, is in identifying which of the independent components produced by the ICA algorithm correspond primarily to motion artefact. Using the knowledge that the signals at the co-located channels correspond more to motion artefact than to any other phenomenon, one can examine the weight matrix A to determine which components have a large contribution from these co-located channels. This method was used in [169] for retrieving the event-related fast response without the interference of superficial signals. ICA has also been used to filter skin blood flow signal from the NIRS task-related response [74]. In the PCA whitening step prior to FastICA, we retained 99% of the data set variance, then calculated 60 independent components. For each co-located channel, the component to which it contributed most was identified from the weight matrix and removed. Components were also removed if their greatest single contribution from the weight matrix came from a co-located channel.

3.1.3.6 Calculation of SNR change after filtering

The methods were compared using the change in SNR calculated as follows:

$$\Delta SNR = SNR_{filtered} - SNR_{original} \quad (3.12)$$

where

$$SNR_{original} = 10 \log_{10} \left(\frac{\sigma_s^2}{\sigma_m^2} \right) \quad (3.13)$$

$$SNR_{filtered} = 10 \log_{10} \left(\frac{\sigma_s^2}{\sigma_r^2} \right) \quad (3.14)$$

and σ_s^2 is the variance of the motionless data, σ_m^2 is the motion variance, and σ_r^2 the variance of the residual noise after filtering. The median change in SNR across all channels was calculated for each wavelength and each data set.

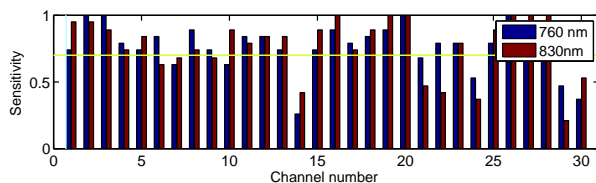


Figure 3.3: Sensitivity from ROC curve for each co-located channel, restricting 1-specificity to 0.01 (16 false positives).

3.2 Results

3.2.1 Motion artefact detection in datasets with deliberate motion

Because of the unequal number of examples in each class (19 motion events and 1816 non-motion events), the ROC curves reveal an AUC of above 0.9 for all channels at both wavelengths. This makes it difficult to use the AUC to separate channels that demonstrate good motion detection from those that do not.

A better method to determine which co-located channels are sensitive to motion is to decide on an acceptable number of false positive and false negative detections. To be able to use a channel for motion detection it should miss few of the motion events: we selected a maximum of 5, whereas the number of false positives should certainly be less than the number of motion events in the data set. For the data set under consideration a sensitivity of 0.7 corresponds to a correct positive rate of 14 out of 19 motion events. The value for 1-specificity only becomes acceptable at about 0.01, corresponding to 16 false positives. Figure 3.3 shows the thresholds T , and sensitivities located from the ROC curves when 1-specificity is restricted to 0.01. It can be seen from figure 3.3 that with this restriction on false positives, the sensitivity becomes unacceptable in channels 6, 7, 9, 10, 14, 21, 22, 24, 29 and 30. However, channels 2, 3, 16, 19, 20, 26 and 27 perform very well.

Figure 3.4 shows the signal on channels with good motion discrimination (sensitivity > 0.7 and specificity > 0.99) and bad motion discrimination (sensitivity $<< 0.7$ or specificity < 0.99) for all three data sets. Visually examining the time courses from these channels together with the timing of the motion events, it is easy to see the difference between channels that have good or bad motion discrimination.

Some of the channels with poor motion discrimination appear to show signal changes at particular motion events and not at others. This is particularly evident in figure 3.4d, where motion events around time point 200 do not appear. This suggests that some channels may have sensitivity to particular types of motion only. It should also be noted that the “false positives” in figure 3.4c may be due to actual motion which was not recorded as such, as it is possible that the subject moved even when not instructed to do so. This phenomenon is not apparent in the other two data sets.

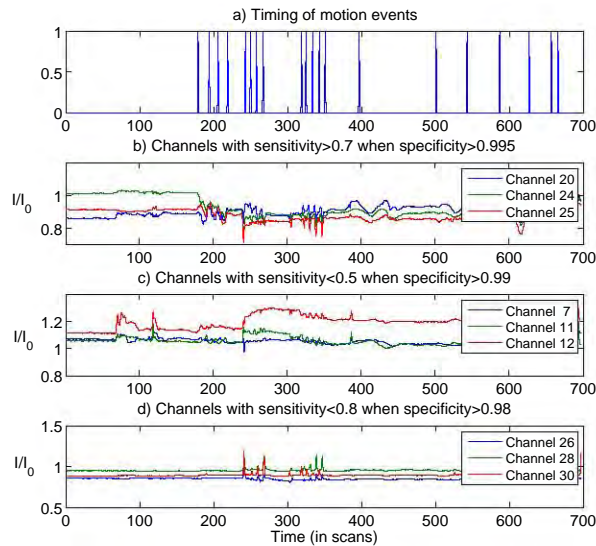


Figure 3.4: Subject 2: (a) motion events and channels with (b) good and (c,d) bad motion discrimination. I/I_0 represents measured light intensity normalised to the mean intensity during a baseline period.

3.2.1.1 Dependence on type of motion

The preceding results appear to indicate that although deliberate motion tends to cause detectable artefact on at least some of the co-located channels, motion is not detectable on all these channels, and not every motion event is detectable on a particular channel. This may be because the direction and magnitude of a particular movement affects some channels more than others. To investigate this we looked at the co-located channel signal according to motion type, and calculated the ratio of the signal variance during each type of motion σ_m^2 compared to the signal variance where there was no motion σ_s^2 .

Figure 3.5 shows the amplitude of the motion artefact in every co-located channel for each type of motion in one of the subjects. It is clear that different channels have sensitivities to different types of motion: for example channel 16 shows a large artefact for facial movement and a relatively small one for nodding, whereas for channel 30 the reverse is true. Although motion might be expected to affect both wavelengths in an identical manner, the artefacts detected at different wavelengths are similar but not always the same.

3.2.1.2 Threshold selection and motion classification

A threshold can be selected by examining the operating range between the thresholds of 0.7 for sensitivity and 0.01 for specificity for each channel and selecting a value where the largest number of channels shows good discrimination. Using this technique the best overall threshold is 2.34 for data set 1, 4.5 for data set 2 and 1.84 for data set 3. Settling upon a universal threshold of $T=2$ for all data sets and all channels, the detected motion events for one subject are shown in figure 3.6, together with the true motion timing.

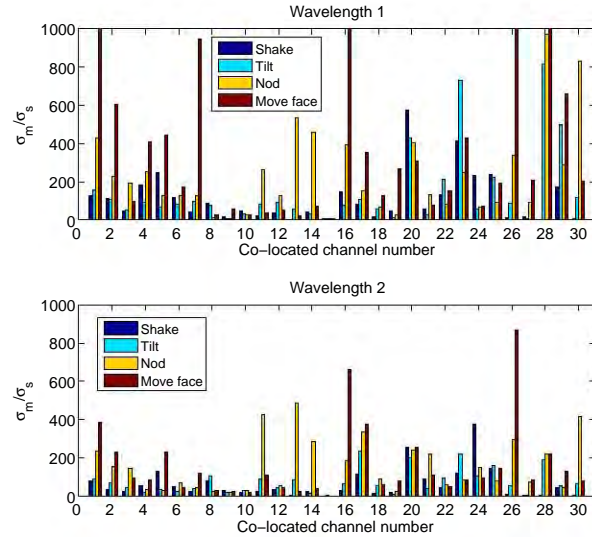


Figure 3.5: Amplitude of motion artefact in each co-located channel for each motion type

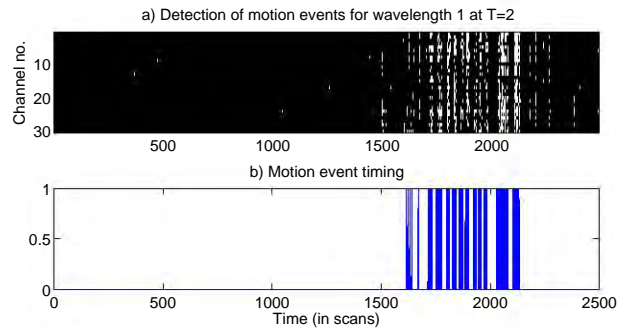


Figure 3.6: Data set 3 motion detection

It is apparent that although there are false positives (and misses) in individual channels, by looking at the consensus from all channels, accurate motion detection can be achieved.

Because each channel appears to have sensitivity to different motion events, detection of motion can be performed by classifying a detected event as a motion event when it appears in more than 20 of the 60 channels. Doing this using a universal threshold of 2 for all data sets results in the performance summarised in table 3.1.

3.2.1.3 Motion artefact on measurement channels

Despite being able to detect known motion on many of the co-located channels, it is obvious that motion will not necessarily cause an artefact, and even when motion artefacts are present, they may not appear in

Table 3.1: Motion event detection using all channels using a threshold $T=2$.

	Sensitivity	Specificity	False positives	False negatives
Data set 1	0.74	0.99	8	5
Data set 2	0.75	0.98	44	5
Data set 3	0.99	0.99	3	3

As shown in figure 3.4, the large number of false positives in data set 2 may be because of actual motions that were not recorded.

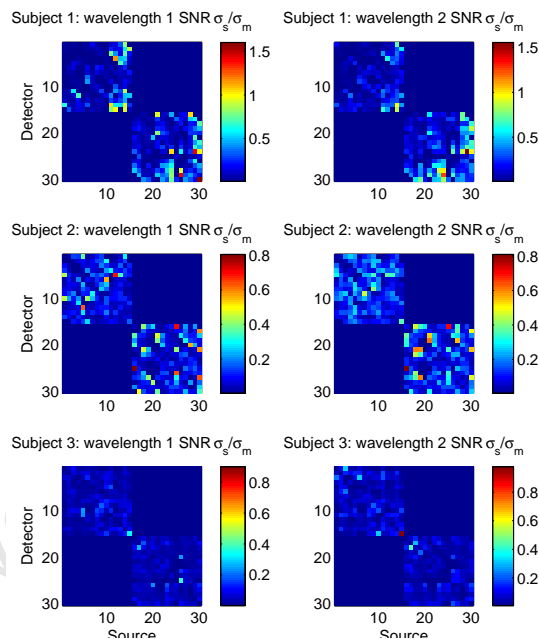


Figure 3.7: Relative amplitude of motion artefact for each data set.

all measurement channels. To determine whether the motion artefacts detected on the co-located channels were present in the measurement channels we calculated the ratio of the variance during non-motion periods σ_s^2 , to the signal variance during motion periods σ_m^2 , for every channel. In the channel maps shown in figure 3.7 a ratio near 1 indicates that there is no significant motion artefact on that channel, whereas a ratio close to zero indicates large motion artefact.

It is assumed that channels with large motion artefact should be correlated to some degree with either the motion from the co-located channel representing the source or the channel representing the detector or a combination of both. It might be expected that the motion artefact be most prominent in channels where the source-detector separation is small, as these channels will contain less signal variation due to absorption changes, or noise due to scatter. For example, figure 3.8 shows the signal from co-located channel 1, together with the signal from source 1 detector 2, and source 12 detector 1, which have small source-detector separation distances ($< 2.5\text{cm}$). Both signals are highly correlated with the motion reference (co-located channel 1).

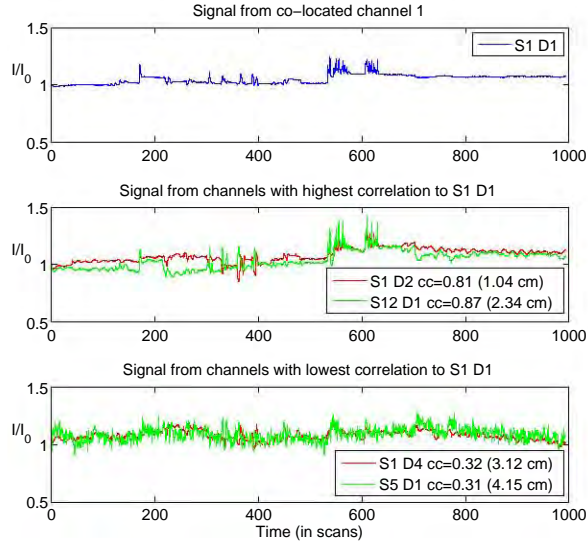


Figure 3.8: Example of a motion reference (co-located) channel and dependent measurement channels. I/I_0 represents measured light intensity normalised to the mean intensity during a baseline period; cc is the correlation coefficient between the signal shown and the signal from co-located channel 1; the separation distance in cm is given in brackets.

The signal from widely separated channels source 1 detector 4 and source 5 detector 1, however, show much lower correlation to the motion reference, because they contain other sources of signal variation.

Channels that are affected by a combination of source and detector motion may also show low correlation to individual co-located channels. For example, the signal from source 14 detector 7 (and its reciprocal from source 7 detector 14) show no greater than 0.2 correlation with the detected signal in either the source or detector reference (co-located channels 7 and 14). However, upon examination of figure 3.9, which shows the signal(s) together with the source and detector references at co-located channels 7 and 14, it appears that the low correlation with either is because of the contribution of both source and detector motion to the signals.

3.2.2 Motion artefact removal

All of the filtering methods were applied to three data sets with deliberate motion and one data set containing activation signal from a motor task, but without known motion.

3.2.2.1 Application of filtering methods to data sets containing known motion

The variable parameters for the two-input RLS filter described in 3.2, 3.3 and 3.4 are the filter order M (number of weights) and λ . The forgetting factor λ was held constant at 0.99 and the filter order was varied between 3 and 15 as shown in table 3.2 (results not shown for filter orders where a decrease in SNR was obtained after filtering).

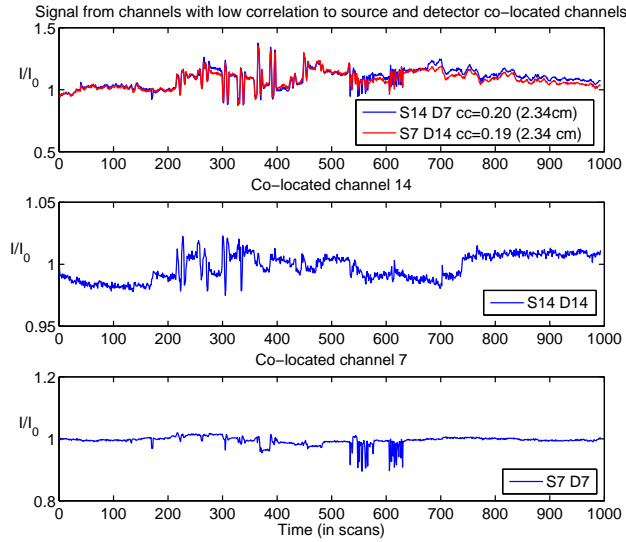


Figure 3.9: Example of a measurement channel with the detected signal in its source and detector reference. I/I_0 represents measured light intensity normalised to the mean intensity during a baseline period; cc is the correlation coefficient between the signal shown and the signal from the co-located channel representing motion of the source (co-located channels 14 and 7 respectively); the separation distance in cm is given in brackets.

	Subject 1		Subject 2		Subject 3	
Filter	760 nm	830 nm	760 nm	830 nm	760 nm	830 nm
order						
3	0.74	0.83	0.24	0.88	0.86	0.61
4	0.81	0.88	0.31	0.96	0.87	0.63
5	0.95	0.91	0.41	1.04	0.94	0.70
6	1.08	0.95	0.51	1.10	0.72	0.72
7	1.13	0.96	0.59	1.08	0.56	-2.84
8	1.18	0.97				
10	1.22	0.98				
15	0.99	0.63				

Table 3.2: Median change in SNR in dB using RLS adaptive filtering, averaged over all channels for 3 different data sets

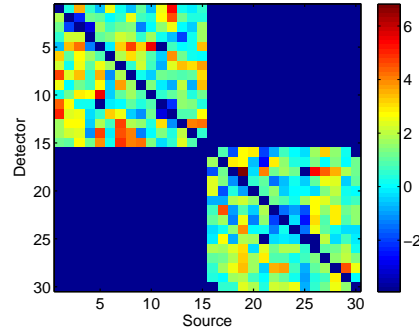


Figure 3.10: Map of SNR change in dB for subject 1 after RLS adaptive filter of order 10.

	Subject 1 (n=446)		Subject 2 (n=452)		Subject 3 (n=448)	
	760 nm	830 nm	760 nm	830 nm	760 nm	830 nm
RLS adaptive (order 6)	1.08	0.95	0.51	1.10	0.72	0.72
Wavelet filter	3.92	3.04	9.63	8.86	4.32	2.90
ICA	5.20	4.97	6.59	6.29	5.48	4.64
Regression (two channels)	0.59	0.69	0.70	0.97	0.61	0.40
Regression (all channels)	4.77	3.68	7.59	7.08	4.64	2.93

Table 3.3: Median SNR change in dB over all channels using each filtering method

Because the motion artefact is not equally severe on all channels, particularly those where the source and detector are widely separated, the SNR change varies substantially from channel to channel. Certain channels also show an apparent decrease in SNR. For this reason the median across channels is used as an indicator of overall SNR change, or filtering efficiency, rather than the mean. The map of SNR change after filtering for subject 1 (figure 3.10) illustrates that the increase in SNR for individual channels is as high as 6dB, whereas for many channels there appears to be no change in SNR at all. Figure 3.11 shows example time courses from channels where there was an increase or a decrease in SNR after filtering. A decrease in SNR may occur when the filter alters the signal corrupted by motion artefact without reducing the variance, possibly while reducing the variance in the segment unaffected by motion.

The optimal RLS filter order varies between subjects, presumably due to different motion characteristics caused by individual variation and optode setup.

Table 3.3 shows the median SNR change across all measurement channels for each filtering method on each data set.

3.2.2.2 Application of filtering methods to data set containing unknown motion

The same methods were applied to the data set containing motor task activation and no known motion artefact. In this case the SNR calculation $SNR = 10\log_{10}(\frac{\sigma_s^2}{\sigma_m^2})$ was performed where σ_s^2 was the variance of

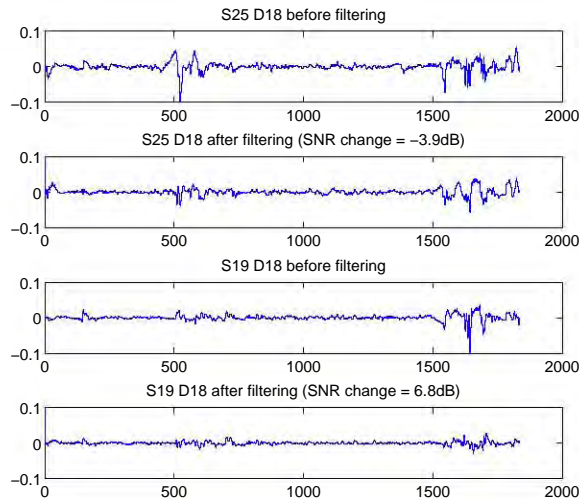


Figure 3.11: Sample results from RLS filtering for a channel with decreased SNR after filtering (S25 D18), and a channel with increased SNR (S19 D18).

	760 nm	830 nm
RLS adaptive (order 10)	0.13	0.33
Wavelet filter	0.89	0.58
ICA	2.97	3.06
Regression (two channels)	0.35	0.44
Regression (all channels)	3.01	2.54

Table 3.4: Median SNR change in dB over all channels using each filtering method for data set 4 (n=879)

the signal containing motor task activation and σ_m^2 the variance of a period during which the subject was not asked to perform any task.

The results, shown in table 3.4, are qualitatively similar to those from the data sets containing deliberate motion, in that two-channel regression and adaptive filtering produce a modest median SNR improvement, wavelet filtering performs slightly better and ICA and multiple channel regression produce the largest SNR changes. Naturally, the SNR changes are smaller than is the case when the data sets contain large deliberate motion artefacts.

3.2.2.3 Correlation of signals with source and detector references

Because the greatest improvements in SNR were obtained by multivariate methods rather than methods that relied on the source and detector references only, we examined the multiple correlation of each signal firstly with its source and detector reference, and secondly with all 30 co-located channels, to determine how much

	Subject 1		Subject 2		Subject 3		Subject 4	
	760 nm	830 nm	760 nm	830 nm	760 nm	830 nm	760 nm	830 nm
median R^2 for two channel regression	0.41	0.32	0.40	0.38	0.35	0.26	0.30	0.28
median R^2 for 30 channel regression	0.81	0.75	0.89	0.86	0.75	0.64	0.69	0.65
% channels where $\max(a) = a_s$	37	15	31	15	30	18	36	20
% channels where $\max(a) = a_d$	10	11	13	11	14	14	5	7
% channels where $\max(a)$ is neither a_s nor a_d	53	74	56	74	56	68	59	73

Table 3.5: Value for two-channel and all-channel regression and percentage of channels where the largest regression coefficient is from neither source nor detector

variance was explained by the source and detector reference channels and whether more variance could be explained using all 30 co-located channels.

Table 3.5 shows that, considering only the reference channels for source and detector motion, the median multiple correlation coefficient R^2 is less than 0.5 for all data sets, but using all 30 reference channels increases the median R^2 to around 0.8. Moreover, in all data sets, for more than 50% of the channels, the largest regression coefficient was obtained for a co-located channel other than that representing the source or detector.

3.3 Discussion

Functional brain imaging using near infrared spectroscopy is becoming increasingly common, as technological and theoretical advances make it easier to apply to the study of brain function. NIRS presents advantages over functional MRI in that it is easy to use on patients and infants, and it produces semi-quantitative results, measuring changes in the concentrations of oxyhaemoglobin and deoxyhaemoglobin during functional activation.

However, if attention is not paid to sources of signal change other than functional activation, researchers risk drawing the wrong conclusions from their data. The sources of physiological noise in NIRS are well-known, and some effort has already been made towards identifying these and finding signal processing techniques to deal with them [67]. Motion artefact removal, however, has been quantitatively explored to a lesser degree, although individual researchers have developed methods for use in their own studies [93, 91, 89]. There is no set of standards for dealing with motion artefact in NIRS, as there is in functional MRI. This is no doubt in part because of the large differences between instruments and imaging parameters used by different research groups.

We have investigated the use of co-located channels to identify motion artefacts in NIRS time series containing periods with known motion. Motion artefact can be detected with high sensitivity on these co-located channels. The signal from the co-located channels can also be used to filter artefact from the remaining channels which contain signals of physiological interest as well as varying degrees of contamination by motion. The type of motion has a large influence on the resulting artefact - this is to be expected, as movement in a particular direction causes different acceleration effects at different parts of the head, but the motion of the

optodes is largely constrained by the rigid helmet.

We compared five different methods for removing motion artefact from the measured signal, namely adaptive filtering, wavelet filtering, ICA and linear regression using two, and all co-located channels respectively. All of these methods make use of the co-located channels to identify signal that was related to motion, rather than originating from some other source.

Regressing or adaptively filtering the signal from the co-located channels representing source and detector motion references produces a moderate average improvement in SNR for data sets with known motion and unknown motion. Linear regression of estimated source and detector motion cannot be expected to remove artefact entirely if different types of artefact affect co-located channels differently, that is, the relationship between the motion estimate and the artefact changes over time. Adaptive filtering, which is equivalent to regression in the case where $M = 1$ and $\lambda = 1$ [170], should work better in this situation, however, the results indicate that the RLS technique is sensitive to the order of filter used, and the optimum filter order varies between subjects, possibly because of differing motion characteristics in each dataset. Although RLS adaptive filtering can be effective and can be used with multiple noise references, this sensitivity to filter order makes it difficult to adopt as a generic solution for motion artefact noise cancellation.

The wavelet-based filtering method produces good improvements in SNR for data sets with deliberate motion, but the SNR improvement for the data set without known motion was hardly better than regression or adaptive filtering. This may be because no large excursions due to motion were present. The excellent (~ 9 dB) wavelet filtering results for data set 2 are additional evidence that the wavelet filtering method is useful when the artefact takes the form of large sudden movements, or spikes.

The best motion artefact removal results in all data sets were produced by the methods that take into account the signal changes in all 30 co-located channels, namely ICA and regression. This shows that although motion artefact is represented in the co-located channels' signal, the assumption that one channel represents the motion of each of the source and detector is too simplistic. This was confirmed by looking at the amount of variance in each channel that could be explained by the signal variation on the co-located channels. Better SNR increases can be achieved by filtering the signal on all co-located channels from the signals originating from deeper tissue.

The results from applying these filtering methods to real data indicate that it may not be necessary to visually or heuristically identify motion artefacts and remove affected segments of data from the time series. Of course, some degree of data checking is always necessary, but it is desirable that motion artefact removal require as little user intervention as possible. Using the co-located channels as indicators of motion goes some way towards achieving this. Existing artefact removal methods such as PCA require the selection of a number of principal components to be removed from the data. The requirement that the largest covariance in the data results from motion must also be met. Using ICA for artefact removal requires the identification of components that correspond to motion artefact. This can be achieved automatically through comparison with the co-located channels.

The principle we have used here for motion artefact removal is the same as the one that has previously been used to filter superficial signal such as skin blood flow effects, and global signal like blood pressure fluctuations and cardiac pulsation, from functional NIRS data, using multiple channels with short and long

spacings between the NIR source and detector. Some of the techniques presented here have been used for removal of superficial and global signals, for example ICA [74, 169], regression [2, 70, 60, 68] and adaptive filtering [71, 72], but not for removal of motion artefact.

Motion artefact in NIRS has been identified using wavelet transformation [92], but has not been used for filtering human data. However, wavelet denoising and ICA have been used to remove motion artefact from simulated NIRS data [66]. We have shown that these techniques may also be used for the removal of motion artefact in functional NIRS from human subjects.

3.4 Summary

We proposed the use of redundant imaging channels with negligible distance between light source and detector compared to actual measurement channels, to detect subject motion without the need for an additional motion sensor. Data sets containing deliberate motion artefacts were obtained from three subjects. Motion artefacts could be detected in the signal from the co-located channels with a minimum sensitivity of 0.75 and specificity of 0.98. Five techniques for removing motion artefact from the functional signals were compared, namely two-input recursive least squares (RLS) adaptive filtering, wavelet-based filtering, independent component analysis (ICA), and two-channel and multiple-channel regression. In most datasets the median change in signal to noise ratio (SNR) across all channels was greatest using ICA or multiple channel regression. RLS adaptive filtering produced the smallest increase in SNR. Where sharp spikes were present wavelet filtering produced the largest SNR increase. We find that ICA and multiple-channel regression are promising ways to reduce motion artefact in functional NIRS without requiring time-consuming manual techniques.

Chapter 4

Investigation of NIRS-DOT data analysis in a motor execution and observation task and on null data

To investigate the analysis of NIRS data, a preliminary experiment consisting of a motor performance, observation and imitation task was run on a small set of subjects. The main aim of this preliminary investigation was to investigate the use of SPM for the analysis of DOT data produced by the NAVI software (Near-Infrared Analysis, Visualization and Imaging Suite, NIRx Medical Technologies, NY), in single subjects. We also wished to determine whether a bilateral or contralateral NIRS response to motor stimulation and motor observation could be measured and whether this response was consistent in both oxyHb and deoxyHb. Finally we wished to examine empirically the rate of false positives in this type of data by doing the same analysis on null (task-free) data. Using additional data we then assessed the impact of preprocessing parameters and block length on the occurrence of false positives in fixed effects group analyses.

4.1 A motor execution and observation task in single subjects using NIRS

Because the motor cortex shows a reliable and robust haemodynamic response to stimulation, motor tasks are frequently used in functional neuroimaging as a benchmark or a means to obtain an activation data set for testing analysis and processing methods. Motor tasks involving the hands are also easy to perform in any imaging environment; for this reason a large number of neuroimaging studies of motor behaviour have been carried out using fMRI and PET.

In addition, the primary sensorimotor cortex (SM1) and the premotor cortex (PMC), as well as the prefrontal cortex (PFC), which is involved in complex motor learning and motor control, are located close to the scalp

in humans, making these areas accessible to surface-based measurements such as NIRS.

The portability, robustness to motion artefact and good temporal resolution of NIRS make this technique suitable for investigating realistic everyday motor tasks (e.g. [106, 80]), which are less practical with other imaging techniques such as PET or fMRI [81]. Because of these advantages there is also much interest in using NIRS for brain-computer interfacing (BCI). Consequently, in addition to studies on motor task execution, there are several NIRS studies that investigate motor imagery, usually with a BCI as the end goal (e.g. [171, 90]). However, there are few NIRS studies of action observation and imitation, although the neural mechanisms of observing actions performed by others has been studied fairly extensively using fMRI. To our knowledge the only NIRS studies of action observation are in [126, 172, 173, 174, 175, 127] and [176].

The pattern of haemoglobin concentration change common to most motor task experiments is a rapid increase in oxyHb in contralateral primary motor cortex (M1) peaking 5-10 s after the start of motor stimulation and a slower, lower amplitude decrease in deoxyHb, which may take as long as 15 s to reach a minimum [177, 95, 101, 96, 105, 178, 79, 2, 179, 180, 181, 100, 107]. This is compatible with findings using BOLD fMRI, thought to reflect a disproportionate change in regional cerebral blood flow (rCBF) which occurs in an activated brain region. The deoxyHb response to motor stimulation has been found to be delayed with respect to oxyHb by 1-2 s [101, 2, 78, 82].

The large number of NIRS studies on motor tasks has been thoroughly reviewed in [81]. Simple hand movement tasks have been studied using a single NIRS source and detector [102], and with multichannel configurations covering several locations, or the whole head [182]. Multichannel NIRS has also been developed into topographic and more recently tomographic imaging methods, where a time series of three-dimensional images can be reconstructed from NIRS surface measurements. This raises the possibility that software developed for functional MRI may also be used for NIRS-DOT data, with some consideration of appropriate adaptations specific to optical data.

Lateralization of motor activity in NIRS

Consistent with findings from fMRI, many NIRS studies have reported a lateralised effect, with larger haemodynamic responses over the contralateral motor cortex during motor execution [95, 101, 96, 105, 123], as well as imagery [183]. Smaller [95, 101, 82, 123] and delayed [103] ipsilateral responses to motor tasks have also been reported, although some studies fail to find significant ipsilateral change [100]. Other studies have found bilateral NIRS activation during unilateral movements [184, 120] and imagery [120], a result that has also been found using fMRI [185, 186]. OxyHb responses have been suggested to be less specific, with no clear differences between ipsi- and contralateral movements, while deoxyHb responses have been found to be smaller for ipsi- than for contralateral finger movements [184].

Action observation

Observation of actions is known to activate a motor network similar to that involved in the performance of the same actions. This network which includes the primary motor cortex (M1) and secondary motor areas has been named the mirror neuron system, because of the finding in monkeys of neurons which fire when an

action is observed as well as when it is executed. The same areas are also activated by motor imagery. In a rehabilitation context, activation of these brain areas to observation or motor imagery may facilitate the subsequent relearning and execution of that movement [176]. Regions activated during both the execution and observation of actions include the ventral premotor (BA6/44) and inferior parietal cortex, and the dorsal premotor, supplementary motor, middle cingulate, somatosensory (BA3, BA2, and OP1), superior parietal, middle temporal cortex and cerebellum [187]. A recent meta-analysis found consistent activation across 104 action observation experiments symmetrically across both hemispheres in frontal areas BA 44/45, lateral dorsal premotor cortex (dPMC, BA 6), supplementary motor area (SMA, BA 6), rostral inferior parietal lobule (IPL, area PFt), primary somatosensory cortex (S1, BA 1,2), superior parietal lobule (SPL, area 7A), intraparietal cortex (IPS, area HIP3), posterior middle temporal gyrus (pMTG) at the transition to visual area V5, and fusiform face area/fusiform body area [188]. Somatosensory areas have also been found to be modulated by observation of hand actions [189].

As with imagery, activation is smaller for observation than for execution [187] and is more pronounced upon observation of goal-directed behaviours [190] and live action as opposed to video [191].

4.1.1 Methods

Because this was a preliminary investigation to determine the feasibility of analyzing DYNOT data using SPM, few subjects were included in the experiment and analysis was performed on a single subject basis.

Subjects

Five neurologically normal right-handed subjects (one female, age range 25-39 years) underwent NIRS imaging with a DYNOT system (NIRx Medical Technologies, NY). Subjects were seated comfortably in a dentist's chair, in front of a computer monitor on which the task cues were displayed using E-Prime software (Psychology Software Tools, Pittsburgh, PA, USA). The DYNOT system performs continuous wave measurements using two laser sources of 760 nm and 830 nm in a time-multiplexed scanning fashion at a sampling rate of 1.8 Hz.

NIRS optode setup

Thirty NIRS optodes were placed over the right motor cortex in a 5x6 grid pattern, so that images of oxyhaemoglobin and deoxyhaemoglobin could be reconstructed using one of the finite element mesh (FEM) models in the NAVI software provided by NIRx Medical Technologies. The FEM model for the motor cortex is shown in figure 4.1.

The NIRx helmet system for optode placement consists of an adjustable rigid metal frame into which curved optode-holder strips can be fixed with screws. The optic fibres containing the laser diode light sources and detectors are then mounted into the optode-holder strips with a spring-loaded mechanism for comfort and close contact with the head. This rigid arrangement (by comparison with other systems) allows a repeatable and fixed optode configuration for different subjects, which facilitates image reconstruction on an FEM

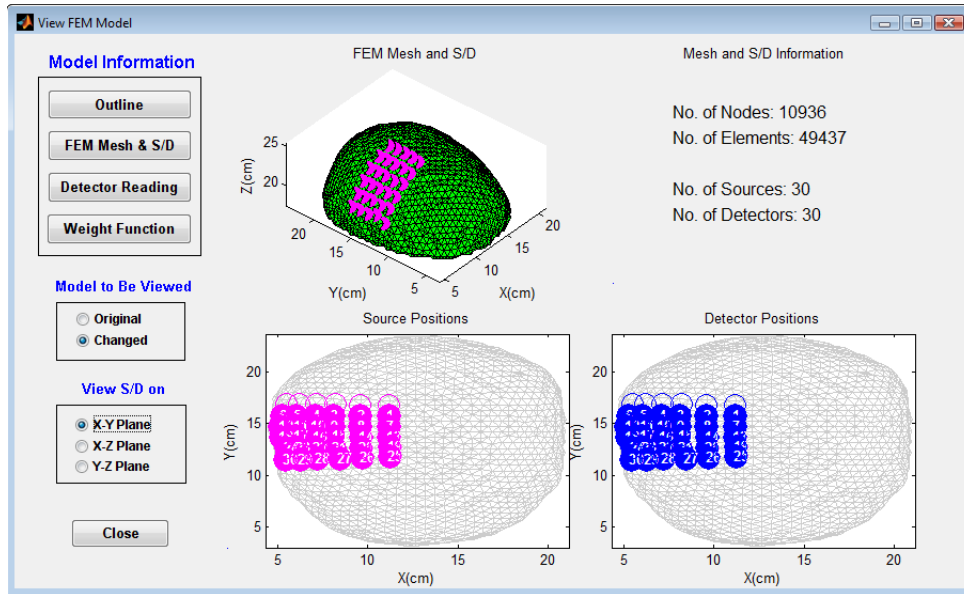


Figure 4.1: FEM model generator utility in NAVI.

model requiring consistent relative placement of sources and detectors. However, since subject head shape and size can vary substantially between subjects, in practice it can be very time-consuming (approximately 45 minutes) to adjust the helmet and optode-holders to fit an individual subject and ensure good contact of the optodes with the scalp, particularly in the presence of hair.

To determine the approximate position of the motor cortex, the C3 site in the 10-20 system for EEG electrode placement was located and used for the centre of the optode grid. This is a commonly-used method for locating sites of interest in surface measurements of brain function.

Task

For the first 8 minutes of imaging, subjects were asked to remain still with their eyes open, as a resting baseline. They were then verbally prompted to start the task when they were ready to do so. The motor task consisted of three 20 s blocks of left tapping alternating with 20 s rest blocks, and three 20 s blocks of right tapping alternating with rest blocks. The prompts for this task consisted of the written instruction “Tap left” or “Tap right” displayed on the screen. An observation task followed this, where subjects were instructed not to tap, but to observe a video of left and right hand movements performed by another person. The videoed hand movements consisted of tapping different fingers in an unpredictable pattern, and were shown as if they were in the first person view. The task sequence was the same as the motor task: three 20 s blocks of observing left-handed movements and three 20 s blocks of observing right hand movements, alternating with 20 s rest blocks. Finally, the same task sequence was repeated, but this time the subject was asked to imitate the hand movements performed by the second person. The whole sequence was repeated twice so that the subject performed 6 repetitions of each task block with each hand.

4.1. A MOTOR EXECUTION AND OBSERVATION TASK IN SINGLE SUBJECTS USING NIRS

	Rejected channels		Gain asymmetry > 1	Correlation < 0.5	
	wl1	wl2		wl1	wl2
Subject 1	89	89	44	134	150
Subject 2	0	0	0	126	230
Subject 3	0	0	0	24	70
Subject 4	0	0	0	2	16
Subject 5	0	0	0	46	218

Table 4.1: Channel diagnostics after bandpass filtering between 0.01 and 0.15 Hz. For each subject, and each wavelength where relevant, the number of channels that fails a specific criterion is shown. The number of rejected channels is the number of channels whose coefficient of variation was greater than 0.25. Gain asymmetry shows the number of reciprocal channels (source x detector y and source y detector x) whose gain setting difference is greater than 1. The two rightmost columns show the number of reciprocal channels whose correlation is less than 0.5.

Preprocessing and image reconstruction

Preprocessing and image reconstruction were performed using the NAVI software (NIRx Medical Technologies, NY), which is a software package written in Matlab, and distributed as Matlab pcode files. The raw data was band pass filtered between 0.01 and 0.15 Hz. Noisy channels were identified and rejected if the coefficient of variation (CV, ratio of standard deviation to the mean) in the 8 minute baseline period was greater than 0.25. Out of a total of 900 channels, the number rejected for each subject is shown in table 4.1. Another measure of data quality is the number of reciprocal channels (source x detector y and source y detector x) with different gain settings. Since the light paths between source x detector y and between source y detector x are the same, the required gain on the detector should be the same. Similarly, since these reciprocal channels sample the same area, a reciprocal correlation of less than 0.5 indicates that these channels are dominated by noise.

Images of oxyhaemoglobin and deoxyhaemoglobin concentration changes were then reconstructed on a 64x64x64 grid using the normalised difference method [192, 193]. In this algorithm the image sensitivity matrix for inversion is precalculated from the solution to the diffusion equation on a Finite Element Method (FEM) mesh obtained from a single template MRI [192]. Reconstructed images were then exported to the Analyze format using NAVI’s export feature, for analysis with SPM5.

Modification of NAVI DOT images for SPM compatibility

The FEM mesh model that NAVI uses for image reconstruction is based on the MRI of an individual head which is available in the NAVI distribution as a 256x256x256 image .mat file. Inside NAVI, DOT images can be displayed overlaid on a cropped version of this anatomical MRI image, shown in figure 4.2. However, the images exported by NAVI are in an arbitrary orientation and the voxel size is not specified in the output - in fact the Analyze header specifies a voxel size of 1 mm, regardless of the resolution (reconstruction grid size) chosen by the user. Because the NAVI source code is not accessible, the parameters used to align the MRI

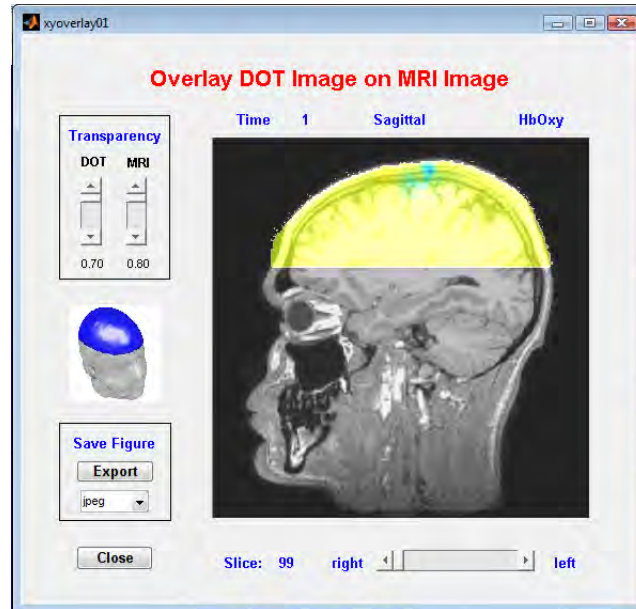


Figure 4.2: DOT/MRI overlay displayed by NAVI.

and the DOT images inside NAVI are not known by the user and have to be calculated as best as possible from the output of the program. To align the images requires rotation, scaling and translation.

First, to get the anatomical MRI and the DOT motor cortex images into the axial space required by SPM, a yaw rotation of $-\pi/2$ is applied to both images.

Scaling factor The next step required to re-register the DOT image to the original anatomical MRI outside of NAVI, is to calculate the DOT voxel size, which is not given because the $64 \times 64 \times 64$ (or user-selected resolution) MRI image displayed and exported by NAVI is cropped, as well as scaled, with respect to the original $256 \times 256 \times 256$ image.

The maximum and minimum co-ordinates of the FEM mesh in each direction can be found on each axis in NAVI's FEM model generator utility (figure 4.1). The minimum and maximum voxel co-ordinates of the head (the bounding box of the information-containing part of the image) in each of the X, Y, and Z directions can also be found from the DOT and MRI images as displayed in NAVI in $64 \times 64 \times 64$ resolution (DOT_64 and MRI_64) and for the $256 \times 256 \times 256$ voxel image supplied with the package (MRI_256). These are shown in table 4.2.

The maximum dimensions of the head in each of the X, Y and Z directions in FEM, MRI and DOT space can therefore be calculated, and are shown in table 4.3. Dividing the FEM dimensions by the number of DOT voxels gives the approximate voxel size, or scaling factor in each dimension for the DOT images. In the X direction the FEM mesh dimension is divided by 2, as the DOT image shows only half of the head whereas the FEM dimension is the entire breadth of the head. Because there is no common inferior limit to the head, the most inferior slice in the MRI image has to be estimated by visual similarity with the bottom

4.1. A MOTOR EXECUTION AND OBSERVATION TASK IN SINGLE SUBJECTS USING NIRS

	Left (X)	Right (X)	Anterior (Y)	Posterior (Y)	Inferior* (Z)	Superior (Z)
NAVI DOT_64 (vox.)	1	26	1	64	40	64
FEM (mm)	4.4554	21.0186	3.2401	23.4385	17.4005	25.2932
NAVI MRI_64 (vox.)	15	54	1	64	1	64
MRI_256 (vox.)	46	205	23	226	47	249

Table 4.2: Boundaries of the head in various images used by NAVI: the 64x64x64 voxel NAVI DOT image (DOT_64), the FEM mesh co-ordinates (FEM), the 64x64x64 voxel NAVI MR image (MRI_64) and the original 256x256x256 voxel MR image (MRI_256). *Because there is no common inferior limit to the head, the most inferior slice in the MRI image has to be estimated by visual similarity with the bottom slice shown in the NAVI display.

	DOT_NAVI	FEM	DOT voxel size (FEM/DOT_NAVI)
L - R (X)	26 voxels	165.632 mm ($\div 2$)	3.184 mm*
A - P (Y)	64 voxels	201.984 mm	3.156 mm
I* - S (Z)	25 voxels	78.927 mm	3.156 mm

Table 4.3: Actual head dimensions and calculated DOT voxel size. *Because there is no inferior limit to the head, the most inferior slice in the MRI image has to be estimated by visual similarity with the bottom slice shown in the NAVI display.

slice shown in the NAVI display.

Translation Once the DOT voxel size has been calculated, to align the DOT images exported by NAVI with the original MRI, the offset of DOT image relative to the MRI image must first be calculated, and then the translation required to align image landmarks (the head extremes in the X, Y and Z directions) needs to be determined. The steps required to align the image centres are listed below and the results of each step are shown in table 4.4.

1. The voxel co-ordinates of the DOT and MRI image centres, corresponding to mm co-ordinates (0, 0, 0) mm are determined by displaying the image in SPM.
2. The number of voxels either side of the centre, that is the difference between the centre voxel co-ordinate and the co-ordinate of the first and last voxel along each dimension is calculated.
3. The distance in mm from the centre to the image border is calculated for DOT and MRI images, by multiplying the voxel distance by the voxel size.
4. The offset of the DOT image with respect to the MRI image is calculated by subtracting the distance from the centre to the image border in the DOT image from that of the MRI image.

To align the images, the co-ordinates of the rightmost and most posterior, anterior, and superior voxel belonging to the head are used, as these are present, and able to be unambiguously determined, in both

		X	Y	Z
1	MRI head centre (voxels)	128.5	128.5	128.5
	DOT head centre (voxels)	32.5	32.5	32.5
2	MRI voxels to edge	127.5	127.5	127.5
	DOT voxels to edge	31.5	31.5	31.5
3	MRI mm to edge	127.5 mm	127.5 mm	127.5 mm
	DOT mm to edge	100.30 mm	99.41 mm	99.41 mm
4	Image offset	27.2 mm	28.09 mm	28.09 mm

Table 4.4: Calculation of the DOT offset with respect to the MRI in X, Y and Z directions.

		Right (X)	Posterior (Y)	Anterior (Y)	Superior (Z)
1	Extreme head voxel in DOT image	64	1	64	64
2	Extreme head voxel in MRI image	205	23	226	249
3	DOT head extremes in MRI space	227.70	28.01	226.84	226.84
4	MRI head extremes	205	23	226	249
5	Shift required (mm)	-22.7	-5.01	-0.84	22.16

Table 4.5: Calculation of the required translation to align DOT and MRI images .

the DOT and MRI images. The co-ordinates of the DOT voxel in MRI space can then be calculated by subtracting 1 from the most extreme voxel co-ordinate, multiplying the result by the scaling factor for that dimension (table 4.3) and adding the image offset calculated in table 4.4. The translation required to align the heads in the DOT image is then the difference between the co-ordinates of the head extremes in the MRI image and the co-ordinates of the head extremes in the DOT image in MRI space (rows 3 and 4 in table 4.5). This value (shown in row 5) is then rounded to the nearest integer.

The calculated rotation, scaling and translation can then be applied to DOT images using SPM and the alignment of the DOT with the original MRI confirmed visually. The MRI image can also be transformed into MNI space using SPM, and the resulting transformation used to transform the DOT images into MNI space. Of course the accuracy of the transformation to MNI space depends on the accuracy of the optode placement so that there is little difference between the actual positioning and positioning assumed by the FEM model in NAVI.

SPM masking and NIRS data scaling SPM makes some assumptions about the range of fMRI data values in order to mask non-brain voxels. While fMRI data in arbitrary units are in the range 500-1000, NIRS data are orders of magnitude smaller and may be negative. Because the values of NIRS data are so different from typical functional MRI values the masking procedure used to identify brain voxels in SPM does not work for NIRS image data. This problem can be overcome either by adding a large constant to the NIRS data, or more practically, by changing a line of code in SPM so that masking is not used, as unlike fMRI data, the NIRS images do not contain numerical values - or noise - outside of the limits of the FEM

head model, so are in effect already masked.

Determination of the optimal HRF for DOT data

In order to examine the HRF selection for different subjects and haemoglobin species, Bayesian model comparison [194] was used to compare the standard haemodynamic basis sets available in SPM: Inf-1: the canonical response, Inf-2: the canonical and its temporal derivative, Inf-3: the canonical and temporal and dispersion derivatives, F: a Fourier basis set with 10 sinusoids covering 20 s, FH: a Hanning windowed Fourier set, Gamm3: a set of three Gamma basis functions and FIR: a finite impulse response, corresponding to a block average. Using SPM a region of interest of 3 mm radius was extracted around the most activated voxel from the L_TAP contrast and used as input to the `spm_vb_roi_basis.m` function provided in SPM.

The model selection problem involves choosing between two models M_i on the basis of observed data D . The posterior probability $p(M_i|D)$ given by Bayes formula in 4.1 can be used for model comparison.

$$p(M_i|D) = \frac{p(D|M_i)P(M_i)}{P(D)} \quad (4.1)$$

where $p(D|M_i)$ is the model evidence: the probability of the data given model M_i , $P(M_i)$ is the prior probability of the model M_i and $P(D)$ is the unconditional marginal likelihood of the data. If no model is preferred a priori the their prior probabilities are equal and the model with the highest posterior probability also has the largest evidence.

Taking the model parameters θ into account, the model log-evidence can be written as

$$L(M) = q(\theta|D, M) \log \frac{p(D, \theta|M)}{q(\theta|D, M)} d\theta + \int q(\theta|D, M) \frac{q(\theta|D, M)}{p(\theta|D, M)} d(\theta|D, M)$$

where $q(\theta|D, M)$ is an approximate posterior density whose parameters are updated to maximise the first (negative free energy) term, and the second term is the Kullback Leibler divergence for probability densities p and q and [194].

Data analysis with SPM

First level analysis was performed on the oxyHb and deoxyHb images for each of the 5 subjects using the general linear model (GLM) as implemented in SPM5. Regressors were included for each of the task conditions left tapping (L_TAP), right tapping (R_TAP), observing left hand movement (L_OBS), observing right hand movement (R_OBS), and imitating left (L_IMIT) and right (R_IMIT) convolved with SPM's canonical haemodynamic response function. High pass filtering was performed to remove signal drifts with a period longer than 128s. Correction for serial autocorrelation in the data was performed using an AR1 model. Contrasts for testing for increases in oxyHb and decreases in deoxyHb for the conditions L_TAP, R_TAP, L_OBS and R_OBS were constructed for each subject. The imitation condition was not analysed. In the data of one subject (subject 5) no significant voxels were found in the early stages of SPM analysis. This subject was excluded from further analysis.

Empirical determination of the false positive rate in single subjects using DOT null data

To obtain an idea of the likelihood of false positives in this kind of analysis on single subject NIRS data, exactly the same analysis was run using null data for each subject which was obtained from an 8 minute baseline prior to the start of the task.

4.1.2 Results

Bayesian model comparison of haemodynamic basis sets

As shown in figure 4.3 for oxyhaemoglobin in 2 subjects (subjects 1 and 2) the combination of gamma functions has the highest model log-evidence and for 2 subjects (3 and 4) the canonical HRF shows the highest model log-evidence. For deoxyhaemoglobin in subjects 1 and 3 the canonical HRF shows the highest model log-evidence and for subjects 2 and 4 the combination of gamma functions is the best model.

Although this is not an event-related design and specification of an accurate HRF is not as critical, there is some discrepancy between subjects and haemoglobin species over the optimal HRF which is either the canonical HRF or combination of 3 gamma functions. Little or no advantage appears to be gained by including the derivatives of the canonical HRF in the model, even for oxyHb. The canonical HRF shows the highest log-evidence for 4 out of 8 cases and it being simple to implement and perform statistical testing, there seemed to be no motivation for using any other HRF in further analysis. Although it may not be the optimal basis set for all subjects and all Hb species, interpretation is simplified by the ability to perform ANOVAs and t-tests at the second level.

Single subject responses to action execution and observation

The number of significant voxels for each subject, haemoglobin species, and condition are listed in table 4.6. All four subjects showed large significant clusters of activation for oxyHb in the L_TAP condition, and smaller clusters of activation for deoxyHb. However, the significant oxyHb and deoxyHb clusters only showed spatial overlap in two of the subjects. The overlap area for one subject is shown in figure 4.4. In the R_TAP (ipsilateral) condition, three out of four subjects showed large oxyHb and deoxyHb clusters of activation, with some overlap in each case. In the L_OBS condition one subject showed a large cluster of activation in oxyHb and deoxyHb with overlap, and another two showed activation clusters in deoxyHb without any significant voxels in oxyHb. In the R_OBS condition two subjects showed activation clusters in oxyHb without any significant voxels in deoxyHb. There were significant differences between left and right conditions in oxyHb only for two subjects.

The location of the activation region found with DOT in figure 4.4 extends to a greater depth than might be expected to be probed with near infrared light. The inclusion of fifth nearest-neighbour measurements in image reconstruction, at a source-detector separation distance of 54 mm, as used here, has been shown to be able to recover changes up to 20 mm deep within the brain; sufficient to measure activity within sulcal folds [195]. However, artefact in DOT image reconstruction is also a probable source of the apparent

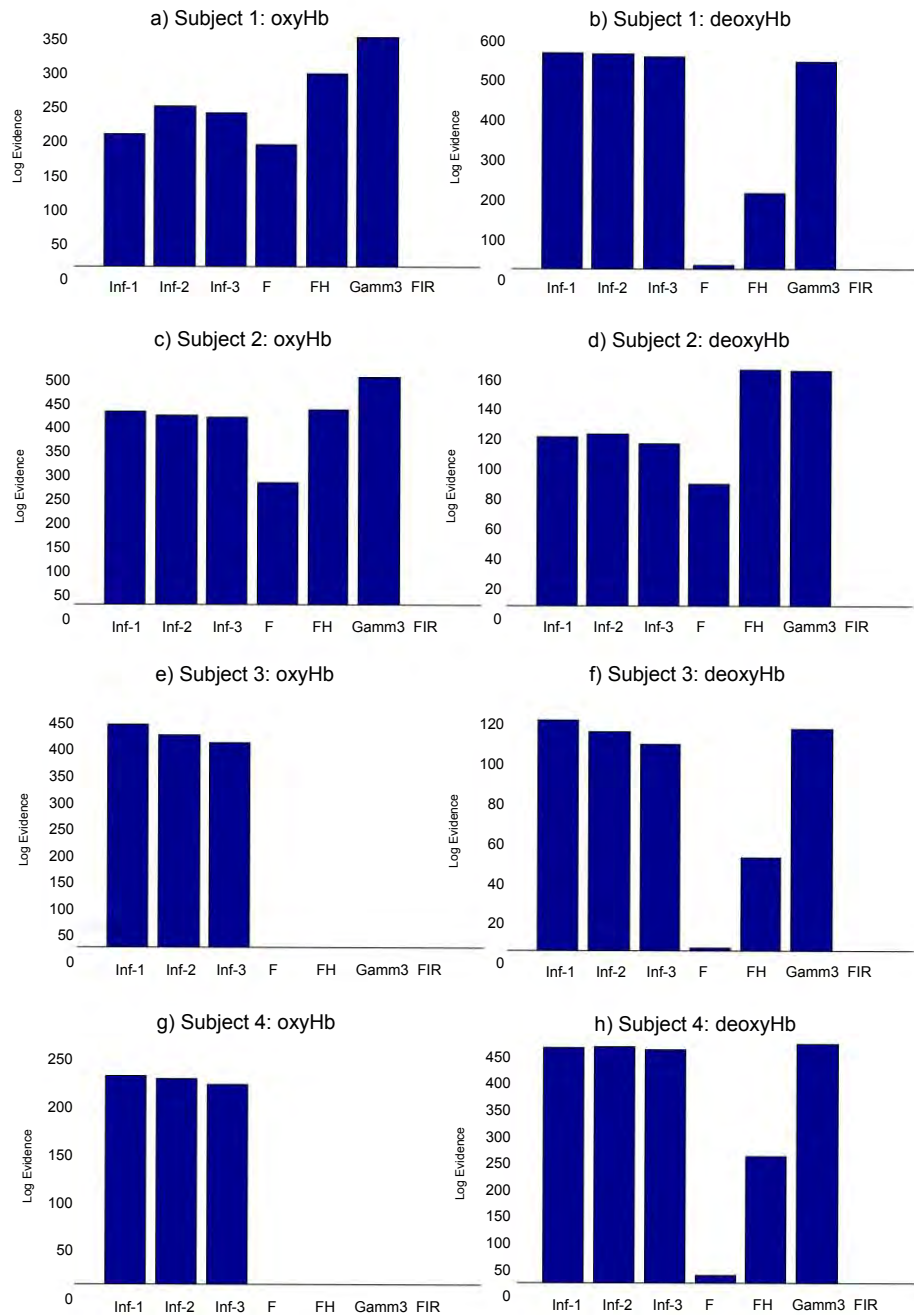


Figure 4.3: Model evidence for different haemodynamic basis sets: Inf1 - Canonical HRF, Inf2 - Canonical plus temporal derivative, Inf3 - Canonical plus temporal and dispersion derivatives, F - Fourier, FH - Fourier with a Hanning Window, Gamm3 - 3 Gamma basis functions and FIR - a Finite Impulse Response function. The evidence values have been normalised by subtraction so that the smallest log-evidence is zero.

		L_TAP	R_TAP	L_OBS	R_OBS	L_TAP vs RTAP	L_OBS vs R_OBS
Subject 1	OxyHb	11112	0	3	11144	0	2819,18,34
	DeoxyHb	60, 11	0	6116, 58, 18	0	0	170
	Overlap	1	0	0	0	0	0
Subject 2	OxyHb	9148	9224, 87, 42	8090, 7	0	52,15,843	4460
	DeoxyHb	1664, 29, 8	2505, 4	8243, 13	0	0	0
	Overlap	235	621	5143	0	0	0
Subject 3	OxyHb	836, 59	12180	0	0	0	0
	DeoxyHb	12, 7, 4, 16	12339, 5	79, 27	0	0	0
	Overlap	0	7782	0	0	0	0
Subject 4	OxyHb	13756	96,16, 147, 10, 12	0	6723	12041,64	0
	DeoxyHb	3878	8270, 220	0	0	0	0
	Overlap	3257	16	0	0	0	0

Table 4.6: Number of significant voxels in each cluster for each contrast $p < 0.05$ FDR corrected.

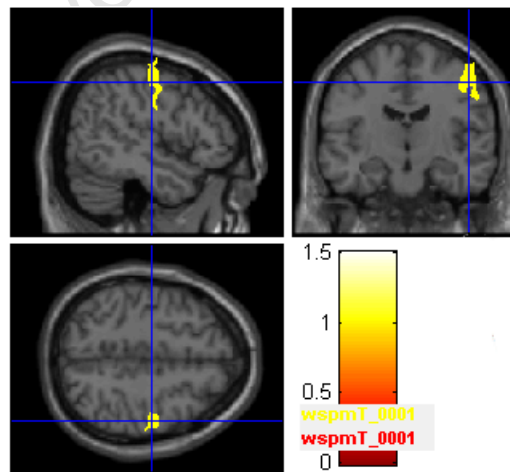


Figure 4.4: Area of overlap between significant oxyHb and deoxyHb clusters for the L_TAP contrast for subject 2, thresholded at $p < 0.05$ FDR corrected. The DOT activation image has been transformed to MNI space and overlaid on a T1-weighted structural MRI.

4.1. A MOTOR EXECUTION AND OBSERVATION TASK IN SINGLE SUBJECTS USING NIRS

		p<0.001 uncorrected		p<0.05 FDR	
		L_TAP	R_TAP	L_TAP	R_TAP
Subject 1	OxyHb	0	0	0	0
	DeoxyHb	0	22,1,1,3,1	0	0
Subject 2	OxyHb	1	1,1	0	0
	DeoxyHb	1,6	2,2,13,1,1	0	0
Subject 3	OxyHb	2	0	0	0
	DeoxyHb	290,435,1,1,1	54,54,6,1,10,2,1,1	385,662,2	6,1
Subject 4	OxyHb	0	3,1	0	0
	DeoxyHb	0	11,4,49,7,1,1	0	0

Table 4.7: Number of significant voxels in each cluster for each contrast tested on null (baseline) data.

activation at this depth. Firstly, the activated regions may occupy larger regions of image space due to blurring inherent in diffuse image reconstruction. Secondly, the diffusion approximation to the radiative transfer equation which is most commonly used for forward modelling is not accurate when a heterogenous medium includes non-scattering regions such as CSF, and may overestimate the depth sensitivity. However, using the normalised difference method for image reconstruction, as is used here, accurate reconstructions of scatter and absorption have been obtained despite the inclusion of a non-scattering layer [196]. Lastly, because the sensitivity of diffuse light measurements drops off quickly with increased depth, the sensitivity of the imaged area is weighted to superficial regions closest to the source and detector. To improve the depth accuracy, a spatially variant regularization parameter is often used in the solution of the inverse problem. Equivalently, Pei et al. [196] solve the inverse problem using a scaled weight matrix. However, this means that image reconstruction algorithms may tend to push the recovered perturbation into regions of the medium with the lowest weight [197], which here is the inferior boundary of the FEM model (shown in figure 4.1).

False positive rate determined with null data

The number of false positive voxels occurring at significance levels of $p < 0.001$ uncorrected and $p < 0.05$ FDR corrected are shown in table 4.7. Except for one subject the false positive voxels are small in number and isolated.

4.1.3 Discussion

DYNOT images reconstructed by NAVI were successfully modified for use with SPM. However, the results of analysis on single subjects was quite variable. A contralateral response to the motor task was observed in all subjects and an ipsilateral response was observed in three out of four, while responses to the observation task appeared inconsistent. Only two subjects showed a significantly greater response to contralateral than ipsilateral tapping, and only in oxyHb. The number of subjects available for analysis was very small, not really allowing conclusions to be drawn, however, discrepancies may be due to differences in data quality,

which can vary widely in NIRS due to differences in optode contact with the scalp which may depend on subject factors such as head shape and hair thickness and colour.

Uncontrolled experimental factors could contribute to differences in response between subjects. The NIRS-measured response to motor activity is known to increase with increasing frequency [101, 198, 199], intensity [199, 108] or complexity [123] of finger tapping, with complex tasks evoking both larger contra- and ipsilateral oxyHb changes than simple (one-finger) tapping [123]. Although the complexity of the task in our case was the same between subjects, the frequency and intensity of tapping was not strictly controlled.

Consistency between oxyHb and deoxyHb responses

Although both oxyHb and deoxyHb responses were observed in all subjects in response to the contralateral motor task and in three subjects in response to the ipsilateral task, there was only substantial spatial overlap between the oxyHb and deoxyHb responses in two subjects, both contralaterally and ipsilaterally. Strictly, an increase in oxyHb without a significant decrease in deoxyHb should not be taken to represent activation as it would not result in activation if BOLD fMRI were used [81]. However, many investigators choose only to analyse oxyHb: because the deoxyHb response is small it is often difficult to show statistically significant effects in this parameter. DeoxyHb also has a lower signal to noise ratio than oxyHb and is more likely to be affected by inaccuracies in optical path length and cross talk [181]. The deoxyHb response may be more spatially localised than that of oxyHb [105, 107], but may vary more between subjects, as some studies have been unable to find equally reliable deoxyHb responses [96, 123, 124, 176].

Good spatial and temporal correlation has been found between motor-task induced haemodynamic changes measured with fNIRS and cerebral blood flow velocity measured using transcranial Doppler sonography (TCD) [105] and the BOLD response quantified using fMRI [184, 2, 1, 15, 3]. However, it is not certain which haemoglobin species correlates best with the BOLD response or which best reflects cortical activation. Although deoxyHb should be expected to correlate best with BOLD only a few studies have demonstrated good correlation between deoxyHb and fMRI BOLD signals [184, 2, 15, 3], perhaps because of lower SNR in deoxyHb, while some have shown better spatiotemporal correlations between oxyHb and BOLD fMRI [200, 1].

However, because the oxyHb signal is most likely to be contaminated with systemic physiological noise [81], caution should be exercised when interpreting activations using only oxyHb data.

NIRS studies of action observation

A significant oxyHb and deoxyHb response to observation of contralateral (left) motor observation was observed in one subject, and significant deoxyHb response in a second subjects. Activation to ipsilateral (right) motor observation was found in oxyHb in two subjects, and in the fourth subject no response at all was observed.

Action observation tasks most consistently evoke activation in an extended bilateral network comprising frontal (BA 44), premotor cortex (BA 6) and adjacent superior frontal gyrus (SFG), the SMA (BA 6),

S1 (area 2), IPL (area Pft), and visual area V5 [188]. However some studies have found more premotor and parietal mirror activation in the left hemisphere [187, 201] in right-handed subjects observing right hand actions. The left-lateralization is present but less strong in right-handed subjects observing left hand movement. Very left-handed subjects show a similar pattern of lateralization on the right, while the activation of more ambidextrous left-handed subjects is more bilateral [201]. Without measuring the left hemisphere it is unclear whether the responses to observation of the ipsilateral (right) hand in our study were bilateral or left-lateralised.

Holper et al. [176] observed bilateral oxygenation changes using NIRS, both during action observation and imitation, and found that the averaged oxyHb response during observation and motor imagery were approximately one-third lower than during an imitation task. We did not observe bilateral response to action observation in any subject.

A number of factors appear to influence the NIRS-measured motor response to action observation. As with fMRI [191], smaller, different or non-existent responses have been found for the observation of televised action compared to that of live action in both adults and infants [126]. In one NIRS study, recognition and integration of nursing actions was found to be modulated by expertise [172]. In another set of studies, activity in the motor area has been found to be modulated by the outcome - win or loss - of a competitive game [173, 174]. View of the player also modulated the NIRS-measured motor activation: activity over the dorsal anterior region of the motor area was greater when the player was presented in third person view (facing the subject), regardless of the outcome of the game, although the dorsal posterior region of the motor area was activated only when the supported player won and was observed with a first-person view [175]. The oxyHb response has also been found to be sensitive to the appearance and kinematics (human vs robot) of the observed action [127].

Laterality of motor execution and imagery

In three of four subjects a response was measured to movement of both the contralateral and ipsilateral hand, and in two subjects there was no significantly greater response to left than right tapping in the contralateral motor cortex. NIRS is known to be sensitive to haemoglobin changes over the contralateral motor cortex both in response to a motor stimulus [177, 101, 117] and to motor imagery [202, 90, 203, 121], although the response to imagery is smaller than that of action execution [120, 124]. NIRS studies measuring cortical oxygenation during motor imagery have found the expected activation in primary, premotor and supplementary motor areas [79, 202, 171, 90, 120] with a delayed oxygenation response to imagery compared to execution [120].

However, several studies have, like us, measured a bilateral response to motor execution [184, 120, 103], and imagery [120], with smaller ipsilateral activation [95, 101, 82, 123] or a contralaterally dominant response only to left [120, 176], or right [183] hand movement, which may be dependent on subjects' handedness. Since we measured only the right motor cortex in our right-handed subjects, we assume our response to right hand movement is bilateral, although possibly with contralateral dominance, but cannot say anything about the laterality of the response to the left hand stimulus. It is possible that systemic changes may also contribute to the frequently observed ipsilateral activation to motor stimulation. This is worth investigation, as many

NIRS studies that use motor tasks only measure the hemisphere contralateral to the executed movement [117, 78, 3].

Systemic changes and latency between oxyHb and deoxyHb responses

Motor activity has been found to be accompanied by an autonomic response, which results in systemic changes, such as an increase in heart rate, which is correlated to extra-cerebral changes in blood flow and oxyHb concentration [82]. Systemic changes may therefore affect the interpretation of an oxyHb response to stimulation and may also alter the latency between the oxyHb and deoxyHb responses.

One of the early studies on cerebral oxygenation in response to a motor task found a biphasic change in oxyHb, with a fast initial increase and a pronounced poststimulus undershoot, while the deoxyHb response was monophasic, with a greater response latency [101]. This latency may help to explain the existence of transients sometimes observed in BOLD responses: the initial dip and post-stimulus undershoot.

However, the latency between oxyHb and deoxyHb responses observed over M1 during motor stimulation appears to be different over the visual cortex (V1) during visual stimuli [179, 78]. In the motor cortex the oxyHb increase precedes the deoxyHb decrease with a mean latency of 1.6 ± 0.2 s [101, 184, 179, 78, 82, 204, 3] while in the visual system the change is nearly simultaneous (0.1 ± 0.3 s) [205, 206, 179, 78]. Although the peak response time for oxyHb, deoxyHb and totHb is similar for motor and visual stimulation (6-7.5s), an early (2s post stimulus) deoxygenation response has been found in the visual but not the motor cortex [78]. This difference in delay between the oxyHb and deoxyHb response may be attributable to differences in the vascular and neuronal architecture of the motor and the visual cortex, or differences in the coupling mechanisms [179]. Alternatively, these differences may arise because the surface measurements used in NIRS are also sensitive to haemodynamic changes in the scalp, meaning that changes in systemic haemodynamics are a confound [119]. A motor paradigm may evoke a much larger pulse and CBF change than a passive sensory stimulus [82], and a sensory stimulus results in a negligible latency between oxyHb and deoxyHb. Boden et al. [119] found that when ipsilateral finger tapping was used instead of a resting period the increase in oxyHb occurred 2s later than when periods of rest were used, while the deoxyHb response was the same for both tasks, suggesting that early oxygenation is a systemic confound. They also applied a global correction scheme, which was found to eliminate the delay observed in the stimulation vs. rest paradigm [119].

False positives and the effect of data quality

The varying responses to motor execution and observation tasks observed in individual subjects leads to the question of how many of these results are false positives or negatives. Although the rate of false negatives at different noise levels could be examined using simulated data, a simple method to investigate the rate of occurrence of false positives using task-free data from the resting baseline. This does not address the problem of false positive activation resulting from systemic changes that occur as a result of the task, only that which results from the structured noise in NIRS data.

Using FDR correction for multiple comparisons on analyses of null data, false positive voxels occur in only one subject (subject 3). Given the number of voxels in the (masked) image, the expected number of significant

voxels occurring by chance is 262 for an uncorrected significance level of $p < 0.001$, and for all other subjects the actual false positive rate is well below this number. Interestingly the subject that does show false positives shows them in deoxyHb and not in oxyHb which is contrary to expectation given the known low SNR of deoxyHb measurements and the structured noise in oxyHb time series which might lead to synchronization with a block design stimulus.

The absence of false positives may of course merely indicate low SNR data, particularly where little activation could be measured. Subject 1 had several channels which did not survive the CV threshold. This indicates low SNR in those channels, which may be due to poor contact with the scalp or dark skin pigmentation. (Subject 3 was also darkly pigmented.) Subject 1, together with subject 2 also shows the largest number of reciprocal channel correlations less than 0.5 for the 760 nm wavelength. Subjects 1, 2 and 5 also show a larger number of noisy (low correlation) channels at 830 nm, although all channels for all other subjects are within the CV threshold limit. The lower number of reliable channels for subject 1 may explain why little significant activation was observed for this subject. Subject 2, however, who also had a large number of low correlation channels although all survived the CV threshold, shows significant activation in three conditions in both haemoglobins. Subject 3 was the only subject who had a significant number of false positives using null data - although these are only in deoxyHb and so are easily distinguishable using the strict criterion of activation as significant increase in oxyHb as well as decrease in deoxyHb. The data quality for subject 3 was also very good: very few channels had low SNR. Subject 4 also had good SNR but much fewer false positives - this may be because of different spontaneous physiological processes in these 2 subjects.

4.2 The effect of preprocessing parameters on the false positive rate in group analyses

In functional MRI, data is usually high pass filtered but rarely smoothed, and some form of correction for autocorrelation is performed. The prewhitening method necessitates high pass filtering. However, in NIRS, smoothing is usually required to improve the SNR. In this experiment we investigated the rate of false positives for various high and low pass filter cutoff frequencies, with and without AR1 autocorrelation correction used in SPM5 and with two different task block lengths.

4.2.1 Methods

Eight minutes of null data was collected from the right motor cortex of 10 subjects while they rested with eyes open. The optode locations were the same as for the motor task and are described in section 4.1.1. Three minutes of resting state data were acquired in the same way from a further 7 subjects.

Data were preprocessed and images reconstructed as described in section 4.1.1, except that band pass filtering was not performed. Instead two sets of images were reconstructed using low pass filtered data: one with a cutoff frequency of 0.5 Hz and one with a cutoff frequency of 0.15 Hz. The 0.15 Hz cutoff frequency should exclude variation at the respiration frequency (0.2-0.4 Hz).

Block length	LPF	HPF	p<0.001 unc	p<0.05 FDR
10 s	0.5 Hz	0.005 Hz	3	0
		0.02 Hz	68	0
		0.04 Hz	260	216
	0.15 Hz	0.005 Hz	18	0
		0.02 Hz	226	104
		0.04 Hz	1112	1825
20 s	0.5 Hz	0.005 Hz	77	56
		0.02 Hz	186	160
	0.15 Hz	0.005 Hz	111	86
		0.02 Hz	309	296

Table 4.8: OxyHb: False positive voxels in a fixed effects group analysis of null data from 10 subjects

Two analyses were performed.

First, fixed-effects group analyses were carried out on the last 320 s of the 8 minute null data from 10 subjects in SPM5 on both the oxyHb and deoxyHb images, with different temporal low pass filter cutoffs. Two different block design frequencies were investigated: one with a 40 s period (20 s stimulation and 20 s rest alternating 8 4 times) and one with a 20 s period (10 s stimulation and 10 s rest alternating 16 8 times). Three different high pass filter cutoffs: 0.005 Hz, 0.02 Hz and 0.04 Hz, were investigated for the 10 s block length and two HPF cutoffs were investigated for the 20 s block length. The third HPF cut off frequency (0.04 Hz) is higher than the frequency of the 20 s block design paradigm (0.025 Hz) so it was assumed that all noise at the stimulation frequency would be filtered out and no false positives would result [140]. The number of activated voxels at thresholds of $p < 0.001$ uncorrected and $p < 0.05$ corrected using the FDR method, was recorded.

Second., to look at the effect of using more subjects with less data per subject, 160 s of the three minute null data from 17 subjects were analysed in a fixed effects model using the same filtering and block length variations, except that there were 8 repetitions of 20 s on/off blocks and 16 repetitions of the 10 s on/off blocks. For each filter/block length combination one analysis was conducted using AR1 prewhitening in SPM, and one with no correction for serial correlation.

4.2.2 Results

Fixed effects group analysis on 10 subjects

The number of false positives in oxyHb and deoxyHb in a fixed-effects group analysis of the last 320 s of null data in the 8 minute recordings from 10 subjects are shown in tables 4.8 and 4.9.

In oxyHb, the number of false positives tends to increase with HPF cutoff frequency (as in [140]) and moderately with increased smoothing as well as with longer block length.

4.2. THE EFFECT OF PREPROCESSING ON FALSE POSITIVES IN GROUP ANALYSES

Block length	LPF	HPF	p<0.001 unc	p<0.05 FDR
10 s	0.5 Hz	0.005 Hz	13	0
		0.02 Hz	1	0
		0.04 Hz	1	0
	0.15 Hz	0.005 Hz	866	3362
		0.02 Hz	1071	4655
		0.04 Hz	2088	6739
20 s	0.5 Hz	0.005 Hz	2206	4256
		0.02 Hz	2087	4679
	0.15 Hz	0.005 Hz	4361	10151
		0.02 Hz	8158	352

Table 4.9: DeoxyHb: False positive voxels in a fixed effects group analysis of null data from 10 subjects

FDR correction for multiple comparisons reduces the number of false positives, but where a large number of false positives occurs, even larger clusters are found using FDR correction.

In general there are substantially more false positives for deoxyHb than oxyHb. False positives also increase with increased smoothing and with longer block length when correction for multiple comparisons is not applied, but not always for increasing HPF cutoff frequency. No false positives were found for similar random effects analyses under any of the conditions.

Fixed effects group analysis on 17 subjects

The number of false positive voxels occurring in a fixed-effects group analysis of 160 s of null data in 17 subjects with various preprocessing and analysis parameters are shown in tables 4.10 and 4.11 respectively. FDR correction for multiple comparisons reduces the number of false positives almost to zero in most cases. However, in seven cases where AR1 prewhitening is not used and a large number of false positives occurs, even larger clusters are found using FDR correction.

When AR1 prewhitening is used for deoxyHb no false positives are found in any instance. For oxyHb when AR1 prewhitening is used, the number of false positives is greatly reduced, or eliminated.

With AR1 correction, false positives for the 10 s block length only occur at the lowest high pass filter cutoff frequency (0.005 Hz). False positives in oxyHb and deoxyHb for the 10 s blocks without AR1 correction and without correction for multiple comparisons are shown in figure 4.5. The effect of the different low pass filters is smaller for deoxyHb than for oxyHb where increased temporal smoothing increases the number of false positives. The effect of high pass filtering is opposite for oxyHb and deoxyHb: an increase in high pass filter cutoff frequency up to the block frequency (0.05 Hz) in general increases the false positive rate for oxyHb, while decreasing it for deoxyHb. The absence of false positives for oxyHb at a cutoff frequency of 0.02 Hz is difficult to explain. The false positive problem appears to be worse in deoxyHb than in oxyHb.

No false positives are found for deoxyHb when the block length is 20 s. False positives for oxyHb are

Block length	LPF	HPF	Whitening	p<0.001 unc	p<0.05 FDR
10 s	0.5 Hz	0.005 Hz	no AR1	5	0
			AR1	5	0
		0.02 Hz	no AR1	0	0
			AR1	0	0
		0.04 Hz	no AR1	27	0
			AR1	0	0
	0.15 Hz	0.005 Hz	no AR1	40	7
			AR1	29	17
		0.02 Hz	no AR1	0	0
			AR1	1	0
		0.04 Hz	no AR1	66	0
			AR1	0	0
20 s	0.5 Hz	0.005 Hz	no AR1	1155	2760
			AR1	17	0
		0.02 Hz	no AR1	158	3221
			AR1	36	0
		0.04 Hz	no AR1	264	0
			AR1	25	4
	0.15 Hz	0.005 Hz	no AR1	2358	6036
			AR1	76	43
		0.02 Hz	no AR1	2358	6036
			AR1	76	43
		0.04 Hz	no AR1	2358	6036
			AR1	76	43

Table 4.10: OxyHb: False positive voxels in fixed effects analysis of null data from 17 subjects

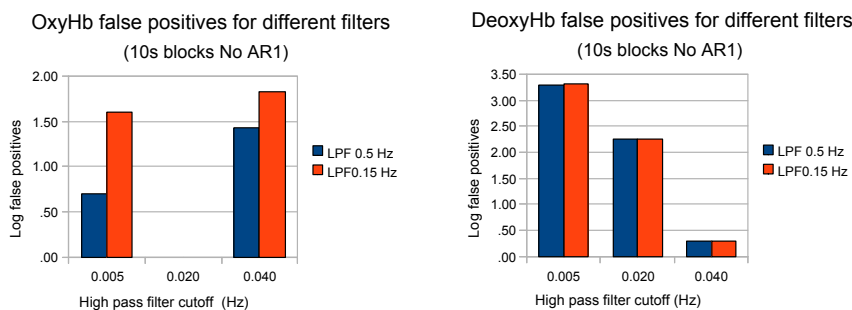


Figure 4.5: False positives for 10 s blocks without AR1 correction and p<0.001 uncorrected for multiple comparisons. With AR1 correction no false positives are found except in oxyHb at 0.005 Hz. Note the different y-axis scales for oxyHb and deoxyHb.

Block length	LPF	HPF	Whitening	p<0.001 unc	p<0.05 FDR	
10 s	0.5 Hz	0.005 Hz	no AR1	1956	10685	
			AR1	0	0	
		0.02 Hz	no AR1	180	1480	
			AR1	0	0	
		0.04 Hz	no AR1	2	0	
			AR1	0	0	
	0.15 Hz	0.005 Hz	no AR1	2057	11056	
			AR1	0	0	
		0.02 Hz	no AR1	176	1500	
			AR1	0	0	
		0.04 Hz	no AR1	2	0	
			AR1	0	0	
20 s	0.5 Hz	0.005 Hz	no AR1	1	0	
			AR1	0	0	
		0.02 Hz	no AR1	0	0	
			AR1	0	0	
		0.15 Hz	0.005 Hz	no AR1	1	0
				AR1	0	0
	0.02 Hz	no AR1	0	0		
		AR1	0	0		

Table 4.11: DeoxyHb: False positive voxels in fixed effects analysis of null data from 17 subjects

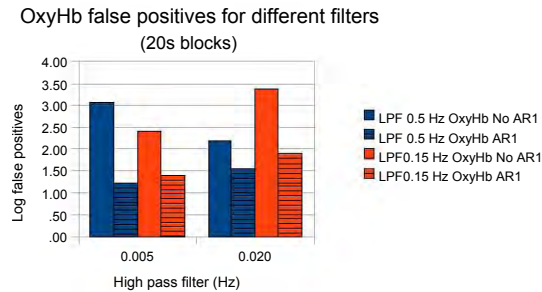


Figure 4.6: False positives for oxyHb with a block length of 20 s. No false positives were found for deoxyHb with a 20 s block length.

shown in figure 4.6. Here again, the false positive problem is reduced, although not eliminated using AR1 prewhitening. The effect of low pass filtering depends on the high pass filter used: at the lower high pass filter cutoff increased smoothing leads to fewer false positives whereas at the higher high pass filter cutoff increased smoothing leads to increased false positives, as in the 10 s block length.

There were no false positives in random effects analyses.

4.2.3 Discussion

AR1 prewhitening greatly reduces the false positives in all cases. FDR correction for multiple comparisons reduces the number of false positives in some cases, but increases it in others. A FDR threshold is determined from the observed p-value distribution, and therefore adapts to the amount of signal in the data. The larger the signal is, the lower the FDR threshold will be and the more false positives will occur. Since FDR correction depends on the p value distribution, if p values are severely underestimated due to incorrect autocorrelation modelling, FDR correction does not necessarily help to control false positives. However, if the null hypothesis is true everywhere, a FDR procedure controls the chance of a false positive anywhere in the brain at the specified level. The procedure guarantees that the average proportion of false alarms among the voxels identified as significant will be below the specified bound on average over many replications of an experiment. For any given data set the FDR may not be below the bound [207].

Smith et al. [140] did an empirical investigation of the false positive rate in null (resting) fMRI data. They found that without correction for multiple comparisons the actual rate of false positives at a probability threshold of $p < 0.001$ was about 25 times the expected rate. They regard this as a conservative estimate of the effect of non-white noise, due to the long TR (3 s) which should reduce the temporal correlations. This false positive rate was substantially reduced when prewhitening or precolouring was used to correct for serial correlation. In principle the autocorrelation problem should be more severe in NIRS since the sampling rate is higher.

In the 17 subject analysis using 10 s blocks produces a large number of false positives in deoxyHb if no AR1 prewhitening is used, but for the 20 s blocks the false positive problem is non-existent. However, in the 10 subject analysis there are more false positives in deoxyHb for the 20 s block length. For oxyHb the false

positive problem is worse with 20 s blocks than 10 s blocks, both with and without AR1 prewhitening and in both sets of data.

The effect of filtering is somewhat variable. In general increased smoothing increases false positives - this effect is particularly pronounced for deoxyHb in the 10 subject analysis. The effect of high pass filtering is not consistent for deoxyHb, but increasing the high pass filter cutoff increases the number of false positives in oxyHb.

In [140] the number of false positives was found to increase with high pass filter cut-off, up to the frequency of the stimulus. With and without AR1 correction the number of false positives was much larger with this optimal high pass filter (just below the stimulus frequency) than with no filter. The number of false positives obtained with the optimal high pass filter and with AR(1) correction was similar to the number obtained with no high pass filter and no AR(1) [140]. This suggests that correction for non-white noise is necessary for single subject and fixed-effects GLM analyses of fMRI data, and recommended [142], although less important, for random effects analyses. These authors also found that including a larger number of subjects in both fixed and random effects analyses reduced the number of false positives. Our finding is that the larger number of subjects (17) reduced the number of false positives in about half of the cases considered.

We found no false positives in random effects analyses of null DOT data, however, in fixed effects analyses it is recommended that methods to correct for serial correlation and multiple comparisons be employed, so as to control the rate of false positives.

4.3 Summary and conclusions

We explored the use of SPM for the analysis of NIRS tomographic images. In our block design data we found the best HRF was a combination of gamma functions or SPM's canonical HRF. Unlike others [63], we did not find evidence for including temporal or dispersion derivatives.

In three individuals we found similar activation to both left tapping and right tapping in the right motor cortex, however, the spatial locations of the oxyHb and deoxyHb responses did not always coincide. Two of these subjects showed the expected greater response to tapping with the left (contralateral) hand than with the right, but only in oxyHb. In two subjects we found some activation to the right hand observation task, and in the other two we found activation to the left hand task, but these responses were not consistent across haemoglobin species. To investigate whether these disparate results could come about by chance, we did the same analysis on task-free data. Small clusters of false positive voxels were found in deoxyHb for all subjects, however with FDR correction for multiple comparisons only one subject retained any false positives.

Next we investigated the effect of preprocessing parameters: temporal smoothing, high pass filtering and AR1 prewhitening on the false positive rate in group analyses of null data from 10 and 17 subjects. We found no false positives in random effects analyses. In fixed effects analyses, AR1 prewhitening and FDR correction for multiple comparisons eliminated the false positives, as has previously been found for fMRI data [140]. The number of false positives increased with increased temporal smoothing, and in oxyHb with increasing high pass filter cutoff frequency. In deoxyHb the effect of high pass filtering was variable. A block length of

20 s appears to produce more false positives than a 10 s block length and a larger number of false positives occurs in deoxyHb than oxyHb.

Although we did not investigate the efficiency of actually detecting a response, we conclude that to avoid false positive results, random effects analyses should be used as in fMRI, with AR1 prewhitening and correction for multiple comparisons. From the point of view of false positives, less temporal smoothing, a lower HPF cutoff-frequency and a block length closer to 10 than 20 s appear to be optimal. However, in selecting design and preprocessing parameters, a compromise should be sought to ensure that a true response can be detected, and false negative findings avoided.

University of Cape Town

Part II

Group level comparisons of fNIRS and fMRI in sensory and motor tasks

Chapter 5

Responses to sensorimotor stimulation: experiment description and physiological data analysis

The aim of this part of the thesis was to investigate selected topics in neuroimaging of the sensorimotor system using both fNIRS and fMRI and to contrast the results obtained using each of these imaging techniques. Because facilities for performing simultaneous imaging using NIRS and fMRI were not available and comparisons of these modalities at the individual level have been performed previously [1, 2, 208], the research question posed is rather whether equivalent group level results in a given experiment can be obtained using either modality. Although there are many known limitations to the use of NIRS that have yet to be resolved or improved, some of which have been discussed in Part 1, we wished to establish whether in typical current use NIRS could be substituted for fMRI and similar results obtained. If NIRS results prove equivalent to fMRI with little additional effort, this is encouraging for neuroimaging research in developing countries where fMRI is an expensive and often unavailable research tool, and NIRS could provide a more affordable and convenient solution.

Continuing in the sensorimotor theme which is easily accessible to NIRS, the neuroscientific issues we chose to address are:

- ipsilateral activations and deactivations in motor tasks and noxious sensory stimulation
- modulation of spontaneous fluctuations and connectivity during the same tasks

Because systemic interference is a critical issue in NIRS, and is becoming more recognised as an issue for fMRI, we selected a task that is known to perturb the autonomic nervous system, namely noxious cold stimulation. We also recorded respiration and heartbeat during imaging in order to determine whether changes in systemic variables as well as in cerebral haemodynamics occurred during the task, and to eliminate these as possible confounding factors.

In section 5.1 the experiment used to investigate systemic and cerebral responses to motor and noxious thermal stimulation is described. The processing and results of physiological data analysis are discussed in section 5.2, whereas the analysis and results of the neuroimaging components of this experiment are presented in subsequent chapters (7, 8 and 9).

5.1 An investigation of systemic and cerebral responses to motor and noxious thermal stimulation

5.1.1 Task

The task protocol for functional imaging consisted of two different block design sequences that were each repeated twice. The task cues for each block were programmed using E-Prime software (Psychology Software Tools, Pittsburgh, PA, USA) and were presented to the subject on a personal computer during NIRS scanning and in the MRI scanner via a data projector, and a rear projection screen and mirror.

The first task sequence, Short_Blocks, was 288 s long and consisted of 12 s blocks of left hand finger tapping (LTAP), right hand finger tapping (RTAP), and a cold stimulus which was applied to the left or right hand (LCOLD and RCOLD). The 12 s task blocks were interspersed with 12 s fixation blocks (FIX) during which subjects focused their attention on a block displayed in the centre of the screen. This sequence was repeated three times. The task design is shown in figure 5.1.

During left and right finger tapping subjects were required to tap the fingers of their left or right hands against the thumb of that hand at a constant pace which they selected themselves. During the cold stimulus blocks the experimenter applied an ice pack to the entire palm and fingertips of the subject's left or right hand.

The second sequence Long_Blocks was 600 s long and consisted of 150 s blocks, in which only the right hand was used. An initial fixation block was followed by 150 s of sequential finger tapping of the right hand, followed by a second 150 s fixation period, and then a cold pressor challenge in which an ice pack was applied to the palm of the right hand for 150 s.

5.1.2 Subjects

Twenty right-handed subjects between the ages of 22 and 35 were recruited for functional MRI and NIRS imaging. Subjects were healthy, without neurological or cardiovascular disorders or contraindications for MR scanning, and gave their written informed consent to a protocol approved by the human ethics committees of the Universities of Cape Town and Stellenbosch. Volunteers were compensated R100 for each scan in which they participated and were given a CD with an MR image of their brain.

The data from one male subject was excluded because he was found subsequent to MRI scanning not to fit the recruitment criteria, leaving 19 subjects: 11 who were scanned with both NIRS and fMRI, 4 with NIRS only and 4 with fMRI only. The Short_Blocks fMRI data for one female subject was also discarded

5.1. AN INVESTIGATION OF SYSTEMIC AND CEREBRAL RESPONSES TO MOTOR AND NOXIOUS THERMAL STIMULATION



(a) Short_Blocks sequence with 12 s blocks



(b) Long_Blocks sequence with 150 s blocks

Figure 5.1: Task design for the Short_Blocks and Long_Blocks sequences. Each run was repeated twice. In the fMRI experiment each run was measured using a different TR (1100 ms and 2200 ms).

	Total subjects scanned	Short blocks useable data		Long blocks useable data	
		Imaging	Physiological	Imaging	Physiological
NIRS	16 (10 male)	15	15 (1 run) 14 (2 runs)	15	15 (1 run) 13 (2 runs)
fMRI	16 (9 male)	14	10	15	13 (1 run) 12 (2 runs)
Both NIRS and fMRI	12 (6 male, one excluded)	10	6 (1 run) 5 (2 runs)	11	9 (1 run) 8 (2 runs)

Table 5.1: Summary of useable data obtained for study session.

because of errors in the performance of the task. An acquisition error during one subject's NIRS recording resulted in the loss of physiological data for one short run and one long run, and during fMRI recording the physiological data for one of the long runs for one subject was accidentally overwritten. In addition, some of the physiological data acquired during fMRI scanning (4 subjects' short block data and 2 subjects' long block data) was too noisy to use and had to be discarded. The number of subjects whose data was available for each part of the analysis is shown in table 5.1.

5.1.3 Functional imaging

Functional MRI and NIRS scanning took place at the Cape Universities Brain Imaging Centre, a facility situated on the medical campus of the University of Stellenbosch. Due to logistical considerations functional MRI scanning always took place prior to NIRS scanning. Subjects were given a short break between scanning sessions.

5.1.3.1 Functional MRI

MRI scans were acquired using a 3T Allegra MRI scanner (Siemens Medical Systems, Erlangen, Germany). High-resolution anatomical images were acquired in the sagittal plane using a three-dimensional

magnetisation-prepared rapid gradient echo (MPRAGE) sequence (160 slices, TR=2399 ms, TE=3.93 ms, slice thickness 1 mm), 240 x 256 mm field of view. During the fMRI protocol, functional volumes sensitive to blood oxygen level dependent (BOLD) contrast were acquired with a T2*-weighted gradient echo, echo planar imaging sequence (18 interleaved axial slices, in-plane resolution 3 mm x 3 mm, thickness 5 mm, gap 1.5 mm, TE=30 ms). The field of view covered most of the brain but excluded the cerebellum in most subjects. For the first run of each task sequence a TR of 1100 ms was used with a flip angle of 55°, and for the second a TR of 2200 ms and flip angle of 90°. T2-weighted structural images (18 slices, TR=5000 ms, TE = 33 ms, slice thickness 5 mm) were also acquired with the same slice-orientation as the fMRI volumes.

5.1.3.2 NIRS

Imaging was performed using a DYNOT system. During scanning, subjects were reclined comfortably in a dentist's chair, which was reclined approximately 60 degrees to the vertical in an attempt to replicate the supine posture used for fMRI scanning and so that subjects could still see the task cues on the computer monitor in front of them. Fifteen source-detector pairs were placed over each of the left and right motor cortices, as illustrated in fig. 3.1 on page 28, using Cz from the 10-20 system for EEG electrode placement as a reference point for consistent positioning between subjects.

5.2 Physiological responses to sensorimotor stimulation

5.2.1 Methods

During fMRI, pulse, ECG and respiration was monitored for each subject using the Siemens optical plethysmograph, ECG leads and respiratory belt which are provided for gating using the Physiological Monitoring Unit (PMU). The fMRI pulse sequence was modified to allow the physiological data to be recorded to a file on the host computer.

During NIRS, respiration and ECG were monitored using a Biopac MP150 system.

The synchronisation, processing and analysis of physiological data are described in the sections that follow.

5.2.1.1 Synchronising physiological recordings with fMRI data

The Siemens PMU records pulse and respiration at approximately 50 Hz and ECG at approximately 400 Hz. However, there is some variation in sampling frequency from the nominal frequencies [27]. Also, since the PMU is a separate acquisition system from that used to record the MRI data, timing information from the MRI acquisition is needed in order to synchronise the recordings [27]. This means that the true sampling rate needs to be determined for each subsystem, as well as the offset of the physiological data with respect to the functional MRI time series.

Because this was not known before scanning commenced, data collection proceeded based on the assumption that the nominal sampling rates were correct, and that the start of physiological recording was synchronous

5.2. PHYSIOLOGICAL RESPONSES TO SENSORIMOTOR STIMULATION

	N	ECG	Respiration	Pulse
288.2s TR 1.1	13	-0.036 ±0.012 s	0.435 ±0.012 s	0.931 ±0.013 s
288.2s TR 2.2	13	-0.069 ±0.0076 s	0.414 ±0.013 s	0.907 ±0.010 s
600.6s TR 1.1	15	-1.173±0.007 s	-0.695±0.009 s	-0.199±0.005 s
600.6s TR 2.2	14	-1.187±0.010 s	-0.706±0.009 s	-0.217±0.007 s

Table 5.2: Time difference between length of fMRI run and physiological recording assuming a fixed sampling rate of 50 Hz for pulse and respiration and 400 Hz for ECG for N subjects.

with the start of the scan. This meant that synchronisation of the physiological and fMRI data had to be done after the fact.

1) Assuming a nominal sampling rate of 50/400 Hz The Siemens PMU inserts an additional data point, a logical HIGH, to indicate when an event has been detected for use in gating. These values are much larger than the possible values recorded for any physiological signal. Since these are extra data points and do not reflect actual samples of the signal they need to be removed so as not to affect the apparent number of samples in the log file. An initial attempt at processing the physiological data therefore consisted of the following stages:

1. The PMU event marker peaks (identified by their value of 5000) were removed from each signal.
2. The number of dummy scans performed by the scanner prior to the start of the scan was established from the pulse sequence code. The scanner performs two dummy scans if the TR is greater than 1500 ms and three if it is less than or equal to 1500 ms.
3. Assuming a fixed sampling rate of 50 Hz for pulse and respiration and 400 Hz for ECG, the number of samples corresponding to the dummy scans for each sequence was discarded in an attempt to align the start of each functional MRI run with the start of the physiological recording.

Assuming the nominal, fixed, sampling rate, it was found that there was a timing difference between the end of the fMRI run and the end of the physiological recording, where the physiological recording appeared to end slightly before or slightly after the functional MRI scan. These time differences were different for respiration, pulse and ECG and also differed depending on the length of the fMRI run, but were very consistent between fMRI runs of the same length as shown in table 5.2.

As can be seen from the second column of table 5.2, the number of subjects N whose physiological data was useable for each run was not always equal to the number of subjects scanned (15). Because of idiosyncrasies in the physiological logging the physiological data from one short 1.1s TR run and one short TR 2.2s run (from different subjects) was longer than the fMRI run, because the scan was restarted without clearing the physiological log. The 600s 2.2s TR data from one subject was accidentally overwritten. The fMRI data for the short runs from one subject were excluded because of an error in stimulus delivery.

	ECG (Hz)	Respiration (Hz)	Pulse (Hz)
288.2s TR 1.1	399.953	50.159	50.074
288.2s TR 2.2	399.920	50.153	50.070
600.6s TR 1.1	399.232	49.984	49.943
600.6s TR 2.2	399.262	49.982	49.943

Table 5.3: Apparent sampling rates based on length of log file.

2) Assuming synchronous start and end of fMRI scans and PMU logging It was subsequently established, from [27], that the start and end of sampling and storage of physiological data occurs simultaneously across the PMU subsystems, and that there is some deviation from the nominal sampling rate. These authors found a sampling rate offset of 0.3% which in their data (run length 4 - 6 minutes) meant that the apparent position of cardiac pulses at the end of the run would be off by as much as a second. Obviously this effect is much worse in the 10 minute runs used here.

In the absence of markers for calculating the offset of the physiological acquisition with respect to the fMRI acquisition, a second attempt at aligning the data was performed under the assumption that the start and end of the physiological recordings and the fMRI scans were simultaneous. The actual sampling rate was then calculated based on the length of the fMRI run (including dummy scans and the 4 additional volumes discarded from the beginning of each run), and the number of samples in each physiological data file. Under this new assumption the actual sampling rates were calculated as in table 5.3.

If the physiological recording is offset with respect to the fMRI scans, this alignment of the physiological data with the fMRI data would be incorrect. However, if the assumption of simultaneous starting and stopping of PMU subsystems in [27] is correct, the physiological data sets should be properly aligned with each other. Beall and Lowe [27] used triggers at the beginning of every fMRI volume acquisition to align the physiological data with the fMRI data, but also assumed a fixed sampling rate and simultaneous starting and stopping of PMU data logging. However, upon examination of the aligned ECG and pulse data towards the end of the 600s runs, the pulse peak appeared to precede the QRS wave of the ECG, while at the beginning of the recording a pulse peak followed the QRS complex within a physiologically plausible time delay. This delay decreased consistently across data sets to reach zero after approximately five minutes, and after this time the pulse appeared shortly before the closest ECG. The most plausible explanation for this seemed to be that the sampling rate of the PMU changes over time, and that this drift is different between subsystems. This does not appear to be well-documented although there is one implication in the literature that this type of drift in sampling rate may occur in the Siemens PMU [209].

However, based on the consistency of the lengths of the physiological recordings and the location of the shift between the ECG and pulse timecourse, it seemed that the drift over time should be fairly deterministic and repeatable and therefore might be corrected retrospectively.

3) Determining time offset or sampling rate variation In order to determine a drift or offset of the physiological recording with respect to the functional MRI scan without any further modifications to the

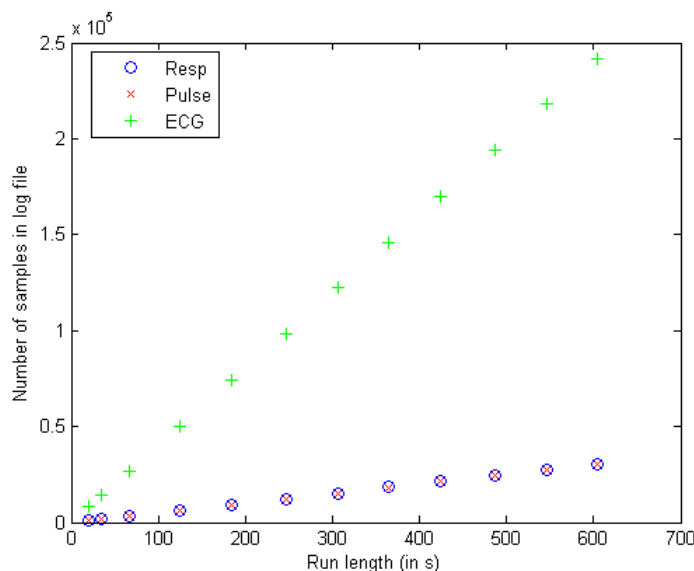


Figure 5.2: Number of samples in PMU log file vs length of scan showing linear relationship.

pulse sequence, the number of samples in the physiological data files were recorded for 20 fMRI runs varying in length from approximately 15 s to 10 minutes (table 5.4). This was done for a TR of both 1100 ms and 2200 ms. Because the number of dummy scans is different for the different TRs, the number of TRs in each run was chosen so that the duration of the run in seconds, including dummy scans, would be the same for equivalent runs with different TRs. The shorter runs were repeated 3 times to assess the variation in the number of samples for scans of the same length.

From the repeated scans of the same length in table 5.4 it is apparent that there is very little variation in the number of samples in the physiological log files. This variation is greater for ECG probably because of the higher sampling rate.

Because the apparent sampling rate (samples/scan length) of the shorter runs is much greater than that of the successively longer ones it suggests that, rather than a drift of sampling rate, there is a constant time offset at the beginning and/or end of the scan which increases the number of samples in the short log files by a relatively larger amount. To determine this offset, as well as the average sampling rate, for the pulse, ECG and respiration log files a linear regression of samples against scan length was performed (figure 5.2). The x-intercept and slope representing the offset and sampling rate, respectively, are shown in table 5.5.

This result indicates that there is consistently almost an extra 2s (± 100 samples) in the respiration log file, 1.5s (± 75 samples) in the pulse oximeter log file, and 1s (± 406 samples) in the ECG log file compared to the length of the fMRI run, and that the average sampling rates are somewhat below the expected sampling rate for each instrument. Because the number of samples does not appear to vary greatly between runs of the same length, however, the average sampling rate is probably a fairly accurate indication of the actual sampling rate at any time.

Table 5.4: Number of samples in PMU log file for various scan lengths and TRs.

Scan length (s)	TR 1100s					TR 2200s				
	TRs (incl. 3 dummy scans)	resp samples	pulse samples	ECG samples	TRs (incl. 2 dummy scans)	resp samples	pulse samples	ECG samples		
19.8	18	1087	1062	8302	9	1086	1061	8299		
		1086	1061	8295		1086	1061	8296		
		1086	1068	8375		1086	1061	8296		
35.2	32	1854	1829	14435	16	1853	1828	14437		
		1853	1829	14435		1853	1829	14434		
		1854	1829	14435		1854	1829	14434		
66	60	3388	3363	26709	30	3387	3362	26712		
		3388	3363	26711		3387	3363	26710		
		3389	3365	26721		3387	3362	26709		
125.4	114	6347	6322	50384	57	6347	6322	50386		
		6347	6322	50391		6347	6322	50384		
		6347	6322	50386		6348	6323	50385		
184.8	168	9307	9282	74059	84	9306	9281	74063		
246.4	224	12375	12350	98609	112	12375	12350	98610		
305.8	278	15334	15309	122285	139	15335	15311	122293		
365.2	332	18293	18269	145959	166	18294	18269	145961		
424.6	386	21253	21228	169633	193	21253	21229	169633		
486.2	442	24322	24297	194191	221	24322	24298	194188		
545.6	496	27282	27257	217859	248	27282	27258	217867		
605	550	30241	30216	241534	275	30240	30216	241534		

	Resp	Pulse	ECG
Offset	1.9983s	1.4996s	1.0181s
Average sampling rate	49.8200 Hz	49.8207 Hz	398.5625 Hz

Table 5.5: Average sampling rate and offset for each log file calculated by linear regression of samples-per-file vs scan length.

It is still not clear whether the offset occurs at the beginning or end of the scan. Assuming that the PMU subsystems start logging simultaneously [27] results in a physiologically plausible distance from the QRS of the ECG to the pulse peak for the entire duration of a 10 minute run. Since the offsets are different for each subsystem, it was further assumed that the start of physiological logging was synchronous with the start of the fMRI imaging and that the offset in the physiological log files resulted from a delay in stopping logging at the end of the fMRI run.

In order to solve this problem in the future a trigger should be written to the external channel of the PMU every TR to ensure precise alignment of physiological data with fMRI. Alternatively, time-stamps at which logging started and stopped could also be used to align data, by comparison with the time-stamps in the DICOM headers of the functional images. However, no time-stamps were recorded in the physiological log files from our system.

5.2.1.2 Processing of ECG and pulse oximeter data

The measurement of ECG in a scanner environment is not straightforward. Electrical signals are subject to artefacts from the static magnetic field as well as from the rapid gradient switching and RF pulses. Gradient artefacts are particularly problematic for EPI because of the high slew rate. The static magnetic field can cause artefacts in ECG recordings via moving loop induction and the Hall effect. Wire loops moving in a magnetic field induce a voltage according to Faraday’s law. This causes artefacts in bioelectrical recordings which are hard to remove because of their varying spectral content, but which can be minimised by restricting subject movement and avoiding loops in the cables as much as possible. The magnetohydrodynamic Hall effect results from charged particles in blood moving quickly through the aorta which get deflected by the Lorenz force and generate a Hall potential across the vessel walls, perpendicular to the B0 field and to the direction of blood movement. The distortion caused by the Hall effect is usually enhancement of the T-wave which makes its amplitude comparable to that of the R-wave, causing problems for triggering [210]. The pump and valves in the cold-head of the MRI scanner can also cause artefacts in physiological recordings.

Because ECG recorded in the MR scanner is distorted and noisy, particularly at 3T, a pulse oximeter was also used to record the peripheral pulse on the little finger of the left hand. However, in some subjects a good pulse signal was also not easily obtainable, and in one or two subjects tapping of the left hand during the short block runs caused obvious pulse oximetry artefacts. For many subjects the ECG and pulse data was fairly clean for long periods, but intermittently corrupted by noise or artefacts. Since the requirement was only to extract the peaks of each waveform to calculate an interbeat interval, it was decided to use both pulse oximeter and ECG signals and to attempt to create an automatic peak detection algorithm for each

signal, followed by a comparison of detected peaks in each waveform in order to eliminate spurious peaks and interpolate missing beats. If both signals are fairly clean with short periods of artefact, it should be possible to use the ECG to locate peaks in regions where the pulse data was corrupted and vice versa. A program was written in Matlab to process the physiological data. Some of the initial processing was based on the PhLEM package (at <http://https://sites.google.com/site/phlemtoolbox/>) with the addition of automatic error-checking for peak detection and a GUI for manual inspection and editing of peaks if required.

The steps of the algorithm used for locating pulse and ECG waveform peaks are as follows:

1. Align and remove scanner triggers from physiological data logs.
2. Filter the raw signal. The respiration and pulse data are low pass filtered and wavelet denoising is applied to preserve high frequency peaks in the ECG data.
3. Locate peaks in the smoothed signals. A peak detection algorithm (`peakdet.m` <http://billauer.co.il/peakdet.html>) was used to locate even quite small peaks in the ECG signal. Because the QRS peak was not larger than the noise level in most recordings, and the distorted elevated T-wave is easily confused with a QRS complex, it is easier to detect the negative deflection of the S wave, than the positive R-wave. In order not to miss peaks that are smaller than typical, a small threshold is used which results in the detection of spurious peaks to be eliminated at a later stage. For pulse data, peaks were located with a specified minimum amplitude.
4. Calculate the power spectrum of the waveform. For pulse oximeter data the location of the largest spectral peak can be used as an estimate of the average interbeat interval (IBI). The ECG waveform is often dominated by harmonics, so a prominent peak in the spectrum that was close to 1 Hz was used as the IBI estimate.
5. Select a subset of the negative ECG peaks detected in step 3 by using an optimisation algorithm to minimise the deviation of the IBI from the average calculated in step 4.
6. Calculate the median interbeat interval m_IBI of the detected peaks across the entire run and attempt to locate missing peaks using a smaller threshold if the distance between adjacent beats is in the order of a multiple of 1, 2 or 3 times m_IBI or to delete extra peaks if merging two adjacent IBIs results in a new IBI closer to m_IBI .
7. Plot waveforms and detected peaks, marking detected peaks as possible outliers if the interbeat interval is more than $m_IBI/4$ greater or less than m_IBI .

The subsequent step depends on the results of the preceding algorithm. If the discrepancy between beats detected using ECG and pulse waveforms is small, the peaks can be automatically corrected by the user selecting a menu option on the GUI. If, however, the entire run of ECG or pulse data is unreliable, the user may have to manually add or remove beats in the more reliable waveform via the GUI.

The automatic peak correction algorithm locates outlying IBI values and finds the corresponding peaks in the other waveform. If, for example an outlier IBI is detected in the ECG data and the interval between

the corresponding pulse peaks is closer to the median, one of the ECG peaks is selected for deletion and a corrected ECG peak is added before the pulse at the median ECG-to-pulse-peak distance.

The user can then inspect these corrections for accuracy and edit if necessary. The algorithm is considered to have been successful when either no IBI outliers are detected or the detected outliers have been inspected to ensure they correspond to valid ECG or pulse peaks (true short or long beats IBIs should exist in both pulse and ECG data) and when no visually obvious extra or missing peaks can be seen on inspection of the waveform plot.

Table 5.6 shows the outcome of the processing algorithm for each subject's pulse and ECG data. In many subjects, very little intervention was necessary to detect peaks correctly. Out of 15 subjects who received MRI scanning, 4 subjects' Short_Blocks data and 2 subjects' Long_Blocks data had to be rejected altogether, as it was not possible to process either the pulse or ECG, even manually. In one case ECG data could be used but not pulse data, and in 5 cases the pulse data, but not the ECG data, was useable.

The same algorithm with one modification (detection of positive R wave) was used to process the ECG data recorded during NIRS. Because no pulse data was recorded during NIRS imaging no automatic correction could be made, but because the ECG in this case was not noisy, correction was hardly ever necessary.

5.2.1.3 Analysis of physiological data

Repeated measures ANOVAs in OpenStat and ezANOVA software were used to analyse physiological changes with task condition.

Changes in heart rate (mean interval between beats) with condition during the Short_Blocks MRI run were assessed using the 10 subjects from whom adequate physiological data was obtained during fMRI scanning, and for NIRS for 14 subjects. The reader is referred to table 5.1 for a summary of the physiological data available in each modality in each run.

In the Long_Blocks runs, the mean interval between beats (IBI) and its standard deviation (SDNN) was extracted for each subject for each task condition: REST1, TAP, REST2, and COLD for both NIRS and MRI physiological recordings. These variables were used to assess changes in heart rate and heart rate variability, respectively. Physiological changes were assessed using 13 subjects scanned using NIRS who had physiological data for both runs, and the 12 subjects from whom adequate physiological data was obtained in both runs during fMRI scanning. Eight of these subjects had physiological data in both scans.

The heart rate response to the cold pressor test is known to be variable between subjects, and not the same for the entire duration of the test period [211]. In order to assess differences in response during different parts of the testing period, the 150s duration was split into three 50s intervals and the mean heart rate was calculated during each of these three test periods as well as the 50s directly preceding application of the ice pack. This was done for the first run only, so the recordings during NIRS from 15 subjects and during fMRI from 13 subjects, and 9 of these subjects who had both scans, was used.

Subject	Short	Long
1	successful	successful
2	successful	successful
3	successful	successful
4	successful (one manual fix)	successful
5	data rejected >50 pulse and ECG outliers	data rejected >50 pulse and ECG outliers
6	data rejected > 50 ECG outliers, pulse could not be corrected manually	> 50 ECG outliers, no correction to pulse required
7	successful	> 50 ECG outliers, pulse corrected manually
8	data rejected > 50 pulse and ECG outliers	data rejected > 50 pulse and ECG outliers
9	data rejected > 50 pulse and ECG outliers	> 50 ECG outliers, no correction to pulse required
10	successful	successful (few manual fixes)
11	successful	successful (few manual fixes)
12	successful (few manual fixes)	successful (one run overwritten)
13	successful (one manual fix)	> 50 ECG outliers, pulse corrected manually
14	> 50 pulse outliers, ECG corrected manually	> 50 pulse outliers, ECG corrected manually
15	data not used (acquisition error)	> 50 ECG outliers, pulse corrected manually

Table 5.6: Outcome of semi-automatic processing of pulse oximeter and ECG data.

		MSE	df	F	p
HR MRI (N=10)	COND	0.001	4, 36	2.40	0.068
	RUN	0.006	1, 9	2.92	0.122
	COND x RUN	0.000	4, 36	1.09	0.378
HR NIRS (N=14)	COND	0.002	4, 52	0.69	0.043*
	RUN	0.011	1, 13	8.36	0.013*
	COND x RUN	0.000	4, 52	0.51	0.728

Table 5.7: Results of two way repeated measures ANOVA with factors COND (task condition) and RUN for heart rate during NIRS and MRI Short_Blocks runs. An asterisk indicates significance at $p < 0.05$.

5.2.2 Results

5.2.2.1 Short blocks: task-related physiological changes

A two way repeated measures ANOVA was performed on the interbeat intervals (IBI) extracted from the ECG or pulse oximeter data, with five levels of factor “Condition”: LTAP, RTAP, LCOLD, RCOLD and REST, and two levels of factor “Run”, reflecting the two short runs (table 5.7). Where Mauchly’s test for sphericity was significant at $p < 0.05$, Huynh–Feldt correction was applied. There were no significant effects in the MRI heart rate data, however, for NIRS both main effects were significant at $p < 0.05$, where the IBI for the second run was significantly shorter than the first. The opposite effect appeared in the mean IBI for MRI (figure 5.3), although this was not significant.

Post-hoc tests using the Newman-Keuls method revealed significant differences in IBI between the cold and other conditions during NIRS, shown in table 5.8.

5.2.2.2 Long blocks: task-related physiological changes

The mean IBI for each condition in the Long_Blocks task, and its standard deviation across subjects are shown in figure 5.4. Separate repeated measures two way ANOVAs with within-subject factor “Run” and “Condition” were performed on the interbeat intervals (HR) and their standard deviations (HRV). Although the mean IBI in TAP is smaller than in the other conditions in both data sets, as shown in table 5.9, there was no significant effect of Condition or Run on IBI in either data set. ANOVAs on the HRV data, shown in table 5.10 reveal no significant effects for HRV measured during NIRS. The effect of Condition was significant for in the HRV measured during MRI, however, post-hoc tests on individual means were not significant.

Qualitatively similar patterns in the mean IBI occurred in both runs and in both NIRS and MRI (as shown for 8 subjects for whom physiological recordings were available in both NIRS and MRI in figure 5.5). The mean HRV responses are more variable between runs.

The number of subjects whose heart rate increased, decreased or remained the same in TAP and COLD compared to REST in the first and second runs is shown for NIRS and fMRI in table 5.11. In the second MRI run, nine subjects showed the same responses as in the first run and three showed different responses

Run 1			
	q	df	p
LCOLD>REST	4.27	3, 52	0.011
LCOLD>LTAP	4.98	4, 52	0.005
LCOLD>RTAP	4.16	2, 52	0.005
RCOLD>REST	4.82	4, 52	0.007
RCOLD >RTAP	4.71	3, 52	0.005
RCOLD>LTAP	5.53	5, 52	0.002
Run 2			
	q	df	p
LCOLD>REST	4.80	5, 52	0.011
LCOLD>LTAP	3.99	3, 52	0.018
LCOLD>RTAP	4.71	4,52	0.009
RCOLD>RTAP	3.46	3, 52	0.046

Table 5.8: Significant Newman-Keuls post-hoc tests for differences between mean IBI in each NIRS Short_Blocks run.

		MSE	df	F	p
HR MRI (N=12)	COND	0.01	3, 33	2.73	0.060
	RUN	0.01	1, 11	0.54	0.477
	COND x RUN	0.01	3, 33	0.18	0.912
HR NIRS (N=13)	COND	0.01	3, 36	2.78	0.055
	RUN	0.01	1, 12	4.26	0.061
	COND x RUN	0.01	3, 36	2.104	0.117

Table 5.9: Results of two way repeated measures ANOVA with factors COND (task condition) and RUN for heart rate during NIRS and MRI Long_Blocks runs. An asterisk indicates significance at $p < 0.05$.

		MSE	df	F	p
HRV MRI (N=12)	COND	0.01	3, 33	5.11	0.007*
	RUN	0.01	1, 11	0.06	0.815
	COND x RUN	0.01	3, 33	0.26	0.854
HRV NIRS (N=13)	COND	0.01	3, 36	2.49	0.076
	RUN	0.01	1, 12	1.22	0.2910
	COND x RUN	0.01	3, 36	2.301	0.093

Table 5.10: Results of two way repeated measures ANOVA with factors COND (task condition) and RUN for heart rate variability during NIRS and MRI Long_Blocks runs. An asterisk indicates significance at $p < 0.05$.

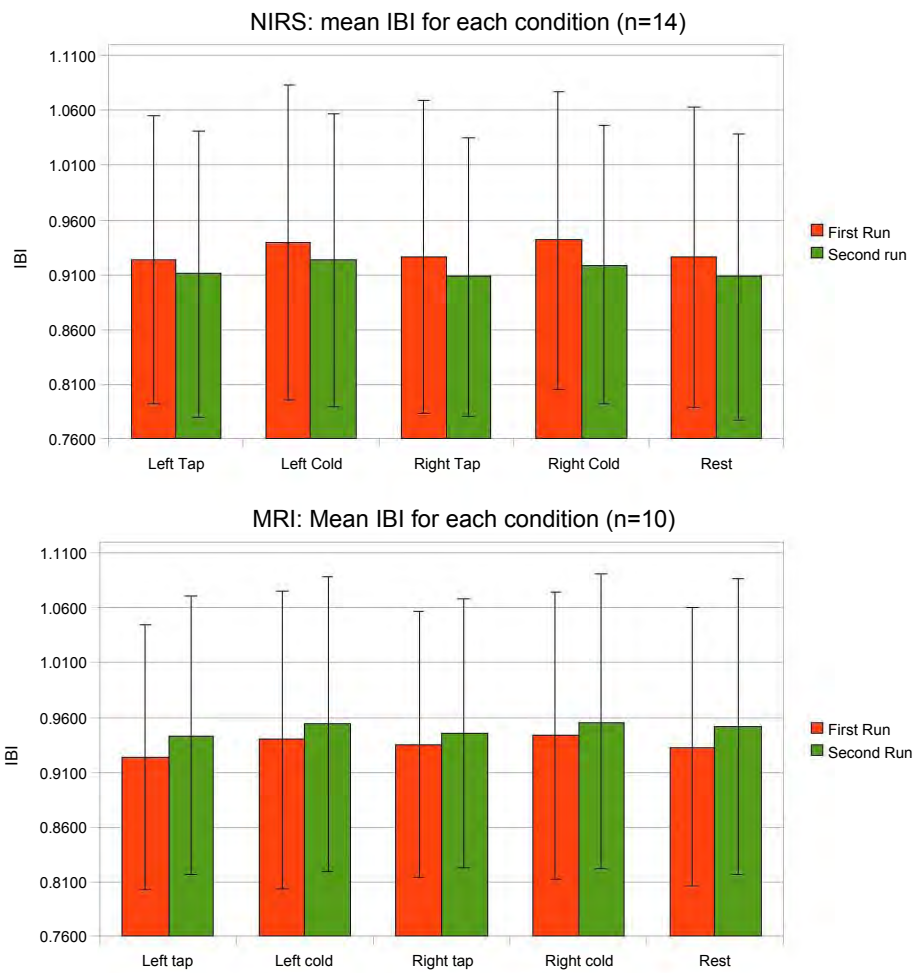


Figure 5.3: Mean IBI in the Short_Blocks runs during NIRS and MRI scanning.

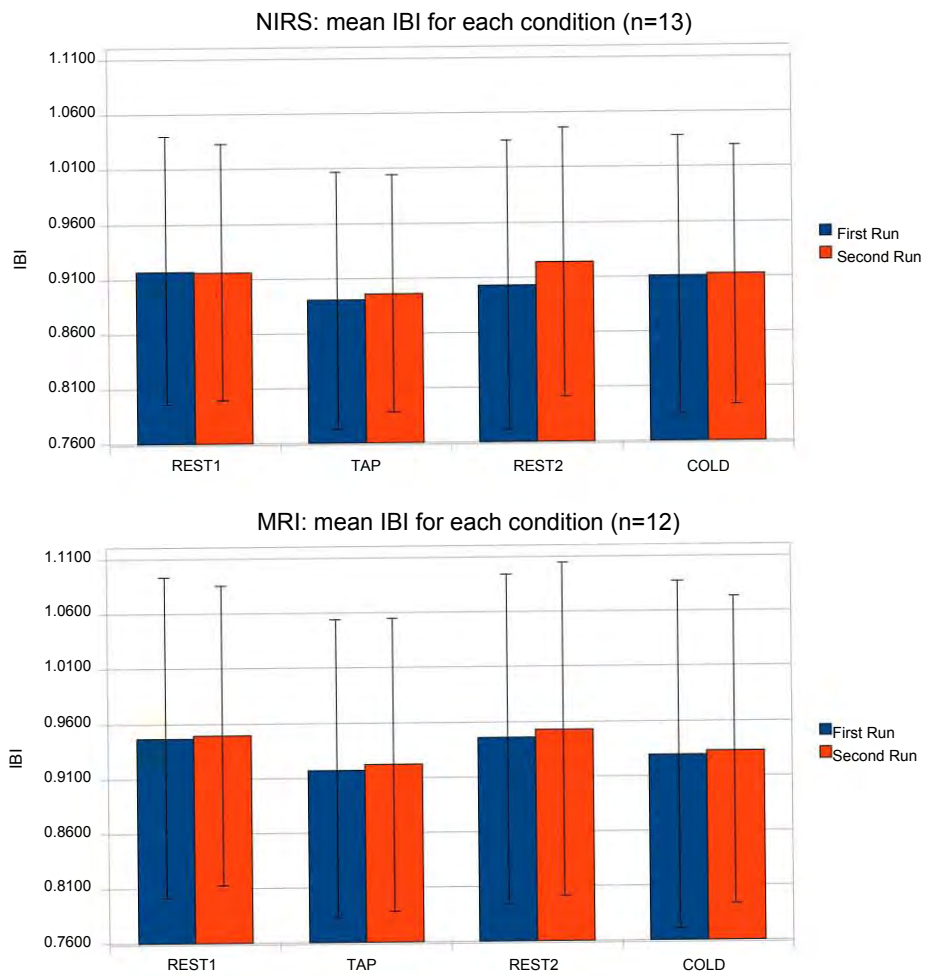


Figure 5.4: Mean IBI in the Long_Blocks runs during NIRS and MRI scanning.

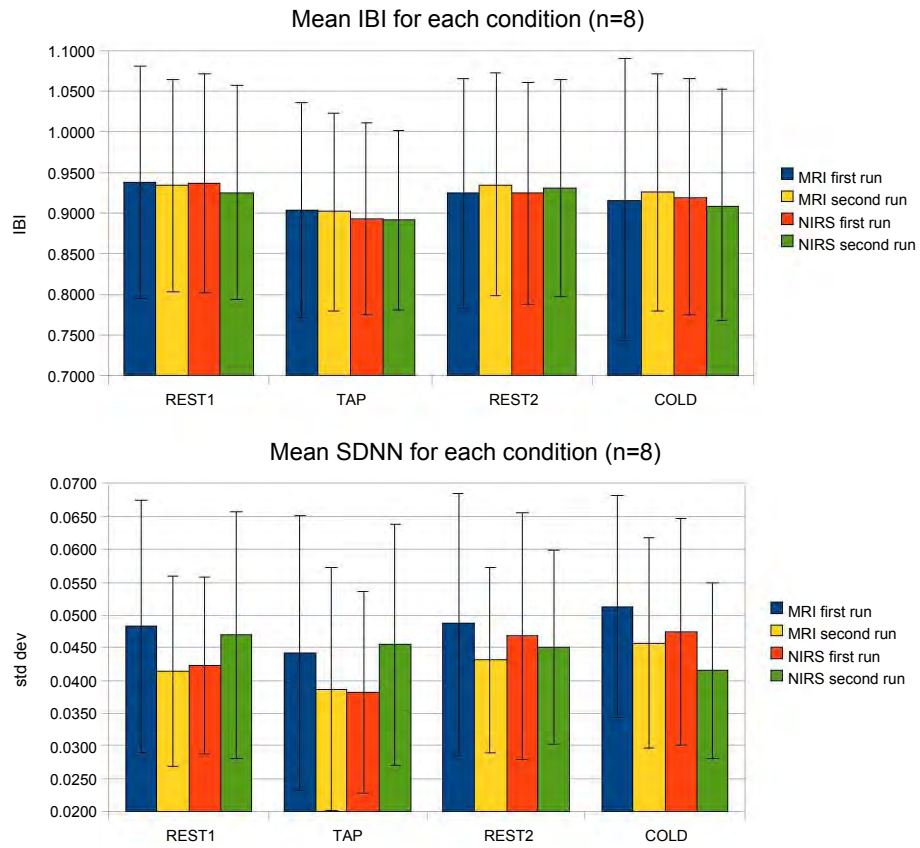


Figure 5.5: Mean IBI and SDNN for first and second runs during fMRI and NIRS for 8 subjects.

	MRI		NIRS	
	N=13 (12)		N=15 (13)	
	Tap vs Rest	Cold vs Rest	Tap vs Rest	Cold vs Rest
Increased HR	10 (8)	6 (6)	9 (9)	5 (5)
Decreased HR	2 (1)	4 (3)	2 (3)	7 (3)
No change	1 (3)	3 (3)	4 (1)	3 (5)

Table 5.11: Number of subjects whose heart rate increased, decreased or remained the same in TAP and COLD compared to REST in the first run. The number in parentheses is the number of subjects whose heart rate did this in the second run.

	MSE	df	F	p
HR MRI	0.01	3, 36	1.74	0.175
HR NIRS	0.01	3, 42	2.70	0.058

Table 5.12: Results of one way repeated measures ANOVA with 4 levels of factor “Cold” for heart rate during NIRS and MRI.

to tap and three to cold (one subject’s data was not available). In the second NIRS run five subjects show a different response to tap and five showed a different response to cold.

5.2.2.3 Physiological changes during the cold pressor test

The results of a four level one way repeated measures ANOVA on the mean IBI during the PRE-TEST period, and the first, second and third 50s period of the COLD stimulus (COLD1, COLD2, COLD3) are shown in table 5.12. Although changes are not significant, in both sets of physiological recordings the mean heart rate appears to change during the first 50 s after application of the cold stimulus and then drop to or below baseline levels some time afterwards. However, the direction of the initial change is different during the NIRS and MRI recordings (figure 5.6). In the MRI recordings the initial effect is an increase in heart rate (decrease in interbeat interval) while in the NIRS recordings there appears to be on average a decrease in heart rate (increased IBI). In the MRI recordings only 4 out of 13 subjects showed an increased IBI from rest in the first cold interval, while in the NIRS recordings 11 out of 15 subjects showed an increased IBI from rest in the first cold interval. This effect remained when only the 9 subjects were considered who had physiological recordings in both MRI and NIRS.

To locate different patterns of heart rate change in subject subgroups, for each subject the difference in average interbeat interval was calculated between each cold segment (COLD1, COLD2, COLD3) and the PRE-TEST period. If this difference was larger than 2% of the PRE-TEST interbeat interval it was counted as an increase or decrease, otherwise no change was deemed to have occurred. Subjects were then categorised into one of five groups: those that showed an increased heart rate compared to the PRE-TEST period for all cold segments, those that showed a decreased heart rate for all cold segments, those that showed no sufficiently large change across all segments and those that showed an initial increase or decrease followed by

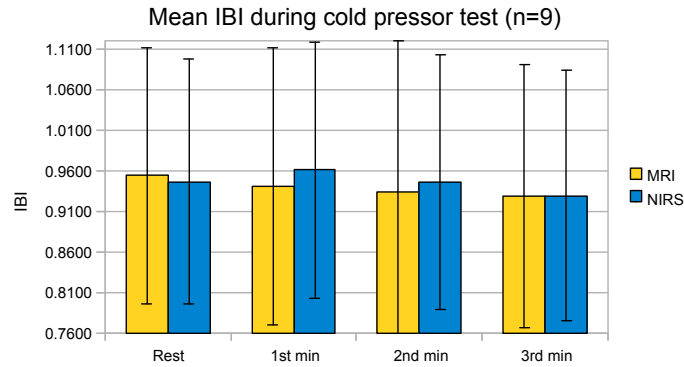


Figure 5.6: Mean IBI in 50s intervals, pre- and during cold pressor test.

	Sustained increase	Sustained decrease	No change	Increase and return to baseline	Decrease and return to baseline
MRI (n=13)	8	1	1	2	1
NIRS (n=15)	5	4	1	1	4

Table 5.13: Number of subjects showing an increase, decrease or no change in heart rate during the stages of the cold pressor test.

a return to near baseline levels. The number of subjects in each group are listed in table 5.13.

5.2.3 Conclusions

During the 12 s blocks, heart rate did not change significantly with condition during fMRI, but during NIRS heart rate was slower during the cold conditions than during tapping and rest. In the long blocks, although the mean heart rate increased and heart rate variability tended to decrease during TAP, there was no significant effect of condition on heart rate or heart rate variability. This may be because an initial autonomic response to the task stabilises over time and returns to baseline levels by the end of the 150 s block. However, no significant effect of period was found when a one way ANOVA was performed on the IBIs from a pre-test period and three consecutive 50 s periods of cold stimulation. There is some variability in response between subjects and between runs.

There are of course several differences between the situations under which the changes are monitored as well as the data itself used for the analysis. During MRI, recording takes place in slightly more stressful circumstances (a confined environment with ambient noise), the subject is supine, and unable to see the investigator applying the cold stimulus to his or her hand. During NIRS, because the subject is not able to see the visual cues on the computer monitor when in a completely supine position, it is not possible to fully recline the dentist's chair. Therefore, the subject is only semi-reclined. Furthermore, the surroundings are a more usual environment with less noise than during MRI, and although the subject is instructed to look at the computer screen, he/she is able to see at least in peripheral vision the experimenter preparing to apply

the cold stimulus. Since the NIRS session always followed the MRI session, this was also the third time each subject had experienced the cold pressor challenge.

In addition, pulse data was used for MRI and ECG data for NIRS. Because of some difficulties with obtaining physiological recordings using the built-in scanner physiological recording equipment it is possible that the peak identification is very slightly less accurate for MRI physiological data than for NIRS. The nature of the pulse waveform, which is smooth, means that peaks may not be as accurately localised in time as the QRS complex in ECG. The measurement of peripheral pulse is an indirect measure of cardiac activity. The time it takes the pulse pressure waveform to propagate from the left ventricle through a length of the arterial tree (the pulse transit time) is affected by blood pressure; as the blood pressure increases due to the cold pressor stimulus the pulse transit time decreases.

University of Cape Town

Chapter 6

Registration of NIRS and MRI data

This chapter describes an experiment investigating the registration of NIRS data to the head surface of individual subjects.

6.1 Background

The registration of locations on the head surface, measured in physical space using a magnetic, optical or ultrasonic position tracker, to locations on the surface of a 3D volume image has been an important consideration for EEG-MRI [212, 213] MEG/EEG-MRI [214, 215, 216] studies, and TMS-MRI studies [217]. Because NIRS also requires the localisation of surface optodes on a 3D structural MRI image the same principles may be applied. However the localised nature of the response measured using NIRS means that registration accuracy may be more critical here than in EEG, where each surface electrode may measure an electrical signal that is conducted through the entire head volume.

6.1.1 Landmark-based registration

The simplest registration method is to identify a minimum of three corresponding landmarks in both image and real-world space, as measured with a 3D tracker, and to calculate the optimal transformation between these co-ordinate systems. The type of transformation depends on the number of parameters calculated: this is most often either a 7 parameter rigid body transformation - 3 rotation, 3 translation and a global scaling parameter, or a 12 parameter affine transformation, incorporating scaling in each of the x,y and z directions and three shear parameters as well as the rotation and scaling parameters.

Given a number N of fiducial landmarks in each space, the optimal transformation minimises the least squares distance between corresponding points in the two spaces. This optimal transformation $Y = Rx + T$ may be calculated iteratively, although several closed form solutions exist [218, 219]. For landmark-based registration at least 3 non co-linear points are required, although registration error decreases as the number N of fiducials increases, according to $1/\sqrt{N}$ [109] and increases with distance from the fiducials [214].

In EEG anatomical landmarks are often used, namely the left and right pre-auricular points and the nasion, which are then aligned using least squares minimisation. However, variability of the order of several millimeters may be associated with the repeated identification of anatomical landmarks [220, 214]. This can produce a larger transformation error when a small number of fiducials is used [213]. MRI-visible markers may also be placed for use as landmarks, or at the sites of surface electrodes [221]. Bite-bars may be used to reduce error [214, 222], although these may cause discomfort to the subject.

Although landmark-based registration is computationally very fast, identifying fiducials in both physical and image co-ordinate spaces can be time-consuming and inaccurate. There are many sources of error associated with landmark identification. Markers in MRI images may be large compared to the desired registration accuracy [213], and the marker centroid has to be consistently located by hand. Markers may also be shifted 1- 3 mm in position because of magnetic susceptibility changes from air to skin or marker, and due to chemical shifts. In addition, markers need to be firmly attached to the scalp, and may become physically displaced during scanning, or between scanning and digitisation [109].

6.1.2 Surface-based registration

Surface-based alignment matches two representations of the head surface: one a head surface segmented from MRI and the other a set of digitised head-surface points. This has been done to register both EEG [223, 224] and MEG data [225, 226] to MRI. This technique has the advantage that it does not require identification of corresponding points in two spaces and thus eliminates the need for MRI markers, meaning that the MRI image does not have to be taken in the same session as the surface recording [213]. However, there are also several difficulties associated with surface-based techniques. Firstly the scalp needs to be accurately segmented from the MRI image. Secondly, hundreds or thousands of surface points usually need to be digitised, as the registration error decreases as the number of surface points increases [215, 216]. The latter problem has been overcome in various ways: by using spline interpolation of real EEG points [212], by using a specific digitisation pattern [217], and by using anatomical image information in the registration [227].

Finally, the most serious drawback to the method is that because the shape of the head is nearly spherical, a surface-matching algorithm that iteratively minimises the distance between the segmented scalp surface and the digitised scalp points may converge upon an incorrect solution. To overcome this, a good initial alignment can be used as a starting point for the scalp-matching minimisation. Sometimes centroids or moments are used for this initialisation [216]. Another method is to use three or four fiducial landmarks to perform an initial rough alignment to use as a starting point for surface matching [109]. For convenience these fiducials are often anatomical landmarks, which do not require markers in MRI scans.

There are several component steps to surface registration where different choices can be made that may affect the result. These are: the choice of type of transformation between image spaces, the selection of a representation of the surfaces and measure of distance between them, the initialisation method used to roughly align the two co-ordinate systems, and the choice of optimisation technique to fine-tune the alignment between the two surfaces [228].

6.2 Methods

The most practical registration algorithm, which allows MRI imaging and NIRS scanning to be done in separate sessions which may be far apart in time, is to use anatomical-landmark-based initialisation, followed by surface registration, as done by Whalen et al. [109]. There are logistical difficulties with using markers attached to the heads of subjects, as well as acquiring reliable head surface data - in fact in [109] only bald subjects were used.

6.2.1 Head shape data

Head shape data were obtained for seven subjects who had both NIRS and MRI scans in a separate imaging session. Eight vitamin E markers were attached using tape to a swimming cap on the subject's head. The swimming cap had holes cut out of the sides to allow the positioning of NIRS optodes on the scalp. The positions of the markers were also drawn onto the cap to allow the markers to be removed after MRI and before NIRS scanning. The marker positioning was chosen so as to cover as wide an area of the head as possible, while at the same time avoiding posterior markers becoming dislodged as the subject lay supine in the scanner. A further constraint was that the marker locations had to remain visible while the frame containing the NIRS optodes was in place for NIRS scanning. The distribution of the markers was as follows: one in the centre of the forehead (approximate Fp position), one halfway between nasion and inion (Cz), one along the same central anterior to posterior line posterior to Cz, but not as inferior as the inion, since the subject was to be lying supine, one marker each (L ant and R ant) on the left and right anterior of the head, slightly superior and lateral to the Fp marker, one marker each (L post and R post) at the left and right posterior of the head, inferior to the nasion-inion central line, and one marker on the left forehead (L ForeHd). Four anatomical landmark points were also used: the nasion (Nz), nose tip (NoseTip), and left and right pre-auricular points (LPA and RPA).

A T1-weighted anatomical MPRAGE image was taken while the subject lay in the scanner, before the functional MRI run was completed. After the MRI session, the subject went directly into a NIRS scanning session, where the vitamin E markers were removed to allow the NIRS frame to be placed on the head over the swimming cap. Targeting of the motor area was performed using MRIreg [229], which allows on-the-fly registration of an MRI scan with the subject's real head geometry in order to locate specific brain regions using a 3D position tracker. However, this method was found to perform no better than location of the motor area using the Cz position of the 10-20 system (as judged by functional responses) and required more time to perform.

Once the set up of the NIRS optodes was completed, the positions of the anatomical landmarks, and vitamin E markers (known from the marks on the swimming cap) were recorded using a Polhemus Fastrak magnetic digitiser. The positions of the edges of the NIRS frame were also recorded, as well as a selection of head surface points. The surface points had to be recorded from areas of the head that were accessible in spite of the NIRS helmet.

6.2.2 Evaluation of registration accuracy

It is difficult to compare the accuracy of different surface registration methods because of the variety of different ways in which authors have evaluated this. Whalen et al [109] recommend using the following different error measures in combination:

- the map error (or total registration error - TRE): the error in positions of known markers when these markers are not used for the alignment. Target registration error is an upper limit for the error.
- the fiducial registration error (FRE): the registration error in the landmarks that were used in the registration after the registration. This may be biased and under represent the map error.
- the residual error (RE): the mean or root-mean-square distance between the MRI surface and the registered head points. It is also biased, and serves as a lower bound for the registration error.

Because of the difficulty of using markers in MRI images, map accuracy is often assessed by means of simulations [214, 216]. If markers are used to evaluate map accuracy, TRE includes not only the map error but also other forms of error such as marker shifts between digitisation and MR scanning. Therefore the TRE may be considered an upper limit for the map error.

6.2.3 Landmark registration

The transformation between real-world and individual MRI space was calculated using the fiducial markers and both Horn's algorithm for closed form solution of rigid body parameters [219], and least squares affine transformation [230].

To evaluate the fiducial registration error and the map error resulting from using the landmark positions in the MRI and Polhemus space, we performed affine (12 parameter) and rigid body (7 parameter, including a global scaling parameter) transformations multiple times using $n - x$ fiducials, where n was the total number of landmarks available for that subject and x ranged from 1 to $n - 4$ since a minimum of 4 landmarks are required to calculate the affine transformation. (For most subjects $n = 12$, but on one subject a marker slipped off while the subject was in the MR scanner.) For each registration using $n - x$ fiducials the remaining x known landmarks were used to evaluate the map error resulting from that registration.

6.2.4 Surface registration

Surface registration was performed using a Matlab-based volume registration toolbox [230], which calculates an initial affine transformation from real-world (digitiser) space to MRI space using landmark pairs in each co-ordinate space. This initial mapping is optimised by minimising the distance of a set of digitised head surface points to a head surface mesh extracted from a segmented MRI using Gauss-Newton optimisation. The points are then projected onto the head surface. The landmark locations and digitisation pattern for the surface points are shown in figure 6.1.

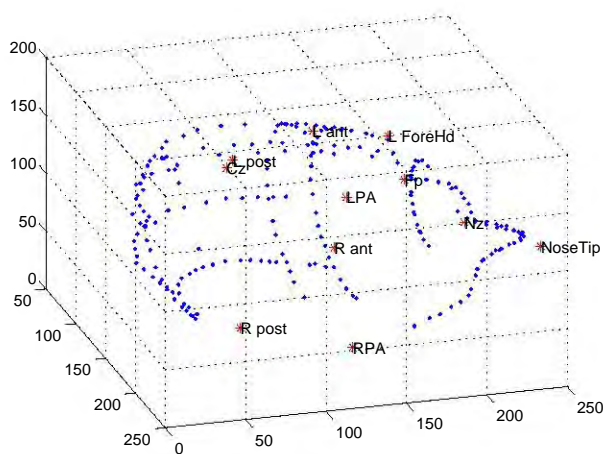


Figure 6.1: Simulated landmark and surface point data extracted from a subject's MRI

6.2.5 Simulated surface registration: the effect of fiducial and surface point error

To evaluate the effect of error in the location of fiducial markers and surface points used for registration, simulated data was constructed by manually selecting landmark and surface points from one of the subject's MRIs. Two hundred surface points were drawn from the selected subject's MRI using the same digitisation pattern used for the real data, which incorporated the subject's nose shape. Different levels of Gaussian noise were then added to the four fiducials and the surface points and for each noise level 50 random rigid body transformations were applied to the data to simulate digitised head surface data. The simulated data was then aligned with the MRI data using a least squares affine transformation initialisation from the four fiducials, followed by iterative alignment using Gauss-Newton optimisation (`metchgui`). The resulting map error was evaluated using the remaining landmark points, and average residual error of each point from the head surface was calculated.

6.3 Results

6.3.1 Landmark registration

The accuracy with which an unknown point can be mapped increases with the number of fiducials used to calculate the mapping transformation. However, the registration error associated with the fiducials increases with the number of fiducials. Figure 6.2 shows the RMS fiducial registration error for one subject as a function of number of fiducials used for both affine and rigid body registration methods. Rigid body registration always has a higher FRE than affine, approaching a max of 21 mm for rigid and 13 mm for affine. However, because of overfitting, the map error is greater for affine registration than rigid when fewer than 6 fiducials are used

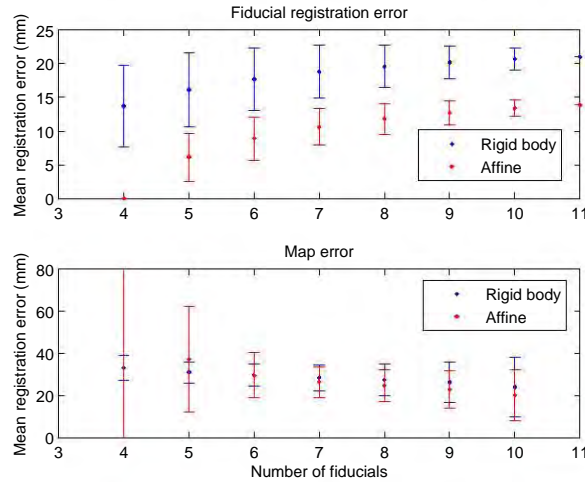


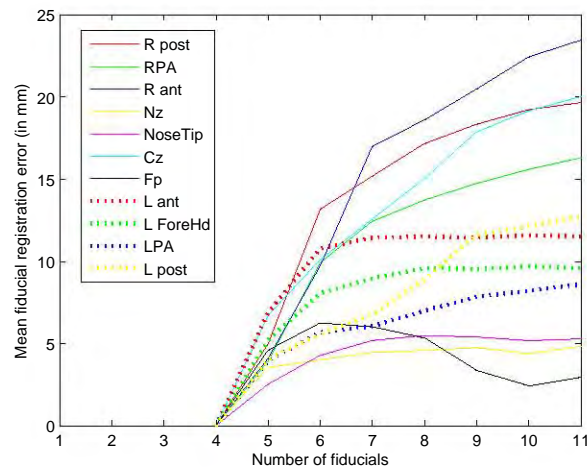
Figure 6.2: Map error and fiducial registration error for increasing number of fiducials

(where TRE is 29 mm) and variance is much larger. With greater than 6 fiducials TRE is smaller using affine than rigid body registration approaching a minimum of 20 for affine and 24 mm for rigid body. (It should be noted that the number of target points used to calculate mean map error also decreases as the number of fiducials increases.)

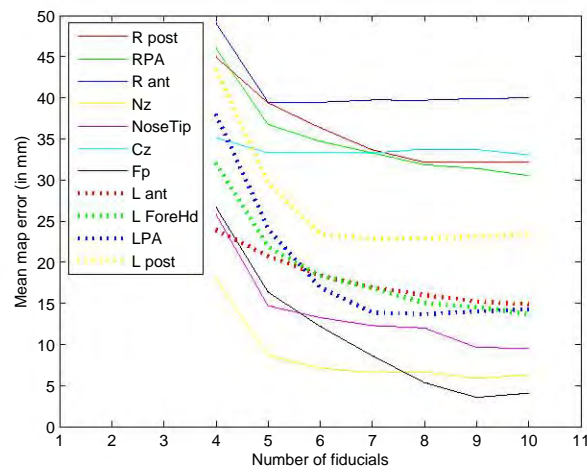
Because there may be error in the landmarks used to evaluate registration accuracy (targets) as well as in the fiducials used for registration, we examine for every individual landmark the average FRE over all possible registrations that use that landmark as a fiducial, as a function of the number of fiducials, as well as the average map error for all possible registrations that do not use it. This also allows identification of landmarks that consistently contribute to large registration error. Figure 6.3 shows that the landmarks R ant, R post, Cz and RPA can be separated from the others as being registered consistently badly (FRE > 15 mm and map error > 30 mm). R ant has the worst map error (~40 mm) and FRE (~23 mm) whereas Fp has the smallest average FRE (~3 mm) and map error (4 mm).

Table 6.1 shows for 7 subjects the mean FRE and median map error over all landmark points for all registrations using $n - 1$ fiducials. The landmarks from four subjects (1,2,3, and 5) were digitised twice.

Data set 6 clearly had large errors in digitisation: the median map error was greater than 6 cm. Only 4 datasets produced median map errors of less than 3 cm, which is rather inaccurate, suggesting either errors in digitisation or that there is too much movement of markers between the MRI session and digitisation. Upon examining the distribution of errors according to landmark position, it appears that the more posterior and lateral markers R post, RPA, Lpost, LPA are badly registered, as well as Iz. R post is particularly bad. The anterior central and lateral markers (R ant, Lant, Nz, L Forehead, Fp and to a lesser degree Cz) are more accurately registered.



(a) Mean fiducial registration error (FRE) for each landmark after least-squares affine registration.



(b) Mean map error (TRE) for each landmark after least-squares affine registration.

Figure 6.3: Mean FRE and map error for each landmark after least-squares affine registration.

Subject	No. fiducials	Mean FRE	Std dev	Median map error
1a	10	11.53	1.03	15.74
1b	10	11.85	1.18	14.90
2a	11	22.37	2.29	25.91
2b	11	24.75	1.99	37.63
3a	11	27.54	2.01	35.59
3b	11	20.67	1.38	32.05
4	11	16.24	1.26	20.17
5a	11	36.92	4.16	42.03
5b	11	26.04	1.77	42.57
6	11	39.42	2.87	69.57
7	11	16.91	1.66	22.16

Table 6.1: Mean FRE and median map error over all landmark points for all registrations using $n - 1$ fiducials

6.3.2 Initial landmark-based registration followed by surface registration

For technical reasons the head surface data for only 4 subjects was useable. One subject's head surface was digitised twice, yielding 5 data sets. The mean map error was calculated over all landmark points that were not used in the initial registration (7 for subject 1 and 8 for the others). The fiducial registration error is the average error of the 4 fiducials used in the registration, and the residual error is the RMS distance of the digitised surface points from the head surface extracted from the MRI.

In general optimisation using surface points and projection onto the head surface improved the average map error (table 6.2). This difference was significant at the 0.05 level using the Wilcoxon signed rank test for all data sets. The residual error after optimisation was similar for all data sets, although slightly smaller for data set 1.

6.3.3 Conclusions

For simulated registrations with different levels of fiducial and surface point noise, the map error using the Gauss-Newton optimisation method was 3.39 mm even when the standard deviation of added noise was 7.5 mm, suggesting that with accurate head surface and fiducial data, and an accurate head surface extracted from MRI, acceptable registration accuracy can be achieved.

However, both registration using landmarks only and surface-based registration using landmark initialisation produced map errors between 1 and 4 cm which is not acceptably accurate in relation to the resolution of NIRS, and compared to the 2-4 mm accuracy achieved by others [109]. This suggests that digitisation is not accurate or that the swimming cap and/or markers moved too much between the MRI session and the NIRS digitisation session. There appears to be no qualitative difference between the two methods, however the same landmarks were used to evaluate the error with both methods, so if markers moved or digitisation was inaccurate the targets would also be incorrect.

Subject		Init	Opt	Proj
1	Mean map error	37.53	17.47	12.24
	Mean FRE	0	11.48	10.39
	Residual	16.40	5.94	0
2a	Mean map error	90.79	40.78	40.21
	FRE	0	34.40	32.20
	Residual	35.39	7.32	0
2b	Mean map error	72.56	42.96	41.07
	FRE	0	34.17	31.81
	Residual	31.26	7.93	0
4	Mean map error	48.17	23.84	22.57
	FRE	0	30.01	26.80
	Residual	17.29	7.51	0
7	Mean map error	38.46	31.46	28.12
	FRE	0	35.86	42.91
	Residual	27.14	6.40	0

Table 6.2: Map, fiducial and residual error after registration: initial landmark-based, optimisation using surface alignment, and projection to head surface.

It is not recommended to use a magnetic digitiser in the presence of large amounts of metal, however, since the digitisation had to occur next to the NIRS system which is contained in a large metal cabinet this was unavoidable, and may have contributed to inaccuracy in digitisation. In fact, the head shape data from some subjects was very obviously distorted and had to be discarded.

The use of markers attached to swimming caps or hair appears to be an ineffective method for registering NIRS data. In [109] it was also found that a swimming cap produced too much movement. In addition, this magnetic digitiser system appears to be unreliable in this particular experimental situation. Although some data sets produced target registration accuracy in the desired range (± 1 cm), in general registration error appears to be large.

Because of the unsatisfactory results of the initial co-registration attempt, no markers were used for the main study, but anatomical landmarks - namely left and right pre-auricular points, nasion and nose tip were used to align the NIRS and MRI spaces, and a collection of surface points was used to optimise the co-registration.

The NAVI software which was used for image reconstruction provides a set of 36 predefined optode locations on the FEM model (figure 6.4). In order to reconstruct an image when using a 5 x 3 optode configuration (for example at the locations shown in magenta) there are 8 different locations that may be selected while maintaining the interoptode distance required for image reconstruction. Although with image reconstruction perfect registration cannot be achieved, alignment to anatomical location and between subjects is optimised by selecting the appropriate grid location for each subject before reconstructing functional images. Visualisation of the real-world optode locations and FEM model optode positions in the same space was done by aligning the

digitised head surface points with the subject's MRI, transforming these to MNI space and then transforming the FEM model co-ordinates to MNI space.

Using surface rather than landmark-based alignment has the advantage that only one MRI is required for each subject. The subject's MRI may be acquired at any time, instead of having to acquire an MRI image for each NIRS session. Registration to a subject's individual anatomy is highly desirable, and knowledge of individual anatomy may be used in the forward problem solution [111] in order to increase the accuracy of reconstructed DOT images. However, in many cases it may be impractical or too expensive to obtain an MRI image for each subject. In these cases, registration to an atlas, possibly the MRI of a representative subject, may be used as a general anatomical head model. The error in localisation of cortical activations when registration is performed to an atlas, is due to a combination of imperfect registration, anatomical differences between atlas and subject anatomies and the localisation error associated with diffuse optical image reconstruction, whereas when using a subject-specific MRI, any localisation error is due to diffuse optical image reconstruction only [231]. It has recently been shown that registering NIRS probe locations to an atlas results in an average localisation error of approximately 18 mm, compared to an error of 9.1 mm using the subject's own MRI. However reasonable anatomical localisation is possible even when subject-specific anatomy is not available [231].

Effectively what was done in this study was to register NIRS probes to the individual subject's anatomy, and then as best as possible to the DOT template used in the image reconstruction software. To summarise, alignment of NIRS data was performed as follows:

1. Bilateral motor cortex was targeted using the Cz position from the 10-20 system and a 5x3 optode grid placed over this location in each of the left and right hemispheres.
2. Locations of the anatomical landmarks, head surface points and the four corners of the optode grid were digitised in 3D using the Polhemus magnetic tracker.
3. Using landmark and surface registration methods described in this chapter, the co-ordinates of the optode grid corners were transformed to the subject's MRI space.
4. The subject's MRI was transformed to MNI space and the same transformation applied to locate the optode grid corners in MNI space.
5. The MRI template used by NAVI to create the FEM model was transformed to MNI space, and the same transformation used for the FEM co-ordinates.
6. The optode grid corners and the NAVI FEM model with possible optode locations are plotted in MNI space and the closest of the 8 possible grid positions (figure 6.4) is specified for image reconstruction using NAVI.

However, the DOT images that are produced are in an unknown NAVI space and must be realigned with the template MRI. This procedure is described in section 4.1.1.

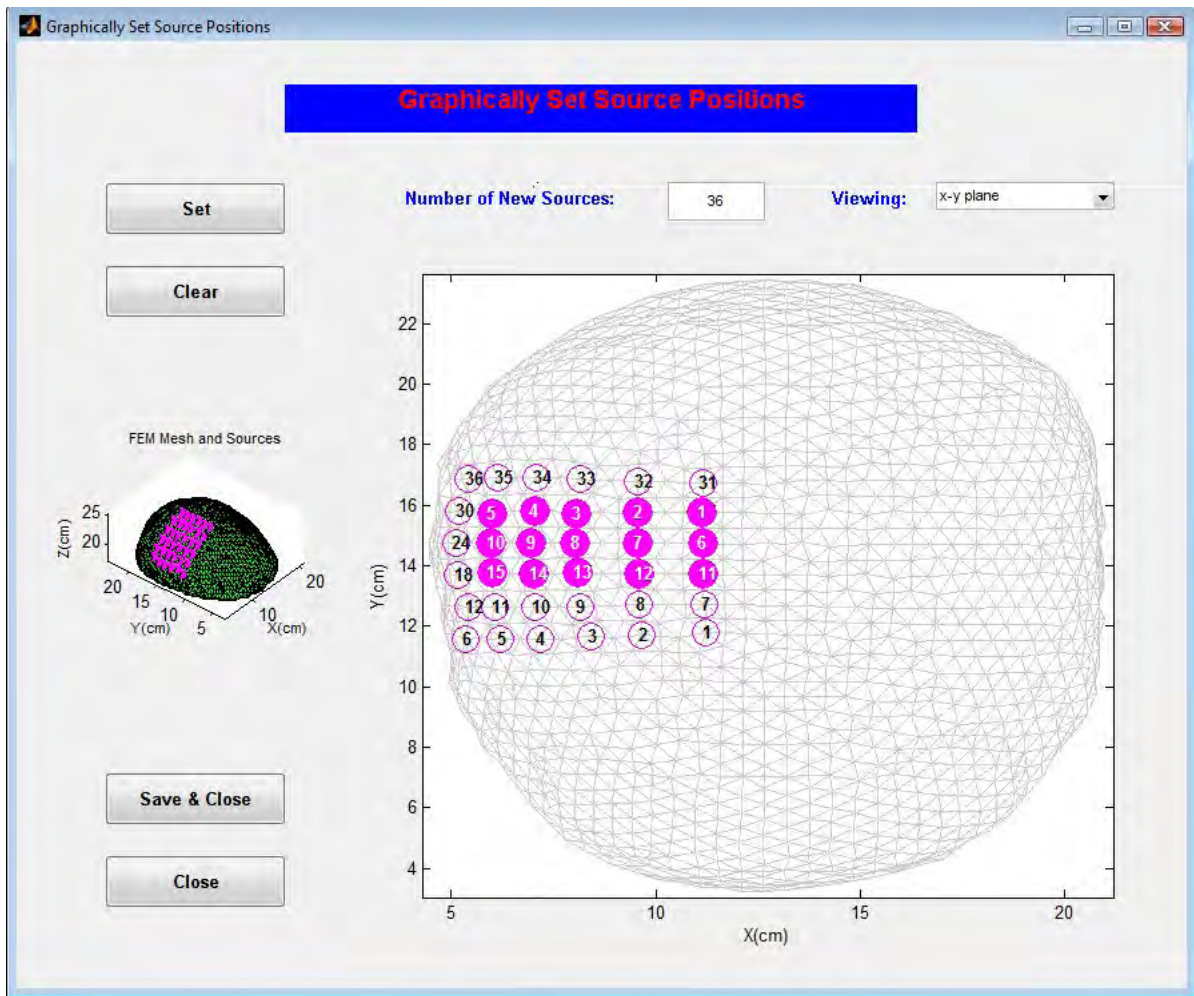


Figure 6.4: The 36 predefined optode positions offered in NAVI software. When using a 5x3 optode configuration the grid, shown in magenta, may be shifted one position left or right along the x-axis and one position backward or two positions forward along the y-axis, for a total of 8 possible grid positions while maintaining the interoptode distance.

Chapter 7

Ipsilateral activations and deactivations in unilateral motor tasks

The aims of the motor component of this experiment were to investigate ipsilateral activations and deactivations for left and right hand motor tasks using both functional MRI and NIRS. We wished to see if we could replicate the findings of ipsilateral activations particularly for left tapping and ipsilateral deactivations that are more prominent for the dominant (right, in this case) hand and whether the analysis of NIRS images could produce the same results. We also investigated whether there was any relationship across subjects between the magnitude of the ipsilateral activations/deactivations in particular regions of interest to the magnitude of activation in contralateral motor regions.

7.1 Introduction

It is well known that in response to a unilateral hand motor task, right-handed subjects produce robust activation in the contralateral primary motor (M1) and sensory (S1) cortex as well as the ipsilateral cerebellum. Many PET and fMRI studies have also reported activation of the ipsilateral precentral gyrus in normal adults [232, 233, 234, 235, 186, 236].

However, converging evidence suggests that the ipsilateral precentral gyrus activation found in fMRI studies is situated more anteriorly, ventrally and laterally than the M1 activation produced by a contralateral hand task [235, 186, 237, 236, 238]. It has been suggested that ipsilateral precentral gyrus activation considered to be M1 in early studies is more likely to be premotor cortex (BA6) [186], since it does not differentiate between hand and face movements [186]. A recent study found ipsilateral precentral gyrus activation in all subjects, mainly in the dorsal and ventral premotor areas (PMv and PMd) while ipsilateral M1 was less consistently activated and occurred anteriorly, close to the border of M1 and premotor cortex [238].

Deactivation, that is a decrease in BOLD signal in ipsilateral M1, has also been reported in fMRI studies of unilateral hand movement [239, 240, 241, 242, 243, 244]. Allison et al. [240] found that the same regions that

were activated by one hand were deactivated by the other (including the cerebellum, as did [242]). Other groups have used a low force pinch grip task to produce BOLD [241] and CBF and CMRO₂ [243] signal decreases in the ipsilateral M1 cortex.

Some studies have also found ipsilateral deactivation in only a subset of subjects (e.g. [238]) with some subjects producing simultaneous ipsilateral precentral gyrus activation and postcentral gyrus deactivation [238]. The results of this latter study suggest that ipsilateral sensorimotor (SM) deactivation when it occurred was more posterior, located over the postcentral gyrus, while ipsilateral SM activation was more anterior, situated directly over the central sulcus or over the precentral gyrus [238].

Newton et al. [244] found BOLD signal decreases in ipsilateral M1 for movements of each hand, with larger magnitude and volume of deactivation in the M1 ipsilateral to movement for the right, dominant hand than for the left hand. This is notably opposite to ipsilateral M1 activation which occurs more frequently to movement with the non-dominant hand.

However, a study of BOLD deactivations during tongue movement found signal decreases only in the posterior parietal cortex, precuneus, and middle temporal gyrus, while the primary somatosensory-motor area (SM1) was activated bilaterally. This is not consistent with studies involving unilateral hand movements which show deactivation of motor-related cortical areas including the ipsilateral M1 [245].

7.1.1 BOLD deactivations

In comparison with BOLD signal increases during a task, BOLD signal decreases relative to an inactive condition (fixation or rest) are much less frequently studied. One of the first reasons for interest in deactivation came with the discovery that a consistent set of brain regions showed signal decreases during a variety of tasks, relative to a baseline resting state. The finding that this network of regions, which came to be termed the default mode network [246], had greater activity during rest than during goal-directed tasks evoked much research interest. Correlations in spontaneous activity between the same regions during a task-free resting state, support the idea that this is a functionally connected network [247].

In addition to “default mode” deactivation, BOLD signal decreases have also been observed in task-specific regions. There appear to be two main types of task-specific deactivation: sensory cross-modal deactivation, which involves the suppression of sensory cortex that is not relevant to the task, for example deactivation of auditory cortex during a visual task; and lateralised deactivation, where during a unilateral task, the relevant sensory cortex of the ipsilateral hemisphere shows a BOLD signal decrease. The study of functional connectivity between regions activated or deactivated by a particular task may help to dissociate between these three possibly different modes of deactivation.

The meaning of these BOLD signal decreases is not entirely clear. It has been suggested that since blood flow to the brain is relatively constant, local BOLD signal decreases may simply reflect the reallocation of oxygenated blood towards activated areas in response to metabolic demand [248, 249]. However, it is unlikely that negative BOLD responses observed in the opposite hemisphere to the positive BOLD change [240, 241, 250, 251, 243] are a consequence of this effect, since the blood supply to each hemisphere is via different carotid arteries [251]. Additionally, there is accumulating evidence that a negative BOLD response

is an indicator of decreased neuronal activity [252].

7.1.2 Transcallosal inhibitory and uncrossed descending pathway hypotheses

Interhemispheric control of motor action has been suggested to involve deactivation in order to prevent interference from the opposite hemisphere [240]. Ipsilateral M1 deactivation is believed to result from transcallosal inhibitory inputs from the contralateral motor area [240, 244]. This is supported by evidence of decreases in CMRO₂ [243] and studies which indicate that a negative BOLD response indicates neural inhibition [252].

Because either inhibitory or excitatory dendritic inputs may cause an increase in BOLD signal [253], ipsilateral precentral gyrus activation may similarly correspond to transcallosal inhibitory signals from the contralateral motor regions [237, 236]. A second possibility is that ipsilateral activation may represent neuronal activity in uncrossed descending motor pathways [232, 233, 235, 186, 236].

Supporting the former hypothesis, a relationship has been found between BOLD activation in the ipsilateral precentral gyrus and transcallosal inhibition detected with TMS [237]. During nondominant (left) finger movements, 5 of the 10 subjects showed significant activation on their ipsilateral (left) sensorimotor hand area. Dominant (right) finger movement did not activate the sensorimotor area of the ipsilateral side in any subject. The paired-pulse TMS study suggests that interhemispheric, transcallosal influences rather than ipsilateral descending pathways account for the activation of the motor cortex ipsilateral to the hand movement [237].

However, in nonhuman primates ipsilateral motor representations have been demonstrated in M1 [254, 255]. Also ipsilateral motor evoked potentials (MEPs) have been produced in response to transcranial magnetic stimulation (TMS) of M1 in children [256] and adults [257]. It is possible that initial motor responses are bilateral, but that the ipsilateral motor cortex is subsequently partially inhibited by the motor cortex contralateral to the active hand [258]. It has been suggested that if ipsilateral fMRI activation corresponds to transcallosal inhibition, activations during an ipsilateral task should be spatially distinct from activations during contralateral and bilateral tasks [238]. However, ipsilaterally activated regions were also found to be activated during bilateral (as well as contralateral) tasks, with smaller signal change during ipsilateral finger tapping. The authors of this study suggest that ipsilateral fMRI activation in unilateral motor tasks may reflect part of a bilateral network involved in the planning or execution of ipsilateral hand movement [238].

7.1.3 Factors affecting ipsilateral activation and deactivation

Neither ipsilateral M1 activation [233, 237] nor deactivation occur in all subjects. Ipsilateral activation has been found to occur more commonly when movements are performed with the non-dominant hand [232, 234, 237, 186] or paretic hand following a stroke [232], while ipsilateral deactivation of sensorimotor cortex appears with larger magnitude and volume of activation in the M1 ipsilateral to movement for the right, dominant, hand than for the left hand in right-handed subjects [250, 244, 259].

Ipsilateral activation also occurs more frequently during complex movements suggesting that ipsilateral M1 is recruited to complete more challenging tasks. Finally although distal movements, of the hand for ex-

ample, activate only ipsilateral secondary somatosensory areas, while possibly deactivating the ipsilateral primary sensorimotor cortex; proximal movements have been found to activate both primary and secondary somatosensory areas ipsilaterally [250].

Simple motor tasks which do not involve independent finger movement result in small ipsilateral activations [233, 235, 237, 236], while tapping of a sequence using multiple fingers produces robust ipsilateral motor-related activation for both right and left hand tapping [238]. The number of finger transitions in a sequence has been found to correlate with increased ipsilateral dorsal premotor activation [260], while tapping a complex sequence produces greater ipsilateral activation than tapping out chords involving simultaneous movement of multiple fingers, which in turn produces greater ipsilateral activation than simple finger tapping [236].

Deactivation of the ipsilateral motor area can be reliably produced by a low force pinch grip task [241, 243]. Movement frequency [259] and duration have been found to have an effect on the magnitude of ipsilateral BOLD signal decrease, where increased movement duration results in larger BOLD increase in contralateral M1 as well as a larger ipsilateral decrease for both hands [244] and increasing movement frequency increases contralateral BOLD signal for both hands, but has opposite effects on ipsilateral BOLD deactivations in the different hemispheres [259].

7.2 Methods

7.2.1 Subjects and task

The short blocks fMRI data from 14 subjects (8 male) and NIRS data from 15 subjects (9 male) was used. Of these subjects 10 participated in both NIRS and fMRI imaging. The task and data acquisition have been described in 5.1.3.1 and 5.1.3.2 on page 74.

7.2.2 Image preprocessing and quality control

Functional images for each fMRI run were motion-corrected using SPM5 (<http://www.fil.ion.ucl.ac.uk/spm>), and co-registered to the T2-weighted structural image which was in turn co-registered to each subject's T1-weighted high-resolution anatomical image. Each subject's data were normalised to MNI space (resliced to 3x3x3 mm voxels) and spatially smoothed using a Gaussian kernel of 8 mm FWHM.

The ArtRepair toolbox for SPM (<http://cibsr.stanford.edu/tools/ArtRepair/ArtRepair.htm>) was used to detect bad volumes. In the first run (with short, 1100 ms TR) several subjects showed either large or sudden motions which had an impact on the global signal. In the second (2200 ms TR) run all subjects showed less than 1 mm or 1 degree movement in any direction, and only one subject's data showed a few volumes of large change in the global signal. The bad volumes in this subject's data were repaired and deweighted in the first level analysis. Because the data for the second run had fewer artefacts, the data from the first run was discarded and only the 2200 ms TR data were analysed.

NIRS preprocessing and image reconstruction were performed using the NAVI software (NIRx Medical Technologies, NY). The raw data files were first split into two separate files containing measurements from channels

located over the left and right hemispheres. For 15 optodes over each hemisphere this is 225 channels in each file. Raw data was band pass filtered between 0.01 and 0.5 Hz. Noisy channels were identified and rejected if the coefficient of variation (CV) in a 3 minute baseline period was greater than 0.25. Images of oxyhaemoglobin and deoxyhaemoglobin concentration changes for the left and right hemisphere were then reconstructed separately on a 64x64x64 grid and exported to “Analyze” format using NAVI’s export feature, for analysis with SPM.

Diagnostic plots of the data quality for each subject are shown in figure 7.1.

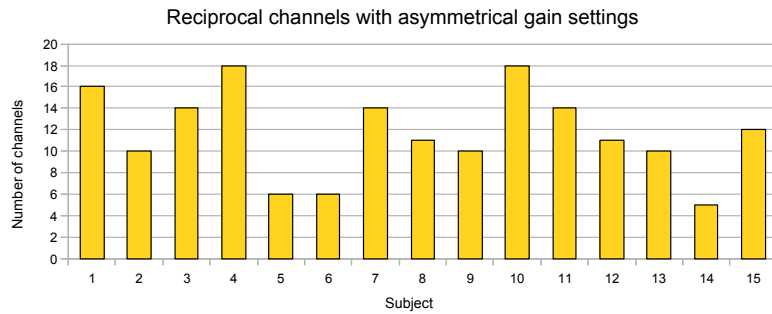
7.2.3 Analysis

For both sets of images, first level analysis was performed using the general linear model (GLM) as implemented in SPM5. Regressors were included for each of the task conditions (LTAP, RTAP, LCOLD, RCOLD) convolved with SPM’s canonical haemodynamic response function. For fMRI analysis the six motion parameters resulting from realignment were also included. High pass filtering was performed to remove signal drifts with a period longer than 128 s. Correction for serial autocorrelation in the data was performed using an autoregressive model of order 1.

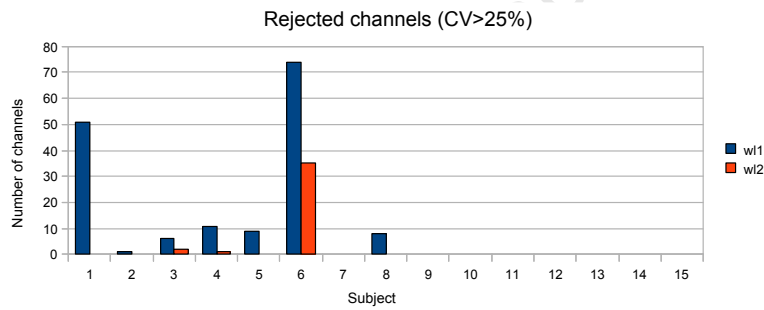
At the group level, the first-level contrast images for each subject (LTAP vs FIX, RTAP vs FIX, LCOLD vs FIX, and RCOLD vs FIX) were included in a flexible factorial design (2-way ANOVA) with factors subject and condition. Including subject as a factor helps to explain variability that is based on individual differences in BOLD response across all conditions, in the same way that a paired t-test does for comparing means of two conditions.

For the second level ANOVA, contrasts were generated to test for activation (RTAP > FIX, LTAP > FIX) and deactivation (RTAP < FIX, LTAP < FIX) and differences between the left hand and right hand conditions LTAP > RTAP and RTAP > LTAP. This was done for both tapping and cold conditions. The latter contrasts test where contralateral activation for a task is greater than ipsilateral activation for the task performed with the opposite hand. Because of the many comparisons made (RTAP > FIX, LTAP > FIX, RTAP < FIX, LTAP < FIX, RTAP > LTAP and LTAP > RTAP), statistical maps for both imaging modalities were thresholded at a conservative p threshold of 0.001 with false discovery rate (FDR) correction to account for simultaneous hypothesis testing across multiple voxels. This corresponds to a p threshold of 0.006 Bonferroni-corrected for the number of comparisons (0.001 x 6 comparisons).

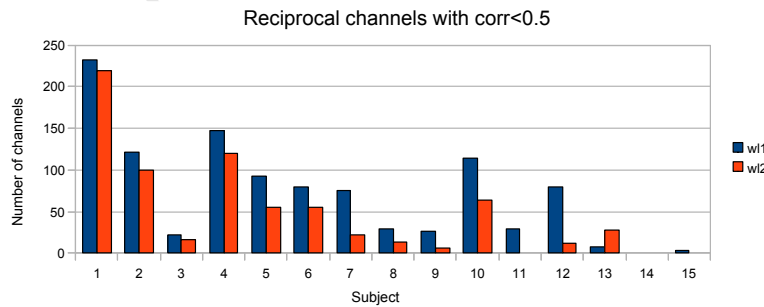
Areas that appear activated in one hemisphere for one hand but not in the other hemisphere for the opposite hand may not indicate that any significant differences exist in homologous areas between conditions. In other words the presence of right hemisphere activation to a left hand stimulus without significant left hemisphere activation in response to right hand stimulation does not allow the conclusion that contralateral activation is significantly greater for the left hand. In order to investigate hemispheric activation bias, and whether there were significant differences in contralateral and ipsilateral activation between the dominant (right) and non-dominant (left) hand, two different analyses were performed: a region of interest analysis, which was performed on both fMRI and NIRS data, and a voxelwise analysis on flipped fMRI images.



(a) Number of reciprocal channels (source x detector y and source y detector x) with asymmetric gain settings



(b) Number of rejected channels ($CV > 25\%$) for each wavelength in each subject



(c) Number of reciprocal channels with correlation less than 0.5 for each subject and each wavelength

Figure 7.1: Diagnostic plots of data quality. Subjects 1-5 had dark skin and hair. Subjects 6-7 had light skin and dark hair, and the remainder had fairly light skin and brown/fair hair with subjects 14 and 15 being particularly fair. Subjects 10 and 12 had many low correlation channels in spite of light colouring. The data for subject 3 was good in spite of darker pigmentation .

Region of interest analysis

In the first method, regions of interest were created differently for fMRI and NIRS images. For fMRI spherical regions of interest (ROIs) with 5 mm radius were created based on the results of the activation and deactivation analyses for left and right conditions separately. Where a region was identified as significant for a cold stimulus applied to one hand but no corresponding activated region in the opposite hemisphere was identified for cold applied to the opposite hand, a mirror ROI was created by changing the sign of the x co-ordinate of the ROI centre in MNI space. For NIRS images, the ROIs encompassed the entire left and right sensorimotor cortex measurement areas.

For each ROI the median beta value from the first level analysis for each subject was extracted and entered into a two factor ANOVA, with factors active hand (two levels: left and right) and hemisphere (two levels: contralateral and ipsilateral). Using the median parameter value in the ROI as opposed to the mean was intended to allow for a smaller extent of activation than the ROI size, and possible differences in extent of activation between hemispheres. Using this analysis, main effects of hand (left and right) and hemisphere (contralateral and ipsilateral) could be investigated. A significant interaction indicates a hemispheric lateralisation, that is greater activity in one hemisphere (left or right) regardless of hand used.

Voxelwise analysis on flipped fMRI images

In the second method used for fMRI data, the first level contrast images for the left hand conditions for each subject were flipped about the x-axis. These flipped images were entered into a second level analysis along with the unflipped contrast images for the right hand condition, to directly test for significant differences in contralateral activation between left and right conditions, and in ipsilateral activation between left and right conditions. This method has the advantage of being able to use voxelwise statistics over the whole brain as in a conventional SPM analysis. Comparing mirrored images does assume that functional regions are mirrored in corresponding voxels in the opposite hemisphere, however, it avoids the need to select regions of interest from among many possible candidate regions.

Intersubject correlation analysis

A correlation analysis across subjects was performed on the median first-level parameter estimates between selected ROIs that deactivated ipsilaterally in one condition and those that activated contralaterally in the same condition. The aim of this was to investigate whether there were contralaterally activated areas whose increased activity corresponded with decreased activity in the opposite hemisphere. If deactivation occurs via transcallosal inhibition this might be expected to be the case between corresponding regions of primary sensorimotor cortex.

7.3 Results

7.3.1 Motor task activation

Contrasts testing for activation by left and right tapping compared to fixation revealed significant BOLD activations in contralateral thalamus, putamen, primary and secondary somatosensory areas, premotor and supplementary motor areas. At the threshold used, there was more extensive contralateral and ipsilateral activation for left tapping than for right tapping. Contralateral activation for the left tap condition formed large connected clusters encompassing several regions of interest, while contralateral activation for right tapping produced more discrete clusters. These areas of activation are listed in table 7.1.

The same contrasts on NIRS data revealed significant activations (oxyHb increase and deoxyHb decrease) throughout the measured contralateral and ipsilateral sensorimotor cortex area. The extent of activation in voxels for each contrast is listed in table 7.2. While the extent of activation was similar for all contrasts because of the relatively small area covered, contralateral activation for right tapping produced higher t-values than for left tapping and ipsilateral activation for left tapping produced higher t-values (and extent) than right tapping.

While significant bilateral activation to unilateral finger tapping was measured with NIRS, activation was qualitatively more bilateral (less lateralised) for left tapping, as peak t-values and extent were similar in both hemispheres. Activation for right tapping appeared more lateralised to the contralateral hemisphere; ipsilateral activation in this case was smaller in magnitude and extent.

From the fMRI data it was apparent that the putamen, thalamus, and primary S1/M1 regions responded to the contralateral stimulus. Activation in supplementary motor area and premotor regions was bilateral for both left and right tapping, but there was qualitatively more ipsilateral and contralateral BOLD activation to left hand tapping than to right tapping. In fMRI left and right tapping produced similar contralateral peak t-values, but larger activation extent for left tapping, while in NIRS contralateral activation for right tapping produced higher t-values than for left tapping. However, ipsilateral activation in both fMRI and NIRS was greater in extent (and larger t-values) for left than for right tapping.

7.3.2 Motor task deactivation

BOLD deactivations in response to a unilateral finger tapping task are listed in table 7.3

Right tapping deactivated a very large extent of ipsilateral and contralateral cortex, while deactivation to left tapping was more restricted. Ipsilateral precentral/postcentral gyrus (SM1) was deactivated in both cases, as well as areas belonging to the default mode network (posterior cingulate, precuneus and medial frontal cortex). Regions of occipital cortex (cuneus) were deactivated in both conditions.

No regions of significant deactivation (oxyHb decrease and deoxyHb increase) were found with NIRS.

RTAP > FIX			
Contralateral area	No. voxels	Co-ordinates	Peak t
L putamen	37	-27 -6 -3	6.4
L thalamus	13	-12 -18 3	7.04
L precentral gyrus (BA4)	901	-39 -21 57	24.46
L supplementary motor area (R supplementary motor area)	159 (29)	-3 -3 57	10.52
L middle/inferior frontal gyrus (BA6,9) (ventral premotor)	9	-60 3 24	5.92
Ipsilateral area			
R middle/inferior frontal gyrus (BA6) (dorsal premotor)	35	54 0 45	6.9
LTAP > FIX			
Contralateral area	No. voxels	Co-ordinates	Peak t
R putamen	522 (169)	30 -3 0	10.12
(R thalamus)	(81)		
R precentral gyrus (BA4)	2061	45 -15 57	23.75
(R supplementary motor area)	(202)		
(L supplementary motor area)	(139)		
R middle/inferior frontal gyrus (BA6,9) (premotor)			
R middle/inferior frontal gyrus (triangular and orbital parts of IFG)	10	39 42 0	5.21
Ipsilateral area			
L middle/inferior frontal gyrus (BA6,9)	169	-54 -3 45	7.44
L middle/superior frontal gyrus	36	-27 42 18	6.03
L thalamus	9	-15 -6 15	4.92
L middle/superior frontal gyrus (BA10)	8	-12 30 -6	4.9
L inferior temporal gyrus	7	-42 -24 -18	5.04

Table 7.1: Positive BOLD responses to unilateral finger tapping of each hand ($p < 0.001$ FDR), clusters > 6 voxels. Regions that are listed in brackets each appeared as part of a larger cluster that is listed above it. The notation TAP > FIX indicates a contrast testing for greater BOLD signal in the tapping condition than during fixation.

RTAP vs FIX		
Left hemisphere (contralateral)	No. voxels	Peak t
oxyHb increase	21909	54.10
deoxyHb decrease	21898	57.75
Right hemisphere (ipsilateral)		
oxyHb increase	20214	6.74
deoxyHb decrease	10606	6.78
LTAP vs FIX		
Right hemisphere (contralateral)	No. voxels	Peak t
oxyHb increase	21396	27.17
deoxyHb decrease	21204	30.72
Left hemisphere (ipsilateral)		
oxyHb increase	21847	13.76
deoxyHb decrease	21331	18.44

Table 7.2: NIRS activation (oxyHb increase and deoxyHb decrease) to unilateral finger tapping of each hand ($p < 0.001$ FDR), clusters > 6 voxels .

7.3.3 Differences between left and right tapping

Regions that were found by fMRI to be significantly differently activated in the left and right tapping conditions are listed in table 7.4.

As shown in figure 7.2, the right putamen, thalamus, and insula as well as primary motor cortex and parts of SMA were activated significantly more by contralateral tapping than by ipsilateral tapping, while in the left hemisphere only the primary motor cortex was activated more by contralateral than ipsilateral tapping. The hemisphere and extent of areas that were found by NIRS to be significantly differently activated in the left and right tapping conditions are listed in table 7.5. Because activation corresponds to a decrease in deoxyHb, deoxyHb concentration is greater in the hemisphere ipsilateral to the tapping hand (that is, there is a contralateral decrease).

Figures 7.3 and 7.4 show peak regions of activation in oxyHb and deoxyHb respectively, transformed into MNI space and overlaid on a template brain MRI. Consistent with fMRI results, the measured areas over the sensorimotor cortex in both right and left hemispheres were activated significantly more by contralateral tapping than by ipsilateral tapping. Although the location of peak activation is comparable to that found using fMRI, as can be seen from the images the localisation of activation foci by the DOT image reconstruction is less than perfect. In both oxyHb and deoxyHb the contrast testing for greater signal in RTAP than LTAP (shown in blue) results in apparent activation in the skull and skin. In some cases the activation also extends deeper than might be expected to be measured with NIRS. Notably, the peak activation for deoxyHb appears in a more anterior location than the peak activation for either oxyHb or BOLD. This is also possibly an image reconstruction artefact. In spite of possible inaccuracies in location, the direction of the changes observed with NIRS in each hemisphere are consistent with expectation and with fMRI results.

RTAP < FIX			
Area	No. voxels	Co-ordinates	Peak t
R precuneus/ postcentral (BA40)	6960	21 -39 57	11.29
(L middle temporal gyrus)	(343)		
(R middle temporal gyrus)	(256)		
(L&R precuneus/ cuneus (BA5,19)			
L calcarine	27	-27 -60 3	4.95
L parahippocampal/ fusiform gyri	43	-24 -42 -12	5.22
R parahippocampal gyrus	68	33 -33 -15	5.39
L caudate	81	0 9 0	6.02
R superior frontal gyrus	38	30 60 3	5.76
L superior frontal gyrus	96	-21 60 27	6.63
R anterior cingulate	14	6 27 15	4.17
R superior frontal gyrus	18	60 24 11	
L inferior parietal lobule	42	-63 -39 39	5.14
L&R medial superior frontal gyrus	301	0 36 39	7.14
L middle frontal gyrus	136	-33 30 45	7.03
L superior frontal gyrus	8	-15 12 63	4.5
LTAP < FIX			
Area	No. voxels	Co-ordinates	Peak t
L postcentral gyrus (BA 3,40)	9	-24 -39 60	5.52
R middle temporal gyrus	53	45 -78 24	6.78
L middle temporal gyrus	52	-45 -72 18	6.38
L&R precuneus/ cuneus (BA5,19)	496	3 -48 57	8.23
R posterior cingulate/ calcarine (BA 30)	44	12 -57 9	5.67
L posterior cingulate/calcarine (BA30)	14	-21 -63 3	5.96
L&R posterior cingulate/ calcarine/ cuneus (BA18)	12	0 -72 12	5

Table 7.3: Negative BOLD responses to unilateral finger tapping of each hand ($p < 0.001$ FDR) . Regions that are listed in brackets each appeared as part of a larger cluster that is listed above it. The notation TAP < FIX indicates a contrast testing for smaller BOLD signal in the tapping condition than during fixation, i.e. deactivation.

LTAP > RTAP			
Area	No. voxels	Co-ordinates	Peak t
R precentral/ supplementary motor area (BA3,4,6,40)	981	36 -21 54	16.2686
R putamen/ thalamus/ pallidum/ claustrum	328	33 -6 0	8.0904
R postcentral/ Rolandic operculum/ insula	107	51 -15 18	7.9865
L medial superior frontal gyrus (BA8)	7	-6 30 45	5.127
RTAP > LTAP			
Area	No. voxels	Co-ordinates	Peak t
L precentral (BA3,4,6,40)	430	-36 -24 57	14.7054

Table 7.4: Regions activated for LTAP > RTAP and RTAP > LTAP with fMRI (FDR corrected $p < 0.001$). The notation LTAP > RTAP indicates a contrast testing for greater activation in the LTAP than in the RTAP condition. RTAP > LTAP indicates a contrast testing for greater activation in the RTAP than the LTAP condition.

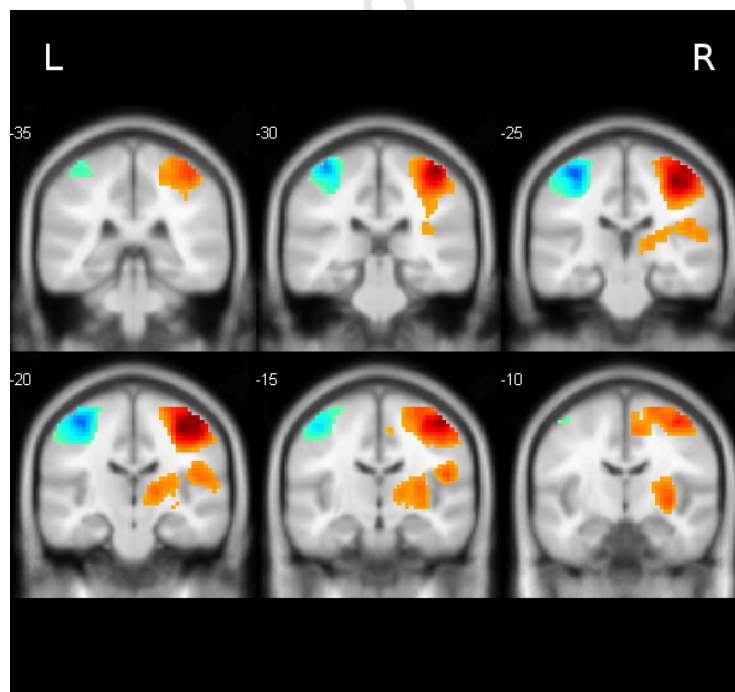


Figure 7.2: Functional MRI statistical map of LTAP > RTAP (orange) and RTAP > LTAP (blue) thresholded at $p < 0.001$ FDR. The notation LTAP > RTAP indicates a contrast testing for greater activation in the LTAP than in the RTAP condition. RTAP > LTAP indicates a contrast testing for greater activation in the RTAP than the LTAP condition.

LTAP > RTAP		
Left hemisphere	No. voxels	Peak t
deoxyHb	18128	6.20
Right hemisphere		
oxyHb	21015	7.28
RTAP > LTAP		
Left hemisphere	No. voxels	Peak t
oxyHb	17965	5.47
Right hemisphere		
deoxyHb	20406	8.24

Table 7.5: Regions with greater oxyHb or deoxyHb signal in LTAP condition than in the RTAP condition (LTAP > RTAP) and in the RTAP than the LTAP condition (RTAP > LTAP), FDR corrected at $p < 0.001$.

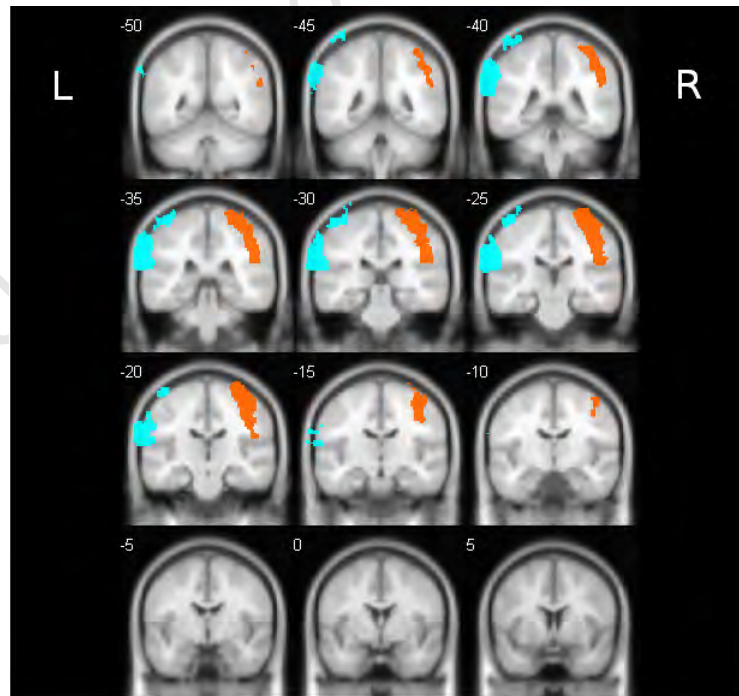


Figure 7.3: Thresholded oxyHb map of LTAP > RTAP (orange) and RTAP > LTAP (blue) transformed into MNI space and overlaid on a template brain MRI. The notation LTAP > RTAP indicates a contrast testing for greater oxyHb in the LTAP than in the RTAP condition. RTAP > LTAP indicates a contrast testing for greater oxyHb in the RTAP than the LTAP condition.

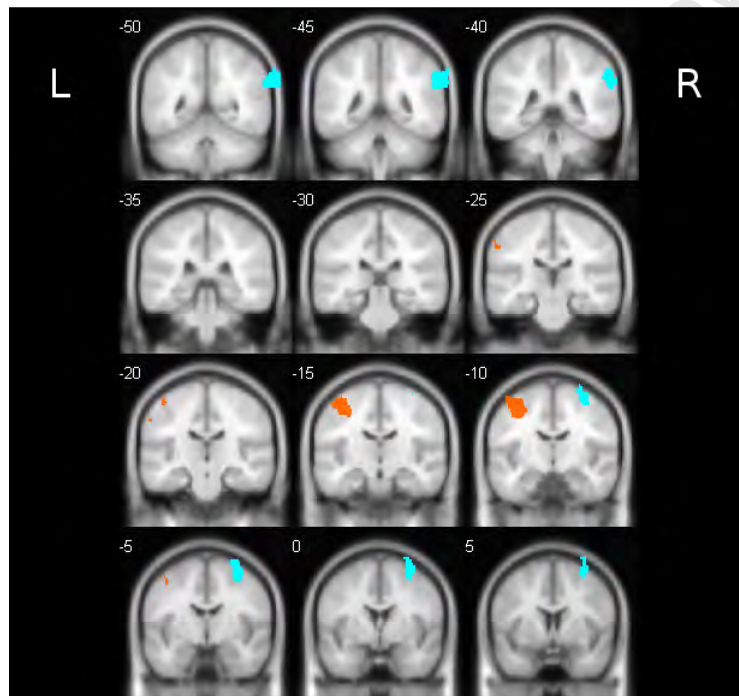


Figure 7.4: Thresholded deoxyHb map of $LTAP > RTAP$ (orange) and $RTAP > LTAP$ (blue) transformed into MNI space and overlaid on a template brain MRI. The notation $LTAP > RTAP$ indicates a contrast testing for greater deoxyHb in the LTAP than in the RTAP condition. $RTAP > LTAP$ indicates a contrast testing for greater deoxyHb in the RTAP than the LTAP condition.

Contralateral SM1 was activated by unilateral tapping. The NIRS analysis appears symmetric: corresponding regions in each hemisphere show significantly greater activation to contralateral finger tapping than ipsilateral activation for the task performed with the opposite hand. However, in the fMRI analysis there is a larger area of right hemisphere than the left that is activated significantly more by contralateral tapping than by ipsilateral tapping. The apparent asymmetry does not reveal whether there is significantly more contralateral activation for left tapping than right tapping or less ipsilateral activation for right tapping than left tapping or whether greater variability means the comparison in left hemisphere regions fails to reach significance.

7.3.4 Activation asymmetry: effect of tapping hand and hemisphere of activation

In order to test for contralateral or laterally biased activation, the 10 ROIs shown in table 7.6 were extracted from the fMRI analyses in tables 7.1, 7.3 and 7.4. For NIRS two regions of interest were defined for each haemoglobin species and each hemisphere - one activated by contralateral tapping and one by ipsilateral tapping.

Two factor repeated measures ANOVA on ROI data

To account for the 10 fMRI regions tested, a p-value of $0.05/10=0.005$ was required for significance. For the main effect of hemisphere of activation the regions of interest in the putamen, thalamus, SM1 and SMA were significant. From figure 7.5 it can be seen that these regions have larger parameter values in the hemisphere contralateral to the hand used, for both left and right hands. From the plots of mean effects it appears that the parameter estimates for left tap were larger than right tap, however this effect was only significant in the ACC ROI. This suggests that the ACC is more activated for left tap than for right tap (both ipsi- and contralaterally). No interactions were significant.

The absence of significant main effects for the premotor ROI implies that contralateral premotor area is not more activated than ipsilateral premotor area for left or right tapping, and ipsilateral (and contralateral) premotor areas are not preferentially activated by dominant or nondominant hand tapping, in spite of the larger extent of activation observed in the left hemisphere.

For the NIRS data in table 7.7, a p-value of 0.05 was required for significance. In the sensorimotor cortex area the main effects of hemisphere of activation and tapping hand were both significant for both oxyHb and deoxyHb, as illustrated in figure 7.6, indicating a larger increase in oxyHb and decrease in deoxyHb (activation) for contralateral tapping, consistent with fMRI results, as well as a larger activation for left tapping than for right tapping both ipsilaterally and contralaterally, which is consistent with the non-significant trend in the fMRI data.

Voxelwise statistics using flipped fMRI images

To directly compare contralateral BOLD activation in the LTAP and RTAP conditions as well as ipsilateral BOLD activation in the LTAP and RTAP conditions a voxelwise analysis was performed where the first level

Contralateral area	Co-ordinates	Factor	p
Putamen	-27 -6 -3	Tapping hand	0.0300*
		Hemisphere	0.00001
		Interaction	0.6517
Thalamus	-12 -18 3	Tapping hand	0.0978
		Hemisphere	0.00001
		Interaction	0.0811
SMA	-3 -3 57	Tapping hand	0.1084
		Hemisphere	0.0001
		Interaction	0.7187
V. premotor (BA6,9)	-60 3 24	Tapping hand	0.1117
		Hemisphere	0.2954
		Interaction	0.6795
Orb./tri. inf. frontal gyrus	-39 42 0	Tapping hand	0.0101*
		Hemisphere	0.6176
		Interaction	0.0542
Mid./sup. frontal gyrus	27 42 18	Tapping hand	0.0121*
		Hemisphere	0.5643
		Interaction	0.3500
Ant. cingulate/BA10	12 30 -6	Tapping hand	0.0037
		Hemisphere	0.0372*
		Interaction	0.1611
Inf. temp. gyrus	42 -24 -18	Tapping hand	0.0186*
		Hemisphere	0.3497
		Interaction	0.8692
SM1 (activation peak)	39 -21 57	Tapping hand	0.1061
		Hemisphere	0.00001
		Interaction	0.0889
SM1 (deactivation peak)	-24 -39 60	Tapping hand	0.0516
		Hemisphere	0.00001
		Interaction	0.2230

Table 7.6: Results of two way ANOVA with factors hemisphere and hand for selected ROIs. Because 10 comparisons were made, a Bonferroni-corrected p value of $0.05/10=0.005$ was required for significance. Significant effects are shown in bold. Effects that are not significant at the corrected p threshold but are significant at $p<0.05$ uncorrected are marked with an asterisk.

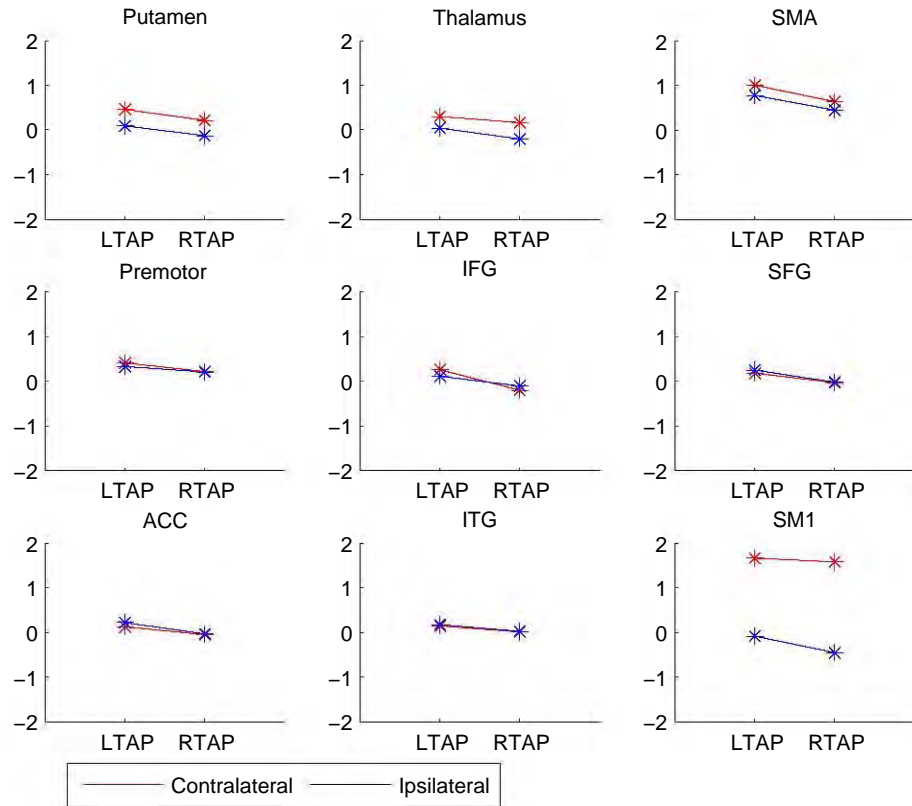


Figure 7.5: Mean parameter estimates for ROIs used in two-way ANOVA

OxyHb			
df	Factor	F	p
14	Tapping hand	98.790	0.0001
	Hemisphere	723.703	0.0001
	Interaction	1.049	0.3231
DeoxyHb			
df	Factor	F	p
14	Tapping hand	184.065	0.0001
	Hemisphere	464.266	0.0001
	Interaction	0.452	0.5122

Table 7.7: Results of two way ANOVA with factors hemisphere and hand for selected NIRS ROIs. A p value of 0.05 was required for significance. Significant effects are shown in bold.

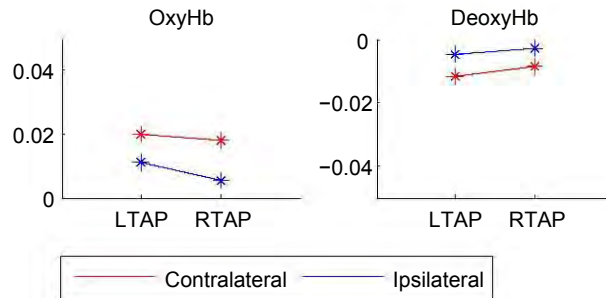


Figure 7.6: Mean parameter estimates for oxyHb and deoxyHb in sensorimotor area, used in two-way ANOVA

images for one of the contrasts was flipped about the x-axis.

As shown in table 7.8, no regions were significant for the $RTAP > LTAP$ contrast, but many contralateral and ipsilateral regions were activated significantly more in LTAP than RTAP. To dissociate regions that appeared significant in this analysis because of greater deactivation for RTAP from those that appeared because of greater activation for LTAP this contrast was masked with $RTAP < FIX$ ($p < 0.001$ uncorrected) and $LTAP_flipped > FIX$ ($p < 0.001$ uncorrected) respectively. From this analysis it appears that there is greater contralateral activation for LTAP than RTAP in parts of premotor area and SMA, greater deactivation for RTAP in ipsilateral inferior parietal lobule and triangular and orbital parts of the inferior frontal gyrus and putamen. In the ipsilateral posterior and anterior SMA region and in the contralateral insula and middle temporal gyrus there is both significant deactivation for RTAP and activation for LTAP. There was no significant difference in contralateral activation or ipsilateral deactivation in primary sensorimotor areas, but there is significantly greater ipsilateral activation for LTAP than RTAP in parts of the SMA and premotor areas.

7.3.5 Intersubject variability of activation and deactivation

To attempt to determine how reliable BOLD motor deactivations are across subjects especially in relation to activation by the same task, we performed a first level fixed effects analysis of the same fMRI data in order to carry out a conjunction analysis across subjects. Using multi-subject conjunction analysis for each of the contrasts $LTAP > FIX$, $RTAP > FIX$, $LTAP < FIX$ and $RTAP < FIX$, we tested the intermediate null hypothesis of $k=6$, that is that less than 7 subjects activate with a lenient threshold of FDR 0.05

The activated areas for each contrast in the conjunction analysis are shown in table 7.9. For the deactivation contrasts ($LTAP < FIX$ and $RTAP < FIX$) there is no area in which the null hypothesis, of activation in less than half of the subjects, can be rejected. For the activation contrasts ($LTAP > FIX$ and $RTAP > FIX$) the null hypothesis can be rejected in the contralateral primary motor areas, allowing the conclusion that more than half of the subjects studied activate in that location. Therefore ipsilateral activation appears to be much more variable between subjects than contralateral activation.

LTAP > RTAP				
Hemisphere	Region	Co-ordinates	Voxels	Max t
Contra	Tri./orb. inf. frontal gyrus	-42 39 -3	249	5.2329
Contra	Insula/ putamen	-33 -12 9	87	3.9917
Contra	Sup./ mid. temporal gyrus (BA 21,22 41)	-45 -33 3	108	4.585
Contra	Precentral/ mid. frontal gyrus (BA 6) (premotor)	-39 -9 51	60	3.5795
Contra	Sup. frontal gyrus/ SMA (BA6)	-15 3 57	53	4.2274
Ipsi	Tri./orb. inf. frontal gyrus/ insula/ putamen	36 18 27	195	4.5028
Ipsi	Inf. parietal lobule (BA 40)	45 -60 39	82	4.3174
Ipsi	Medial frontal gyrus/ SMA/ anterior SMA (BA 6,8,9)	6 36 36	182	4.9872
Ipsi	Post. SMA/ cingulate/ M1 (BA6,4)	12 -9 54	183	4.6244
RTAP > LTAP				
No significant regions				

Table 7.8: Test for dominant response to one hand in contralateral and ipsilateral hemispheres (RTAP > LTAP where LTAP images were flipped about the x-axis) $p < 0.05$, clusters > 50 voxels. The notation LTAP > RTAP indicates a contrast testing for greater activation in the LTAP than in the RTAP condition. RTAP > LTAP indicates a contrast testing for greater activation in the RTAP than the LTAP condition.

Contrast	Area	No. voxels	Co-ordinates	Peak t
LTAP > FIX	R SM1	315	42 -15 60	3.82
	R SMA	26	3 -3 60	0.84
RTAP > FIX	L SM1	288	-36 -24 60	
LTAP < FIX		-		
RTAP < FIX		-		

Table 7.9: Results of multi-subject conjunction analysis. The notation LTAP > FIX indicates a contrast testing for greater activation in the LTAP than in the fixation condition. LTAP < FIX indicates a contrast testing for greater activation in the fixation than the LTAP condition.

BOLD				
	Bilateral response	Contra. response only	Ipsi. response only	No response
LTAP > FIX	9	5	0	0
RTAP > FIX	5	8	0	1

Table 7.10: Summary of individual subject BOLD responses in SM1 region for each contrast. The notation LTAP > FIX indicates a contrast testing for greater activation in the LTAP than in the fixation condition. RTAP > FIX indicates a contrast testing for greater activation in the RTAP than the fixation condition.

7.3.5.1 Individual ipsilateral activation in fMRI and NIRS

To attempt to determine how reliably ipsilateral and contralateral activations to the motor task are measured in individual subjects we examined the results of the contrasts LTAP > FIX, RTAP > FIX, LTAP < FIX and RTAP < FIX for each subject in each hemisphere and in NIRS for both oxyHb and deoxyHb. The results were thresholded at $p < 0.05$ FDR corrected.

fMRI Examining subject's individual fMRI activation maps for ipsilateral activation at a p threshold of 0.05 FDR corrected, 9 subjects showed a significant activation cluster anywhere in the left hemisphere for left tapping, mostly in premotor area (BA 6) and two were restricted to the inferior parietal lobule. Five subjects showed a significant activation cluster in the right hemisphere for right tapping. All subjects except one displayed widespread contralateral activation at the same threshold. In this one subject there was no contralateral activation to RTAP. These results are summarised in table 7.10.

NIRS Where NIRS activation (increased oxyHb or decreased deoxyHb) occurred, it was usually widely distributed over the entire measurement area, although in some cases only smaller regions were identified at this threshold. The contralateral and ipsilateral activations for each hand and each haemoglobin species are listed in table 7.11.

Three subjects did not show any activation in any of the contrasts at this significance threshold. This may have been because of improper optode placement (poor contact or not covering the correct area) or because of anatomical or physiological factors affecting these subjects, such as skull thickness, skin pigmentation (all had dark skin and hair), or large amplitude physiological interference making it harder to separate the motor response from background noise processes.

There is some inconsistency between oxyHb and deoxyHb responses, with more oxyHb responses than deoxyHb responses being found. As can be seen in table 7.11 there is often a significant oxyHb response without a significant deoxyHb response or with a deoxyHb response that is confined to a much smaller cluster (marked with an asterisk). This suggests either that the SNR of the deoxyHb response is indeed lower and hence harder to detect in individual subjects or that the deoxyHb response is more localised, or both. There are however 3 cases where a response was detected for deoxyHb but not for oxyHb (subjects 4, 11 and 12). It is possible that these small clusters are false positive activations, since subjects 11 and 12 show little or no activation in other conditions and the number of significant voxels for subject 4 is extremely small (13 voxels).

Subject	Contralateral		Ipsilateral	
	LTAP	RTAP	LTAP	RTAP
1	Oxy, Deoxy	Oxy, Deoxy	Oxy, Deoxy	Oxy, Deoxy*
2	Oxy, Deoxy	Oxy, Deoxy*	Oxy, Deoxy*	Oxy, Deoxy*
3	Oxy, Deoxy*	Oxy, Deoxy	Oxy, Deoxy	None
4	Oxy, Deoxy	Oxy, Deoxy	Oxy	Deoxy*
5	Oxy*, Deoxy*	Oxy, Deoxy	Oxy**	None
6	Oxy, Deoxy	Oxy		None
7	Oxy, Deoxy	Oxy		None
8	Oxy	Oxy, Deoxy		None
9	Oxy	None	None	Oxy, Deoxy
10	Oxy**	None	Oxy**	None
11	None	Oxy**	Deoxy**	None
12		None		Deoxy*
13		None		
14		None		
15		None		

Table 7.11: Activations for individual subjects for the LTAP > FIX and RTAP > FIX contrasts. . The notation LTAP > FIX indicates a contrast testing for greater activation in the LTAP than in the fixation condition. RTAP > FIX indicates a contrast testing for greater activation in the RTAP than the fixation condition. A single asterisk indicates an activation smaller than 100 voxels and a double asterisk a cluster smaller than 250 voxels.

OxyHb				
	Bilateral response	Contra. response only	Ipsi. response only	No response
LTAP > FIX	6	4	0	5
RTAP > FIX	2	7	1	5
LTAP < FIX	0	0	0	15
RTAP < FIX	0	0	2	13
DeoxyHb				
	Bilateral response	Contra. response only	Ipsi. response only	No response
LTAP < FIX	3	4	1	7
RTAP < FIX	3	3	2	7
LTAP > FIX	0	0	1	14
RTAP > FIX	0	0	0	15

Table 7.12: Summary of individual subject activations and deactivations in SM1 region for each contrast.

A summary of oxyHb and deoxyHb responses by number of subjects in which a response was measurable is shown in table 7.12, from which it can be seen that the expected contralateral response to unilateral finger tapping is more reliably measured in oxyHb (10 subjects) than in deoxyHb (7 subjects) in individual subjects. Only five subjects showed the expected contralateral activation for both LTAP and RTAP in both oxyHb and deoxyHb, although a further three showed contralateral activation to both LTAP and RTAP in oxyHb, but not necessarily deoxyHb. Four subjects showed no contralateral activation at all, and the remaining three showed activation to either LTAP or RTAP only in oxyHb.

As expected, ipsilateral activation was even more variable than contralateral activation. Two subjects showed ipsilateral activation for LTAP and RTAP in both oxyHb and deoxyHb and one showed ipsilateral activation for RTAP and one for LTAP in both oxyHb and deoxyHb. Three subjects showed ipsilateral activation in oxyHb to LTAP, two subjects had ipsilateral deactivations in deoxyHb to RTAP and one had ipsilateral deactivation to LTAP.

It must also be mentioned that in NIRS there is the possibility of measuring the motor area of one hemisphere but not the other, due to unilateral optode misplacement or poor contact. It is possible that this is the case for subjects who demonstrate activation in one hemisphere only, whether this is to left or right finger tapping (subjects 9 and 11 have activation in only one hemisphere).

7.3.5.2 Individual ipsilateral deactivation in fMRI and NIRS

Examining subject's individual fMRI activation maps for ipsilateral deactivation at a p threshold of 0.05 FDR corrected, only 3 subjects showed a significant deactivation cluster anywhere in the left sensorimotor cortex for left tapping and 5 subjects showed a significant deactivation cluster anywhere in the right sensorimotor cortex for right tapping. This suggests that these deactivation effects in addition to occurring only in some subjects are generally very small effects and show up in a group analysis better than in individual subjects.

Ipsilateral deactivation was not found reliably using NIRS. Deactivation occurred in oxyHb for 2 subjects in response to RTAP and in deoxyHb for one subject in response to LTAP (table 7.12).

The correlation across subjects between activation parameter estimates for oxyHb and deoxyHb was $r = -0.90$ for contralateral activation and $r = -0.71$ for ipsilateral de/activation to RTAP ($n=15$, significant at $p < 0.05$ two tailed) and $r = -0.96$ for contralateral activation and $r = -0.73$ for ipsilateral de/activation to LTAP ($n=15$, significant at $p < 0.05$ two tailed).

7.3.6 Intersubject correlations between activation and deactivation

We hypothesised that the degree of ipsilateral deactivation should be related to the degree of contralateral activation if the mechanism for deactivation is transcallosal inhibition, i.e. that subjects who have larger contralateral activation should also show increased ipsilateral deactivation. Regions of interest for the correlation analysis were selected from ipsilaterally deactivated and contralaterally activated brain areas for the left and right tapping conditions. In addition an area of “maximum overlap” was created for each hemisphere whose centre was the co-ordinate (reflected about the x-axis) which has the largest amount of ipsilateral deactivation and contralateral activation (the peak voxel resulting from a conjunction of contralateral activation and ipsilateral deactivation when one of these was flipped along the x-axis). This area was posterior to the activation peak and anterior to the deactivation peak, and was probably located in the precentral gyrus (M1). Correlation between the ipsi- and contralateral responses to RTAP and LTAP are listed in tables 7.13 and 7.14 respectively. For both hands, activity in the SMA in corresponding hemispheres was highly correlated; this is not a surprising finding since the SMA tended to activate bilaterally. For the right-hand task, activity in the contralateral thalamus was correlated with activity in ipsilateral M1 (overlap) and activity in the contralateral putamen was correlated with ipsilateral premotor activity. For the left tapping task only the ipsilateral SMA was correlated with contralateral thalamus, putamen and SMA.

For NIRS, the intersubject correlation between the mean activation to RTAP in a contralateral and ipsilateral ROIs of the 65 most-activated voxels was $r = 0.70$ for oxyHb and $r = 0.62$ for deoxyHb which were both significant at $p < 0.05$ (two tailed). The relationship across subjects between ipsilateral and contralateral activation to RTAP for oxyHb and deoxyHb is shown in figure 7.7. The intersubject correlation between the mean activation to LTAP in a contralateral and ipsilateral ROI was $r = 0.75$ for oxyHb ($p < 0.05$) and $r = 0.48$ for deoxyHb ($p > 0.05$).

7.4 Discussion

As has been observed previously using fMRI, we found ipsilateral deactivation in SM1 in response to a unilateral sequential finger tapping task [240, 241, 250]. The deactivation peak was however, posterior to the corresponding activation peak in the opposite hemisphere, suggesting this may be in S1, rather than

	Contralateral	L putamen -27 -6 -3	L thalamus -12 -18 3	L M1 (BA4) -39 -21 57	L SMA -3 -3 57	L v. premot. (BA6,9) -60 3 24	L M1 (overlap) -36 -24 54
Ipsilateral							
R S1 (BA3)	21 -39 57	0.36	0.48	-0.2	0.43	0.65 *	0.12
R M1 (overlap)	36 -24 54	0.76 *	0.8	0.22	0.6	0.72 *	0.13
R precuneus (BA5)	3 -45 57	0.34	0.45	-0.19	0.35	0.22	0.14
R cuneus (BA7)	12 -75 36	0.1	0.24	-0.17	0.39	0.33	0.11
R paracent. lob. (BA 24,31)	9 -33 45	0.5	0.69*	0.02	0.6	0.73 *	0.11
R insula/putamen	36 -27 18	0.74*	0.74 *	0.32	0.71 *	0.57	0.27
R SMA#	3 -3 57	0.56	0.62	0.39	0.93	0.66 *	0.69 *
R v. premot. #	60 3 24	0.83	0.7	0.66 *	0.72*	0.64	0.27

Table 7.13: Pearson correlation between ipsilaterally activated or deactivated ROIs and contralaterally activated ROIs for RTAP. Correlations in bold are significant at $p < 0.001$ ($p < 0.05$ corrected for multiple comparisons). An asterisk marks correlations that are significant at $p < 0.01$, uncorrected. A # indicates an ipsilateral activated area, rather than a deactivation.

Ipsilateral	Contralateral	R putamen (30 -3 0)	(R thalamus) (12 -18 3)	R M1 (BA4) (39 -21 54)	R SMA (3 -3 57)	R d. premot. (54 0 45)	R IFG (39 42 0)	R M1 (overlap) (30 -33 60)
L BA3	-24 -39 60	0.35	0.61	0	0.62	0.53	0.13	0.06
L M1 (overlap)	-30 -33 60	0.61	0.64	0	0.64	0.71	0.39	0.04
Precuneus	3 -48 57	0.07	0.19	0.05	0.34	-0.08	0.04	0.19
Post. Cing.	0 -72 12	0.3	0.48	0.11	0.71	0.17	0.05	0.2
L SMA #	-3 -3 57	0.82 *	0.89*	0.53	0.95*	0.56	0.25	0.6
L d. premotor#	-54 -3 45	0.53	0.66 *	0.38	0.57	0.48	0.15	0.33
L SFG#	-27 42 18	0.55	0.56	0.23	0.61	0.48	0.48	0.23

Table 7.14: Pearson correlation between ipsilaterally activated or deactivated ROIs and contralaterally activated ROIs for LTAP. Correlations in bold are significant at $p < 0.001$ ($p < 0.05$ corrected for multiple comparisons). An asterisk marks correlations that are significant at $p < 0.01$, uncorrected. A # indicates an ipsilateral activated area, rather than a deactivation.

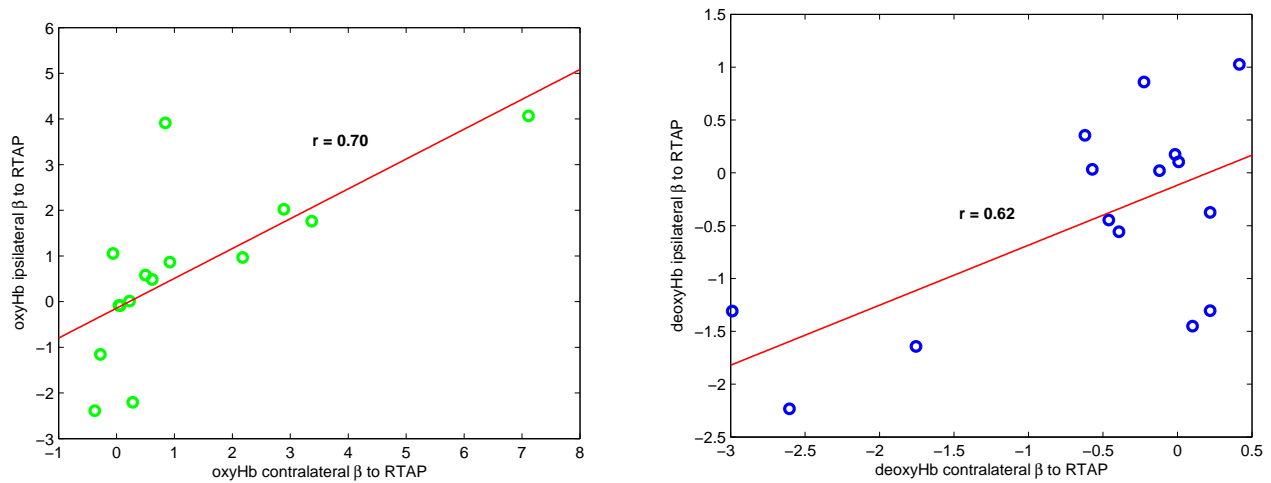


Figure 7.7: Correlation across subjects between mean β parameter estimates to RTAP in contralateral and ipsilateral ROIs for oxyHb and deoxyHb.

the precentral gyrus. We found more extensive ipsilateral deactivation for right hand tapping, which is consistent with previous studies in right-handers [250]. Premotor areas showed bilateral activity without contralateral bias, while SMA showed bilateral activity with stronger activity contralaterally. In a direct comparison between contralateral responses to left and right tapping several areas showed significantly greater activation for left tapping and/or significantly greater ipsilateral deactivation for right tapping. This suggests that tapping with the non-dominant hand recruits a wider network of brain regions to assist with a more challenging task, while tapping with the dominant hand requires suppression of the ipsilateral cortex to reduce interference from the opposite hemisphere, as has been suggested by others [240]. A similar result was found with NIRS data which in general suggested greater ipsilateral and contralateral activation to left tapping than to right tapping. However, group-level deactivation was not observed using NIRS.

NIRS results are somewhat less consistent than fMRI. Although deoxyHb responses occur less frequently than might be expected based on fMRI results, if oxyHb responses are considered to be evidence of activation even in the absence of a significant deoxyHb response, the contralateral response appears to be fairly reliably measurable in individual subjects. In fact, because the BOLD signal depends on a relative change in deoxyHb, a BOLD signal increase can occur without a decrease in deoxyHb concentration if there is a blood volume increase. However, it has been found previously that the BOLD signal to motor activation depends more on deoxyHb concentration changes than on changes in blood volume [15].

Furthermore, it happens more frequently with NIRS than with fMRI that a response is not measurable at all in particular subjects. This is easily explainable, because of uncertainties in optode location or poor contact of optodes with the scalp in individual subjects, both of which are factors which do not affect imaging using fMRI. Ipsilateral activation too is consistent with the fMRI results showing that the response occurs more frequently with use of the non-dominant (left) hand, although in the fMRI cohort ipsilateral activation to

LTAP appeared in 9 subjects, compared to 6 in fNIRS and ipsilateral activation to RTAP appeared in 5 subjects in fMRI compared to 3 in fNIRS.

Although in a previous study increased contralateral activation in M1 was found to correspond to larger ipsilateral negative responses [244], we did not find a clear relationship across subjects between the degree of ipsilateral deactivation and contralateral activation using fMRI. For NIRS, however, in which ipsilateral deactivations were not observed, the intersubject correlation between contralateral and ipsilateral activation to RTAP was positive, and significant for oxyHb and deoxyHb, and to LTAP for oxyHb only. It is possible that systemic interference in NIRS may mask ipsilateral deactivation or enhance activation. If a contralateral functional response is superimposed onto a bilaterally symmetric systemic response, this would result in positive correlation between left and right hemisphere activation across subjects, as we observed. This is worth further investigation, particularly as the same effect was not observed using fMRI.

As expected, the negative correlation between the amplitude of oxyHb and deoxyHb responses across subjects is high, although higher for contralateral than ipsilateral activation.

7.5 Summary

We performed group analyses of the same task in mostly the same subjects, using both functional MRI and NIRS. We used an experimental paradigm where known and robust contralateral activation could be expected, to use as a benchmark, and then focussed on investigating the ipsilateral response, about which previous studies have not reached consensus. The main findings were as follows:

- A contralateral response to unilateral tapping could reliably be found in the BOLD and oxyHb data, but not in deoxyHb.
- Consistent with previous studies in right-handers [250], in both the NIRS and fMRI data a larger ipsilateral and contralateral response to left than to right tapping was observed, and the response to left tapping was more frequently bilateral.
- The fMRI group-level ipsilateral deactivation which was particularly evident for right tapping could not be found in the NIRS data, in which bilateral activation tended to occur. However, at the individual level, deactivations were variable in both fMRI and NIRS
- No clear relationship across subjects between the degree of ipsilateral deactivation and contralateral activation was found using fMRI, but in NIRS there was high intersubject correlation between contralateral and ipsilateral activation.

In conclusion, the oxyHb response appears more reliable than the deoxyHb response. In studies of contralateral motor activation the same conclusions could be reached using either fMRI or NIRS. However, there are distinct differences in the measurement of ipsilateral activations, which are worthy of further study.

Chapter 8

Activation and deactivation to a noxious thermal stimulus

Functional MRI responses to a cold stimulus have mostly been studied in the context of pain which is thought to involve sensory, motor and cognitive components [261, 262]. Many cortical areas, including the primary and secondary somatosensory cortex (S1, S2), anterior insula and the anterior cingulate cortex, are involved in the sensation of thermal pain, as well as the thalamus. The motivational-affective component of pain is evidenced by activations in the cingulate, insula, limbic, telencephalic and prefrontal cortex resulting from projections from medial thalamic nuclei [263]. However, studies involving noxious hot and cold stimuli are characterised by a large amount of intersubject variability [264, 262].

Given the lack of consistent activation of contralateral S1 to painful stimulation, we wished to determine whether contralateral S1 and ipsilateral S2 activation would be obtained in response to a noxious cold stimulus applied to each hand, across a group of healthy subjects. We also wished to determine whether a noxious cold stimulus produces ipsilateral deactivations in S1 similar to those observed for tactile and median nerve stimulation, as well as for noxious heat [265]. The noxious heat stimulus in [265] was applied only to the right side of the body, so we wished to determine whether ipsilateral sensory deactivation is more prominent for the dominant hand (right in the case of these right-handed subjects), in the same way as has been observed for ipsilateral motor deactivation. Another goal was to establish whether there is evidence for a (particularly right) hemisphere bias for a noxious cold stimulus as has been found previously [266, 267]. Finally we investigated whether there was any relationship between the degree of activation in activated areas and ipsilaterally deactivated areas across subjects in order to try and propose a mechanism for ipsilateral deactivation.

8.1 Introduction

Tactile information from the skin is transmitted to the brain via spino-cortical tracts terminating in the contralateral thalamus, which relays it mainly to the primary somatosensory cortex (S1) of the same hemisphere [268, 269]. This contralaterally dominant representation of tactile input is present in most animal species [270, 269, 271]. Although S2 cortex and the S1 representations for head, trunk and proximal limbs commonly show bilateral responses to unilateral stimulation [272], the S1 hand region has long been thought to process predominantly contralateral input. However, there is also evidence for an ipsilateral representation of tactile stimuli [273], which may be stronger for the right (dominant) hand [272].

Sensory stimulation of body parts including the hands evokes a bilateral response in the secondary somatosensory cortex (S2) [274, 275, 276, 277, 278, 279], although ipsilateral activations are variable [272]. This is consistent with the known existence of transcallosal projections between S2 of each hemisphere in animals [272].

8.1.1 Activations and deactivations to different types of sensory stimulation

The results of imaging experiments on somatosensory processing depend on the type of sensory stimulation used, which may be purely mechanical tactile, or involve electrical stimulation of the median nerve or a noxious stimulus which may be thermal or electrical.

Tactile stimulation

Tactile stimuli are known to activate the whole contralateral primary somatosensory (S1) and S2 cortex. Ipsilateral S2 activation is not observed as frequently [280, 281, 282, 283, 284], and ipsilateral S1 activation even less so [285, 286, 273]. Although tactile stimuli have been found in some studies to activate both contra- and ipsilateral S1 and S2 [287, 286, 288], often with a stronger contralateral activation [82, 279, 289, 290], it is thought that ipsilateral tactile stimuli activate only the more posterior parts of the postcentral gyrus (subarea 2) of the S1 cortex [272]. Tactile stimuli have also been found to transiently deactivate anterior ipsilateral postcentral gyrus (area 3b) for stimulation of both left and right hands [273, 272]. In the study by Hlushchuk et al. [273], the contralateral S1 cortex (positive) response was found to be significantly longer lasting than the deactivation response in the ipsilateral rolandic cortex. Small regions of primary motor cortex (M1) were also found to be transiently deactivated in response to both ipsilateral and contralateral touch [273]. Eickhoff et al. [272] similarly found that tactile stimulation of either hand resulted in deactivation of ipsilateral areas 3b and 1, but that while tactile stimulation of the left hand deactivated ipsilateral area 2, right hand stimulation showed a positive response in the same region ipsilaterally as well as contralaterally.

Electrical median nerve stimulation

In contrast to mechanical stimulation it is possible that electrical stimulation does not evoke an ipsilateral S1 response. In a sensory evoked field study, no ipsilateral S1 response to electrical stimulation was found,

while a mechanical stimulus produced responses in both contralateral and ipsilateral S1 and bilateral S2 [291]. Similarly in fMRI, electric median nerve stimulation produces positive BOLD signal changes in the contralateral primary and bilateral secondary somatosensory areas (ipsilateral S1 area 2 and/or the posterior parietal area 5 [286], as well a decreased BOLD signal in the ipsilateral primary somatosensory cortex (S1) [292]. Decreased deoxyHb levels in contralateral S1 and increased deoxyHb levels in ipsilateral S1 in response to median nerve stimulation, have also been measured with NIRS [82]. Ipsilateral deactivation was observed in response to median nerve stimulation, but not to motor and tactile stimulation, possibly either because systemic increases in blood flow resulting from changes in heart rate during motor and tactile stimulation cancel out localised deactivation or because motor and tactile stimuli activate and deactivate neighboring ipsilateral areas which could not be spatially resolved [82]. A recent study found that in addition to deactivations in ipsilateral primary somatosensory cortex, deactivations also occurred in the ipsilateral supplementary motor area, insula, the dorsal part of the posterior cingulate cortex, and the contralateral cerebellum. These negative responses had a different time course compared to the positive responses in the opposite hemisphere, with an onset time delay of 2.4 s and a peak delay of 0.7 s [293]. This ipsilateral sensory deactivation may have a functional purpose: Kastrup et al. [292] found that the degree of negative BOLD signal change in S1 correlated with an increase in current perception threshold of the contralateral, unstimulated finger, suggesting that the ipsilateral negative BOLD response reflects somatosensory inhibition.

Painful/thermal stimulation

In comparison to tactile stimulation, which reliably activates contralateral S1 and S2, painful stimulation does not reliably activate contralateral S1 [294], although contralateral S2 is consistently activated [295]. Thalamus activation to both tactile and painful stimulation is variable. S1 activations to tactile stimuli are stronger and larger compared to painful stimuli, however, ipsilateral deactivation in S1 has been found to be larger for painful than tactile stimuli [295]. In a study of deactivations in response to thermal pain, low pain deactivated bilateral motor cortex, while high pain produced significant deactivation in ipsilateral (right) S1. The high pain condition was found to produce greater activation than low pain in many areas, although not S1, while the low pain produced deactivation in many more areas than high pain [265]. The variability of S1 activation in pain studies as well as the smaller pain-related activation in S1 compared with tactile responses may indicate that S1 is not the primary cortical processing area for pain [295].

8.1.2 Lateralisation of somatosensory processing

Although processing of both painful and nonpainful somatosensory information is thought to take place primarily in contralateral brain regions, lesions to the right, but not left, posterior parietal cortex have been reported to produce a unilateral tactile neglect syndrome. In behavioral and clinical studies the pain threshold on the left side of the body has been found to be lower and the perception of pain intensity higher than that on the right (e.g., [296, 297, 298, 299]. This has prompted investigations into a possible right-hemispheric lateralisation of pain [267, 266, 300, 301, 302].

Five imaging studies have investigated the lateralisation of pain-related activation. In a PET study using

painful thermal stimuli delivered to the right or left forearm [266], pain intensity-dependent activation was demonstrated in contralateral regions of the primary somatosensory cortex, secondary somatosensory cortex, insular cortex, and bilaterally in regions of the cerebellum, putamen, thalamus, anterior cingulate cortex, and frontal operculum without lateralisation. However, portions of the thalamus, inferior parietal cortex (BA 40), dorsolateral prefrontal cortex (BA 9/46), and dorsal frontal cortex (BA 6) exhibited right lateralised activation during both innocuous and painful stimulation, regardless of the side of stimulation [266]. Symonds et al. [267] similarly found right-lateralised activation in response to an electrical pain stimulus applied to the finger in the middle frontal gyrus (BA 9/46), anterior cingulate (BA 32), inferior frontal gyrus, medial/superior frontal gyri (BA 6/8), and inferior parietal lobule, while contralateral activations were observed in the somatosensory cortex and posterior insula, and bilateral activations in the mid/posterior insula, anterior insula, and posterior cingulate, regardless which hand was stimulated [267]. Another study [300] demonstrated right-lateralised activity to heat pain in a portion of the anterior cingulate and in the anterior insula only when pain was attended to. Bingel et al. [301] and Youell et al. [302] using painful laser stimuli found that regions in S1, S2, and insula [301, 302], and a portion of the cingulate gyrus [301] were bilaterally active during stimulation of either the left or right hand [301] or lower leg [302]. In the insula, activation in the left brain hemisphere was greater than in the right hemisphere regardless of stimulus side [302].

8.2 Methods

The methods used were the same as for the motor component of the experiment. The subjects and task are described in sections 5.1.1 on page 72 and 5.1.2 on page 72 and preprocessing and analysis in section 7.2 on page 106, only the contrasts investigated in this case were $RCOLD > FIX$, $LCOLD > FIX$, $RCOLD < FIX$, $LCOLD < FIX$, $RCOLD > LCOLD$ and $LCOLD > RCOLD$.

8.3 Results

8.3.1 Areas activated by a cold stimulus applied to each hand

Brain regions activated by a cold stimulus applied to the left or right hands are listed in table 8.1, and shown in figures 8.1 and 8.2.

Because of the many comparisons made ($RCOLD > FIX$, $LCOLD > FIX$, $RCOLD < FIX$, $LCOLD < FIX$, $RCOLD > LCOLD$ and $LCOLD > RCOLD$) statistical maps were thresholded at a conservative p threshold of 0.001 with false discovery rate (FDR) correction to account for simultaneous hypothesis testing across multiple voxels. This corresponds to a p threshold of 0.006 Bonferroni-corrected for the number of comparisons (0.001 x 6 comparisons). There was qualitatively more ipsilateral and contralateral activation to the right-hand cold stimulus than to the left-hand cold stimulus. The primary S1/M1 regions including the inferior parietal lobule, and the thalamus in both hemispheres responded to the contralateral stimulus. The ipsilateral middle/superior frontal gyrus (BA 8,9) and orbital frontal gyrus (BA 38,47) were also activated for both hands. The cuneus was activated along the midline for both tasks, and ipsilateral S1 and thalamus

RCOLD > FIX			
Contralateral area	No. voxels	MNI co-ordinates	Peak t
L SM1/ S2/ inf. par. lob. (BA3,4,40)	1275	-39 -30 63	14.2
(L insula)	35		
L insula (middle)	24	-36 0 12	6.5
L thalamus/ hippocampus	89	-24 -27 -6	7.28
L paracentral lobule	20	-6 -27 45	6.68
Ipsilateral			
R S2/ inf. par. lob. (BA 2)	291	60 -21 27	9.5
R thalamus	11	21 -27 -3	5.88
R mid./sup. frontal gyrus (BA 8,9)	40	36 33 42	6.42
R orb. frontal cortex (BA 38,47)	22	30 18 -21	8.28
Bilateral			
R,L cuneus/ calcarine/ post. cing.	569	12 -66 6	10.75
L sup. temp. gyrus (BA 39)	13	-48 -66 18	5.98
R sup. temp. gyrus (BA 39)	39	57 -60 18	6.37
L tri. inf. frontal gyrus (BA46)	76	-45 39 15	7.24
R inf. frontal gyrus (BA 46)	30	48 39 9	5.8
LCOLD > FIX			
Contralateral area	No. voxels	Co-ordinates	Peak t
R SM1/ inf. par. lob. (BA2,3,4,40)	506	42 -33 60	12.71
R mid./post. insula/ S2/ inf. par. lob.	599	48 -15 15	12.36
R thalamus	53	21 -24 3	5.62
<i>R paracentral lobule</i>		<i>9 -12 51</i>	<i>4.72</i>
Ipsilateral			
<i>L S1/ inf. par. lob. (BA2)</i>		<i>57 -21 21</i>	<i>3.85</i>
<i>L thalamus</i>		<i>-21 -27 -3</i>	<i>4.35</i>
L sup. frontal gyrus (BA 8,9)	38	-12 24 60	5.95
L orb. frontal gyrus (BA 38,47)	33	-24 15 -15	7.23
Bilateral			
R,L cuneus/ calcarine/ post. cing.	485	12 -66 6	10.51
<i>R tri. inf. frontal gyrus (BA46)</i>		<i>42 36 15</i>	<i>4.56</i>
<i>L inf. frontal gyrus (BA 46)</i>		<i>-36 42 12</i>	<i>3.28</i>

Table 8.1: BOLD activation for RCOLD > FIX and LCOLD > FIX ($p < 0.001$ FDR corrected). The notation COLD > FIX indicates a contrast testing for greater BOLD signal in the cold condition than during fixation. Regions in italics are homologous regions which were not significantly activated for both conditions at this threshold, but were activated at a less stringent p threshold of 0.05 FDR.

RCOLD vs FIX		
Left hemisphere (contralateral)	No. voxels	Peak t
oxyHb increase	20346	7.28
deoxyHb decrease	0	-
Right hemisphere (ipsilateral)	No. voxels	Peak t
oxyHb increase	0	-
deoxyHb decrease	0	-
LCOLD vs FIX		
Right hemisphere (contralateral)	No. voxels	Peak t
oxyHb increase	6590	4.56
deoxyHb decrease	0	-
Left hemisphere (ipsilateral)	No. voxels	Peak t
oxyHb increase	7	12.16
deoxyHb decrease	2	7.42

Table 8.2: NIRS activation (oxyHb increase and deoxyHb decrease) to unilateral cold stimulus applied to each hand ($p < 0.001$ FDR), clusters > 6 voxels

as well as bilateral inferior frontal gyrus (BA 46) were activated significantly at this threshold for the right cold stimulus only. For the left hand stimulus these regions were activated at a lower threshold of $p < 0.05$ (FDR corrected) as shown in italics in table 8.1, but at this threshold there was also extensive activation throughout the brain.

The same contrasts on NIRS data revealed significant activations as measured by increase in oxyHb throughout the measured contralateral sensorimotor cortex area. However, the decrease in deoxyHb in these regions was not significant. The extent of activation in voxels for each contrast is listed in table 8.2. Ipsilateral activation was negligible.

8.3.2 Regions deactivated by a cold stimulus applied to each hand

Deactivated regions are listed in table 8.3 and shown in figures 8.1 and 8.2.

For cold stimulation of the left hand, significant deactivations were observed in the ipsilateral precuneus, a large region of ipsilateral precentral and postcentral gyrus including supplementary motor area, as well as a small portion of the ipsilateral thalamus. There were also a few significantly deactivated voxels in the contralateral (right) premotor area. There were no significant regions of deactivation for cold stimulation of the right hand at the chosen significance level, but at a lower significance threshold deactivations in ipsilateral precentral and postcentral gyri and supplementary motor area were observed.

Deactivations in NIRS data (oxyHb decreases and deoxyHb increases) are listed in table 8.4. Ipsilateral sensorimotor cortex deactivation is robust, in that it is measurable in both oxyHb and deoxyHb at this threshold. Interestingly, the deoxyHb response is larger in extent and has higher t-values than the oxyHb

RCOLD < FIX			
Area	No. voxels	Co-ordinates	Peak t
<i>R SM1</i>	11	42 -18 57	5.14
<i>R SMA</i>	58	9 -12 63	6.48
<i>R S1 (BA3)</i>	9	21 -30 63	4.98
LCOLD < FIX			
Area	No. voxels	Co-ordinates	Peak t
L precuneus (BA5,7)	80	-9 -48 60	7.961
L SM1/ SMA (BA3,4,6,40)	790	-39 -9 60	8.55
R premotor (BA4,6)	6	66 -3 21	5.41
L caudate/ thalamus	6	-12 -6 15	5.07

Table 8.3: BOLD activation for RCOLD < FIX and LCOLD < FIX ($p < 0.001$ FDR corrected). The notation COLD < FIX indicates a contrast testing for smaller BOLD signal in the cold condition than during fixation, i.e. deactivation. Regions in italics are homologous regions which were not significantly activated for both conditions at this threshold, but were activated at a less stringent p threshold of 0.01 FDR.

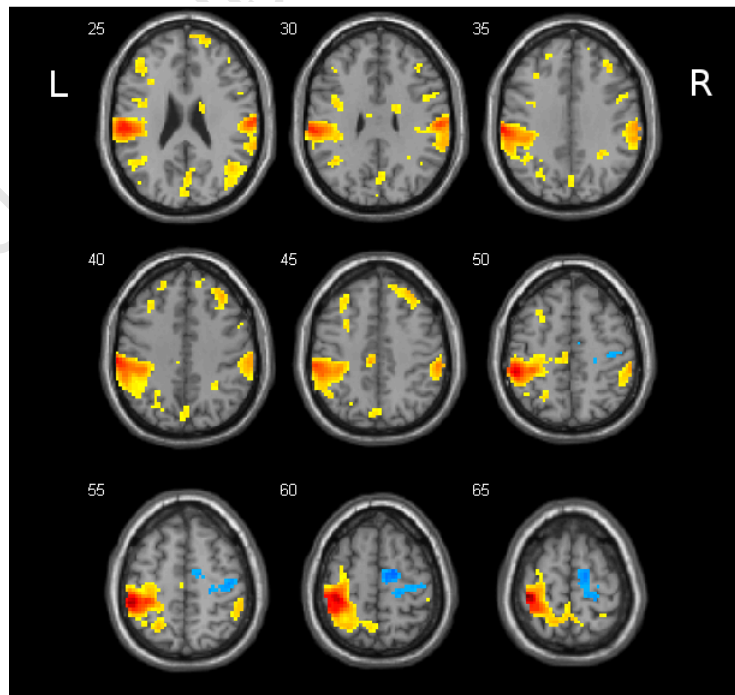


Figure 8.1: BOLD activation (orange) and deactivation (blue) for RCOLD vs FIX thresholded at $p < 0.001$.

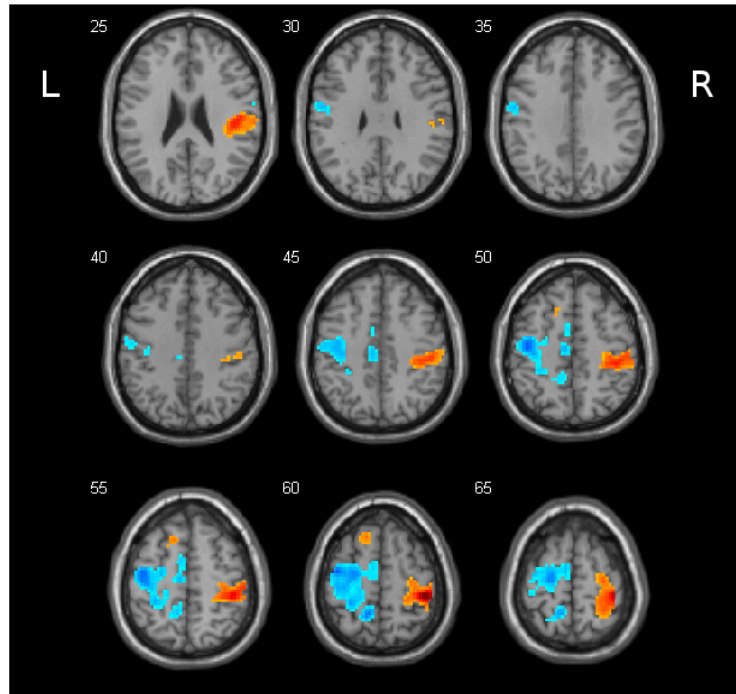


Figure 8.2: BOLD activation (orange) and deactivation (blue) for LCOLD vs FIX thresholded at $p < 0.001$.

response. The contralateral increase in deoxyHb for LCOLD is surprising, although the areas of significant increase in oxyHb and significant increase in deoxyHb are completely distinct from each other.

Figures 8.3 and 8.4 show NIRS peak regions of activation in oxyHb and deoxyHb for RCOLD and LCOLD vs FIX, respectively, transformed into MNI space and overlaid on a template brain MRI. The oxyHb activation and deactivation responses to RCOLD are comparable with those measured using fMRI, although located in more superior axial slices. Ipsilateral activation of the secondary somatosensory cortex observed with fMRI was not measurable with NIRS. The oxyHb response to LCOLD is poorly localised, with the activation peak more posterior than in fMRI and an artefactual deactivation near the ventricles, which are too deep to be assessed by NIRS. However, the direction of the concentration change is consistent with expectation and with fMRI. In deoxyHb, although no significant contralateral activation was measured, ipsilateral deactivation was robust and the deactivation peak was localised to more inferior slices than in fMRI.

8.3.3 Difference between left and right hand cold stimulus

Areas that were activated significantly differently in the left cold and right cold conditions are listed in table 8.5.

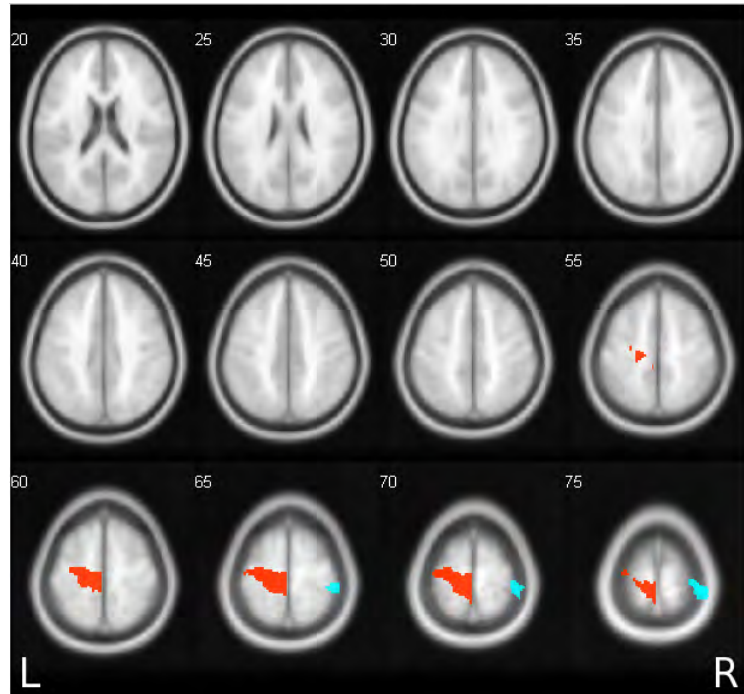
Greater activation for contralateral than ipsilateral cold stimulus was apparent in the postcentral gyrus of both hemispheres, with greater extent in the left hemisphere, as well as in the right insula and in the left cingulate gyrus.

FIX vs RCOLD		
Left hemisphere (contralateral)	No. voxels	Peak t
oxyHb decrease	0	-
deoxyHb increase	0	-
Right hemisphere (ipsilateral)		
oxyHb decrease	12141	7.28
deoxyHb increase	19949	11.61
FIX vs LCOLD		
Right hemisphere (contralateral)	No. voxels	Peak t
oxyHb decrease	0	-
deoxyHb increase	6080	5.85
Left hemisphere (ipsilateral)		
oxyHb decrease	20600	10.61
deoxyHb increase	21543	26.91

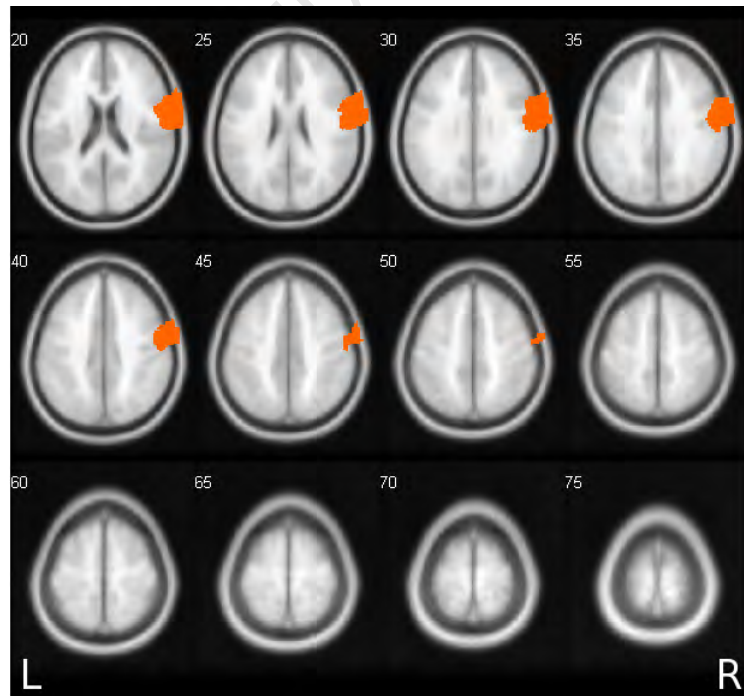
Table 8.4: NIRS deactivation (oxyHb decrease and deoxyHb increase) to unilateral cold stimulus applied to each hand ($p < 0.001$ FDR), clusters > 6 voxels

LCOLD > RCOLD			
Contralateral area	No. voxels	Co-ordinates	Peak t
R SM1 (BA3,4)	132	42 -30 60	6.99
R post. insula/ S2 (BA 13)	50	45 -18 18	6.86
<i>R cing./ SMA (BA 31)</i>		<i>9 -9 51</i>	<i>4.76 (4.20)</i>
RCOLD > LCOLD			
Contralateral area	No. voxels	Co-ordinates	Peak t
L SM1/ precuneus (BA3,4,6,5,7)	634	-39 -30 63	11.21
<i>L insula/ S2</i>		<i>-45 -24 18</i>	<i>4.75</i>
L cing./ SMA (BA31)	35	-6 -27 45	6.58

Table 8.5: BOLD activation for LCOLD > RCOLD and RCOLD < LCOLD ($p < 0.001$ FDR corrected). The notation LCOLD > RCOLD indicates a contrast testing for greater BOLD signal when the cold stimulus was applied to the left hand than when it was applied to the right. RCOLD > LCOLD indicates the reverse contrast. Regions in italics are homologous regions which were not significantly activated for both conditions at this threshold, but were activated at a less stringent p threshold of 0.05 FDR.

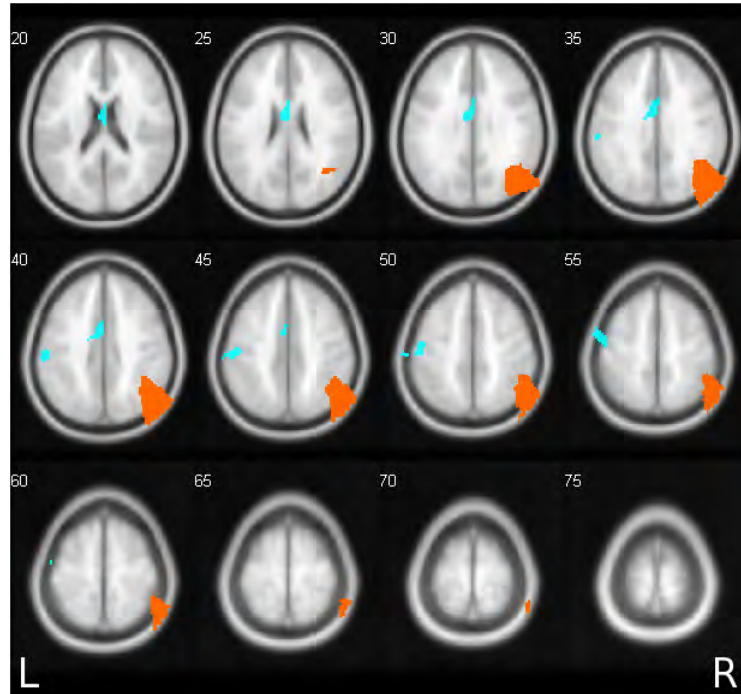


(a) OxyHb activation (orange) and deactivation (blue) for RCOLD vs FIX

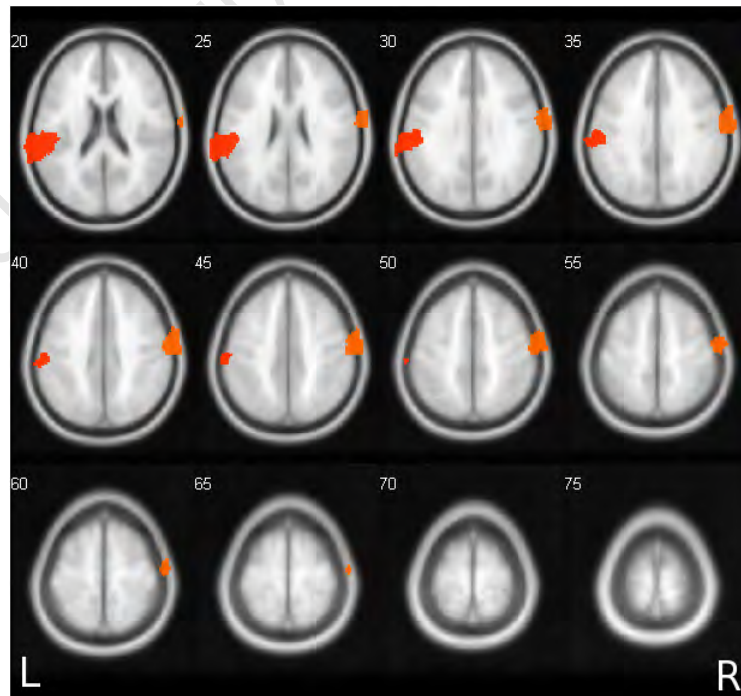


(b) DeoxyHb deactivation (orange) for RCOLD vs FIX

Figure 8.3: Thresholded NIRS maps of $\text{RCOLD} > \text{FIX}$ (orange) and $\text{RCOLD} < \text{FIX}$ (blue) transformed into MNI space and overlaid on a template brain MRI. The notation $\text{RCOLD} > \text{FIX}$ indicates a contrast testing for greater oxyHb or deoxyHb in the RCOLD than in the fixation condition. $\text{RCOLD} < \text{FIX}$ indicates the reverse contrast. Note significant ipsilateral deactivation but no contralateral activation for deoxyHb.



(a) OxyHb activation (orange) and deactivation (blue) for LCOLD vs FIX



(b) DeoxyHb ipsilateral (red) and contralateral (orange) deactivation for LCOLD vs FIX

Figure 8.4: Thresholded NIRS maps of LCOLD > FIX (orange) and LCOLD < FIX (blue) transformed into MNI space and overlaid on a template brain MRI. The notation LCOLD > FIX indicates a contrast testing for greater oxyHb or deoxyHb in the LCOLD than in the fixation condition. LCOLD < FIX indicates the reverse contrast. Note significant bilateral deactivation but no contralateral activation for deoxyHb.

LCOLD > RCOLD		
Left hemisphere	No. voxels	Peak t
deoxyHb	16379	5.27
Right hemisphere		
oxyHb	11368	5.91
RCOLD > LCOLD		
Left hemisphere	No. voxels	Peak t
oxyHb	20569	6.07
Right hemisphere		
deoxyHb	0	

Table 8.6: Number of voxels activated for LCOLD > RCOLD and RCOLD > LCOLD (FDR corrected $p < 0.001$). The notation LCOLD > RCOLD indicates a contrast testing for greater oxyHb or deoxyHb signal when the cold stimulus was applied to the left hand than when it was applied to the right. RCOLD > LCOLD indicates the reverse contrast.

The hemisphere and extent of areas that were found by NIRS to be significantly differently activated in the left and right cold conditions are listed in table 8.6. Because activation corresponds to a decrease in deoxyHb, deoxyHb concentration is greater in the hemisphere ipsilateral to the tapping hand (that is, there is a contralateral decrease). There is a larger area of left hemisphere than right that is activated significantly more by contralateral than ipsilateral cold stimulus. In fact, there are no voxels in the right hemisphere where deoxyHb is significantly smaller for contralateral than ipsilateral stimulus.

8.3.4 Investigation of activation asymmetry: effect of stimulus side and hemisphere of activation

The results of the analysis in table 8.5 do not indicate whether the apparent right lateralised activation in the insula for LCOLD > RCOLD and the left lateralised activation for the cingulum in the RCOLD > LCOLD comparisons indicate hemispheric/hand bias or activation which is below the significance threshold in the other hemisphere.

In order to test for contralateral or laterally biased activation, the ROIs shown in table 8.7 were extracted from the analyses in tables 8.1, 8.3 and 8.5. For NIRS the regions of interest encompassed the entire measured area.

Two factor repeated measures ANOVA on ROI data

Table 8.7: Results of two way ANOVA with factors hemisphere and hand for selected fMRI ROIs. Because 15 comparisons were made a p value of $0.05/15=0.003$ was required for significance. Significant effects are shown in bold. Effects that are not significant at the corrected p threshold but are significant at $p<0.05$ uncorrected are marked with an asterisk.

Contralateral area	Co-ordinates	Factor	F	p
SM1 (activation peak)	39 -33 60	Hand	1.173	0.2985
		Hemisphere	68.971	0.00001
		Interaction	0.000	0.9941
SM1 (deactivation peak)	39 -12 60	Hand	0.319	0.5816
		Hemisphere	51.799	0.00001
		Interaction	0.739	0.4055
S2	60 -21 27	Hand	1.729	0.2113
		Hemisphere	6.176	0.0273*
		Interaction	0.035	0.8539
Post. insula	48 -15 15	Hand	0.638	0.4387
		Hemisphere	46.820	0.00001
		Interaction	5.711	0.0327*
Mid. insula	42 -3 6	Hand	0.147	0.7073
		Hemisphere	1.914	0.1898
		Interaction	11.580	0.0047*
Thalamus	21 -24 0	Hand	0.347	0.5660
		Hemisphere	8.970	0.0103*
		Interaction	1.847	0.1973
Paracentral lobule	6 -27 45	Hand	2.385	0.1465
		Hemisphere	16.267	0.0014
		Interaction	7.622	0.0162*
Inf. par. lobule	63 -30 30	Hand	3.501	0.0840
		Hemisphere	0.426	0.5252
		Interaction	0.757	0.4000
Sup. frontal gyrus	12 24 60	Hand	0.910	0.3575
		Hemisphere	2.157	0.1657
		Interaction	0.934	0.3513
Inf. frontal gyrus (BA 38,47)	27 15 -18	Hand	1.275	0.2792
		Hemisphere	1.091	0.3152
		Interaction	2.980	0.1080
Mid. frontal gyrus (BA 8,9)	36 33 42	Hand	1.847	0.1972
		Hemisphere	1.164	0.3003
		Interaction	0.330	0.5753

CHAPTER 8. ACTIVATION AND DEACTIVATION TO A NOXIOUS THERMAL STIMULUS

Inf. frontal gyrus (BA 46)	45 39 12	Hand	3.614	0.0797
		Hemisphere	3.639	0.0788
		Interaction	0.001	0.9749
Sup. temp. gyrus	51 -63 18	Hand	1.370	0.2629
		Hemisphere	0.664	0.4298
		Interaction	0.246	0.6283
Sup. parietal lobule	30 -51 63	Hand	1.023	0.3303
		Hemisphere	8.279	0.0130*
		Interaction	6.866	0.0212*
Precuneus	9 -51 66	Hand	5.053	0.0426*
		Hemisphere	4.077	0.0646
		Interaction	1.344	0.2671

To account for the 15 fMRI regions tested, a p-value of $0.05/15=0.003$ was required for significance. As can be seen from table 8.7, the interaction of hand and hemisphere approached significance in the middle and posterior insula, paracentral lobule and superior parietal lobule. A significant effect of hemisphere (contralateral > ipsilateral) was found for the two regions of the postcentral gyrus (SM1), the posterior insula and the paracentral lobule and approached significance in the thalamus, S2 and superior parietal lobule. No significant effect of stimulus side was found, although this effect approached significance in the precuneus. No significant effects of hemisphere, stimulus side or their interaction were found for the superior, middle or inferior frontal gyri, inferior parietal lobule or superior temporal gyrus. Thus no evidence was found for right hemisphere lateralisation in the superior, middle or inferior frontal gyri or the inferior parietal lobule.

This suggests that activation and deactivation in S1 to a noxious cold stimulus has a contralateral bias, as does activation in the posterior insula and paracentral lobule. Although the thalamus and S2 show a tendency for contralateral bias this is not significant, suggesting that activation may be bilateral. From the plot (figure 8.5) it can be seen that there is little difference between contralateral and ipsilateral activation for RCOLD particularly. The interaction present in the middle insula suggests that its activity may be right lateralised for stimuli to left and right hands.

Although the effect was not significant, there is a tendency for an effect of hand in the inferior parietal lobule, the inferior frontal gyrus, and the precuneus. To investigate this further, the simple main effects of hand (stimulus side) were tested separately for contralateral and ipsilateral hemispheres in a voxelwise analysis (described in 7.2.3 on page 109).

For the NIRS data a p-value of 0.05 was required for significance. As shown in table 8.8, the main effects of hemisphere of activation and hand were both significant for both oxyHb and deoxyHb indicating a larger increase in oxyHb and decrease in deoxyHb (activation) for contralateral stimulation as well as a larger activation for right than left cold stimulus, particularly contralaterally. However, as can be seen in figure 8.6, the mean parameter estimate for deoxyHb in the right hemisphere for LCOLD is positive, indicating an average deactivation rather than activation to the contralateral stimulus, in deoxyHb only, although not

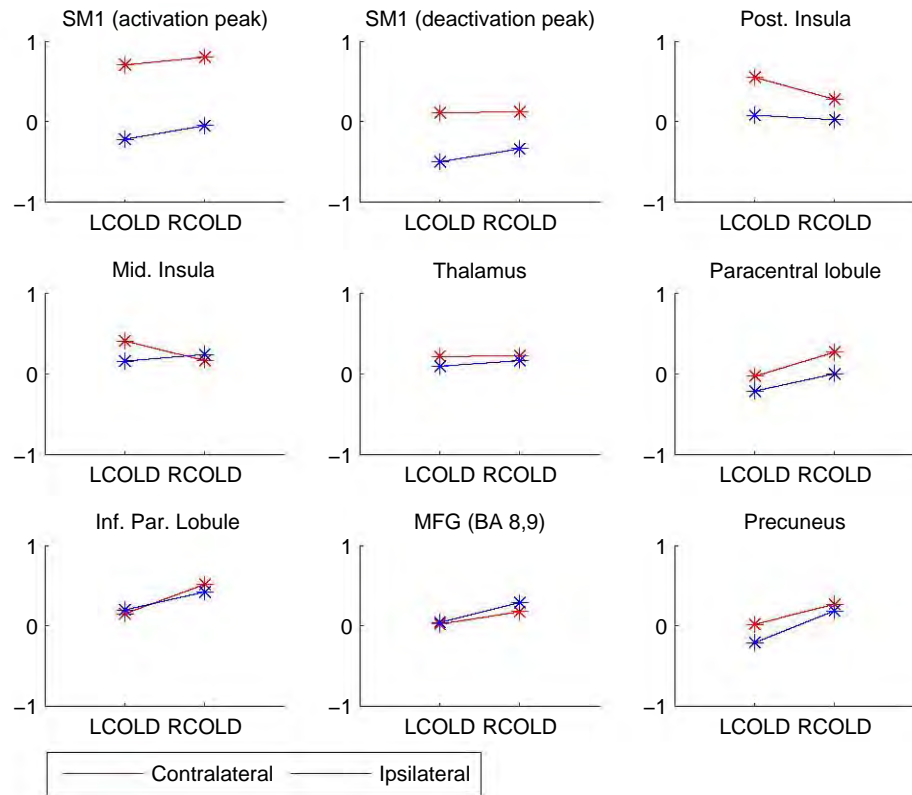


Figure 8.5: Mean BOLD effect for right cold (RCOLD) and left cold (LCOLD) conditions in contralateral and ipsilateral ROIs

OxyHb			
df	Factor	F	p
14	Hand	8.944	0.0097
	Hemisphere	220.964	0.0000
	Interaction	0.297	0.5945
DeoxyHb			
df	Factor	F	p
14	Hand	86.711	0.0000
	Hemisphere	221.192	0.0000
	Interaction	2.542	0.1332

Table 8.8: Results of two way ANOVA with factors hemisphere and hand for selected NIRS ROIs. A p value of 0.05 was required for significance. Significant effects are shown in bold.

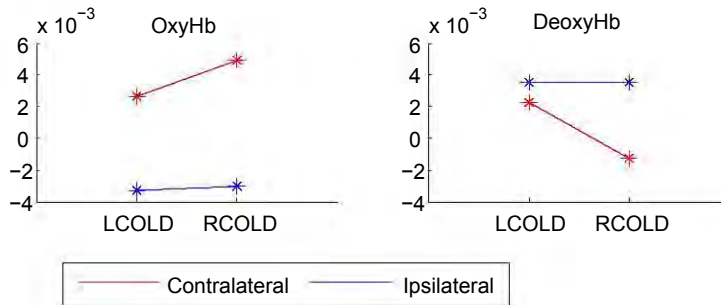


Figure 8.6: Mean NIRS parameter estimates for oxyHb and deoxyHb in sensorimotor area, used in two-way ANOVA

RCOLD > LCOLD				
Hemisphere	Region	Co-ordinates	Voxels	Max t
Contra	Paracentral lobule	-3 -27 45	16	4.9632
Contra	Inf. par. lobule/ supramarginal (BA2,40)	-60 -30 39	72	5.8323
Ipsi	Inf. par. lobule / supramarginal (BA40)	63 -39 27	15	4.6201
Ipsi	SM1 (BA3,4)	57 -15 36	14	4.6201
Ipsi	Sup. parietal lobule	30 -51 63	11	4.4372
Ipsi	Precuneus (BA5,7)	9 -51 66	15	9 -51 66
LCOLD > RCOLD				
No significant regions				

Table 8.9: Test for dominant response to a cold stimulus applied to one hand in contralateral and ipsilateral hemispheres, where LCOLD images were flipped about the x-axis ($p < 0.05$ FDR). The notation RCOLD > LCOLD indicates a contrast testing for greater BOLD signal when the cold stimulus was applied to the right hand than when it was applied to the left.

as great as in the ipsilateral hemisphere. Although the difference is small, the significantly larger ipsilateral activation for RCOLD in oxyHb and deoxyHb can be interpreted as a greater ipsilateral deactivation to LCOLD than RCOLD.

Voxelwise statistics using flipped images

The results of a voxelwise analysis on flipped images testing for the simple main effects of hand for contralateral and ipsilateral hemispheres separately are shown in table 8.9. There was a significantly greater response to right cold than to left cold in ipsilateral and contralateral supramarginal gyrus, as well as in ipsilateral precuneus, superior parietal lobule and postcentral gyrus. The contralateral paracentral lobule was also more activated for right than left cold. There were no regions in which there was significantly more ipsilateral or contralateral activation for left cold than for right cold.

The interpretation of this is that the right hemisphere supramarginal gyrus, superior parietal lobule, postcentral gyrus and precuneus are more activated for right cold than the same regions in the left hemisphere

	Contralateral	S1	Inf. Par.	S2	Thalamus	Max overlap
Ipsilateral	MNI co-ords	-39 -30 63	-51 -36 54	-57 -21 21	-24 -27 -6	-36 -24 57
Precuneus	15 -42 57	0.77	0.5	0.74	0.84	0.65
M1	42 -18 57	0.87	0.49	0.69	0.85	0.81
SMA	9 -12 63	0.84	0.38	0.65	0.88	0.77
S1	21 -30 63	0.86	0.41	0.69	0.88	0.78
Max overlap	36 -24 57	0.78	0.4	0.64	0.82	0.7

Table 8.10: Pearson correlation between ipsilaterally deactivated ROIs and contralaterally activated ROIs for RCOLD. Correlations in bold are significant at $p < 0.002$ ($p < 0.05$ corrected for 25 comparisons)

are for left cold. Also, activation in the left hemisphere supramarginal gyrus and paracentral lobule during right cold are greater than the same regions in the right hemisphere during left cold. Therefore, although activation in the primary somatosensory area is contralateral, there is significantly greater ipsilateral (right hemisphere) activation for RCOLD than there is for LCOLD.

This confirms in a quantitative manner the qualitative observation of more widespread ipsilateral activation for the right cold than left cold condition. However, because greater activation for right than left cold could result from larger deactivation for left cold or increased activation for right cold, the RCOLD > LCOLD_flipped contrast was masked with the RCOLD > FIX contrast and LCOLD_flipped < FIX contrast respectively to determine whether one of these effects was responsible for the observed differences between right and left cold stimulation. In the RCOLD > LCOLD_flipped contrast ($p < 0.05$ FDR) masked with RCOLD > FIX ($p < 0.001$ uncorrected) a region of contralateral inferior parietal lobule was significant implying that the contralateral inferior parietal lobule has significantly greater activation for right than left cold. In the RCOLD > LCOLD_flipped contrast ($p < 0.05$ FDR) masked with LCOLD_flipped < FIX ($p < 0.001$ uncorrected), the ipsilateral precuneus was significant, suggesting that ipsilateral deactivation in the precuneus is greater for left than right sided stimulation. For the remaining areas it is not possible to establish whether the asymmetry between the left and right cold conditions resulted from increased activation for right cold or decreased activation for left cold.

8.3.4.1 Intersubject correlations

Regions of interest for the correlation analysis were selected from ipsilaterally deactivated and contralaterally activated brain areas for the left and right cold conditions separately. Where a large cluster was found in the activation analysis encompassing several relevant regions (for example S1 and S2), local maxima within the cluster were used as centres for the ROIs. In addition an area of “maximum overlap” was created for each hemisphere whose centre was the co-ordinate (reflected about the x-axis) which has the largest amount of ipsilateral deactivation and contralateral activation (the peak voxel resulting from a conjunction of contralateral activation and ipsilateral deactivation when one of these was flipped along the x-axis). The results of the correlation analysis for RCOLD and LCOLD are shown in tables 8.10 and 8.11 respectively.

	Contralateral	S1	Inf Par	S2	Thalamus	Max overlap
Ipsilateral	MNI co-ords	42 -33 60	51-30 27	48 -15 15	21 -24 3	33 -24 57
Precuneus	-9 -48 60	0.38	0.6	0.51	0.55	0.59
M1	-42 -15 51	0.38	0.69	0.66	0.83	0.69
SMA	-18 -15 66	0.63	0.51	0.58	0.67	0.61
S1	- 27 -36 57	0.47	0.6	0.59	0.78	0.75
Max overlap	-33 -24 57	0.26	0.56	0.55	0.78	0.65

Table 8.11: Pearson correlation between ipsilaterally deactivated ROIs and contralaterally activated ROIs for LCOLD. Correlations in bold are significant at $p < 0.002$ ($p < 0.05$ corrected for 25 comparisons)

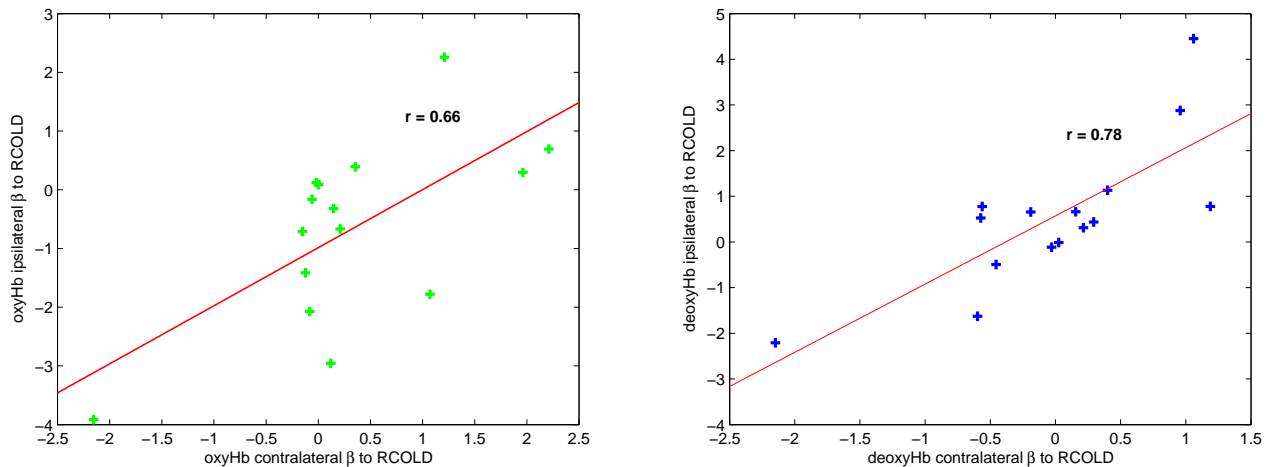


Figure 8.7: Correlation across subjects between mean β parameter estimates for RCOLD in contralateral and ipsilateral ROIs for oxyHb and deoxyHb.

For the right cold stimulus activity in the contralateral S1 and thalamus was significantly correlated with ipsilateral deactivated regions. For the left cold condition contralateral thalamus activity was correlated with deactivation in the M1, S1 and 'maximum overlap' ROIs. Activity in S2 was not significantly correlated with ipsilateral deactivation in either condition.

For NIRS, the intersubject correlation (figure 8.7) between the mean activation to RCOLD in a contralateral and ipsilateral ROIs of the 65 most de/activated voxels was $r = 0.66$ for oxyHb and $r = 0.78$ for deoxyHb which were both significant at $p < 0.05$ (two tailed). The intersubject correlation between the mean activation to LCOLD in a contralateral and ipsilateral ROI was $r = 0.33$ for oxyHb ($p > 0.05$) and $r = 0.86$ for deoxyHb ($p < 0.05$).

8.3.4.2 Between subject variability of activation and deactivation in fMRI and NIRS

Because activations to a cold stimulus have been reported to be variable among subjects [264, 262], and deactivations appear to be even more variable, we attempted to investigate how frequently these effects occur in our subjects.

Multi-subject conjunction analysis In the fMRI data, using multi-subject conjunction analysis on a fixed effect first level analysis for LCOLD > FIX, RCOLD > FIX, LCOLD < FIX and RCOLD < FIX, we tested the intermediate null hypothesis of $k=6$, that is that less than 7 subjects activate with a lenient threshold of FDR 0.05. There were no regions that exceeded the threshold for significance in any of the contrasts (activation or deactivation), suggesting that fewer than half the subjects show this effect. This supports the idea that activations to noxious stimulation are variable and suggests that deactivations may be as variable between subjects.

Individual ipsilateral deactivation Examining subject's individual fMRI activation maps for ipsilateral deactivation at a p threshold of 0.001 uncorrected only 5 subjects showed a significant deactivation cluster anywhere in the left hemisphere for LCOLD and 1 subject showed a significant deactivation cluster anywhere in the right hemisphere for RCOLD. This suggests that these deactivation effects in addition to occurring only in some subjects are generally very small effects and show up in a group analysis better than in individual subjects.

Individual ipsilateral activation Examining subject's individual fMRI activation maps for ipsilateral activation at a p threshold of 0.001 uncorrected only 4 subjects showed a significant activation cluster anywhere in the left hemisphere for LCOLD and 4 subjects showed a significant activation cluster anywhere in the right hemisphere for RCOLD. However, 6 subjects also showed no contralateral activation for LCOLD and 4 subjects showed no contralateral activation for RCOLD.

A summary of oxyHb and deoxyHb responses by number of subjects in which a response was measurable is shown in table 8.12. The responses were extremely variable, and in most subjects activation was not found. The correlation across subjects between parameter estimates for oxyHb and deoxyHb was $r = -0.44$ ($p > 0.05$ two tailed) for contralateral activation and $r = -0.52$ ($p < 0.05$ two tailed) for ipsilateral deactivation ($n=15$) to RCOLD and $r = -0.60$ ($p < 0.05$) for contralateral activation and $r = -0.33$ ($p > 0.5$) for ipsilateral de/activation to LCOLD.

OxyHb				
	Bilateral response	Contra. response only	Ipsi. response only	No response
LCOLD > FIX	1	4	1	9
RCOLD > FIX	4	3	0	8
LCOLD < FIX	1	0	4	10
RCOLD < FIX	3	1	2	9
DeoxyHb				
	Bilateral response	Contra. response only	Ipsi. response only	No response
LCOLD < FIX	0	1	1	13
RCOLD < FIX	2	3	0	10
LCOLD > FIX	2	2	3	8
RCOLD > FIX	4	0	0	11

Table 8.12: Summary of individual subject activations and deactivations in SM1 region for each contrast. The notation COLD < FIX indicates a contrast testing for smaller signal in the cold condition than during fixation and the notation COLD > FIX indicates a contrast testing for greater signal in the cold condition than during fixation.

8.4 Discussion

8.4.1 Activation of contralateral and ipsilateral somatosensory areas (S1 and S2)

Contralateral S1 activation was found in response to a cold stimulus applied to either hand. Although S1 activation to a noxious stimulus is inconsistent [303, 294], and has been found in meta-analyses to be present in only about half of studies on pain [304, 305], the observed contralateral activation is consistent with several studies that have found contralateral S1 responses to noxious stimulation ([306] provides a comprehensive review). Some fMRI studies on painful stimulation have also reported bilateral activation following unilateral stimulation [263, 307, 308]. Cognitive modulation, inhibitory processes, and methodological differences may be reasons for this discrepancy [294, 91]. In fact, cold stimulation with an ice pack includes a tactile component which may be at least partially responsible for the contralateral activation observed in this study.

We also found activation of contralateral S2 as well as ipsilateral S2, which was significant only for stimulation of the right hand. However, no significant main effects of hand or hemisphere were found for S2 in the ROI analysis, suggesting that S2 activation may be bilateral. In other studies of pain activation of insular and S2 cortices had been found to be primarily contralateral to stimulation but also ipsilateral [304], which agrees with our results. Consistent with [301] and [267] we found contralaterally dominant activation in the posterior insula.

In NIRS only contralateral activation was found, indicating that the measured area was indeed SM1.

In a similar manner to S2, unilateral cold stimulation of the hand appeared to activate predominantly contralateral thalamus, with an additional significant ipsilateral activation for the right hand cold stimulus.

However, in the ROI analysis hemispheric differences did not reach the significance threshold. Thalamic activation may be bilateral with a more prominent contralateral response. It is known that thalamus activation to both tactile and painful stimulation is variable [295], and a higher resolution investigation which allows separate examination of the lateral and medial parts of the thalamus may be more illuminating.

8.4.2 Deactivation in response to cold stimulation

Ipsilateral deactivation occurred in the primary sensory, motor and premotor regions, as well as the supplementary motor area, parietal lobule and precuneus. This effect was significant only for the left hand cold stimulus at the selected threshold, but similar regions were found for the right hand stimulus at a lower significance level. Ipsilateral deactivation was also found using NIRS, with a significantly greater deactivation for cold applied to the left hand than to the right. Unlike [273], no contralateral regions were deactivated except a small premotor region for the left hand cold stimulus. Also no evidence was found for ipsilateral S1 activation for the right hand as in [272], however, the spatial resolution or smoothing used may have hidden any activations with a very small spatial extent.

This ipsilateral SM1 deactivation confirms that a noxious cold stimulus produces similar deactivations to those that have been found for tactile [273, 272], electric median nerve [82, 292, 293], painful [295] and noxious heat [265] stimulation. Ipsilateral supplementary motor area deactivation was also reported in [293], however, our results using cold stimulation differ from this study as the ipsilateral insula was not found to be significantly activated, and deactivation was found in the precuneus rather than the dorsal part of the posterior cingulate cortex.

We expected to find ipsilateral somatosensory cortex deactivations to a noxious cold stimulus because ipsilateral deactivation to pain has been found to be larger than that for tactile stimuli [295], while tactile stimuli produce greater S1 activation. In [265], ipsilateral S1 was also been found to be deactivated in response to a high pain, but not a low pain condition.

To our knowledge, there are only two previous studies on painful or noxious thermal stimulation using DOT [91, 290]. The stimulation used in these cases was noxious heat, rather than cold, and bilateral activation in S1 was found, rather than ipsilateral deactivation.

8.4.3 Pathways for ipsilateral deactivation

Similarly to ipsilateral motor deactivation found in fMRI studies [240, 250, 241, 243, 244], ipsilateral S1 deactivation could result from transcallosal inhibition by contralateral S1. Other possibilities are direct uncrossed afferent projections to ipsilateral S1 [309] or input from higher-level processing areas such as S2 [310, 311]. Although interhemispheric connections between the hand regions in S1 are sparse [312, 313, 314, 315], the mechanism for deactivation has been proposed to be via area 2 which has the densest connections [313, 316, 317, 273]. Deactivation of areas 3b and 4 would occur via corticocortical projections from BA 2 to areas 3b and 4 [273].

Alternatively, since the hand representation in area 3b appears to lack direct thalamic inputs by the ipsilateral

hand, and has few callosal connections [312, 313] whereas transcallosal connections are known to exist between S2 in the different hemispheres, the ipsilateral deactivation might be mediated by an input from contralateral S2 to ipsilateral S2 and then to S1 [292]. The results of fMRI studies on callosotomised subjects suggest that ipsilateral S2 activations to touch [318], but not pain [289], are mediated by callosal connections, and S2 regions are also known to have connections with both contralateral and ipsilateral areas of S1 [319, 320].

8.4.4 Lateral asymmetry of activations and deactivations

Ipsilateral deactivation of sensorimotor cortex appears with larger magnitude and volume of activation in the M1 ipsilateral to movement for the right, dominant hand than for the left hand in right-handed subjects [250, 244, 259]. Because of the greater significance and extent of deactivations in the left hemisphere to stimulation of the left hand, we were interested to know whether there was a significant difference between ipsilateral deactivation to stimulation of the dominant (right) or non-dominant hand. Using a region of interest centred around the peak of deactivation in each hemisphere, which was situated somewhat anteriorly to the corresponding activation peak in the opposite hemisphere we found that, as expected, there was a significant effect of hemisphere, where deactivation was stronger for the ipsilateral hemisphere, but there was no significant main effect of hand of stimulation.

Although there was no significant difference in contralateral activation measured with fMRI, using NIRS contralateral activation to the right hand stimulus was greater than activation to the left hand stimulus. This is consistent with the more widespread activation noted from fMRI for right hand stimulation. Similarly, using NIRS greater ipsilateral deactivation was found for the left hand stimulus.

Investigating the ipsilateral and contralateral hemispheres separately, significantly less deactivation (or greater activation) was present for right cold in ipsilateral superior and inferior parietal lobule (BA 40), SM1 (BA 3,4) and precuneus (BA 5,7). The intersection of these regions with regions that significantly deactivated compared to fixation revealed a larger ipsilateral deactivation in the precuneus to the left hand stimulus. In the hemisphere contralateral to stimulation, there was greater activity to the right cold stimulus in the paracentral lobule and inferior parietal lobule (BA 2,40). Because no behavioural data was collected it is not clear whether the experience of noxious stimulation was the same for both hands, which would influence the apparent asymmetry of activations to stimulation of the dominant compared to the non-dominant hand.

The greater extent of significant activation for stimulation of the right (dominant) hand and greater deactivation for stimulation of the left hand, mirrors the effect found in the motor system, where non-dominant hand action produces a larger extent of activation, ipsilaterally as well as contralaterally [321], and dominant hand action more often produces deactivation [250, 244, 259]. Studies on the lateralisation of thermal pain have found that the perceived intensity of heat [297, 298] and cold [298, 322] pain applied to the left hand is higher than that of the right. It has been suggested that the right hemisphere is less efficient than the left in processing cutaneous sensory input, but is dominant for emotional experience resulting in a left-sided dominance for pain [323]. Our findings in right-handed subjects appear to indicate the opposite, with stronger, or more consistent responses to right-sided cold stimulation in the left hemisphere.

The only evidence for right hemispheric bias in fMRI was found in the middle insula, which was more activated

on the right for both left and right hand cold stimulation. The insula has usually been found to be activated bilaterally to pain [301, 302, 267], although one study found greater activation in the left brain hemisphere than in the right hemisphere regardless of stimulus side [302], and another found right-lateralised activity to heat pain in a portion of the anterior cingulate and in the anterior insula only when pain was attended to [300]. These differences may arise because of different definition of regions of interest within the insula.

8.4.5 Relation between activations and deactivations

We found significant positive relationships between contralateral S1 and thalamus activation and ipsilateral deactivation for the RCOLD condition, and significant positive correlation between contralateral thalamus and ipsilateral SM1 in the LCOLD condition. This, however, suggests that increased contralateral activity corresponds to increased ipsilateral activation, that is to say decreased deactivation. The interpretation of this is not certain as, if contralateral regions were responsible for inhibiting ipsilateral regions, the expected direction of the correlation would be negative.

8.5 Summary

We investigated the response to noxious thermal stimulation in mostly the same subjects, using both functional MRI and NIRS. This task has not previously been studied using NIRS, and we were able to confirm our group level results using fMRI. The main findings of our group analysis of the response to noxious stimulation in fMRI and NIRS were:

- Using fMRI, contralateral S1 activation and bilateral S2 activation was found in response to a cold stimulus applied to either hand. In NIRS however, only a contralateral response was observed, in oxyHb but not in deoxyHb.
- In fMRI data there was qualitatively more contralateral and ipsilateral activation for a right-hand cold stimulus than the left-hand cold stimulus, and significantly greater ipsilateral activation for the right hand stimulus in primary somatosensory regions. Similarly, using NIRS a larger activation (oxyHb increase and deoxyHb decrease) was found for right than left cold stimulus.
- Ipsilateral deactivation at the group level was particularly evident for left-hand cold stimulation in the fMRI data. In NIRS, robust ipsilateral deactivation in both oxyHb and deoxyHb was observed in both hemispheres. In agreement with the fMRI data, this was greater in extent and magnitude to the left-hand stimulus.
- Across subjects, the activation in ipsilateral and contralateral S1 regions to RCOLD were positively correlated in the fMRI, oxyHb and deoxyHb data. However, the correlation between the mean activation to LCOLD in a contralateral and ipsilateral ROI was significant in deoxyHb but not oxyHb or BOLD.

CHAPTER 8. ACTIVATION AND DEACTIVATION TO A NOXIOUS THERMAL STIMULUS

Surprisingly, the ipsilateral deactivation response to a cold stimulus in deoxyHb is more reliably measured than the deoxyHb activation response. The results obtained from the fMRI and NIRS experiments correspond well.

University of Cape Town

Chapter 9

Task-related changes in brain functional connectivity

The aim of this chapter was to examine task-related changes in steady-state, particularly interhemispheric, connectivity during sensory and motor tasks in both fMRI and NIRS, compared to connectivity at rest. Although there have been some studies considering connectivity changes during finger tapping using BOLD fMRI [324, 325], we were particularly interested in the modulation of connectivity during unilateral tapping and cold stimulation between those sensorimotor regions that were activated and those that were deactivated by the sensory and motor tasks, RCOLD and RTAP. (These regions were identified in chapters 7 and 8.) In addition, for both fMRI and NIRS we used a technique for removal of physiological noise [326], which can confound functional connectivity measurements, particularly task-related connectivity, during which there may be simultaneous changes in systemic variables.

9.1 Introduction

There has been a surge of recent interest in the spontaneous fluctuations of cerebral haemodynamics in the low frequency range (below 0.1 Hz). A large number of studies have succeeded in mapping functionally connected networks in the resting human brain, based on low frequency correlations [48] observed using both fMRI [327] and more recently NIRS [328, 329, 330, 331, 332]. Several functional systems have been identified in this way; for example, the same areas that are activated using a conventional fMRI motor task can be identified from the correlations they exhibit at low frequencies, even when the subject is at rest [327].

Other functional networks that show coherence across separated brain regions, include those for the visual [26, 333], sensory [42], motor [327, 42], and language [334] systems, as well as dorsal and ventral attention streams [335]. It should be noted that some of these regions are not only functionally, but also symmetrically, and presumably vascularly, related. Sets of regions that show coherent fluctuations have been termed resting state networks, and several may coexist simultaneously [41]. It has been shown that networks are consistent

across healthy subjects [336], but that they are frequently disrupted in conditions such as multiple sclerosis [337], Alzheimer’s disease [338, 339], schizophrenia [340, 341, 342], autism [343], depression [344], blindness [345] and attention deficit hyperactivity disorder [346].

It has been suggested that spontaneous activity may have similar patterns to those evoked by specific tasks because spontaneous oscillations recall previous simultaneous use of brain areas, coordinate neuronal activity, or predict expected brain use [335]. However, some authors have pointed out that the consistency of resting state networks across subjects may not necessarily reflect a neuronal origin: oscillations could instead result from changes in local physiology or vasculature [40, 336], or autonomic modulations of cerebral blood flow [41].

9.1.1 Functional connectivity in the default-mode network

Functional connectivity has also been used to define networks that are not associated with defined functions. For example Margulies et al. [347] identified separate networks via their correlation with different parts of the anterior cingulate which are suspected to be functionally distinct. Raichle et al. [246] have also described a connected “default-mode” network (DMN) which includes the posterior (PCC) and ventral anterior cingulate cortex (vACC), the hippocampus and the bilateral inferior parietal cortex. Regions belonging to this network also consistently show BOLD deactivation during demanding cognitive tasks when compared to rest [247]. Greicius et al. [247] also found that during the resting state the default mode network showed an inverse correlation with brain regions that show task-related increases in brain activity, and hypothesised that activation of these other regions would suspend connectivity in the default mode network. However, default network connectivity during a visual processing task was the same as during rest, and the PCC and vACC components were not deactivated by the task. The authors suggest that this is because the default mode network is not disrupted by undemanding sensory processing tasks.

Fransson [348] subsequently compared the spontaneous activity during rest and during a continuous working memory task in which the default network does show deactivation. Low frequency spontaneous activity in the default-mode network was still present during the working memory task, but was reduced in spatial extent as well as in spectral power. However, Hampson [349] found that in a demanding working memory task the default network functional connectivity was not decreased. In fact, increased default mode connectivity *during* the task was associated with better task performance. Recently Newton et al. [350] have shown connectivity within the memory and default mode networks to increase with increasing cognitive load, while the dorsal posterior cingulate becomes increasingly negatively correlated with the task-positive memory network. Correlations in the default network are stronger during fixation and eyes open rest than in eyes closed rest or a semantic classification task [351], and decrease during sad mood induction [352] and listening tasks [353]. Activity in the default mode network has been shown to decrease significantly with age [354] even after correction for grey matter volume. The reduced activity also correlates with degree of age-related cognitive decline.

Thus far, the existence of a correlated “default mode” network has been attributed primarily to neurophysiological activity. However, it does not seem impossible that vascular symmetry could result in interhemispheric

correlated fluctuations, even though the blood supply is via different cerebral arteries. The regions constituting the default mode network are also known to be some of the most densely vascularised in the brain. Their deactivation, in BOLD terms, during goal-directed tasks could be a consequence of this. Blood flow could be diverted from these regions to supply some other metabolically active region. It is not strictly necessary that a decrease in blood flow to a region be a consequence of decreased activity in the same way that increased blood flow is a result of increased activity. A diversion of CBF from default mode network regions would result in an increased oxygen extraction fraction, and therefore negative BOLD, without any change in neuronal activity.

9.1.2 The effect of task performance on connectivity

The question of whether deactivation of the default network affects its low frequency connectivity extends to activation of other networks as well. Although structural connectivity does not change, functional connectivity at rest may be different from the connectivity in the same areas when these brain regions are being actively engaged. Several studies have shown that connectivity can be modulated by the continuous performance of a task [355, 356, 333, 357, 348, 324]. Early studies used conventional block designs and removed the task-related activation before merging time-courses from task blocks. More recent studies have measured steady-state connectivity over a longer, continuous, period, which avoids the need for such preprocessing [334, 357, 324].

Biswal and Hyde [355] found that the functional connectivity map created during continuous finger tapping overlapped more with the standard finger-tapping activation map than the functional connectivity map during rest.

Lowe et al. [356] identified a correlated network based on regions activated during conventional block design memory tasks and found that during continuous performance of a working memory task, the correlation amongst the regions of this network increased, as compared to during a control task which did not activate the same network. Similarly, Hampson et al. [334] found functional connectivity between Broca's area and Wernicke's area in healthy subjects at rest which increased when subjects continuously listened to narrative text. Increased motor cortex connectivity has also been found during the performance of motor tasks [358]. Newton et al. [324] found that the mean correlation of the supplementary motor area, ipsilateral cerebellum, and ipsilateral auditory cortex to contralateral primary motor cortex increased during a unilateral finger tapping task relative to rest. The effect of an increased tapping rate was an increased mean correlation to primary motor cortex due to a larger number of correlated voxels within each region. In agreement with this, Amann et al. [325] found that it was the number of correlated voxels that drives changes in overall functional connectivity during task performance. However, their study also investigated ipsilateral regions of the motor network that, although connected at rest, are not activated by a unilateral motor task. They found a reduction in interhemispheric SMI connectivity during continuous motor task performance. Consistent with this, the degree of connectivity of the contralateral M1 and premotor cortex to other motor network nodes has been found to show a tendency to increase during a motor task, as compared to rest, while connectivity of the contralateral cerebellum decreased [359].

Although many studies have found increased task-related connectivity in functional networks, there is no

evidence to suggest that the connectivity in all systems and regions of the brain is affected by regional brain activation in the same manner [357]. A visual processing network correlated with MT/V5 at rest was reduced in extent and magnitude when subjects were viewing motion [333]. Widespread correlated fluctuations in the visual system during rest become spatially decorrelated during visual stimulation, as functionally specialised areas are recruited [360]. Morgan et al. [357] found no significant differences in connectivity between rest and sequential finger tapping in areas activated by a motor task, although there was a trend towards decreasing connectivity during the task. In the study of Amann et al. [325] overall reduced connectivity was observed between some motor areas activated by the task: contralateral M1 and SMA, with some individuals showing a connectivity increase during the task and others a decrease.

The findings of increased connectivity of activated areas during task performance are interesting, since the BOLD response associated with the task presumably involves vasodilation concurrent with an increase in regional CBF. However, local vasodilation in response to non-neuronal stimuli such as hypercapnia and anaesthesia tends to abolish low frequency oscillations [361], suggesting that the mechanism for increasing rCBF in BOLD imaging may be different, or oscillatory.

9.1.3 NIRS functional connectivity

With the advent of large dense arrays of NIRS optodes that allow coverage of more than a small region of the head, it became possible to study resting functional connectivity with NIRS. Using DOT, White et al. [328] mapped correlations in the visual and motor cortex and found high inter-hemispheric correlation in motor and visual networks, but no correlation between visual and motor cortex seed regions. Mesquita and colleagues [331] similarly mapped correlations in sensorimotor, visual and prefrontal cortices, finding higher correlations using totHb and deoxyHb than oxyHb and the lowest correlation to the contralateral side in the prefrontal cortex. Lu et al. [332] found stronger interhemispheric correlation in oxyHb and totHb in the motor and auditory systems. Correlations between areas belonging to the language system have also been found [330]. The motor cortex correlation patterns at rest have been shown to resemble those resulting from the alternation of motor task and rest [362]. Although seed correlation analysis was used in most of the initial studies, ICA may offer better separation of physiology and artefacts, as ICA has been found to produce more localised resting functional connectivity patterns than the seed-correlation-derived ones in the sensorimotor and especially the visual systems [363].

Duan et al. [364] performed a simultaneous fMRI and fNIRS resting state connectivity study. By transforming BOLD data into NIRS space, they were able to compare connectivity indices calculated with each modality. They found good correspondence between BOLD and oxyHb in an analysis using anatomically-defined ROIs, and slightly worse correspondence between BOLD and deoxyHb. Spatial maps of resting functional connectivity generated using NIRS were found to be slightly less accurate than those from BOLD, with a reasonable correspondence between BOLD and oxyHb connectivity maps.

Task-related connectivity in the prefrontal cortex has been shown with NIRS to increase during verbal fluency [365], Stroop [366] and Go-No-Go [367] tasks and in the temporal, parietal, and occipital regions during infant development [368]. Similarly, a larger number of homologous channels were correlated during speech sounds

in infants, compared to rest [369].

The following sections describe the investigation of changes in functional connectivity of the sensory and motor cortices to motor activation and noxious thermal stimulation, using both NIRS and fMRI.

9.2 Methods

9.2.1 Subjects and task

The Long_Blocks data from subjects who also had physiological recordings available were used. This was the fMRI data from 13 subjects (8 male) and NIRS data from 15 subjects (9 male). Of these subjects, 9 participated in both NIRS and fMRI imaging (see table 5.1). Data acquisition has been described in 5.1.3.1 and 5.1.3.2 on page 74. Image preprocessing has been described in 7.2.2, but fMRI images from both 1100 ms TR and 2200 ms TR runs were used. The TRs were chosen to be integer multiples of the sampling interval used for NIRS. Because connectivity measures can be influenced by aliased physiological noise [43], two different TRs were used to examine the effect of sampling interval on the connectivity measures. The image SNR is also decreased at the shorter TR and smaller flip angle, which could also affect physiological noise, since physiological noise increases with increasing image SNR.

Because the NIRS data was acquired continuously (the machine is not stopped between runs) the quality measures in 7.1 apply to the long block data as well. To exclude the transient effects from the haemodynamic response to the task, the first 30 seconds of data for each block were discarded, leaving 120s of steady-state data in each of the REST1, TAP, REST2, and COLD conditions for analysis.

9.2.2 Physiological noise removal

The physiological signals were processed using custom Matlab software, and physiological noise removal was performed using Aztec software [326] (<http://www.ni-utrecht.nl/downloads/aztec>). From the ECG (in NIRS), pulse (in fMRI) and respiration data, the cardiac and respiration phase were assigned to every image in each NIRS and fMRI time series. The RETROICOR method was used to construct regressors for the BOLD and NIRS time series, by fitting a 5th order Fourier series to the cardiac and respiratory phase information [7]. Heart rate and heart rate variability were calculated using the mean and variance respectively of the inter beat interval (IBI) in 6s windows. The amplitude and frequency of the current breath for each image was calculated based on the peaks of exhalation and inhalation, and the respiration volume per unit time (RVT) was calculated as in [370]. After RETROICOR, the BOLD signal was corrected for HR, HRV and RVT effects by shifting the signals with multiple lags to account for the variable delay between these, and fluctuations in the BOLD and NIRS signals. The optimal lags for HR, HRV, and RVT were determined by finding the lag of maximum correlation for every voxel. For HR, optimal lags in the 0 to 20 s range and 0 to 60 s range were found, since peaks of HR - BOLD correlation at two latencies have previously been observed [371]. The time courses of HR, HRV, and RVT at the optimal lag were then regressed from the BOLD, oxyHb and deoxyHb signals at each voxel.

9.2.3 Region of interest definition

Motor regions of interest were extracted using the functional activation maps generated by the short motor task. To identify the contralateral (left) motor cortex, LM1_act, the positive RTAP activation from the Short_Blocks group analysis thresholded at $p < 1e-06$ uncorrected was masked with BA 4 from the AAL Brodmann Area template to produce an ROI of 161 voxels. An ipsilateral (right hemisphere) deactivated ROI, RM1_deact, was defined using the short task deactivation map: RTAP < REST thresholded at $p < 1e-06$ masked with BA4 to produce a region of 56 voxels.

Sensory regions of interest LS1_act and RS1_deact were created using the same procedure, except the mask consisted of BAs 1, 2 and 3.

Since there was no ipsilateral deactivation for NIRS at the group level, left and right hemisphere activation maps for RTAP > REST and LTAP > REST were thresholded so as to produce ROIs of ± 65 voxels.

9.2.4 Connectivity analysis

Connectivity analysis was conducted using the REST toolbox [372]. All data was detrended and band pass filtered between 0.01 and 0.15 Hz. This is a wider frequency range than the 0.01-0.1 Hz band more commonly used for connectivity studies, however, we wished to include both the low frequency (0.01-0.04 Hz) and very low frequency (0.04-0.12 Hz) oscillations that have been previously described using NIRS [373].

For each subject, an average time course was extracted from each region of interest LM1_act, RM1_deact, LS1_act and RS1_deact. Then for each condition (REST1, TAP, REST2, COLD), the Pearson correlation coefficient was calculated between this time course and the whole brain fMRI scan, and with the whole of the ipsilateral and contralateral hemispheres of sensorimotor cortex that were measured with NIRS. An ROI analysis was also conducted by calculating the correlation between the average time courses from left and right ROIs. Only zero-latency correlation was considered.

In each case, the correlation coefficient was converted to a z-score using Fisher's transformation. A one sample t-test was performed on the z-score data for all subjects from the first rest condition (REST1), in order to verify the resting connectivity with M1. The z-scores for each subject and each condition (REST1, TAP, REST2, COLD) were then entered into a one way repeated measures ANOVA to assess changes in connectivity between the M1 ROI and other brain regions with condition. For whole brain/hemisphere analyses, the z-score maps were analysed using SPM5, while ANOVAs on the ROI-ROI correlation z-scores were performed in Matlab.

To establish the relationship between deactivation and connectivity, the Pearson correlation was calculated across subjects between the degree of deactivation to the right hand tasks (RTAP, RCOLD) in the ipsilateral ROIs (see chapters 7 and 8) and the connectivity between left and right ROIs during each long task condition REST1, TAP, REST2, COLD.

9.2.5 Power spectral density analysis

ALFF analysis [374] was performed on NIRS and fMRI data using the REST toolbox [372]. The square root of the amplitude of the power spectrum was taken and averaged over two different frequency bands at each voxel: 0.01 - 0.04 Hz (VLF) and 0.04 - 0.12 Hz (LF). The ALFF at each voxel was divided by the individual global mean of ALFF within a brain-mask. The ALLF maps for every subject and condition were entered into one-way repeated measures ANOVAs in SPM for each frequency band separately, to assess for changes in the amplitude of spontaneous fluctuations with task condition.

9.3 Results

9.3.1 Steady-state and resting functional connectivity

fMRI

Connectivity was calculated during the resting conditions (resting state functional connectivity) and during the continuous task/stimulus blocks, TAP and COLD (steady-state functional connectivity). In the first resting condition, REST1, group statistical analysis of BOLD correlation to the left M1 shows the expected resting connectivity to the ipsi- and contralateral primary and secondary sensorimotor areas, as well as to the thalamus and occipital regions. From examination of the continuous t-maps in shown for REST1 in figure 9.1, connectivity appears more extensive at the 2200 ms TR than the 1100 ms TR, and physiological noise correction reduces the magnitude and extent of connectivity, particularly at the 1100 ms TR. However, in a voxel-by-voxel comparison there are no voxels where the difference in connectivity at the different TRs is significant ($p < 0.05$ FDR). Connectivity to visual areas, although reduced, remains significant, even with physiological noise regression. Regions that survive a significance threshold of $p < 0.05$ FWE corrected are shown in table 9.1.

Only in the 2200 ms TR connectivity analysis do the inferior frontal regions, thalamus and putamen survive the significance threshold.

Connectivity to the right M1 ROI- the area deactivated by the ipsilateral motor task, showed less widespread and more distinct regions of connectivity, listed in table 9.2, which included bilateral primary and secondary somatosensory areas, and superior temporal gyri, insula, rolandic operculum and Heschl's gyrus, but did not include visual cortex.

A paired t-test was performed to determine which areas showed greater connectivity to the left M1 ROI than right one and to the right M1 ROI than the left one. Unsurprisingly a region of left SM1 showed greater correlation with the left ROI and a region of right SM1 showed greater correlation with the right ROI at both TRs (table 9.3). However, at the 1100 ms TR, the right insula, and Rolandic operculum as well as the left superior frontal gyrus and left paracentral lobule were more correlated with the right (deactivation) ROI than the left. Notably, the greater connectivity with the right M1 ROI in the left superior frontal gyrus and left paracentral lobule also appear in the 2200 ms TR run at lower significance threshold. Also, no region,

TR1100					TR2200				
Area	No. voxels	MNI co-ords	Peak t	Region	No. voxels	MNI co-ords	Max t		
L SMI, premotor (BA 3, 4, 6, 40)	593	-39 -21 57	22.86	L/R SMI, SMA, insula, putamen, STG	4999	-39 -21 63	35.74		
L/R SMA, cingulate (BA 6; 24, 31, 32)	360	-3 -12 60	15.41	R SMA		15 -21 45	28.38		
R MI/premotor (BA 6)*	16	48 -18 36	10.11						
R MI (BA 4, 6)*	14	48 -9 51	9.81						
R insula	7	42 -9 0	10.23	R insula		30 -21 18	27.49		
R insula, rolandic operc.	40	48 -15 15	9.98	R rolandic operc., STG		57 -9 3	22.87		
L rolandic operc., putamen, insula (BA 13)	125	-30 -9 -6	11.42	L rolandic operc. L insula		-45 -6 15	20.54		
L STG, rolandic operc.	23	-60 -9 9	11.83	L insula, mid./IFG (tri.)	101	-33 33 12	17.4		
				R cingulate (BA 6, 24)	11	18 -9 42	10.18		
				L IFG (tri.)	14	-42 18 21	10.41		
				R IFG (tri.)	10	39 27 27	16.57		
				L thalamus	14	-12 -21 -6	11.99		
				R thalamus	13	15 -21 0	11.97		
				R sup. temp. gyrus	14	54 -57 21	10.54		
L/R calcarine, cuneus (BA 18)	60	0 -72 -3 **	13.71	R/L cuneus	22	3 -72 30**	11.99		
L occipital cerebellum (BA 19)	13	-15 -51 -6	9.37	L cerebellum, calcarine (BA 18, 19)	25	-9 -54 -6	11.02		
				L cerebellum	10	-18 -57 -15	12.29		
				L fusiform gyrus	12	-36 -36 -18	12.93		

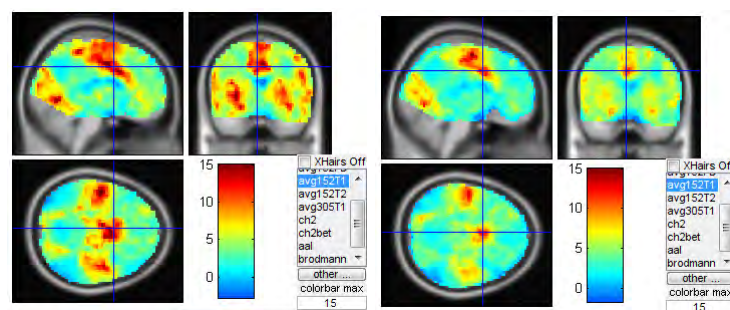
Table 9.1: Brain regions showing connectivity to the left M1 ROI significant at $p < 0.05$ FWE at two different TRs, with RETROICOR/Aztec correction for physiological noise applied. * At a lower threshold these clusters merge - mostly BA 6 (premotor) but several BA 4 and some BA3 voxels.

TR1100			
Area	No. voxels	MNI co-ords	Peak t
R SM1, L/R SMA, L/R paracent. lob. (BA 2, 3, 4, 6, 24, 31, 40)	1021	39 -30 57	19.74
R sup. temp. gyru s, rolandic operc., insula, heschl's gyrus	120	66 -27 0	13.46
L S1 (BA3, 40)	72	-27 -39 60	12.07
L S1	11	-39 -15 42	10.06
L SM1 (BA 3,4)	14	-57 -18 42	9.62
L sup. temp. gyrus, rolandic operc., heschl's gyrus	40	-57 -9 9	11.57
L mid./sup. temp. gyrus	10	-54 -24 -3	10.63
R sup. temp. gyrus	12	54 -39 15	9.45
TR2200			
Area	No. voxels	MNI co-ords	Peak t
R SM1, L/R SMA (BA 2, 3, 4, 6, 24, 31)	873	30 -24 57	18.68
R insula, rolandic operc., heschl's gyrus	27	36 -24 15	11.49
L SM1, insula (BA 2,3,4 6 13 40)	456	-33 -18 57	15.37
L sup. temp. gyrus, insula, rolandic operc.	13	-42 -33 21	11.68
L sup. temp. gyrus	12	-45 -9 -3	10.96
R sup. temp. gyrus	27	57 -15 3	10.55

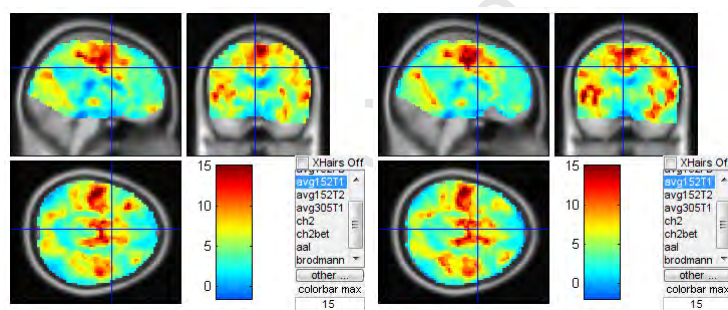
Table 9.2: Brain regions showing connectivity to the right M1 (deactivation) ROI significant at $p < 0.05$ FWE at two different TRs, with RETROICOR/Aztec correction for physiological noise applied.

TR1100					TR2200				
Greater connectivity to left M1 (activation ROI)									
Area	No. voxels	Co-ordinates	Peak t	Area	No. voxels	Co-ordinates	Peak t		
L SMI (BA 2,3,4,6)	274	-42 -18 57	12.58	L SMI (BA 2,3,4,6)	236	-39 -21 60	12.9		
Greater connectivity to right M1 (deactivation ROI)									
Area	No. voxels	Co-ordinates	Peak t	Area	No. voxels	Co-ordinates	Peak t		
R SMI (BA 3,4,6)	398	36 -24 57	12.38	R M1 (BA 3,4)	82	30 -24 57	9.54		
R insula, Heschl's gyrus, rolandic operc.	39	36 -27 12	8.74						
L superior frontal gyrus (BA 10)	19	-21 45 24	6.02	*					
L paracentral lob.	7	-15 -33 60	5.72	*					

Table 9.3: Areas that show greater connectivity to left M1 than right M1 and to right M1 than left M1 ($p < 0.05$ FDR)



(a) 1100 ms TR resting connectivity to left M1 during REST1 without physiological noise removal. (b) 1100 ms TR resting connectivity to left M1 during REST1 with physiological noise removal.



(c) 2200 ms TR resting connectivity to left M1 during REST1 without physiological noise removal. (d) 2200 ms TR resting connectivity to left M1 during REST1 with physiological noise removal.

Figure 9.1: Unthresholded t-maps of BOLD signal connectivity to left M1 during the REST1 condition for 1100 ms and 2200 ms TRs, with and without physiological noise removal.

other than the left SM1 area itself, showed greater connectivity with the left ROI than the right one even at lower thresholds.

In the fMRI ROI analysis, connectivity between the M1 ROIs in each hemisphere and between the S1 ROIs in each hemisphere was significant during all four conditions (table 9.4), as determined using four one sample t-tests across subjects with Bonferroni adjustment, $\alpha = .05/4 = .0125$ for four comparisons.

NIRS

In the hemisphere ipsilateral to each ROI, almost the entire volume was significantly connected to the ROI in each condition and each hemisphere, both with and without physiological noise correction ($p < 0.01$ FDR). The entire left hemisphere was also significantly connected to the right ROI in each condition and the right hemisphere to the left ROI in each condition ($p < 0.01$ FDR). This occurred in both oxyHb and deoxyHb.

Figure 9.2 shows the Pearson correlation between left and right M1 ROIs for each subject during each condition. Three subjects (subjects 3, 6, and 12) showed almost perfect correlation between left and right

		REST1		TAP		REST2		COLD	
		t	p	t	p	t	p	t	p
1100 ms TR (df=12)	M1	7.84	4.64e-6	13.22	1.62e-8	10.45	2.22e-7	4.29	0.001
	S1	8.13	3.18e-6	11.66	6.68e-8	7.34	9.00e-6	3.94	0.002
2200 ms TR (df=11)	M1	10.81	3.36e-7	12.56	7.24e-8	9.24	1.62e-6	9.51	1.22e-6
	S1	9.91	8.09e-7	9.87	8.42e-7	5.17	3.09e-4	7.42	1.32e-5

Table 9.4: T-statistics and p values for one sample t-tests on mean ROI connectivity z-score across subjects for M1 and S1 ROIs in fMRI. All t-tests were significant at $p < 0.05$ with Bonferroni adjustment for four comparisons.

		REST1		TAP		REST2		COLD	
N=14		t	p	t	p	t	p	t	p
Without physiological noise correction	oxyHb	3.25	0.006*	2.85	0.013	3.22	0.006*	2.65	0.018
	deoxyHb	1.95	0.072	1.92	0.075	2.26	0.041	1.99	0.066
With physiological noise correction	oxyHb	2.47	0.027	2.31	0.036	3.01	0.009*	2.70	0.018
	deoxyHb	1.95	0.072	1.96	0.070	2.33	0.035	2.09	0.055

Table 9.5: T-statistics and p values for one sample t-tests on mean ROI connectivity z-score across subjects for M1 ROIs in NIRS. Tests significant at $p < 0.05/4 = 0.0125$ with Bonferroni adjustment for four comparisons are marked with an asterisk.

ROIs in all conditions ($r > 0.95$), and one subject (subject 13) showed negative L-R correlation in all conditions i.e. the left and right M1 ROIs were anticorrelated. This subject was excluded from further analysis.

In oxyHb without physiological noise correction, connectivity between the ROIs in each hemisphere was significant across subjects during both REST conditions, but not during TAP or COLD, as determined using four one sample t-tests (table 9.5). The required significance level was $p < 0.0125$ ($p < 0.05$ Bonferroni-corrected for 4 comparisons). With physiological noise correction, connectivity between the left and right ROIs was only significant during REST2.

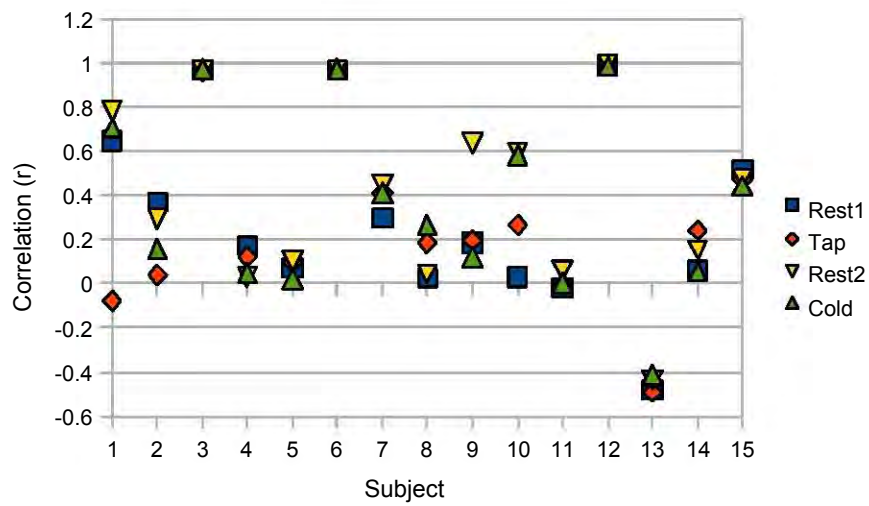
In deoxyHb, connectivity between hemispheres was not significant in any state with or without physiological noise correction.

9.3.2 Effect of TAP and COLD conditions

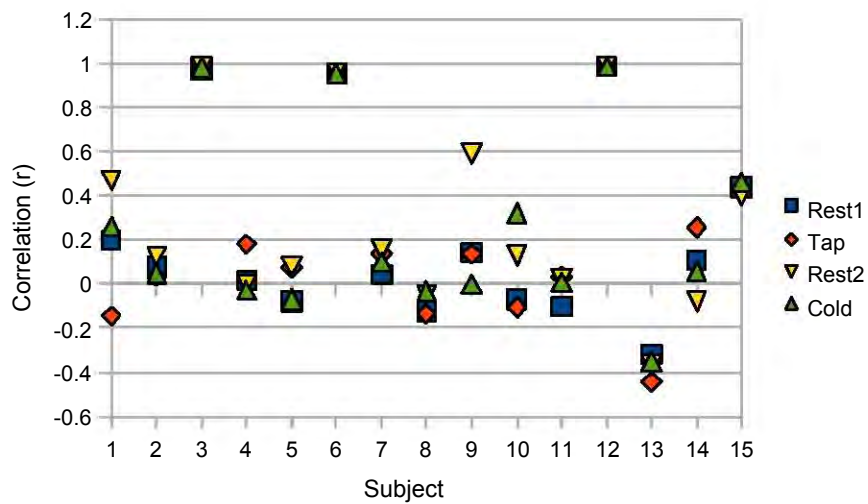
fMRI

No areas showed decreased connectivity with the left (contralateral) M1 ROI during TAP compared to REST, whereas the brain regions listed in tables 9.6, 9.7 and 9.8 showed increased connectivity to left M1 during the TAP condition, the largest clusters being the precuneus and the cingulate/supplementary motor area and the right inferior parietal lobule (BA 40).

With physiological correction, no region showed a difference in connectivity with the left M1 at the 2200



(a) oxyHb



(b) deoxyHb

Figure 9.2: Pearson correlation between left and right M1 ROIs for each subject in each condition measured with NIRS.

TR1100			
Area	No. voxels	MNI co-ords	Peak t
R/L precuneus	656	0 -51 51	5.76
L precentral gyrus (BA 6)	29	-42 -9 45	5.13
L sup. temp. gyrus, rolandic operc.	10	-51 0 3	3.62
R SMA (BA 32)	86	9 12 48	4.29
L/R midbrain, thalamus	80	6 -21 -3	4.35
R inf. par. lob., supramarginal (BA 40)	56	51 -45 24	4.44
R mid. frontal gyrus (BA 9, 10)	73	39 51 21	4.35
R mid. frontal gyrus	11	39 39 42	4.66
R sup. temp. gyrus (BA 38)	10	36 9 -21	3.74
R mid. temp. gyrus (BA 20)	15	54 -48 -12	3.88
R/L post. cingulate	25	3 -39 15	4.13
R fusiform	14	33 -42 -24	4.82
R pallidum	13	15 0 0	3.94

Table 9.6: Areas that show greater BOLD signal connectivity with the left M1 ROI during TAP than REST in the 1100 ms TR data ($p < 0.05$ FDR)

TR1100			
Area	No. voxels	MNI co-ords	Peak t
L/R precuneus, sup. par. lob.	337	-3 -54 51	5.37
L precentral gyrus (BA 6)	24	-42 -6 48	4.06
L insula (posterior)	56	-42 -6 -3	4.57
R mid. cingulate, R/L SMA (BA 32, 6)	113	3 24 42	4.34
R/L thalamus	72	6 -18 -3	4.12
R supramarginal gyrus, inf. par. lob., angular gyrus (BA 40)	197	57 -39 33	5.7
R sup./inf. par. lob., angular gyrus (BA 40)	21	36 -63 48	3.76
R mid. frontal gyrus	18	39 51 18	4.42
R sup. frontal gyrus (BA 9)	16	24 33 33	3.78
R mid./sup. frontal gyrus	15	33 -3 66	4.36
L sup. frontal gyrus	11	-18 -3 69	4.46
L mid./sup. frontal gyrus (BA 9)	13	-30 39 36	3.88
L mid./sup. frontal gyrus	17	-36 51 0	3.87
R mid./ inf. temp. gyrus	19	54 -48 -12	4.38
R inf. temp. gyrus	10	51 -60 -9	4.04
L mid./sup. temp. gyrus	11	-63 -54 12	4.02
L insula (anterior)	21	-33 15 0	4.31
L cerebellum	10	-27 -48 -12	4.22

Table 9.7: Areas that show greater BOLD signal connectivity with the left M1 ROI during TAP than REST in the 1100 ms TR data with physiological correction ($p < 0.05$ FDR)

TR2200			
Area	No. voxels	MNI co-ords	Peak t
R inf. temp gyrus, fusiform gyrus (BA 37)	121	48 -69 -15	5.9
L/R brainstem	21	-3 -30 -21	5.53
R/L precuneus, cuneus, fusiform gyrus	2749	6 -93 3	6.61
R precuneus	104	36 -69 36	4.27
L mid. frontal gyrus	22	-21 27 -12	3.63
R inf. frontal gyrus, insula (BA 13)	26	21 12 -12	3.51
R mid. frontal gyrus (BA 10)	17	42 57 -3	3.92
R mid./ ant. cingulate (BA 9, 32)	26	9 39 27	3.54
L/R SMA	21	6 -9 72	5.04

Table 9.8: Areas that show greater BOLD signal connectivity with the left M1 ROI during TAP than REST.

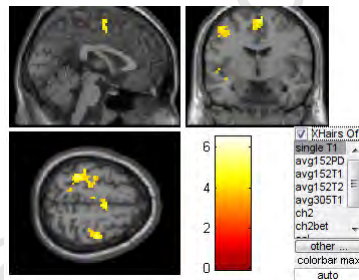


Figure 9.3: Brain regions showing significantly greater BOLD signal connectivity to the precuneus ROI in the TAP than in the REST condition ($p < 0.05$ FDR).

ms TR. However at a lower significance threshold ($p < 0.001$ uncorrected) the bilateral calcarine, cuneus and precuneus showed increased connectivity during tapping.

No region showed a change in connectivity to the ipsilateral (right) M1 during TAP at $p < 0.05$ FDR.

Some areas that increase connectivity with contralateral M1 during right hand tapping also deactivate during tapping, namely parts of the precuneus, L STG (insula), and R supramarginal gyrus.

Because change in connectivity to left M1 during tapping appeared to happen reliably in the precuneus, which is also an area deactivated by the motor task, a third ROI was created using the intersection of the RTAP<REST and LTAP<REST contrasts thresholded at $p < 1e-6$, which produced an ROI of 101 voxels in the (dorsal anterior) precuneus. The change in connectivity to this ROI in TAP vs REST was evaluated. The regions showing greater connectivity during TAP are listed in table 9.9 and shown in figure 9.3 and correspond closely to the motor system, including bilateral M1 and SMA, as well as bilateral IPL/posterior insula.

For the 2200 ms TR there is no significant change in connectivity with the precuneus.

TR1100

Area	No. voxels	MNI co-ords	Peak t
L cerebellum, fusiform gyrus	4.29	26	-15 -45 -15
L lingual, cerebellum	3.78	13	-3 -66 -3
L ant. insula (BA 21)	4.38	17	-39 -3 -6
L sup. temp. gyrus	3.96	14	-51 -3 -3
L precuneus, sup. occipital (BA 7, 19)	4.3	23	-24 -78 36
L calcarine, posterior cingulate, cuneus	4.3	67	-24 -66 6
R calcarine, posterior cingulate, cuneus	3.91	11	21 -72 6
R sup. temp. gyrus, inf. parietal lob., rolandic operc, post. insula (BA 13, 41)	4.97	44	48 -33 21
L sup. temp. gyrus, post. insula, inf. parietal lob., rolandic operc (BA 41)	4.71	29	-42 -36 15
L SMI (BA 2, 3, 4, 6)	6.54	343	-33 -42 63
L/R SMA, L paracentral lobule	5.25	100	6 -6 63
R SMI/premotor (BA 3, 4, 6)	5.08	112	42 -15 60

Table 9.9: Areas that show greater BOLD signal connectivity with the precuneus during TAP than REST ($p < 0.05$ FDR).

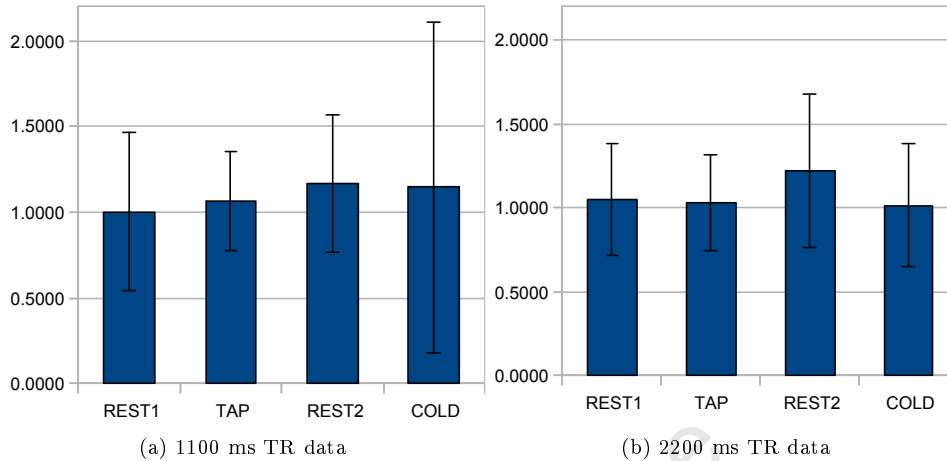


Figure 9.4: Mean and standard deviation across subjects of connectivity z-score between left and right M1 ROIs in each condition.

In a contrast comparing connectivity during the COLD and preceding rest condition, REST2, there was no significant change in connectivity to either the contra- or ipsilateral S1 regions, except in the 1100 ms TR data where the whole brain was significantly less connected to the ipsilateral (R) ROI during COLD than during REST2. This effect remained when correction for physiological noise was applied.

The mean connectivity z-scores across subjects between left and right M1 ROIs are shown in figure 9.4. Although connectivity appears slightly greater in REST2 than in the other conditions, a one-way repeated measures ANOVA found no effect of condition on connectivity between left and right M1 ROIs in the 1100 ms TR ($F(3,36)=0.381$, $p=0.77$) or 2200 ms TR ($F(3,33)=1.03$, $p=0.39$) data.

The mean connectivity z-scores across subjects between left and right S1 ROIs are shown in figure 9.5. Again connectivity appears slightly greater in REST2 than in the other conditions, but a one-way repeated measures ANOVA on the left and right S1 regions (identified by de/activation to COLD) similarly revealed no effect of condition in either in the 1100 ms TR ($F(3,36)=0.283$, $p=0.84$) or 2200 ms TR ($F(3,33)=0.24$, $p=0.865$) data.

In the first run in both ROIs a large standard deviation in the COLD condition indicates varying responses across subjects.

In the TR 1100 run all individual subjects showed significant correlation during the REST1 condition ($df=109$, $r>0.23$, $p<0.01$ one-tailed). In the TR 2200 run all individual subjects showed significant correlation during the REST1 condition ($df=54$, $r>0.32$, $p<0.01$ one-tailed). The number of subjects showing a connectivity increase or decrease in response to TAP and COLD are shown in table 9.10.

Five subjects showed the same direction response (a connectivity increase or decrease) to TAP in both runs, and eight subjects showed the same response to COLD in both runs.

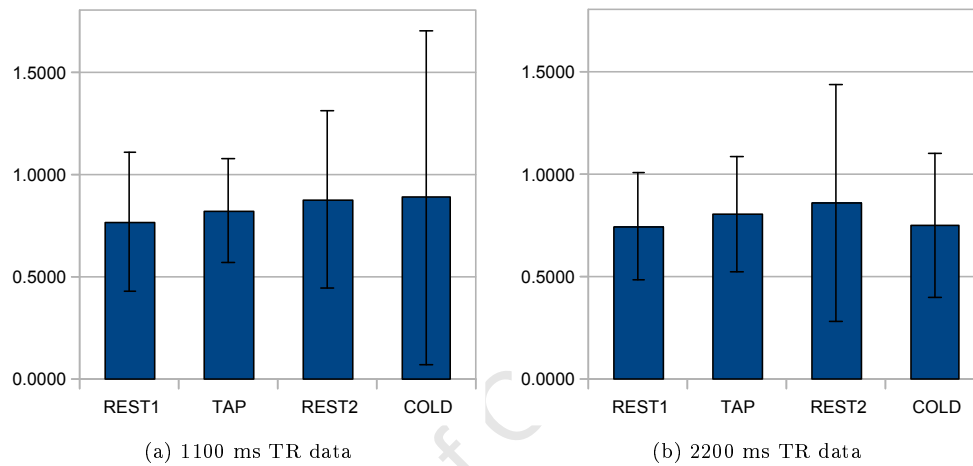


Figure 9.5: Mean and standard deviation across subjects of connectivity z-score between left and right S1 ROIs in each condition.

	1100 TR (n=13)	2200 TR (n=12)
TAP > REST1	6(4)	6(2)
COLD > REST2	6(3)	6(1)
TAP < REST1	7(2)	6(0)
COLD < REST2	7(5)	6(4)

Table 9.10: Number of subjects showing increases or decreases in connectivity with condition. The number in parentheses indicates subjects whose difference in connectivity during the two conditions was significant at $p < 0.01$ two-tailed.

	No correction				With correction			
	L hem - L ROI		R hem - R ROI		L hem - L ROI		R hem - R ROI	
	OxyHb	DeoxyHb	OxyHb	DeoxyHb	OxyHb	DeoxyHb	OxyHb	DeoxyHb
TAP > REST1	2653	0	17697	0	0	290	0	0
TAP < REST1	7528	0	0	0	0	0	0	0
COLD > REST2	0	0	0	0	0	0	0	6332
COLD < REST2	11041	13304	0	0	6499	12747	0	0

Table 9.11: Number of voxels in each hemisphere showing changed connectivity to the ROI in the same hemisphere at $p < 0.01$ FDR, with and without physiological noise correction.

	L hem - R ROI		R hem - L ROI	
	OxyHb	DeoxyHb	OxyHb	DeoxyHb
	TAP > REST1	0	0	18735
TAP < REST1	413	20015	0	0
COLD > REST2	0	0	0	20263
COLD < REST2	0	18794	0	0

Table 9.12: Number of voxels in each hemisphere showing changed connectivity to the ROI in the opposite hemisphere at $p < 0.01$ FDR, with physiological noise correction applied.

NIRS

Table 9.11 shows that the within-hemisphere connectivity to the ROI decreased for COLD compared to REST2 in the left (contralateral) hemisphere in both oxyHb and deoxyHb. However, correction for physiological effects reduced the extent of decreased connectivity. In oxyHb, connectivity increased for TAP compared to REST1 in the right (ipsilateral) hemisphere, and decreased to some degree in the left hemisphere.

In the left hemisphere there was no significant change in connectivity to the right ROI for COLD, but many voxels in both oxyHb and deoxyHb were significantly less connected to the right ROI during TAP than during REST ($p < 0.01$, see table 9.12). This area did not overlap with the left ROI (found by activation to tapping) used in the ROI-ROI analysis.

In the right hemisphere there was greater connectivity in TAP than REST1 in OxyHb only and greater connectivity in COLD than REST1 in deoxyHb only.

The mean ROI-ROI connectivity was slightly greater in REST2 than in the other conditions (figure 9.6), but a repeated measures ANOVA revealed no main effect of condition either with ($F(3,42)=1.53$, $p=0.112$) or without ($F(3,42)=2.13$, $p=0.234$) physiological noise correction.

In deoxyHb there was no main effect of condition with ($F(3,42)=1.94$, $p=0.138$) or without ($F(3,42)=1.14$, $p=0.138$) physiological noise correction.

As shown in figure 9.7, in oxyHb, the mean connectivity between left and right S1 regions (identified by

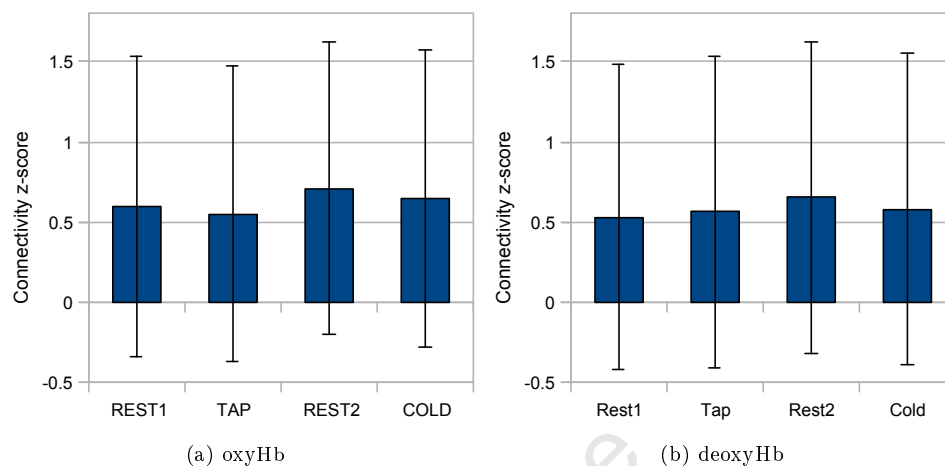


Figure 9.6: Connectivity z-scores between left and right M1 ROIs for each condition, averaged over 14 subjects

	oxyHb (n=9)	deoxyHb (n=6)
TAP > REST1	2	1
COLD > REST2	3	1
TAP < REST1	6 (2)	3 (1)
COLD < REST2	6 (2)	3 (2)

Table 9.13: The number in parentheses indicates subjects whose difference in connectivity during the two conditions was significant at $p < 0.01$ two-tailed.

de/activation to COLD) was close to zero for each condition. In deoxyHb connectivity during TAP was smaller than in the other conditions. A one-way repeated measures ANOVA on the left and right S1 regions revealed no effect of condition in oxyHb ($F(3,39)=0.83$, $p=0.485$) and in the deoxyHb data ($F(3,42)=4.99$, $p=0.004$) post-hoc tests were not significant.

Nine individual subjects showed significant correlation during the REST1 condition in oxyHb ($df=430$, $r > 0.12$, $p < 0.01$ one-tailed). A subset of six of these subjects also showed significant correlation in deoxyHb during REST1. Of the subjects who showed significant connectivity during rest, the number of subjects who showed changes in connectivity with each condition is shown in table 9.13. Two additional subjects whose ROIs were not significantly connected during REST1 nevertheless showed significant increases in connectivity during the TAP or COLD conditions.

9.3.3 Relation of connectivity to activation and deactivation

In the 1100 ms TR fMRI data the correlation across subjects between the mean activation parameter estimates to RTAP in LM1_act and mean z-score of LM1_act - R M1_deact connectivity was not significant during

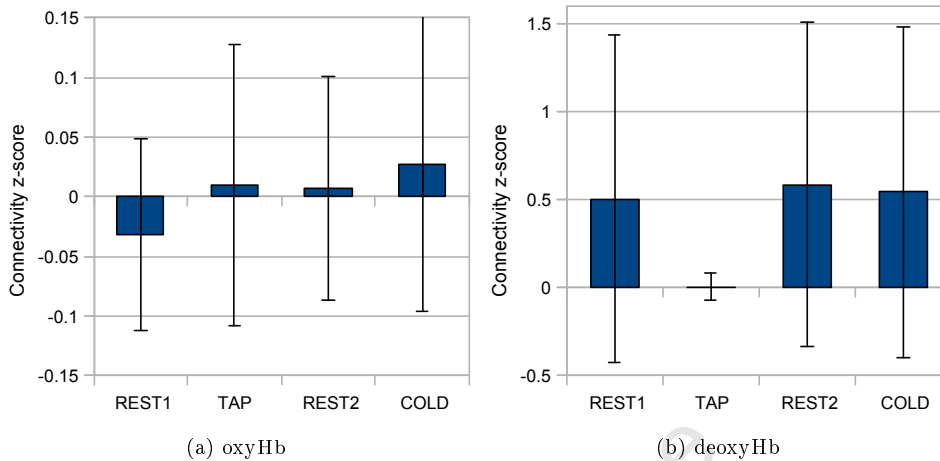


Figure 9.7: Connectivity z-scores between left and right S1 ROIs for each condition, averaged over 14 subjects

REST1 ($r=0.24$, $p=0.41$), TAP ($r=0.09$, $p=0.75$), REST2 ($r=-0.02$, $p=0.95$) or COLD ($r=0.1$, $p=0.73$) and correlation between the mean RTAP deactivation parameter estimate in RM1_deact and connectivity z-score during TAP ($r=-0.57$, $p=0.03$) approached significance for TAP but not during REST1 ($r=0.02$, $p=0.950$), REST2 ($r=0.44$, $p=0.11$) or COLD ($r=0.08$, $p=0.79$). This result was not significant when corrected for multiple comparisons, and may have been driven by extreme subjects as shown in figure 9.8, but was repeatable in the 2200 ms TR run and was not affected by physiological noise correction.

Correlation across subjects between mean activation parameter estimates to RCOLD in LS1_act and mean z-score of LS1_act - RS1_deact connectivity was not significant for REST1 ($r=0.16$, $p=0.58$), TAP ($r=-0.12$, $p=0.68$), REST2 ($r=-0.05$, $p=0.87$), COLD ($r=0.29$, $p=0.31$) and correlation between the mean RCOLD deactivation parameter estimate in RS1_deact and connectivity z-score was not significant for REST1 ($r=-0.04$, $p=0.89$), TAP ($r=-0.15$, $p=0.61$), REST2 ($r=-0.32$, $p=0.27$) or COLD ($r=-0.16$, $p=0.59$).

In the NIRS data there was no relation between deactivation and connectivity in M1 for oxyHb (REST1 $r=-0.11$, $p=0.70$, TAP $r=0.05$, $p=0.86$, REST2 $r=-0.11$, $p=0.69$, COLD $r=-0.03$, $p=0.92$) or deoxyHb (REST1 $r=-0.06$, $p=0.84$, TAP $r=0.18$, $p=0.51$, REST2 $r=-0.01$, $p=0.97$, COLD $r=0.11$, $p=0.69$) and physiological noise correction made no difference to these results.

9.3.4 Power spectral density analysis

No significant changes in the amplitude of fluctuations in the VLF or LF frequency band with condition were found in the fMRI data at $p<0.05$ FDR corrected. In the oxyHb data, there was an increase in VLF power for TAP compared to REST1 in both the left and right hemispheres, and a decrease in LF power in TAP compared to REST1 in the left (contralateral) hemisphere only. In deoxyHb, there were no changes with condition in the VLF range, but in the LF band there was increased power for COLD compared to REST2

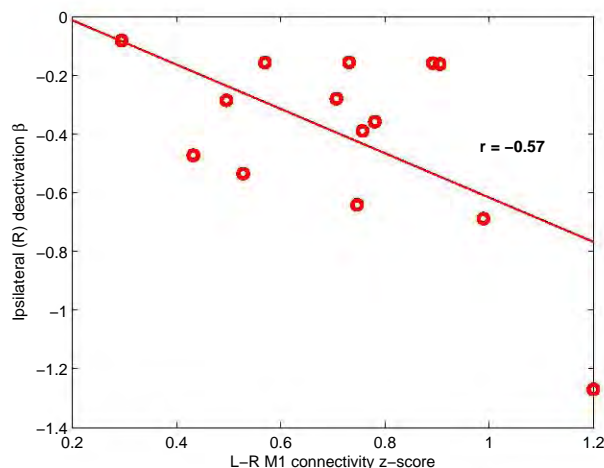


Figure 9.8: Correlation across subjects between ipsilateral deactivation to RTAP and L-R M1 connectivity during the 120 s TAP condition (fMRI).

and decreased power for TAP compared to REST1 in the left hemisphere only.

9.4 Discussion

In the motor system, correlated fluctuations at rest usually exist between (left) SM1 and premotor cortices, thalami and central and postcentral gyri, SMA, middle frontal gyri, insulae, secondary somatosensory cortices and contralateral cerebellum. Steady-state connectivity within these networks may be altered during continuous task performance [324]. The relation between functionally deactivated areas and connectivity is not known. Although using fMRI we were able to investigate whole-brain connectivity to an M1 ROI, since with NIRS measurement is restricted to the surface of the brain, we were limited to investigating interhemispheric sensorimotor cortex connectivity in deoxyHb and oxyHb measurements.

9.4.1 Spurious correlations, the global signal and physiological noise

Using fMRI we found the expected connectivity to a functionally-defined M1 ROI across the motor system during rest, as well as to regions of occipital cortex. Using an ROI defined by deactivation to a motor task we found more restricted connectivity, which did not include visual cortex. The finding of connectivity of M1 to the occipital cortex is not unprecedented (e.g. [375]) but it is thought not to reflect neurophysiological connectivity since the visual and motor networks are separate. Spurious correlations thought to be caused by systemic sources with a global effect across the brain are frequently addressed by removing the global brain signal. This preprocessing step has been found to decrease correlations between the motor and visual systems [375] and improve the specificity of functional connectivity maps [375, 376]. The global signal resembles the breath-to-breath variation in the end-tidal partial pressure of carbon dioxide [38], but it is

not yet clear whether it also correlates with signals of neuronal origin. Its removal is also problematic if negative correlations are to be studied, as this forces the distribution of correlations to centre around zero [376, 377], presenting an ambiguity as to whether the removal of global signal actually produces negative correlations, or reveals existing negative correlations that are masked by global effects [378, 376]. Because of this uncertainty, regression of the global signal was not performed here, but the incorporation of cardiac and respiratory signals in the analysis using RETROICOR and Aztec did not decrease connectivity to occipital regions. By raising the threshold, we found spurious correlation with the visual system could be eliminated: a similar result to [351] who found that identical network maps could be produced by raising the threshold, without performing any preprocessing beyond spatial smoothing.

The removal of respiration-related variation has been shown not to alter default network connectivity maps to any great extent [370, 351]. Correction of both respiratory and heart rate variation, using the method that we used here, resulted in rather small changes in correlations between default network regions ($z(r)$ from 0.57 to 0.53)[326]. Similarly we found little noticeable difference between the connectivity maps and ROI z -scores with or without physiological correction, in both NIRS and fMRI. However, it has also been shown that model-based correction for physiological effects can increase signal correlations [378].

There is evidence that suggests that neuronal activation within resting state networks does not fully account for low frequency BOLD fluctuations in the brain [379]. More global oscillations may be purely vascular, either related to systemic processes such as heartbeat, respiration and arterial blood pressure [7, 38, 370], or the regulation of regional cerebral blood flow [380].

Tong et al. [381] found significant correlations between a prefrontal NIRS signal and the BOLD signal in widespread areas throughout the brain. Lagged correlations also showed a temporal progression through the brain with a pattern resembling the circulatory system, suggesting that the origin of the oscillations is a global haemodynamic rather than neuronal one. These low frequency physiological oscillations may originate both from vasomotion and from Mayer waves in arterial blood pressure.

It is likely that there are both neural and vascular components to the low frequency oscillations in the brain and the presence of purely vascular oscillations may confound the detection of resting-state connectivity networks. Because of its high temporal resolution, NIRS can be used to separate the contributions of the LF spontaneous oscillations and cardiac signals to the modulation of the BOLD signal [382] and has been shown to be useful for regressing low frequency variations from fMRI data, reducing variance more than a RETROICOR model [383].

9.4.2 The effect of different TRs

Slightly different regions of significant connectivity were found using different TRs. Signal fluctuations due to steady-state free-precession are greater at the short TR [22], and cardiac pulsation effects in parenchymal tissue may be aliased to different frequencies with each sampling rate [21, 43, 24]. The image SNR, which is greater at the 2200 ms TR, may also play a role. Higher temporal resolution should facilitate accurate sampling of the low-frequency signal fluctuations and the removal of confounding signals. However, functional connectivity analysis has been shown to be robust to the selection of TR: in [351] no difference was observed

between 2.5 and 5.0 s repetition times. Since the acquisition time was constant, the number of volumes acquired was greater for the 1100 ms TR data set, so for assessment of single subject, but not group-level, connectivity the increased degrees of freedom will result in lower p values.

9.4.3 Steady-state connectivity in task conditions

In the fMRI data, interhemispheric connectivity between M1 and between S1 ROIs was significant in all conditions. In NIRS, although most of the ipsi- and contralateral hemisphere was significantly connected during each condition, the ROI analysis at group level revealed connectivity in oxyHb in the REST conditions only, and no significant ROI-ROI connectivity in deoxyHb. Only nine out of fifteen subjects showed significant positive correlation between the M1 areas at rest. It is probable either that poor optode coupling resulted in low SNR or that inaccurate optode placement, or anatomical variation in these subjects meant that the motor cortex was not optimally sampled. However, two of these subjects showed increased connectivity during the tasks. We hypothesise that autonomic changes during the task which were not adequately accounted for by the physiological noise removal method: for example blood pressure oscillations in superficial tissue, may have contributed to this phenomenon.

The apparent NIRS connectivity to most of the ipsi- and contralateral hemisphere may be due to global noise of physiological origin that was inadequately removed by the physiological noise correction scheme used. However, another possibility is inaccuracy in the image reconstruction algorithm. The area of cortex sampled by the 3 x 5 array of source and detectors is rather small, possibly comprising mostly or only sensorimotor cortex, however, voxels a great distance from this area are included in the image reconstruction. If voxels which are too distant to have an influence at any optode are weighted too heavily, a measured local effect may appear to be more global throughout the image. This is supported by the fact that, although distinct peaks of activation were found for the motor and cold tasks in chapters 7 and 8, activation across most of the hemisphere of the DOT image survived the significance threshold.

9.4.4 Discrepancies between fMRI and NIRS

There were several discrepancies between group-level findings in fMRI and NIRS. Due to interindividual subject variability, steady-state connectivity was not significant in oxyHb and deoxyHb during all conditions and connectivity changes were observed during NIRS but not in fMRI.

There are several possible reasons for these discrepancies between fMRI and NIRS. Most importantly, a major limitation of this study was the inability to perform simultaneous fMRI and NIRS recordings. Since functional connectivity patterns may vary with time [384] and the subject state may vary, the different results obtained here cannot be solely attributed to differences between imaging modalities. In addition, due to practical constraints, the fMRI scan always took place before the NIRS scan, therefore systematic effects due to repetition of the same protocol may exist between NIRS and fMRI. Furthermore, although efforts were made to replicate environmental conditions between the two scans, subject position varied slightly between the two sessions, since it was not possible for subjects to be completely supine during NIRS scanning.

The MRI scanner is a confined environment with high ambient noise levels, whereas the NIRS scanning environment is arguably more comfortable, and certainly quieter, which could lead to variations in subjects' neurophysiological state.

Differences in imaging modalities may also contribute to differences in connectivity measures. Because fNIRS signals are measured transcranially, light must penetrate several superficial layers including skin, skull and CSF. This means that globally distributed physiological noise including cardiac pulsation, respiration, and blood pressure changes may appear in the optic signals. Although we used a physiological noise correction scheme to try to eliminate these sources of interference, because the correction algorithm is optimised for fMRI rather than NIRS data, it is possible that residual physiological noise was partially responsible for discrepancies between connectivity measures obtained using fNIRS and fMRI. Moreover, the biophysical origins of the fMRI and fNIRS signals are not identical [154].

Individual fMRI connectivity maps have been found to be more specific than individual maps obtained using NIRS [364]. In fact, there seemed to be great interindividual variability between NIRS connectivity measures. However, in simultaneous recordings, group-level maps have been found to be comparable to those obtainable with fMRI [364]. However, our results agree with previous findings that although the origins of the deoxyHb and BOLD signals are more similar, resting connectivity is more reliably detected using the oxyHb signal [332, 363, 330], possibly because of the lower SNR of deoxyHb [381].

9.4.5 Considerations for NIRS

It is possible that a normalised connectivity metric independent of temporal SNR and signal amplitude [385] may be particularly helpful for NIRS data, in which the SNR may vary substantially between subjects and between sessions due to variations in optode placement. Despite our lack of finding of interhemispheric connectivity in NIRS, others have shown repeatable functional connectivity in the sensorimotor cortex a week apart using both seed correlation [386] and ICA [387]. Seed-based correlation in the motor cortex has also been demonstrated to be reproducible between two different NIRS systems [388].

The haemodynamics measured by the NIRS are also sensitive to systemic variation associated with the cardiac cycle, respiration, blood pressure oscillations, and heart rate variations. It is important to account for these systemic contributions in order to investigate neuronal oscillations. This can be done either using data from small source-detector separations to account for shallow variation arising from the scalp [328, 331] or by including auxiliary physiological measurements, such as blood pressure, in the analysis [331]. Although low frequency blood pressure oscillations tend to broaden areas of high correlations [331], several studies do not appear to have accounted for the influence of global signal [332, 389, 365]. We adapted a physiological noise correction method [326] previously used for fMRI to account for respiration and cardiac-related variation as well as variations in heart rate, heart rate variability and respiration volume. However, variations in blood pressure which appear to be the biggest confounding factor in NIRS experiments were not accounted for in this method, unless blood pressure was correlated with HR or HRV. Since we used a DOT image reconstruction, in which depth localisation is better than multichannel NIRS, we did not regress signals from source-detector separations to account for shallow variation.

We examined correlations in a wide frequency range from 0.01 to 0.15 Hz. Interhemispheric connectivity maps in NIRS have been demonstrated not to be affected by the frequency range of the band pass filter [332]. OxyHb signals between homologous regions of the contralateral hemisphere show high coherence over a wide frequency range (0.009–0.1 Hz), whereas connectivity between the prefrontal and occipital regions (fronto-posterior connectivity) show high coherence within only a narrow frequency range (0.04– 0.1 Hz) [389].

9.4.6 Change in connectivity with task

No regions showed a decrease in connectivity to contralateral (left) M1 during the motor task, however, connectivity to the precuneus, premotor, cingulate/supplementary motor area and the right inferior parietal lobule (BA 40), as well as the left posterior insula, bilateral thalamus and right MFG was increased. Although previous studies of task-related changes in motor cortex connectivity have emphasised connectivity to selected ROIs, rather than considering the whole brain, our findings of increased connectivity of the SMA and right MFG are consistent with [324] and [325] respectively. However, Amann et al. [325] observed overall reduced connectivity between contralateral M1 and SMA, with some individuals showing a connectivity increase during the task and others a decrease.

Functional correlations have been found to increase during performance of tasks including working memory [356], listening [334], and motor [358, 324] tasks. Regions that are part of the network, but not activated during a unilateral motor task, may even decrease their connectivity to activated regions [359, 325]. However, a tendency for connectivity decrease has also been observed in functionally activated areas (M1 and SMA) [357, 325]. Activation may also affect different networks in different ways: connectivity in visual areas has been found to be reduced during visual stimulation [333, 360].

9.4.6.1 Interhemispheric SM1 connectivity

In fMRI, connectivity between left and right M1 ROIs did not change significantly between conditions, and neither did connectivity between left and right S1 ROIs. Using NIRS we did not find any change in connectivity between conditions between left and right M1 or S1 ROIs. However, in the NIRS data, in the left (contralateral) hemisphere, intrahemispheric connectivity to the left M1 ROI decreased during COLD, and interhemispheric connectivity to the right M1 ROI decreased during COLD and TAP. Also, in the NIRS ROI data from individual subjects, a majority showed decreases in interhemispheric connectivity during TAP and COLD.

Newton et al. [324] found that the mean correlation of contralateral M1 to activated areas: SMA, ipsilateral cerebellum, and ipsilateral auditory cortex ROIs, increased during a finger tapping task relative to rest. They did not investigate the ipsilateral M1 which is not activated, and may even be deactivated, by a unilateral motor task. Although our thresholded group t-maps appeared to show a larger number of significantly connected voxels in right SM1 - probably premotor area - during TAP than during REST, we found no evidence for significantly increased or decreased interhemispheric M1 connectivity when the left and right M1 ROIs were compared directly.

Although echoing the findings of [357], this is in contrast to the findings of decreased interhemispheric M1 connectivity during task performance of [325] and [390]. Differences in ROI definition may have contributed to the varying findings. The ipsilateral M1 ROI of [357] was defined on the basis of motor task activation; in [325] the ipsilateral ROI was defined anatomically; while ours was defined on the basis of deactivation to a unilateral motor task. It is suggested that ROIs should be defined based upon activation, rather than anatomy [325]. It is also possible that defining regions based on individual rather than group activation maps may improve the ROI estimates of connectivity, especially for NIRS data where location is even less precise.

In both NIRS and fMRI data there was a trend for greater interhemispheric M1 connectivity during REST2, directly following the TAP condition. It is known that resting state functional connectivity may be altered by past events. Widespread increases in low frequency spectral power and connectivity in motor regions have previously been observed in the resting period following performance of a task [390]. An increase in connectivity between left and right middle frontal gyri, and between posterior cingulate cortex and medial frontal cortex at rest has been found after a language task, as compared to a before-task rest period [391]. A reduction in connectivity between motor cortices after a fatiguing handgrip exercise has also been demonstrated [392]. The trend we observed was in the other direction, and is unlikely to result from fatigue, since our motor task was not as demanding as handgrip exercise.

The interhemispheric coupling between SM1 may differ during unilateral and bimanual tasks. Unimanual simulation may require greater suppression of inter-hemispheric interaction, in order to prevent mirror symmetric movements. In a passive movement task, Macaluso et al. [393] found increased coupling between left and right SM-regions for bimanual movement and reduced coupling for unilateral passive stimulation [393].

9.4.6.2 Connectivity to precuneus

An interesting finding was the consistent increase in connectivity of M1 with the precuneus: the same subregion that was deactivated by the unilateral motor task. Using this dorsal anterior region of deactivated precuneus as a seed region for connectivity analysis did not reveal significant functional connectivity with primary sensorimotor areas during rest, however, the connectivity to primary and basal ganglia motor regions was significantly increased during the TAP condition.

The precuneus is an understudied region which may be of great importance because of its purported role in the default mode network and consciousness. It is implicated in a range of cognitive functions including visuo-spatial imagery, episodic memory retrieval, self-processing and consciousness [394] and is widely connected to higher association cortical and subcortical regions, including the adjacent parietal cortex, frontal lobes and the dorsal premotor area, the SMA and the anterior cingulate cortex [394].

Resting connectivity in humans and monkeys has shown that subdivisions of the precuneus may each have a distinct functional role. The anterior precuneus is functionally connected with sensorimotor regions including the superior parietal cortex, paracentral lobule, and motor cortex. The central precuneus is functionally connected to cognitive/associative regions including dorsolateral prefrontal, dorsomedial frontal, and multimodal lateral inferior parietal cortex, and the posterior precuneus is connected with adjacent visual cortex. It has been proposed that rather than the precuneus, it is the more ventral posterior cingulate, which shows

functional connectivity to limbic structures, that is a component of the default-mode network [395].

Functional connectivity between the the primary motor cortex and precuneus was found in early studies [327, 396] and has recently been refined to its dorsal anterior portion [395, 387], which is more strongly connected to the somatomotor cortex, insula, supramarginal, Heschl's, and superior temporal gyri than the ventral and dorsal posterior precuneus, the latter of which is more connected with visuomotor areas [387].

To our knowlege increased connectivity between dorsal anterior precuneus and M1 during a motor task has not been reported. It is all the more interesting considering that this region of precuneus was strongly deactivated during the unilateral motor tasks. The dorsal anterior precuneus has been found to be activated in spatially complex bimanual coordination tasks as compared with the unimanual subtasks, and may be involved in spatial motor imagery, such as shifting attention between different locations in space, movement coordination, and mental rotation [397]. A recent study [398] has also found the amplitude of response in the precuneus during motor sequence learning decreases as performance became more consistent. If the precuneus is involved in the co-ordination of complex motor behaviour or facilitation via imagery of the storage of motor sequences in spatial working memory [394] it is possible that the task we used was sufficiently simple and automatic for precuneus activity to be suppressed during the task.

9.4.6.3 Relation to deactivation

Correlation across subjects between the mean RTAP deactivation parameter estimate in RM1_deact and connectivity z-score during TAP approached significance for TAP ($r=-0.57$, $p=0.03$) but did not reach significance for the other conditions. This is opposite to the finding of [325] who observed that individual decrease in left-right SM1 connectivity during a continuous motor task correlates with stronger suppression of collateral SM1 activation during the task. In our data, greater interhemispheric M1 connectivity during the long TAP condition corresponded to greater ipsilateral deactivation during the short RTAP condition. However, in our subjects we also did not observe decreased interhemispheric M1 connectivity during the task. We also investigated the contralateral activation and found that the connectivity was not significantly related to the magnitude of activation across subjects. There was no significant relationship between the magnitude of activation or deactivation to RCOLD and connectivity in any condition. In the NIRS data no relation was found between deactivation and connectivity.

9.4.7 Task design and variation between runs

Because the primary aim of the study was to investigate changes in steady-state connectivity between rest and different task conditions, rather than to examine resting functional connectivity itself, the 150s block lengths selected were shorter than is conventional during pure resting state experiments. However, previous studies that have investigated changes in steady-state characteristics during rest and task states have used blocks of comparable length (e.g 120s [390] or 200s [324]). Because the activation and connectivity tasks were performed in the same imaging session, which was followed by the same protocol repeated during NIRS imaging, the block lengths could not realistically be increased while keeping the total imaging time for each subject to a maximum of two hours.

With regards to resting state functional connectivity, van Dijk et al. [351] have shown that, although one long run is efficient and not much increase in reliability is gained from multiple runs, the run length necessary to reduce noise and stabilise connectivity measures is 5 minutes. However, it has also been shown that concatenating quite short runs, or using only the rest blocks from an interleaved block design experiment, produces equivalent resting functional connectivity [399]. The resting state connectivity during the first 150s block of our experiment was examined in order to verify that sufficiently accurate motor system resting connectivity could be obtained.

Although multisession and multisubject connectivity results are stable [325, 351], the degree of connectivity may also vary between individuals and between sessions in the same individual [325]. In the two fMRI runs, out of twelve subjects only five showed the same direction response (a connectivity increase or decrease) to TAP in both runs, and eight showed the same response to COLD in both runs. In the NIRS data the two runs were concatenated for one connectivity measure. If the direction of connectivity change in an individual differed in the first and second runs these differences would be averaged out. However concatenated runs have been shown to provide nearly identical connectivity results compared to one continuous run [351].

Although it was not explicitly investigated, it is expected that the performance of the motor task would affect the subsequent resting block. Previous studies have found changes in resting state BOLD signal fluctuations before and after performance of a motor task [390] and an n-back memory task [400]. The fractal scaling properties of fMRI time series take some minutes to return to their pre-task values [400]. For this reason, changes in connectivity and PSD due to the TAP and COLD conditions were only calculated in relation to the immediately preceding rest block.

9.4.8 Power spectrum changes

The investigation of spectral power of haemodynamic oscillations is important, since if the amplitude of correlated signals decreases relative to other signal components, measures of connectivity will be reduced [390].

No significant changes in the amplitude of fluctuations in the VLF or LF frequency band with condition were found in the fMRI data. At 120 s, the long blocks were possibly too short and noisy for reliable spectral estimates to be obtained - a multitaper spectral estimate may have been more accurate. Previous studies using the ALFF method have investigated averaged power in the 0.01- 0.08 Hz frequency band. Although a previous study found changes in PSD at specific frequencies in the motor cortex with motor task performance [390], we averaged spectral power in two frequency bands, which may have contributed to differences in results.

The decrease in oxyHb and deoxyHb LF spectral power in the left hemisphere during TAP is consistent with previously-observed reduction in spectral power during motor task performance [390]. However, in [390], the reduction was bilaterally symmetric, and appeared in both activated and non-activated regions. In opposition to this result, we found a significant bilateral increase in VLF power in oxyHb during TAP, as well as contralaterally in deoxyHb during COLD. Although we found no changes in cardiac activity that were significant at the group level, we cannot exclude the possibility that some changes in connectivity and PSD during NIRS occurred as a result of systemic changes that were not accounted for by the physiological noise

correction method, in particular blood pressure oscillations that are induced by activation of the sympathetic nervous system.

In the NIRS data in the left (contralateral) hemisphere, there was some evidence for decreased connectivity to the ipsilateral ROI during TAP in deoxyHb, which corresponds to the observed decrease in LF power during TAP in that hemisphere.

Our NIRS data differed from the fMRI data in that a higher sampling rate was used and correlation was calculated across two runs. However, in an ROI analysis there was no significant effect of task condition on connectivity. The selection of ROIs may have played a part in this. ROIs were selected based on activation/deactivation at the group level, however, since intersubject alignment in this experiment is approximate, a better approach may have been to select the ROIs for each subject based on individual activation maps. Because in individuals there was often no significant activation or deactivation except at a very high p threshold value, defining ROIs based on group activation maps was more practical.

As well as in the motor network, task-induced reductions in low frequency spectral power have also been observed in the default network [348], and in NIRS signals from the visual cortex [373]. However, Yang et al. [374] found increased low frequency BOLD signal fluctuations in the visual cortex, and decreased fluctuations in the PCL, during eyes-open compared to eyes-closed rest.

9.5 Summary

This chapter describes the investigation of connectivity to motor and sensory regions of interest that were activated or deactivated by the short blocks tasks in chapters 7 and 8, and the modulation of steady-state connectivity during tasks that activate or deactivate these regions.

The main findings are summarised as follows.

Steady-state connectivity Connectivity between the M1 ROIs in each hemisphere and between the S1 ROIs in each hemisphere was significant during all four conditions in fMRI. In NIRS there was large interindividual variability, and across the group connectivity was only significant between M1 ROIs in oxyHb during the REST conditions. This is possibly due to poor optode placement and/or low SNR in a few subjects. In both oxyHb and deoxyHb, in the hemisphere ipsilateral to each ROI almost the entire volume was significantly connected to the ROI in each condition and each hemisphere, both with and without physiological noise correction. This may result from inadequate physiological noise correction or inaccurate image reconstruction.

Change in connectivity with task Although some evidence has previously been found for decreased interhemispheric M1 connectivity during unilateral tapping [357, 390, 325], in our fMRI data there was no evidence for changed interhemispheric M1 or S1 connectivity during COLD or TAP. Interestingly, the dorsal anterior precuneus which was deactivated by the short blocks left and right motor tasks, showed increased connectivity to motor areas including bilateral M1 and SMA during the TAP condition compared to REST.

However, in the NIRS data, in the left (contralateral) hemisphere, intrahemispheric connectivity to the left M1 ROI and interhemispheric connectivity to the right M1 ROI decreased during COLD and TAP. Also, in the NIRS ROI data from individual subjects, a majority showed decreases in interhemispheric connectivity during TAP and COLD.

Although there was no significant change in connectivity between the left and right M1 ROIs in either fMRI and NIRS data, the mean connectivity z-scores across subjects in both cases were slightly greater in REST2 than in the other conditions. This is consistent with the observation of increased low frequency spectral power and connectivity in motor regions in a resting period following performance of a task [390].

Change in power spectrum with task Unlike in [390], no significant changes in the amplitude of fluctuations with condition were found in the fMRI data. In the oxyHb data, there was an increase in VLF power for TAP compared to REST1 in both the left and right hemispheres, and a decrease in LF power in TAP compared to REST1 in the left (contralateral) hemisphere only. In deoxyHb, there was increased LF power for COLD compared to REST2 and decreased power for TAP compared to REST1 in the left hemisphere.

Relationship between deactivation and connectivity A negative correlation across subjects between the mean parameter estimate for ipsilateral deactivation to RTAP and the interhemispheric connectivity z-score during the TAP condition approached significance. This is opposite to the finding of [325] who observed that individual decrease in left-right SM1 connectivity during a continuous motor task correlates with stronger suppression of collateral SM1 activation during the task.

Chapter 10

Conclusions

In this thesis, the use of near infrared imaging for brain imaging has been explored, particularly in contrast with fMRI, which is the current gold-standard of functional brain imaging. Because of differences in the data acquired with each technique, there are certain issues in NIRS imaging which remain largely unresolved: these include standardisation of optode placement, intersubject registration, correction for physiological interference and removal of motion artefacts.

We have attempted to address the problem of motion artefact removal by using imaging channels with extremely small distance between source and detector to detect subject motion. In a comparison of several motion artefact removal techniques, independent component analysis and multiple-channel regression were found to improve the signal-to-noise ratio in data sets containing deliberate motion artefacts.

In an investigation of an action execution and observation task in single subjects, all four subjects showed activation in the right motor cortex for left hand tapping, but three also showed almost equal activation for left hand tapping. To test whether these results could have occurred by chance, the same analysis was performed on task-free data collected during a resting baseline period. Because the oxyHb signal represents the arterial component of the vasculature and is subject to spontaneous oscillations resulting from vasomotion and blood pressure fluctuation, we hypothesised that false positives might occur in oxyHb data. However, false positives were only found in deoxyHb and were mostly eliminated when correction for multiple comparisons was used. The reason for false positives occurring in deoxyHb may be because of its lower SNR. By contrast, deoxyhaemoglobin responses to the task, where they occurred, were much smaller in extent than oxyhaemoglobin responses and often did not overlap spatially with significant oxyhaemoglobin responses. If activation is counted only when both oxyHb and deoxyHb signals in a particular area pass the significance threshold, false positives would not be found in null data, but using this criterion true task responses are also likely to be less reliably observed.

In random effects group analyses of null data no false positives were found, but in fixed effects analyses the number of false positives increases with increased smoothing, and is eliminated with prewhitening and correction for multiple comparisons. We recommend the use of prewhitening and correction for multiple comparisons and moderate smoothing (we used a low pass filter cutoff of 0.5 Hz) to reduce the false positive

rate. However even when only some of these precautions are taken, the false positive rate is not very high - because of the low SNR in NIRS, and high intersubject variability, the problem of actually detecting a response when it exists maybe more critical than detecting a significant response by chance when none occurred. However it must be emphasised that from the low incidence of false positives detected in null data one cannot conclude anything about the possibility of detecting a false positive cerebral response as a result of systemic changes that occur simultaneously with a task.

In the second part of this thesis, an experiment investigating deactivation and connectivity in the sensorimotor system was conducted using fMRI and fNIRS in two separate sessions. There are several limitations to this experiment. Although 11 out of the 15 subjects participated in both scanning sessions, a further 4 only participated in one imaging session. In addition, the two scans were done in two sessions because facilities for simultaneous imaging using NIRS and fMRI are not available. This introduces intersession differences in response to the task as well as differences between modalities. Despite attempts to keep the scanning conditions as similar as possible by reclining the subject during NIRS, different levels of noise and a different scanning environment may have contributed to different levels of arousal in each experiment. In order to investigate autonomic responses during the task, as well as to reduce the confounding effect of respiration and cardiac variation on cerebral haemodynamic fluctuations, simultaneous recordings of respiration and pulse or ECG were performed. Differences in cardiovascular variables due to the task were not significant, except that heart rate was slowed during the short blocks cold condition, in the NIRS session only. Although physiological noise was removed from the data using regressors derived from cardiac and respiratory measurement, little effect of this noise removal was observed in the imaging data.

Targeting of the sensorimotor area using each subject's anatomical MRI and a Polhemus magnetic 3D position tracker was found to take significantly longer and to perform no more efficiently than location of the motor area using the Cz position of the 10-20 system. For this reason, optode placement was performed using the 10-20 positions, a method that may lack sophistication, but that has been used successfully in many NIRS studies up till now. NIRS probes were then registered to the individual subject's MRI image, and then as best as possible to the DOT template used in the image reconstruction software. Intersubject alignment was approximate, within the restrictions imposed by the DOT image reconstruction software which only allows optodes at pre-specified locations on the model head.

Using surface-based alignment of NIRS and MRI data means that for each subject only one MRI image is required. This image could be acquired at any time, instead of having to acquire an MRI image for each NIRS session. Registration of NIRS probes to a subject's individual anatomy is highly desirable, and knowledge of individual anatomy may be used in the DOT forward problem solution [111]. However, it is possible to perform NIRS without an MRI of each subject via registration to an atlas, or the MRI of a representative subject. Reasonable anatomical localisation has been shown to be possible using this method [231], and the approximate alignment via registration to the subject's own MRI that was performed here may not have been significantly more accurate than direct registration to a template MRI.

In spite of the aforementioned limitations, NIRS results in the group were similar to the results of fMRI analyses in many cases. Responses are more reliably found in oxyHb than deoxyHb. Because the amplitude of the oxyHb response to functional stimulation is larger than the deoxyHb response, noise due to random

error and cross-talk may disproportionately affect deoxyHb, resulting in lower SNR than in oxyHb [1]. This has been suggested as the reason that in some studies better correlation has been found between BOLD and oxyHb than between BOLD and deoxyHb [200, 1]. Similarly, in the experiments described in this thesis the deoxyHb signal appears to produce fewer significant responses, as well as more false positives than oxyHb, in spite of the fact that physiological noise is more prominent in the oxyHb signal which originates predominantly from the arteries.

Laterality effects to motor and noxious cold stimulation were similar in both sessions in our right-handed subjects. Although it has previously been found that NIRS is equally as powerful as fMRI for comparing conditions within subjects, but fMRI is preferable to NIRS for group comparisons [5], we found group level results to be more reproducible between NIRS and fMRI than individual results. NIRS reproducibility between sessions has similarly been found to be better in group, rather than single-subject analyses [147]. In some subjects responses were not observed, possibly due to poor optode placement, or low CNR. Because it is relatively difficult to detect a response in a single subject, more data may be required for NIRS experiments. Scanning each subject for longer may increase the reliability of response detection in individual subjects and minimise physiological and random noise. This is especially true when brain regions further from the scalp are being studied [4]. However, if there are subjects in which it is not possible to observe a response because of characteristics of head anatomy or tissue properties, it may be necessary to scan more subjects to obtain significant results at the group level.

Robust ipsilateral deactivation to a cold stimulus was apparent in NIRS data, however, the absence in NIRS of ipsilateral deactivation to a unilateral motor task as found in fMRI may be because of systemic changes with the task that mask deactivation. Although we found no significant change in heart rate or heart rate variability during the motor task in NIRS, heart rate slowed significantly during the cold stimulation. It is possible that changes in blood pressure or scalp blood flow may occur without significant change in heart rate. Blood pressure changes may also affect cerebral, as well as scalp haemodynamics [85]. Therefore, in addition to or perhaps more importantly than, measurement of heart rate and respiration, the simultaneous measurement of blood pressure would be a useful addition to most NIRS experiments, particularly when changes in autonomic arousal may occur with the task.

Although activation on the cortical surface can be measured with NIRS, the limited penetration depth of near infrared light means that deeper brain structures are inaccessible. This precludes the study of entire brain networks, although connectivity between cortical components of a functional network may still be investigated, as was done in this study. Using fifth nearest-neighbour measurements in DOT image reconstruction at a source-detector separation distance of 54 mm has been shown to be able to recover changes up to 20 mm deep within the brain; sufficient to measure activity within sulcal folds [195]. However, some apparent activations observed in this study were too deep to have been measured by NIRS and were clearly artefactual. Depth localisation in DOT may not always be entirely accurate due to the blurring inherent in diffuse image reconstruction, overestimation of the depth sensitivity by application of the diffusion approximation in media including non-scattering regions, and the tendency of many image reconstruction algorithms to push the recovered perturbation into deeper regions of the medium, which have the lowest weight [197].

The measurement of changes in the PSD of spontaneous fluctuations is an important adjunct to studies of connectivity. If the amplitude of the correlated oscillations decreases relative to spatially uncorrelated signal components, a decrease in connectivity will be observed [390]. It seems possible that if vasodilation as a result of hypercapnia tends to reduce the amplitude of spontaneous low-frequency fluctuations and decrease connectivity, vasodilation as a response to functional activation may similarly reduce the amplitude of these spontaneous oscillations. However, there is evidence to suggest that changes in network correlations during task performance is associated with widespread changes in the amplitude of low-frequency oscillations, rather than specific changes in the connectivity of particular networks [390].

Although we expected to find a change in connectivity between deactivated ipsilateral primary sensorimotor cortex and contralateral activated primary sensorimotor cortex during motor and cold tasks, no such changes in connectivity or PSD were apparent in our fMRI data with or without correction for physiological effects. We conclude that the short duration of these runs did not allow for stable connectivity measures or spectral estimates to be obtained.

By contrast, in NIRS, the expected tendency for reduced interhemispheric correlations for tap and cold conditions was found in the left hemisphere only. The decrease in oxyHb and deoxyHb LF spectral power in the left hemisphere during TAP is consistent with this reduction in correlated voxels. A significant bilateral increase in VLF power during TAP is in opposition to the finding of reduced PSD at 0.03 Hz in [390]. Although we found no changes in cardiac activity that were significant at the group level, and respiration and heart rate variability were regressed from the data, we cannot exclude the possibility that some changes in connectivity and PSD during NIRS occurred as a result of systemic changes that were not accounted for by the physiological noise correction method, in particular blood pressure oscillations that are enhanced by activation of the sympathetic nervous system [401].

We did not examine the spectral power of physiological recordings for comparison with the PSD of brain haemodynamics. For future studies it would be interesting to look for changes in spectral power in both physiological and cerebral measurements, particularly in tasks that involve autonomic changes. However, given the intersubject variability in autonomic response observed in the cold pressor test in normal subjects, as judged by heart rate and heart rate variability, it is possible that a much larger number of subjects would need to be studied, in order to group subjects who showed similar responses to the task. More work should be done investigating changes in cerebral haemodynamics related to cardiac, respiration and blood pressure changes during task performance in both fMRI and NIRS.

In addition, changes in spontaneous fluctuations with, and after, task performance have to date been investigated in a limited number of tasks and functional networks. It is possible that connectivity and PSD changes differ between networks and between tasks.

As more commercial instruments become available, standards and conventions for the analysis of NIRS data, as there are for fMRI, seem desirable and would simplify the use of NIRS amongst neuroscience researchers. Although this is made complicated by the construction of individual imaging systems, which may differ in many ways, recently several software packages have become available that will address this problem. Standardisation of optode placement using a brain atlas or individual MRIs, and NIRS technology that better accounts for variation in head anatomy and tissue properties between subjects will improve the

reliability of group level analyses.

The NIRS system used in this study provides 30 sources and detectors (900 channels) on 30 optodes. However, for measurement of bilateral motor cortex this leaves only 15 optodes per hemisphere. Because in this system both source and detector are located on the same optode, and because the DOT image reconstruction algorithm requires a dense optode configuration and strictly defined optode locations which are enforced by the rigid optode holder frame, there are few channels with sufficient source-detector separation (>3 cm) to measure as deep as the cerebral cortex. This means that a rather small area of cortex can be sampled for this kind of experiment, making accurate optode placement critical. Also, although a small area of cortex is actually measured, in the pre-calculated weight matrix used for image reconstruction weights exist outside this area, which can result in spurious activations in areas which could not have contributed to the observed surface measurements. An increase in the number of available channels would allow more brain area to be covered and broaden the range of experiments possible with the system.

The main drawback of the DYNOT system is its lack of flexibility. The rigid optode holder helmet and frame makes it challenging to ensure accurate optode placement and to make good scalp contact in subjects with hair. Although fast measurement and image reconstruction is possible using an efficient algorithm, the limited number of FEM models currently available for image reconstruction restricts the possible optode configurations if tomographic imaging is required. Also, using the provided image reconstruction algorithm imposes restrictions on the user as it is difficult to apply preprocessing other than what is provided by the software, and the images that are output require some manipulation before registration or analysis can take place using other software.

Future versions of the DYNOT system are certain to increase the number of imaging channels as improved hardware is developed. Software improvements are relatively simple to implement and the capability of allowing users to plug in their own processing modules could lead to rapid advances which would make significant contributions to the field of functional NIRS imaging.

In spite of the limitations of the study and of the imaging system, we have found that even when performed in separate sessions on similar populations, certain results are reproducible between fMRI and NIRS at the group level. However, the lack of ipsilateral motor cortex deactivation at the group level, and the lack of correspondence between NIRS and fMRI in the study of spontaneous fluctuations deserves further investigation.

Bibliography

- [1] G. Strangman, J. P. Culver, J. H. Thompson, D. A. Boas, and J. P. Sutton, "A quantitative comparison of simultaneous BOLD fMRI and NIRS recordings during functional brain activation," *NeuroImage*, vol. 17, pp. 719–731, Oct 2002.
- [2] V. Toronov, A. Webb, J. H. Choi, M. Wolf, A. Michalos, and E. G. D. Hueber, "Investigation of human brain hemodynamics by simultaneous near-infrared spectroscopy and functional magnetic resonance imaging," *Med. Phys.*, vol. 28, no. 4, pp. 521–7, 2001.
- [3] T. Huppert, R. Hoge, A. Dale, M. Franceschini, and D. Boas, "Quantitative spatial comparison of diffuse optical imaging with blood oxygen level-dependent and arterial spin labeling-based functional magnetic resonance imaging," *J. Biomed. Opt.*, vol. 11, p. 064018, 2006.
- [4] X. Cui, S. Bray, D. M. Bryant, G. H. Glover, and A. L. Reiss, "A quantitative comparison of NIRS and fMRI across multiple cognitive tasks," *NeuroImage*, vol. 54, pp. 2808–2821, Feb 2011.
- [5] L. Minati, E. Visani, N. G. Dowell, N. Medford, and H. D. Critchley, "Variability comparison of simultaneous brain near-infrared spectroscopy and functional magnetic resonance imaging during visual stimulation," *J. Med. Eng. Technol.*, vol. 35, pp. 370–376, 2011.
- [6] F. C. Robertson, T. S. Douglas, and E. M. Meintjes, "Motion artifact removal for functional near infrared spectroscopy: a comparison of methods," *IEEE Trans. Biomed. Eng.*, vol. 57, pp. 1377–1387, Jun 2010.
- [7] G. Glover, T. Li, and D. Ress, "Image-based method for retrospective correction of physiological motion effects in fMRI: RETROICOR," *Magn. Reson. Med.*, vol. 44, pp. 162–167, Jul 2000.
- [8] S. Ogawa, T. M. Lee, A. R. Kay, and D. W. Tank, "Brain magnetic resonance imaging with contrast dependent on blood oxygenation," *Proc. Natl. Acad. Sci. U.S.A.*, vol. 87, pp. 9868–9872, Dec 1990.
- [9] S. Ogawa, T. M. Lee, A. S. Nayak, and P. Glynn, "Oxygenation-sensitive contrast in magnetic resonance image of rodent brain at high magnetic fields," *Magn. Reson. Med.*, vol. 14, pp. 68–78, Apr 1990.
- [10] P. A. Bandettini, E. C. Wong, R. S. Hinks, R. S. Tikofsky, and J. S. Hyde, "Time course EPI of human brain function during task activation," *Magn. Reson. Med.*, vol. 25, pp. 390–397, Jun 1992.

BIBLIOGRAPHY

- [11] K. K. Kwong, J. W. Belliveau, D. A. Chesler, I. E. Goldberg, R. M. Weisskoff, B. P. Poncelet, D. N. Kennedy, B. E. Hoppel, M. S. Cohen, and R. Turner, "Dynamic magnetic resonance imaging of human brain activity during primary sensory stimulation," *Proc. Natl. Acad. Sci. U.S.A.*, vol. 89, pp. 5675–5679, Jun 1992.
- [12] A. Villringer, J. Planck, C. Hock, L. Schleinkofer, and U. Dirnagl, "Near infrared spectroscopy (NIRS): a new tool to study hemodynamic changes during activation of brain function in human adults," *Neurosci. Lett.*, vol. 154, pp. 101–104, May 1993.
- [13] R. B. Buxton, E. C. Wong, and L. R. Frank, "Dynamics of blood flow and oxygenation changes during brain activation: the balloon model," *Magn Reson Med*, vol. 39, pp. 855–864, Jun 1998.
- [14] T. Jin, P. Wang, M. Tasker, F. Zhao, and S. Kim, "Source of nonlinearity in echo-time-dependent BOLD fMRI," *Magn. Reson. Med.*, vol. 55, pp. 1281–1290, Jun 2006.
- [15] V. Toronov, S. Walker, R. Gupta, J. H. Choi, E. Gratton, D. Hueber, and A. Webb, "The roles of changes in deoxyhemoglobin concentration and regional cerebral blood volume in the fMRI BOLD signal," *NeuroImage*, vol. 19, pp. 1521–1531, Aug 2003.
- [16] E. Yacoub and X. Hu, "Detection of the early decrease in fMRI signal in the motor area," *Magn. Reson. Med.*, vol. 45, pp. 184–190, Feb 2001.
- [17] M. Silvennoinen, C. Clingman, X. Golay, R. Kauppinen, and P. van Zijl, "Comparison of the dependence of blood R2 and R2* on oxygen saturation at 1.5 and 4.7 Tesla," *Magn. Reson. Med.*, vol. 49, pp. 47–60, Jan 2003.
- [18] A. Smith, B. Lewis, U. Ruttimann, F. Ye, T. Sinnwell, Y. Yang, J. Duyn, and J. Frank, "Investigation of low frequency drift in fMRI signal," *NeuroImage*, vol. 9, pp. 526–533, May 1999.
- [19] P. Van de Moortele, J. Pfeuffer, G. Glover, K. Ugurbil, and X. Hu, "Respiration-induced B0 fluctuations and their spatial distribution in the human brain at 7 Tesla," *Magn. Reson. Med.*, vol. 47, pp. 888–895, May 2002.
- [20] C. Windischberger, H. Langenberger, T. Sycha, E. Tschernko, G. Fuchsjaeger-Mayerl, L. Schmetterer, and E. Moser, "On the origin of respiratory artifacts in BOLD-EPI of the human brain," *Magnetic Resonance Imaging*, vol. 20, pp. 575–582, Oct 2002.
- [21] M. Dagli, J. Ingeholm, and J. Haxby, "Localization of cardiac-induced signal change in fMRI," *NeuroImage*, vol. 9, pp. 407–415, Apr 1999.
- [22] X. Zhao, J. Bodurka, A. Jesmanowicz, and S. Li, "B(0)-fluctuation-induced temporal variation in EPI image series due to the disturbance of steady-state free precession," *Magn. Reson. Med.*, vol. 44, pp. 758–765, Nov 2000.

- [23] S. Li, B. Biswal, Z. Li, R. Risinger, C. Rainey, J. Cho, B. Salmeron, and E. Stein, "Cocaine administration decreases functional connectivity in human primary visual and motor cortex as detected by functional MRI," *Magn. Reson. Med.*, vol. 43, pp. 45–51, Jan 2000.
- [24] P. K. Bhattacharyya and M. J. Lowe, "Cardiac-induced physiologic noise in tissue is a direct observation of cardiac-induced fluctuations," *Magnetic Resonance Imaging*, vol. 22, pp. 9–13, Jan 2004.
- [25] T. Lund, K. Madsen, K. Sidaros, W. Luo, and T. Nichols, "Non-white noise in fMRI: does modelling have an impact?," *NeuroImage*, vol. 29, pp. 54–66, Jan 2006.
- [26] D. Cordes, V. Haughton, K. Arfanakis, J. Carew, P. Turski, C. Moritz, M. Quigley, and M. Meyerand, "Frequencies contributing to functional connectivity in the cerebral cortex in "resting-state" data," *AJNR Am. J. Neuroradiol.*, vol. 22, pp. 1326–1333, Aug 2001.
- [27] E. B. Beall and M. J. Lowe, "Isolating physiologic noise sources with independently determined spatial measures," *NeuroImage*, vol. 37, pp. 1286–1300, Oct 2007.
- [28] D. Raj, A. Anderson, and J. Gore, "Respiratory effects in human functional magnetic resonance imaging due to bulk susceptibility changes," *Phys. Med. Biol.*, vol. 46, pp. 3331–3340, Dec 2001.
- [29] J. Brosch, T. Talavage, J. Ulmer, and J. Nyenhuis, "Simulation of human respiration in fMRI with a mechanical model," *IEEE Trans. Biomed. Eng.*, vol. 49, pp. 700–707, Jul 2002.
- [30] D. Raj, D. Paley, A. Anderson, R. Kennan, and J. Gore, "A model for susceptibility artefacts from respiration in functional echo-planar magnetic resonance imaging," *Phys. Med. Biol.*, vol. 45, pp. 3809–3820, Dec 2000.
- [31] P. van Gelderen, J. de Zwart, P. Starewicz, R. Hinks, and J. Duyn, "Real-time shimming to compensate for respiration-induced B0 fluctuations," *Magn. Reson. Med.*, vol. 57, pp. 362–368, Feb 2007.
- [32] R. L. Barry and R. S. Menon, "Modeling and suppression of respiration-related physiological noise in echo-planar functional magnetic resonance imaging using global and one-dimensional navigator echo correction," *Magn. Reson. Med.*, vol. 54, pp. 411–418, Aug 2005.
- [33] B. Wowk, M. McIntyre, and J. Saunders, "k-Space detection and correction of physiological artifacts in fMRI," *Magn. Reson. Med.*, vol. 38, pp. 1029–1034, Dec 1997.
- [34] J. Lee, J. Santos, S. Conolly, K. Miller, B. Hargreaves, and J. Pauly, "Respiration-induced B0 field fluctuation compensation in balanced SSFP: real-time approach for transition-band SSFP fMRI," *Magn. Reson. Med.*, vol. 55, pp. 1197–1201, May 2006.
- [35] X. Hu and S. Kim, "Reduction of signal fluctuation in functional MRI using navigator echoes," *Magn. Reson. Med.*, vol. 31, pp. 495–503, May 1994.
- [36] R. L. Barry, L. M. Klassen, J. M. Williams, and R. S. Menon, "Hybrid two-dimensional navigator correction: a new technique to suppress respiratory-induced physiological noise in multi-shot echo-planar functional MRI," *NeuroImage*, vol. 39, pp. 1142–1150, Feb 2008.

BIBLIOGRAPHY

- [37] M. Cohen and J. Taylor, "Short-term cardiovascular oscillations in man: measuring and modelling the physiologies," *J. Physiol. (Lond.)*, vol. 542, pp. 669–683, Aug 2002.
- [38] R. Wise, K. Ide, M. Poulin, and I. Tracey, "Resting fluctuations in arterial carbon dioxide induce significant low frequency variations in BOLD signal," *NeuroImage*, vol. 21, pp. 1652–1664, Apr 2004.
- [39] J. Farthing, J. Cummine, R. Borowsky, P. Chilibeck, G. Binsted, and G. Sarty, "False activation in the brain ventricles related to task-correlated breathing in fMRI speech and motor paradigms," *MAGMA*, vol. 20, pp. 157–168, Jun 2007.
- [40] C. Beckmann, M. DeLuca, J. T. Devlin, and S. M. Smith, "Investigations into resting-state connectivity using independent component analysis," *Philos. Trans. R. Soc. Lond., B, Biol. Sci.*, vol. 360, pp. 1001–1013, May 2005.
- [41] M. De Luca, C. Beckmann, N. De Stefano, P. Matthews, and S. Smith, "fMRI resting state networks define distinct modes of long-distance interactions in the human brain," *NeuroImage*, vol. 29, pp. 1359–1367, Feb 2006.
- [42] M. Lowe, B. Mock, and J. Sorenson, "Functional connectivity in single and multislice echoplanar imaging using resting-state fluctuations," *NeuroImage*, vol. 7, pp. 119–132, Feb 1998.
- [43] T. Lund, "fcMRI—mapping functional connectivity or correlating cardiac-induced noise?," *Magn. Reson. Med.*, vol. 46, pp. 628–629, Sep 2001.
- [44] B. Biswal, A. DeYoe, and J. Hyde, "Reduction of physiological fluctuations in fMRI using digital filters," *Magn. Reson. Med.*, vol. 35, pp. 107–113, Jan 1996.
- [45] R. Deckers, P. van Gelderen, M. Ries, O. Barret, J. Duyn, V. Ikonomidou, M. Fukunaga, G. Glover, and J. de Zwart, "An adaptive filter for suppression of cardiac and respiratory noise in MRI time series data," *NeuroImage*, vol. 33, pp. 1072–1081, Dec 2006.
- [46] G. Turner and D. Twieg, "Study of temporal stationarity and spatial consistency of fMRI noise using independent component analysis," *IEEE Trans. Med. Imaging*, vol. 24, pp. 712–718, Jun 2005.
- [47] V. Kiviniemi, J. Kantola, J. Jauhiainen, A. Hyvärinen, and O. Tervonen, "Independent component analysis of nondeterministic fMRI signal sources," *NeuroImage*, vol. 19, pp. 253–260, Jun 2003.
- [48] B. Rogers, V. Morgan, A. Newton, and J. Gore, "Assessing functional connectivity in the human brain by fMRI," *Magnetic Resonance Imaging*, vol. 25, pp. 1347–1357, Dec 2007.
- [49] M. Gavrilescu, G. Stuart, S. Rossell, K. Henshall, C. McKay, A. Sergejew, D. Copolov, and G. Egan, "Functional connectivity estimation in fMRI data: Influence of preprocessing and time course selection," *Hum. Brain Mapp.*, Oct 2007.
- [50] V. Kiviniemi, H. Haanpää, J. Kantola, J. Jauhiainen, V. Vainionpää, S. Alahuhta, and O. Tervonen, "Midazolam sedation increases fluctuation and synchrony of the resting brain BOLD signal," *Magnetic Resonance Imaging*, vol. 23, pp. 531–537, May 2005.

-
- [51] P. Jezzard, P. Matthews, and S. Smith, eds., *Functional MRI an introduction to methods*. Great Clarendon Street, Oxford OX2 6DP: Oxford University Press, 2001.
- [52] F. F. Jobsis, "Noninvasive, infrared monitoring of cerebral and myocardial oxygen sufficiency and circulatory parameters.," *Science*, vol. 198, no. 4323, pp. 1264–7, 1977.
- [53] A. Gibson, J. Hebden, and S. Arridge, "Recent advances in diffuse optical imaging," *Phys. Med. Biol.*, vol. 50, pp. 1–43, Feb 2005.
- [54] H. Zhao, Y. Tanikawa, F. Gao, Y. Onodera, A. Sassaroli, K. Tanaka, and Y. Yamada, "Maps of optical differential pathlength factor of human adult forehead, somatosensory motor and occipital regions at multi-wavelengths in NIR," *Phys. Med. Biol.*, vol. 47, pp. 2075–2093, Jun 2002.
- [55] Y. Hoshi, "Functional near-infrared spectroscopy: current status and future prospects.," *J. Biomed. Opt.*, vol. 12, no. 6, p. 062106, 2007.
- [56] E. Okada and D. T. Delpy, "Near-infrared light propagation in an adult head model. I. Modeling of low-level scattering in the cerebrospinal fluid layer," *Appl Opt*, vol. 42, pp. 2906–2914, Jun 2003.
- [57] E. Okada and D. T. Delpy, "Near-infrared light propagation in an adult head model. II. Effect of superficial tissue thickness on the sensitivity of the near-infrared spectroscopy signal," *Appl Opt*, vol. 42, pp. 2915–2922, Jun 2003.
- [58] T. Germon, P. Evans, N. Barnett, P. Wall, A. Manara, and R. Nelson, "Cerebral near infrared spectroscopy: emitter-detector separation must be increased," *Br. J. Anaesth.*, vol. 82, pp. 831–837, Jun 1999.
- [59] D. K. Joseph, T. J. Huppert, M. A. Franceschini, and D. A. Boas, "Diffuse optical tomography system to image brain activation with improved spatial resolution and validation with functional magnetic resonance imaging," *Appl. Opt.*, vol. 45, pp. 8142–8151, Nov 2006.
- [60] B. W. Zeff, B. R. White, H. Dehghani, B. L. Schlaggar, and J. P. Culver, "Retinotopic mapping of adult human visual cortex with high-density diffuse optical tomography.," *Proc. Natl. Acad. Sci. U.S.A.*, vol. 104, no. 29, pp. 12169–74, 2007.
- [61] K. Ciftci, B. Sankur, Y. P. Kahya, and A. Akin, "Multilevel statistical inference from functional near-infrared spectroscopy data during stroop interference," *IEEE Trans. Biomed. Eng.*, vol. 55, pp. 2212–2220, Sep 2008.
- [62] H. L. Graber, Y. Pei, and R. L. Barbour, "Imaging of spatiotemporal coincident states by DC optical tomography.," *IEEE Trans. Med. Imaging*, vol. 21, no. 8, pp. 852–66, 2002.
- [63] J. C. Ye, S. Tak, K. E. Jang, J. Jung, and J. Jang, "NIRS-SPM: statistical parametric mapping for near-infrared spectroscopy.," *NeuroImage*, vol. 44, no. 2, pp. 428–47, 2009.

BIBLIOGRAPHY

- [64] S. Prince, V. Kolehmainen, J. P. Kaipio, M. A. Franceschini, D. Boas, and S. R. Arridge, "Time-series estimation of biological factors in optical diffusion tomography," *Phys. Med. Biol.*, vol. 48, pp. 1491–1504, Jun 2003.
- [65] C. H. Schmitz, D. P. Klemer, R. Hardin, M. S. Katz, Y. Pei, H. L. Graber, M. B. Levin, R. D. Levina, N. Franco, W. B. Solomon, and R. L. Barbour, "Design and implementation of dynamic near-infrared optical tomographic imaging instrumentation for simultaneous dual-breast measurements," *Appl Opt*, vol. 44, pp. 2140–2153, Apr 2005.
- [66] U. Emir, C. Akgul, A. Akin, A. Ertuzun, B. Sankur, and K. Harmanci, "Wavelet denoising vs ICA denoising for functional optical imaging," in *Proceedings of First International IEEE EMBS Conference on Neural Engineering*, (Capri Island, Italy), pp. 384–387, IEEE, March 2003.
- [67] F. Matthews, B. A. Pearlmutter, T. E. Ward, C. Soraghan, and C. Markham, "Hemodynamics for brain-computer interfaces," *IEEE Signal Processing Magazine*, vol. 25, pp. 87–94, 2008.
- [68] S. Luu and T. Chau, "Decoding subjective preference from single-trial near-infrared spectroscopy signals," *J. Neural Eng.*, vol. 6, no. 1, p. 16003, 2009.
- [69] T. J. Huppert, S. G. Diamond, M. A. Franceschini, and D. A. Boas, "HomER: a review of time-series analysis methods for near-infrared spectroscopy of the brain," *Appl. Opt.*, vol. 48, pp. D280–298, Apr 2009.
- [70] R. B. Saager and A. J. Berger, "Direct characterization and removal of interfering absorption trends in two-layer turbid media.," *J. Opt. Soc. Am. A. Opt. Image Sci. Vis.*, vol. 22, no. 9, pp. 1874–82, 2005.
- [71] Q. Zhang, E. N. Brown, and G. E. Strangman, "Adaptive filtering to reduce global interference in evoked brain activity detection: a human subject case study.," *J. Biomed. Opt.*, vol. 12, no. 6, p. 064009, 2007.
- [72] Q. Zhang, G. E. Strangman, and G. Ganis, "Adaptive filtering to reduce global interference in non-invasive NIRS measures of brain activation: How well and when does it work?," *NeuroImage*, vol. 45, pp. 788–794, Apr 2009.
- [73] X. Zhang, V. Toronov, and A. Webb, "Simultaneous integrated diffuse optical tomography and functional magnetic resonance imaging of the human brain," *Optics Express*, vol. 13, pp. 5513–5521, Jul 2005.
- [74] S. Kohno, I. Miyai, A. Seiyama, I. Oda, A. Ishikawa, S. Tsuneishi, T. Amita, and K. Shimizu, "Removal of the skin blood flow artifact in functional near-infrared spectroscopic imaging data through independent component analysis," *J. Biomed. Opt.*, vol. 12, no. 6, p. 062111, 2007.
- [75] G. Gratton and P. M. Corballis, "Removing the heart from the brain: compensation for the pulse artifact in the photon migration signal.," *Psychophysiology*, vol. 32, no. 3, pp. 292–9, 1995.

- [76] G. Morren, U. Wolf, P. Lemmerling, M. Wolf, J. H. Choi, E. Gratton, L. D. Lathauwer, and S. V. Huffel, "Detection of fast neuronal signals in the motor cortex from functional near infrared spectroscopy measurements using independent component analysis," *Med. Biol. Eng. Comput.*, vol. 42, no. 1, pp. 92–9, 2004.
- [77] I. Tachtsidis, T. S. Leung, A. Chopra, P. H. Koh, C. B. Reid, and C. E. Elwell, "False positives in functional near-infrared topography," *Adv. Exp. Med. Biol.*, vol. 645, pp. 307–314, 2009.
- [78] G. Jasdzewski, G. Strangman, J. Wagner, K. K. Kwong, R. A. Poldrack, D. A. Boas, and J. P. Sutton, "Differences in the hemodynamic response to event-related motor and visual paradigms as measured by near-infrared spectroscopy," *NeuroImage*, vol. 20, pp. 479–488, Sep 2003.
- [79] I. Miyai, H. C. Tanabe, I. Sase, H. Eda, I. Oda, I. Konishi, Y. Tsunazawa, T. Suzuki, T. Yanagida, and K. Kubota, "Cortical mapping of gait in humans: a near-infrared spectroscopic topography study," *NeuroImage*, vol. 14, pp. 1186–1192, Nov 2001.
- [80] M. Suzuki, I. Miyai, T. Ono, I. Oda, I. Konishi, T. Kochiyama, and K. Kubota, "Prefrontal and premotor cortices are involved in adapting walking and running speed on the treadmill: an optical imaging study," *NeuroImage*, vol. 23, pp. 1020–1026, Nov 2004.
- [81] D. R. Leff, F. Orihuela-Espina, C. E. Elwell, T. Athanasiou, D. T. Delpy, A. W. Darzi, and G. Z. Yang, "Assessment of the cerebral cortex during motor task behaviours in adults: a systematic review of functional near infrared spectroscopy (fNIRS) studies," *NeuroImage*, vol. 54, pp. 2922–2936, Feb 2011.
- [82] M. A. Franceschini, S. Fantini, J. H. Thompson, J. P. Culver, and D. A. Boas, "Hemodynamic evoked response of the sensorimotor cortex measured noninvasively with near-infrared optical imaging," *Psychophysiology*, vol. 40, pp. 548–560, Jul 2003.
- [83] I. Tachtsidis, T. S. Leung, L. Devoto, D. T. Delpy, and C. E. Elwell, "Measurement of frontal lobe functional activation and related systemic effects: a near-infrared spectroscopy investigation," *Adv. Exp. Med. Biol.*, vol. 614, no. NIL, pp. 397–403, 2008.
- [84] I. Tachtsidis, T. S. Leung, M. M. Tisdall, P. Devendra, M. Smith, D. T. Delpy, and C. E. Elwell, "Investigation of frontal cortex, motor cortex and systemic haemodynamic changes during anagram solving," *Adv. Exp. Med. Biol.*, vol. 614, pp. 21–28, 2008.
- [85] L. Minati, I. U. Kress, E. Visani, N. Medford, and H. D. Critchley, "Intra- and extra-cranial effects of transient blood pressure changes on brain near-infrared spectroscopy (NIRS) measurements," *J. Neurosci. Methods*, Mar 2011.
- [86] Y. Zhang, D. H. Brooks, and D. A. Boas, "A haemodynamic response function model in spatio-temporal diffuse optical tomography," *Phys. Med. Biol.*, vol. 50, pp. 4625–4644, Oct 2005.
- [87] F. Orihuela-Espina, D. R. Leff, D. R. James, A. W. Darzi, and G. Z. Yang, "Quality control and assurance in functional near infrared spectroscopy (fNIRS) experimentation," *Phys. Med. Biol.*, vol. 55, pp. 3701–3724, Jul 2010.

BIBLIOGRAPHY

- [88] M. Izzetoglu, A. Devaraj, S. Bunce, and B. Onaral, "Motion artifact cancellation in NIR spectroscopy using Wiener filtering," *IEEE Trans. Biomed. Eng.*, vol. 52, pp. 934–938, May 2005.
- [89] T. Wilcox, H. Bortfeld, R. Woods, E. Wruock, and D. A. Boas, "Using near-infrared spectroscopy to assess neural activation during object processing in infants.," *J. Biomed. Opt.*, vol. 10, no. 1, p. 11010, 2005.
- [90] R. Sitaram, H. Zhang, C. Guan, M. Thulasidas, Y. Hoshi, A. Ishikawa, K. Shimizu, and N. Birbaumer, "Temporal classification of multichannel near-infrared spectroscopy signals of motor imagery for developing a brain-computer interface.," *NeuroImage*, vol. 34, no. 4, pp. 1416–27, 2007.
- [91] L. Becerra, W. Harris, D. Joseph, T. Huppert, D. A. Boas, and D. Borsook, "Diffuse optical tomography of pain and tactile stimulation: activation in cortical sensory and emotional systems," *NeuroImage*, vol. 41, no. 2, pp. 252–9, 2008.
- [92] H. Sato, M. Kiguchi, A. Maki, Y. Fuchino, A. Obata, T. Yoro, and H. Koizumi, "Within-subject reproducibility of near-infrared spectroscopy signals in sensorimotor activation after 6 months," *J. Biomed. Opt.*, vol. 11, p. 014021, 2006.
- [93] M. Pena, A. Maki, D. Kovacic, G. Dehaene-Lambertz, H. Koizumi, F. Bouquet, and J. Mehler, "Sounds and silence: an optical topography study of language recognition at birth.," *Proc. Natl. Acad. Sci. U.S.A.*, vol. 100, no. 20, pp. 11702–5, 2003.
- [94] K. Kotilahti, I. Nissila, M. Huotilainen, R. Makela, N. Gavrielides, T. Noponen, P. Bjorkman, V. Fellman, and T. Katila, "Bilateral hemodynamic responses to auditory stimulation in newborn infants.," *Neuroreport*, vol. 16, no. 12, pp. 1373–7, 2005.
- [95] A. Maki, Y. Yamashita, E. Watanabe, and H. Koizumi, "Visualizing human motor activity by using non-invasive optical topography," *Front. Med. Biol. Eng.*, vol. 7, pp. 285–297, 1996.
- [96] E. Watanabe, Y. Yamashita, A. Maki, Y. Ito, and H. Koizumi, "Non-invasive functional mapping with multi-channel near infra-red spectroscopic topography in humans," *Neurosci. Lett.*, vol. 205, pp. 41–44, Feb 1996.
- [97] H. H. Jasper, "The ten-twenty electrode system of the international federation," *Electroencephalogr. Clin. Neurophysiol.*, vol. 10, no. 2, pp. 371–375, 1958.
- [98] M. Okamoto, H. Dan, K. Shimizu, K. Takeo, T. Amita, I. Oda, I. Konishi, K. Sakamoto, S. Isobe, T. Suzuki, K. Kohyama, and I. Dan, "Multimodal assessment of cortical activation during apple peeling by NIRS and fMRI," *NeuroImage*, vol. 21, pp. 1275–1288, Apr 2004.
- [99] D. A. Boas, T. Gaudette, G. Strangman, X. Cheng, J. J. Marota, and J. B. Mandeville, "The accuracy of near infrared spectroscopy and imaging during focal changes in cerebral hemodynamics," *NeuroImage*, vol. 13, pp. 76–90, Jan 2001.

-
- [100] T. Durduran, G. Yu, M. G. Burnett, J. A. Detre, J. H. Greenberg, J. Wang, C. Zhou, and A. G. Yodh, "Diffuse optical measurement of blood flow, blood oxygenation, and metabolism in a human brain during sensorimotor cortex activation," *Opt Lett*, vol. 29, pp. 1766–1768, Aug 2004.
- [101] H. Obrig, C. Hirth, J. G. Junge-Hulsing, C. Doge, T. Wolf, U. Dirnagl, and A. Villringer, "Cerebral oxygenation changes in response to motor stimulation," *J. Appl. Physiol.*, vol. 81, pp. 1174–1183, Sep 1996.
- [102] H. Obrig, T. Wolf, C. Doge, J. J. Hulsing, U. Dirnagl, and A. Villringer, "Cerebral oxygenation changes during motor and somatosensory stimulation in humans, as measured by near-infrared spectroscopy," *Adv. Exp. Med. Biol.*, vol. 388, pp. 219–224, 1996.
- [103] K. Shibuya, T. Sadamoto, K. Sato, M. Moriyama, and M. Iwadate, "Quantification of delayed oxygenation in ipsilateral primary motor cortex compared with contralateral side during a unimanual dominant-hand motor task using near-infrared spectroscopy," *Brain Res.*, vol. 1210, pp. 142–147, May 2008.
- [104] N. Fujiwara, K. Sakatani, Y. Katayama, Y. Murata, T. Hoshino, C. Fukaya, and T. Yamamoto, "Evoked-cerebral blood oxygenation changes in false-negative activations in BOLD contrast functional MRI of patients with brain tumors," *NeuroImage*, vol. 21, pp. 1464–1471, Apr 2004.
- [105] C. Hirth, H. Obrig, J. Valdueza, U. Dirnagl, and A. Villringer, "Simultaneous assessment of cerebral oxygenation and hemodynamics during a motor task. A combined near infrared and transcranial Doppler sonography study," *Adv. Exp. Med. Biol.*, vol. 411, pp. 461–469, 1997.
- [106] M. Okamoto, H. Dan, K. Sakamoto, K. Takeo, K. Shimizu, S. Kohno, I. Oda, S. Isobe, T. Suzuki, K. Kohyama, and I. Dan, "Three-dimensional probabilistic anatomical cranio-cerebral correlation via the international 10-20 system oriented for transcranial functional brain mapping," *NeuroImage*, vol. 21, pp. 99–111, Jan 2004.
- [107] J. Sato, D. Takahashi, S. Arcuri, K. Sameshima, P. Morettin, and L. Baccalá, "Frequency domain connectivity identification: An application of partial directed coherence in fMRI," *Hum. Brain Mapp.*, Dec 2007.
- [108] M. Shibusawa, T. Takeda, K. Nakajima, K. Ishigami, and K. Sakatani, "Functional near-infrared spectroscopy study on primary motor and sensory cortex response to clenching," *Neurosci. Lett.*, vol. 449, pp. 98–102, Jan 2009.
- [109] C. Whalen, E. L. Maclin, M. Fabiani, and G. Gratton, "Validation of a method for coregistering scalp recording locations with 3D structural MR images," *Hum. Brain Mapp.*, vol. 29, pp. 1288 – 1301, Nov 2008.
- [110] A. Singh, M. Okamoto, H. Dan, V. Jurcak, and I. Dan, "Spatial registration of multichannel multi-subject fNIRS data to MNI space without MRI," *NeuroImage*, vol. 27, pp. 842–51, Oct 2005.

BIBLIOGRAPHY

- [111] A. Custo, D. A. Boas, D. Tsuzuki, I. Dan, R. Mesquita, B. Fischl, W. E. Grimson, and W. Wells, "Anatomical atlas-guided diffuse optical tomography of brain activation," *NeuroImage*, vol. 49, pp. 561–567, Jan 2010.
- [112] M. Caffini, A. Torricelli, R. Cubeddu, A. Custo, J. Dubb, and D. Boas, "Validating an anatomical brain atlas for analyzing NIRS measurements of brain activation," in *Biomedical Optics*, (Miami, Florida), April 2010.
- [113] Y. Xu, Y. Pei, and R. L. Barbour, "An anatomical atlas-based method for fNIRS tomography," in *Proceedings of the Sixteenth Annual Meeting of the Organization for Human Brain Mapping*, (Barcelona, Spain), Organization for Human Brain Mapping, 2010.
- [114] C. Habermehl, C. Schmitz, J. Mehnert, S. Holtze, and J. Steinbrink, "Three-dimensional superposition of diffuse optical tomography results and subjacent anatomic structures," in *Proc. SPIE*, (Munich, Germany), 2011.
- [115] S. Cutini, P. Scatturin, and M. Zorzi, "A new method based on ICBM152 head surface for probe placement in multichannel fNIRS," *NeuroImage*, vol. 54, pp. 919–927, Jan 2011.
- [116] D. Tsuzuki, V. Jurcak, A. K. Singh, M. Okamoto, E. Watanabe, and I. Dan, "Virtual spatial registration of stand-alone fNIRS data to MNI space," *NeuroImage*, vol. 34, pp. 1506–1518, Feb 2007.
- [117] W. N. Colier, V. Quaresima, B. Oeseburg, and M. Ferrari, "Human motor-cortex oxygenation changes induced by cyclic coupled movements of hand and foot," *Exp. Brain Res.*, vol. 129, pp. 457–461, Dec 1999.
- [118] M. Butti, A. Pastori, A. Merzagora, A. Bianchi, A. Bardoni, V. Branca, A. Costa, S. Cerutti, and G. Reni, "Combining near infrared spectroscopy and functional MRI during continuous performance test in healthy subjects," *Conf. Proc. IEEE Eng. Med. Biol. Soc.*, vol. 1, pp. 1944–1947, 2006.
- [119] S. Boden, H. Obrig, C. Kohncke, H. Benav, S. P. Koch, and J. Steinbrink, "The oxygenation response to functional stimulation: is there a physiological meaning to the lag between parameters?," *NeuroImage*, vol. 36, pp. 100–107, May 2007.
- [120] S. C. Wriessnegger, J. Kurzmann, and C. Neuper, "Spatio-temporal differences in brain oxygenation between movement execution and imagery: a multichannel near-infrared spectroscopy study," *Int. J. Psychophysiol.*, vol. 67, pp. 54–63, Jan 2008.
- [121] K. Amemiya, T. Ishizu, T. Ayabe, and S. Kojima, "Effects of motor imagery on intermanual transfer: a near-infrared spectroscopy and behavioural study," *Brain Res.*, vol. 1343, pp. 93–103, Jul 2010.
- [122] S. Nagamitsu, Y. Araki, T. Ioji, F. Yamashita, S. Ozono, M. Kouno, C. Iizuka, M. Hara, I. Shibuya, T. Ohya, Y. Yamashita, A. Tsuda, T. Kakuma, and T. Matsuiishi, "Prefrontal brain function in children with anorexia nervosa: A near-infrared spectroscopy study," *Brain Dev.*, Feb 2010.

-
- [123] L. Holper, M. Biallas, and M. Wolf, "Task complexity relates to activation of cortical motor areas during uni- and bimanual performance: a functional NIRS study," *NeuroImage*, vol. 46, pp. 1105–1113, Jul 2009.
- [124] L. Holper, T. Muehlemann, F. Scholkmann, K. Eng, D. Kiper, and M. Wolf, "Testing the potential of a virtual reality neurorehabilitation system during performance of observation, imagery and imitation of motor actions recorded by wireless functional near-infrared spectroscopy (fNIRS)," *J. Neuroeng. Rehabil.*, vol. 7, p. 57, 2010.
- [125] M. Schroeter, O. Schmiedel, and D. von Cramon, "Spontaneous low-frequency oscillations decline in the aging brain," *J. Cereb. Blood Flow Metab.*, vol. 24, pp. 1183–1191, Oct 2004.
- [126] S. Shimada and K. Hiraki, "Infants' brain responses to live and televised action," *NeuroImage*, vol. 32, pp. 930–939, Aug 2006.
- [127] S. Shimada, "Deactivation in the sensorimotor area during observation of a human agent performing robotic actions," *Brain Cogn.*, vol. 72, pp. 394–399, Apr 2010.
- [128] J. Cohen-Adad, S. Chapuisat, J. Doyon, S. Rossignol, J.-M. Lina, H. Benali, and F. Lesage, "Activation detection in diffuse optical imaging by means of the general linear model," *Med. Image Anal.*, vol. 11, no. 6, pp. 616–29, 2007.
- [129] M. M. Plichta, S. Heinzl, A. C. Ehlis, P. Pauli, and A. J. Fallgatter, "Model-based analysis of rapid event-related functional near-infrared spectroscopy (NIRS) data: a parametric validation study," *NeuroImage*, vol. 35, pp. 625–634, Apr 2007.
- [130] K. Ciftci, B. Sankur, Y. P. Kahya, and A. Akin, "Constraining the general linear model for sensible hemodynamic response function waveforms," *Med. Biol. Eng. Comput.*, vol. 46, pp. 779–787, Aug 2008.
- [131] X. S. Hu, K. S. Hong, S. S. Ge, and M. Y. Jeong, "Kalman estimator- and general linear model-based on-line brain activation mapping by near-infrared spectroscopy," *Biomed. Eng. Online*, vol. 9, p. 82, 2010.
- [132] A. F. Abdelnour and T. Huppert, "Real-time imaging of human brain function by near-infrared spectroscopy using an adaptive general linear model," *NeuroImage*, vol. 46, pp. 133–143, May 2009.
- [133] P. H. Koh, D. E. Glaser, G. Flandin, S. Kiebel, B. Butterworth, A. Maki, D. T. Delpy, and C. E. Elwell, "Functional optical signal analysis: a software tool for near-infrared spectroscopy data processing incorporating statistical parametric mapping," *J. Biomed. Opt.*, vol. 12, p. 064010, 2007.
- [134] J.-M. Lina, M. Dehaes, C. Matteau-Pelletier, and F. Lesage, "Complex wavelets applied to diffuse optical spectroscopy for brain activity detection," *Optics Express*, vol. 16, no. 2, pp. 1029–1050, 2008.
- [135] C. Matteau-Pelletier, M. Dehaes, F. Lesage, and J. Lina, "Wavelet-based estimation of long-memory noise in Diffuse Optical Imaging," in *5th IEEE International Symposium on Biomedical Imaging: From Nano to Macro*, no. 1, (Paris, France), pp. 400–403, IEEE, 2008.

BIBLIOGRAPHY

- [136] C. Matteau-Pelletier, M. Dehaes, F. Lesage, and J. M. Lina, "1/f noise in diffuse optical imaging and wavelet-based response estimation," *IEEE Trans. Med. Imaging*, vol. 28, pp. 415–422, Mar 2009.
- [137] J. M. Lina, C. Matteau-Pelletier, M. Dehaes, M. Desjardins, and F. Lesage, "Wavelet-based estimation of the hemodynamic responses in diffuse optical imaging," *Med. Image Anal.*, vol. 14, pp. 606–616, Aug 2010.
- [138] E. Zarahn, G. K. Aguirre, and M. D'Esposito, "Empirical analyses of BOLD fMRI statistics. I. Spatially unsmoothed data collected under null-hypothesis conditions," *NeuroImage*, vol. 5, pp. 179–197, Apr 1997.
- [139] E. Bullmore, M. Brammer, S. C. Williams, S. Rabe-Hesketh, N. Janot, A. David, J. Mellers, R. Howard, and P. Sham, "Statistical methods of estimation and inference for functional MR image analysis," *Magn. Reson. Med.*, vol. 35, pp. 261–277, Feb 1996.
- [140] A. T. Smith, K. D. Singh, and J. H. Balsters, "A comment on the severity of the effects of non-white noise in fMRI time-series.," *NeuroImage*, vol. 36, no. 2, pp. 282–8, 2007.
- [141] H. Zhang, W.-L. Luo, and T. E. Nichols, "Diagnosis of single-subject and group fMRI data with SPMd.," *Hum. Brain Mapp.*, vol. 27, no. 5, pp. 442–51, 2006.
- [142] M. Bianciardi, A. Cerasa, F. Patria, and G. E. Hagberg, "Evaluation of mixed effects in event-related fMRI studies: impact of first-level design and filtering," *NeuroImage*, vol. 22, pp. 1351–1370, Jul 2004.
- [143] K. J. Worsley and K. J. Friston, "Analysis of fMRI time-series revisited—again," *NeuroImage*, vol. 2, pp. 173–181, Sep 1995.
- [144] K. J. Friston, W. Penny, C. Phillips, S. Kiebel, G. Hinton, and J. Ashburner, "Classical and Bayesian inference in neuroimaging: theory," *NeuroImage*, vol. 16, pp. 465–483, Jun 2002.
- [145] K. J. Friston, O. Josephs, E. Zarahn, a. P. Holmes, S. Rouquette, and J. Poline, "To smooth or not to smooth? Bias and efficiency in fMRI time-series analysis.," *NeuroImage*, vol. 12, pp. 196–208, Aug 2000.
- [146] M. W. Woolrich, B. D. Ripley, M. Brady, and S. M. Smith, "Temporal autocorrelation in univariate linear modeling of FMRI data.," *NeuroImage*, vol. 14, no. 6, pp. 1370–86, 2001.
- [147] M. M. Plichta, M. J. Herrmann, A. C. Ehlis, C. G. Baehne, M. M. Richter, and A. J. Fallgatter, "Event-related visual versus blocked motor task: detection of specific cortical activation patterns with functional near-infrared spectroscopy," *Neuropsychobiology*, vol. 53, pp. 77–82, 2006.
- [148] A. K. Singh and I. Dan, "Exploring the false discovery rate in multichannel NIRS.," *NeuroImage*, vol. 33, no. 2, pp. 542–9, 2006.
- [149] K. J. Worsley, A. C. Evans, S. Marrett, and P. Neelin, "A three-dimensional statistical analysis for CBF activation studies in human brain," *J. Cereb. Blood Flow Metab.*, vol. 12, pp. 900–918, Nov 1992.

-
- [150] J. Sun, "Tail probabilities of the maxima of Gaussian random fields," *The Annals of Probability*, vol. 21, pp. 34–71, Jan 1993.
- [151] Y. Benjamini and Y. Hochberg, "Controlling the false discovery rate: a practical and powerful approach to multiple testing," *Journal of the Royal Statistical Society*, vol. 57, no. 1, pp. 289–300, 1995.
- [152] F. Abdelnour and T. Huppert, "A random-effects model for group-level analysis of diffuse optical brain imaging," *Biomed. Opt. Express*, vol. 2, pp. 1–25, Nov 2010.
- [153] H. Sato, Y. Fuchino, M. Kiguchi, T. Katura, A. Maki, T. Yoro, and H. Koizumi, "Intersubject variability of near-infrared spectroscopy signals during sensorimotor cortex activation," *J. Biomed. Opt.*, vol. 10, p. 44001, 2005.
- [154] V. Y. Toronov, X. Zhang, and A. G. Webb, "A spatial and temporal comparison of hemodynamic signals measured using optical and functional magnetic resonance imaging during activation in the human primary visual cortex," *NeuroImage*, vol. 34, pp. 1136–1148, Feb 2007.
- [155] L. B. Wood and H. Asada, "Low variance adaptive filter for cancelling motion artifact in wearable photoplethysmogram sensor signals," *Conf. Proc. IEEE Eng. Med. Biol. Soc.*, vol. 2007, no. NIL, pp. 652–5, 2007.
- [156] D. A. Tong, K. A. Bartels, and K. S. Honeyager, "Using motion sensors to reduce motion artifact in the ECG.," *Journal of Electrocardiology*, vol. 37, no. NIL, p. 43, 2004.
- [157] J.-A. Jiang, C.-F. Chao, M.-J. Chiu, R.-G. Lee, C.-L. Tseng, and R. Lin, "An automatic analysis method for detecting and eliminating ECG artifacts in EEG.," *Comput. Biol. Med.*, vol. 37, no. 11, pp. 1660–71, 2007.
- [158] P. He, G. Wilson, and C. Russell, "Removal of ocular artifacts from electro-encephalogram by adaptive filtering," *Med. Biol. Eng. Comput.*, vol. 42, no. 3, pp. 407–12, 2004.
- [159] S. Hoffmann and M. Falkenstein, "The correction of eye blink artefacts in the EEG: a comparison of two prominent methods.," *PLoS ONE*, vol. 3, no. 8, p. e3004, 2008.
- [160] S. Haykin, *Adaptive filter theory*. Englewood Cliffs, New Jersey, USA: Prentice Hall, 2 ed., 1991.
- [161] M. Bouchard and S. Quednau, "Multichannel recursive-least-square algorithms and fast-transversal-filter algorithms for active noise control and sound reproduction systems," *IEEE Transactions on Speech and Audio Processing*, vol. 8, pp. 606–618, Sep 2000.
- [162] R. Clemens. <http://www.mathworks.com/matlabcentral/fileexchange/10447>, last accessed on 6 May 2009.
- [163] I. Daubechies, "Ten lectures on wavelets," in *CBMS-NSF conference series in applied mathematics.*, SIAM: Society for Industrial and Applied Mathematics, 1992.

BIBLIOGRAPHY

- [164] S. Mallat, "A theory for multiresolution signal decomposition: the wavelet representation," *IEEE Transactions on Pattern Analysis and Machine Intelligence*, vol. 11, no. 7, pp. 674–693, 1989.
- [165] D. L. Donoho and I. M. Johnstone, "Ideal spatial adaptation via wavelet shrinkage," *Biometrika*, vol. 81, pp. 425–455, 1994.
- [166] D. Donoho, "De-noising by soft-thresholding," *IEEE Transactions on Information Theory*, vol. 41, no. 3, pp. 613–627, 1995.
- [167] A. Hyvärinen, "Fast and robust fixed-point algorithms for independent component analysis," *IEEE Transactions on Neural Networks*, vol. 10, no. 3, pp. 626–634, 1999.
- [168] H. Gävert, J. Hurri, J. Särelä, and A. Hyvärinen. <http://www.cis.hut.fi/projects/ica/fastica/>, last accessed on 6 May 2009.
- [169] A. V. Medvedev, J. Kainerstorfer, S. V. Borisov, R. Barbour, and J. VanMeter, "Event-related fast optical signal in a rapid object recognition task: improving detection by the independent component analysis," *Brain Res.*, vol. 1236, no. NIL, pp. 145–58, 2008.
- [170] B. He, G. Shulman, A. Snyder, and M. Corbetta, "The role of impaired neuronal communication in neurological disorders," *Curr. Opin. Neurol.*, vol. 20, pp. 655–660, Dec 2007.
- [171] S. M. Coyle, T. E. Ward, and C. M. Markham, "Brain-computer interface using a simplified functional near-infrared spectroscopy system," *J. Neural Eng.*, vol. 4, pp. 219–226, Sep 2007.
- [172] T. Shiraishi, H. Saito, H. Ito, and M. Oi, "Observation and imitation of nursing actions: A NIRS study with experts and novices," *Stud. Health Technol. Inform.*, vol. 122, pp. 820–821, 2006.
- [173] S. Shimada, "Modulation of motor area activity by the outcome for a player during observation of a baseball game," *PLoS ONE*, vol. 4, p. e8034, 2009.
- [174] S. Shimada and R. Abe, "Modulation of the motor area activity during observation of a competitive game," *Neuroreport*, vol. 20, pp. 979–983, Jul 2009.
- [175] S. Shimada and R. Abe, "Outcome and view of the player modulate motor area activity during observation of a competitive game," *Neuropsychologia*, vol. 48, pp. 1930–1934, Jun 2010.
- [176] L. Holper and M. Wolf, "Motor imagery in response to fake feedback measured by functional near-infrared spectroscopy," *NeuroImage*, vol. 50, pp. 190–197, Mar 2010.
- [177] A. Maki, Y. Yamashita, Y. Ito, E. Watanabe, Y. Mayanagi, and H. Koizumi, "Spatial and temporal analysis of human motor activity using noninvasive NIR topography," *Med. Phys.*, vol. 22, pp. 1997–2005, Dec 1995.
- [178] V. Toronov, M. Franceschini, M. Filiaci, S. Fantini, M. Wolf, A. Michalos, and E. Gratton, "Near-infrared study of fluctuations in cerebral hemodynamics during rest and motor stimulation: temporal analysis and spatial mapping," *Med. Phys.*, vol. 27, pp. 801–815, Apr 2000.

- [179] M. Wolf, U. Wolf, V. Toronov, A. Michalos, L. Paunescu, J. H. Choi, and E. Gratton, "Different time evolution of oxyhemoglobin and deoxyhemoglobin concentration changes in the visual and motor cortices during functional stimulation: a near-infrared spectroscopy study," *NeuroImage*, vol. 16, pp. 704–712, Jul 2002.
- [180] D. J. Mehagnoul-Schipper, B. F. van der Kallen, W. N. Colier, M. C. van der Sluijs, L. J. van Erning, H. O. Thijssen, B. Oeseburg, W. H. Hoefnagels, and R. W. Jansen, "Simultaneous measurements of cerebral oxygenation changes during brain activation by near-infrared spectroscopy and functional magnetic resonance imaging in healthy young and elderly subjects," *Hum. Brain Mapp.*, vol. 16, pp. 14–23, May 2002.
- [181] G. Strangman, M. A. Franceschini, D. A. Boas, and J. P. Sutton, "Factors affecting the accuracy of near-infrared spectroscopy concentration calculations for focal changes in oxygenation parameters," *NeuroImage*, vol. 18, pp. 865–879, Apr 2003.
- [182] M. A. Franceschini, D. K. Joseph, T. J. Huppert, S. Diamond, and D. A. Boas, "Diffuse optical imaging of the whole head," *J. Biomed. Opt.*, vol. 11, p. 054007, 2006.
- [183] T. Suto, M. Ito, T. Uehara, I. Ida, M. Fukuda, and M. Mikuni, "Temporal characteristics of cerebral blood volume change in motor and somatosensory cortices revealed by multichannel near-infrared spectroscopy," *International Congress Series*, vol. 1232, pp. 383–388, Apr 2002.
- [184] A. Kleinschmidt, H. Obrig, M. Requardt, K. D. Merboldt, U. Dirnagl, A. Villringer, and J. Frahm, "Simultaneous recording of cerebral blood oxygenation changes during human brain activation by magnetic resonance imaging and near-infrared spectroscopy," *J. Cereb. Blood Flow Metab.*, vol. 16, pp. 817–826, Sep 1996.
- [185] C. A. Porro, V. Cettolo, M. P. Francescato, and P. Baraldi, "Ipsilateral involvement of primary motor cortex during motor imagery," *Eur. J. Neurosci.*, vol. 12, pp. 3059–3063, Aug 2000.
- [186] T. Hanakawa, S. Parikh, M. K. Bruno, and M. Hallett, "Finger and face representations in the ipsilateral precentral motor areas in humans," *J. Neurophysiol.*, vol. 93, pp. 2950–2958, May 2005.
- [187] V. Gazzola and C. Keysers, "The observation and execution of actions share motor and somatosensory voxels in all tested subjects: single-subject analyses of unsmoothed fMRI data," *Cereb. Cortex*, vol. 19, pp. 1239–1255, Jun 2009.
- [188] S. Caspers, K. Zilles, A. R. Laird, and S. B. Eickhoff, "ALE meta-analysis of action observation and imitation in the human brain," *NeuroImage*, vol. 50, pp. 1148–1167, Apr 2010.
- [189] S. Avikainen, N. Forss, and R. Hari, "Modulated activation of the human SI and SII cortices during observation of hand actions," *NeuroImage*, vol. 15, pp. 640–646, Mar 2002.
- [190] J. Jarvelainen, M. Schurmann, and R. Hari, "Activation of the human primary motor cortex during observation of tool use," *NeuroImage*, vol. 23, pp. 187–192, Sep 2004.

BIBLIOGRAPHY

- [191] J. Jarvelainen, M. Schurmann, S. Avikainen, and R. Hari, "Stronger reactivity of the human primary motor cortex during observation of live rather than video motor acts," *Neuroreport*, vol. 12, pp. 3493–3495, Nov 2001.
- [192] Y. Pei, H. L. Graber, and R. L. Barbour, "Influence of systematic errors in reference states on image quality and on stability of derived information for DC optical imaging," *Appl. Opt.*, vol. 40, pp. 5755–5769, Nov 2001.
- [193] R. L. Barbour, H. L. Graber, Y. Pei, S. Zhong, and C. H. Schmitz, "Optical tomographic imaging of dynamic features of dense-scattering media," *J. Opt. Soc. Am. A. Opt. Image Sci. Vis.*, vol. 18, pp. 3018–3036, Dec 2001.
- [194] W. Penny, G. Flandin, and N. Trujillo-Barreto, "Bayesian comparison of spatially regularised general linear models," *Hum. Brain Mapp.*, vol. 28, pp. 275–293, Apr 2007.
- [195] H. Dehghani, B. R. White, B. W. Zeff, A. Tizzard, and J. P. Culver, "Depth sensitivity and image reconstruction analysis of dense imaging arrays for mapping brain function with diffuse optical tomography," *Appl Opt*, vol. 48, pp. D137–143, Apr 2009.
- [196] Y. Pei, H. Graber, and R. Barbour, "Normalized-constraint algorithm for minimizing inter-parameter crosstalk in DC optical tomography," *Opt Express*, vol. 9, pp. 97–109, Jul 2001.
- [197] H. L. Graber, Y. Xu, Y. Pei, and R. L. Barbour, "Spatial deconvolution technique to improve the accuracy of reconstructed three-dimensional diffuse optical tomographic images," *Appl. Opt.*, vol. 44, no. 6, pp. 941–53, 2005.
- [198] N. Kuboyama, T. Nabetani, K. Shibuya, K. Machida, and T. Ogaki, "The effect of maximal finger tapping on cerebral activation," *J. Physiol. Anthropol. Appl. Human Sci.*, vol. 23, pp. 105–110, Jul 2004.
- [199] N. Kuboyama, T. Nabetani, K. Shibuya, K. Machida, and T. Ogaki, "Relationship between cerebral activity and movement frequency of maximal finger tapping," *J. Physiol. Anthropol. Appl. Human Sci.*, vol. 24, pp. 201–208, May 2005.
- [200] Y. Hoshi, N. Kobayashi, and M. Tamura, "Interpretation of near-infrared spectroscopy signals: a study with a newly developed perfused rat brain model," *J. Appl. Physiol.*, vol. 90, pp. 1657–1662, May 2001.
- [201] M. Cabinio, V. Blasi, P. Borroni, M. Montagna, A. Iadanza, A. Falini, and G. Cerri, "The shape of motor resonance: right- or left-handed?," *NeuroImage*, vol. 51, pp. 313–323, May 2010.
- [202] C. E. Cooper, D. Pryor, C. Hall, and M. Griffin, "NIRS-detected changes in the motor cortex during mental rehearsal of physical activity (imaginary exercise)," *Adv. Exp. Med. Biol.*, vol. 578, pp. 185–190, 2006.

-
- [203] S. Kanoh, Y. M. Murayama, K. Miyamoto, T. Yoshinobu, and R. Kawashima, "A NIRS-based brain-computer interface system during motor imagery: system development and online feedback training," *Conf. Proc. IEEE Eng. Med. Biol. Soc.*, vol. 2009, pp. 594–597, 2009.
- [204] R. Hoge, M. Franceschini, R. Covolan, T. Huppert, J. Mandeville, and D. Boas, "Simultaneous recording of task-induced changes in blood oxygenation, volume, and flow using diffuse optical imaging and arterial spin-labeling MRI," *NeuroImage*, vol. 25, pp. 701–707, Apr 2005.
- [205] W. N. Colier, V. Quaresima, R. Wenzel, M. C. van der Sluijs, B. Oeseburg, M. Ferrari, and A. Villringer, "Simultaneous near-infrared spectroscopy monitoring of left and right occipital areas reveals contralateral hemodynamic changes upon hemi-field paradigm," *Vision Res.*, vol. 41, pp. 97–102, Jan 2001.
- [206] P. Wobst, R. Wenzel, M. Kohl, H. Obrig, and A. Villringer, "Linear aspects of changes in deoxygenated hemoglobin concentration and cytochrome oxidase oxidation during brain activation," *NeuroImage*, vol. 13, pp. 520–530, Mar 2001.
- [207] C. R. Genovese, N. A. Lazar, and T. Nichols, "Thresholding of statistical maps in functional neuroimaging using the false discovery rate," *NeuroImage*, vol. 15, pp. 870–878, Apr 2002.
- [208] T. Huppert, R. Hoge, S. Diamond, M. Franceschini, and D. Boas, "A temporal comparison of BOLD, ASL, and NIRS hemodynamic responses to motor stimuli in adult humans," *NeuroImage*, vol. 29, pp. 368–382, Jan 2006.
- [209] J. C. Brooks, C. F. Beckmann, K. L. Miller, R. G. Wise, C. A. Porro, I. Tracey, and M. Jenkinson, "Physiological noise modelling for spinal functional magnetic resonance imaging studies," *NeuroImage*, vol. 39, pp. 680–692, Jan 2008.
- [210] M. A. Gray, L. Minati, N. A. Harrison, P. J. Gianaros, V. Napadow, and H. D. Critchley, "Physiological recordings: basic concepts and implementation during functional magnetic resonance imaging," *NeuroImage*, vol. 47, pp. 1105–1115, Sep 2009.
- [211] L. Mourrot, M. Bouhaddi, and J. Regnard, "Effects of the cold pressor test on cardiac autonomic control in normal subjects," *Physiol Res.*, vol. 58, pp. 83–91, Jan 2009.
- [212] C. Lamm, C. Windischberger, U. Leodolter, E. Moser, and H. Bauer, "Co-registration of EEG and MRI data using matching of spline interpolated and MRI-segmented reconstructions of the scalp surface," *Brain Topogr.*, vol. 14, no. 2, pp. 93–100, 2001.
- [213] H. J. Huppertz, M. Otte, C. Grimm, R. Kristeva-Feige, T. Mergner, and C. H. Lucking, "Estimation of the accuracy of a surface matching technique for registration of EEG and MRI data," *Electroencephalogr. Clin. Neurophysiol.*, vol. 106, no. 5, pp. 409–15, 1998.
- [214] K. D. Singh, I. E. Holliday, P. L. Furlong, and G. F. Harding, "Evaluation of MRI-MEG/EEG co-registration strategies using Monte Carlo simulation," *Electroencephalogr. Clin. Neurophysiol.*, vol. 102, no. 2, pp. 81–5, 1997.

BIBLIOGRAPHY

- [215] D. Schwartz, D. Lemoine, E. Poiseau, and C. Barillot, "Registration of MEG/EEG data with 3D MRI: Methodology and precision issues," *Brain Topogr.*, vol. 9, no. 2, pp. 101–116, 1996.
- [216] D. Kozinska, F. Carducci, and K. Nowinski, "Automatic alignment of EEG/MEG and MRI data sets," *Clin. Neurophysiol.*, vol. 112, no. 8, pp. 1553–61, 2001.
- [217] Q. Noirhomme, M. Ferrant, Y. Vandermeeren, E. Olivier, B. Macq, and O. Cuisenaire, "Registration and real-time visualization of transcranial magnetic stimulation with 3-D MR images," *IEEE Trans. Biomed. Eng.*, vol. 51, no. 11, pp. 1994–2005, 2004.
- [218] K. S. Arun, T. S. Huang, and S. D. Blostein, "Least-squares fitting of two 3-d point sets," *IEEE Transactions on Pattern Analysis and Machine Intelligence*, vol. 9, pp. 698 – 700, Sep 1987.
- [219] B. K. P. Horn, "Closed-form solution of absolute orientation using unit quaternions," *Journal of the Optical Society of America*, vol. 4, p. 629, Apr 1987.
- [220] V. Towle, J. Bolanos, D. Suarez, K. Tan, D. Grzeszczuk, R. and Levin, R. Cakmur, S. Frank, and J.-P. Spire, "The spatial location of EEG electrodes: locating the best-fitting sphere relative to cortical anatomy," *Electroencephalogr. Clin. Neurophysiol.*, vol. 86, pp. 1–6, 1993.
- [221] T. Lagerlund, F. Sharbrough, C. J. Jack, B. Erickson, D. Strelow, K. Cicora, and N. Busacker, "Determination of 10-20 system electrode locations using magnetic resonance image scanning with markers," *Electroencephalogr. Clin. Neurophysiol.*, vol. 86, pp. 7–14, Jan 1993.
- [222] P. Adjamian, G. R. Barnes, A. Hillebrand, I. E. Holliday, K. D. Singh, P. L. Furlong, E. Harrington, C. W. Barclay, and P. J. G. Route, "Co-registration of magnetoencephalography with magnetic resonance imaging using bite-bar-based fiducials and surface-matching," *Clin. Neurophysiol.*, vol. 115, no. 3, pp. 691–8, 2004.
- [223] C. A. Pelizzari, G. T. Chen, D. R. Spelbring, R. R. Weichselbaum, and C. Chen, "Accurate three-dimensional registration of CT, PET, and/or MR images of the brain.," *J. Comput. Assist. Tomogr.*, vol. 13, no. 1, pp. 20–6, 1989.
- [224] B. Wang, C. Toro, T. A. Zeffiro, and M. Hallett, "Head surface digitization and registration: a method for mapping positions on the head onto magnetic resonance images.," *Brain Topogr.*, vol. 6, no. 3, pp. 185–92, 1994.
- [225] H. Kober, P. Grummisch, and J. Vieth, "Precise fusion of MEG and MRI tomography using a surface fit," *Biomed. Eng. (Berlin)*, vol. 38, pp. Suppl 355–356, 1993.
- [226] P. D. Bamidis and A. A. Ioannides, "Combination of point and surface matching techniques for accurate registration of MEG and MRI," in *Abstracts of the Tenth International Conference on Biomagnetism.*, (C. Wood, Sante Fe, NM), p. 14, 1996.

- [227] Z. Spiclin, A. Hans, F. H. Duffy, S. K. Warfield, B. Likar, and F. Pernus, "EEG to MRI registration based on global and local similarities of MRI intensity distributions," *Med. Image Comput. Comput. Assist. Interv.*, vol. 11, no. Pt 1, pp. 762–770, 2008.
- [228] M. A. Audette, F. P. Ferrie, and T. M. Peters, "An algorithmic overview of surface registration techniques for medical imaging," *Med Image Anal*, vol. 4, no. 3, pp. 201–17, 2000.
- [229] C. Rorden, "MRIreg." <http://www.cabiatl.com/mricro/mricro/mriregh/index.html>. last accessed 9 Feb., 2012.
- [230] Q. Fang, "metch: a mesh/volume registration toolbox," last accessed 8 June 2009.
- [231] R. J. Cooper, M. Caffini, J. Dubb, Q. Fang, D. Custo, A. and Tsuzuki, B. Fischl, W. Wells, I. Dan, and D. A. Boas, "Validating atlas-guided DOT: A comparison of diffuse optical tomography informed by atlas and subject-specific anatomies," *Neuroimage*, vol. 62, pp. 1999–2006, Sep 2012.
- [232] S. G. Kim, J. Ashe, K. Hendrich, J. M. Ellermann, H. Merkle, K. Ugurbil, and A. P. Georgopoulos, "Functional magnetic resonance imaging of motor cortex: hemispheric asymmetry and handedness," *Science*, vol. 261, pp. 615–617, Jul 1993.
- [233] S. M. Rao, J. R. Binder, P. A. Bandettini, T. A. Hammeke, F. Z. Yetkin, A. Jesmanowicz, L. M. Lisk, G. L. Morris, W. M. Mueller, and L. D. Estkowski, "Functional magnetic resonance imaging of complex human movements," *Neurology*, vol. 43, pp. 2311–2318, Nov 1993.
- [234] R. Kawashima, K. Yamada, S. Kinomura, T. Yamaguchi, H. Matsui, S. Yoshioka, and H. Fukuda, "Regional cerebral blood flow changes of cortical motor areas and prefrontal areas in humans related to ipsilateral and contralateral hand movement," *Brain Res.*, vol. 623, pp. 33–40, Sep 1993.
- [235] S. C. Cramer, S. P. Finklestein, J. D. Schaechter, G. Bush, and B. R. Rosen, "Activation of distinct motor cortex regions during ipsilateral and contralateral finger movements," *J. Neurophysiol.*, vol. 81, pp. 383–387, Jan 1999.
- [236] T. Verstynen, J. Diedrichsen, N. Albert, P. Aparicio, and R. B. Ivry, "Ipsilateral motor cortex activity during unimanual hand movements relates to task complexity," *J. Neurophysiol.*, vol. 93, pp. 1209–1222, Mar 2005.
- [237] M. Kobayashi, S. Hutchinson, G. Schlaug, and A. Pascual-Leone, "Ipsilateral motor cortex activation on functional magnetic resonance imaging during unilateral hand movements is related to interhemispheric interactions," *NeuroImage*, vol. 20, pp. 2259–2270, Dec 2003.
- [238] C. Horenstein, M. J. Lowe, K. A. Koenig, and M. D. Phillips, "Comparison of unilateral and bilateral complex finger tapping-related activation in premotor and primary motor cortex," *Hum. Brain Mapp.*, vol. 30, pp. 1397–1412, Apr 2009.

BIBLIOGRAPHY

- [239] C. Dettmers, G. R. Fink, R. N. Lemon, K. M. Stephan, R. E. Passingham, D. Silbersweig, A. Holmes, M. C. Ridding, D. J. Brooks, and R. S. Frackowiak, "Relation between cerebral activity and force in the motor areas of the human brain," *J. Neurophysiol.*, vol. 74, pp. 802–815, Aug 1995.
- [240] J. D. Allison, K. J. Meador, D. W. Loring, R. E. Figueroa, and J. C. Wright, "Functional MRI cerebral activation and deactivation during finger movement," *Neurology*, vol. 54, pp. 135–142, Jan 2000.
- [241] F. Hamzei, C. Dettmers, R. Rzanny, J. Liepert, C. Buchel, and C. Weiller, "Reduction of excitability ("inhibition") in the ipsilateral primary motor cortex is mirrored by fMRI signal decreases," *NeuroImage*, vol. 17, pp. 490–496, Sep 2002.
- [242] K. Kudo, M. Miyazaki, T. Kimura, K. Yamanaka, H. Kadota, M. Hirashima, Y. Nakajima, K. Nakazawa, and T. Ohtsuki, "Selective activation and deactivation of the human brain structures between speeded and precisely timed tapping responses to identical visual stimulus: an fMRI study," *NeuroImage*, vol. 22, pp. 1291–1301, Jul 2004.
- [243] B. Stefanovic, J. M. Warnking, and G. B. Pike, "Hemodynamic and metabolic responses to neuronal inhibition," *NeuroImage*, vol. 22, pp. 771–778, Jun 2004.
- [244] J. M. Newton, A. Sunderland, and P. A. Gowland, "fMRI signal decreases in ipsilateral primary motor cortex during unilateral hand movements are related to duration and side of movement," *NeuroImage*, vol. 24, pp. 1080–1087, Feb 2005.
- [245] K. Sakamoto, H. Nakata, M. G. Perrucci, C. Del Gratta, R. Kakigi, and G. L. Romani, "Negative BOLD during tongue movement: a functional magnetic resonance imaging study," *Neurosci. Lett.*, vol. 466, pp. 120–123, Dec 2009.
- [246] M. Raichle, A. MacLeod, A. Snyder, W. Powers, D. Gusnard, and G. Shulman, "A default mode of brain function," *Proc. Natl. Acad. Sci. U.S.A.*, vol. 98, pp. 676–682, Jan 2001.
- [247] M. Greicius, B. Krasnow, A. Reiss, and V. Menon, "Functional connectivity in the resting brain: a network analysis of the default mode hypothesis," *Proc. Natl. Acad. Sci. U.S.A.*, vol. 100, pp. 253–258, Jan 2003.
- [248] N. Harel, S. P. Lee, T. Nagaoka, D. S. Kim, and S. G. Kim, "Origin of negative blood oxygenation level-dependent fMRI signals," *J. Cereb. Blood Flow Metab.*, vol. 22, pp. 908–917, Aug 2002.
- [249] A. Shmuel, E. Yacoub, J. Pfeuffer, P. F. Van de Moortele, G. Adriany, X. Hu, and K. Ugurbil, "Sustained negative BOLD, blood flow and oxygen consumption response and its coupling to the positive response in the human brain," *Neuron*, vol. 36, pp. 1195–1210, Dec 2002.
- [250] A. C. Nirkko, C. Ozdoba, S. M. Redmond, M. Burki, G. Schroth, C. W. Hess, and M. Wiesendanger, "Different ipsilateral representations for distal and proximal movements in the sensorimotor cortex: activation and deactivation patterns," *NeuroImage*, vol. 13, pp. 825–835, May 2001.

- [251] A. T. Smith, A. L. Williams, and K. D. Singh, "Negative BOLD in the visual cortex: evidence against blood stealing," *Hum. Brain Mapp.*, vol. 21, pp. 213–220, Apr 2004.
- [252] A. Devor, E. M. Hillman, P. Tian, C. Waeber, I. C. Teng, L. Ruvinskaya, M. H. Shalinsky, H. Zhu, R. H. Haslinger, S. N. Narayanan, I. Ulbert, A. K. Dunn, E. H. Lo, B. R. Rosen, A. M. Dale, D. Kleinfeld, and D. A. Boas, "Stimulus-induced changes in blood flow and 2-deoxyglucose uptake dissociate in ipsilateral somatosensory cortex," *J. Neurosci.*, vol. 28, pp. 14347–14357, Dec 2008.
- [253] N. K. Logothetis, J. Pauls, M. Augath, T. Trinath, and A. Oeltermann, "Neurophysiological investigation of the basis of the fMRI signal," *Nature*, vol. 412, pp. 150–157, Jul 2001.
- [254] J. Tanji, K. Okano, and K. C. Sato, "Neuronal activity in cortical motor areas related to ipsilateral, contralateral, and bilateral digit movements of the monkey," *J. Neurophysiol.*, vol. 60, pp. 325–343, Jul 1988.
- [255] H. Aizawa, H. Mushiake, M. Inase, and J. Tanji, "An output zone of the monkey primary motor cortex specialized for bilateral hand movement," *Exp. Brain Res.*, vol. 82, pp. 219–221, 1990.
- [256] K. Muller, F. Kass-Iliyya, and M. Reitz, "Ontogeny of ipsilateral corticospinal projections: a developmental study with transcranial magnetic stimulation," *Ann. Neurol.*, vol. 42, pp. 705–711, Nov 1997.
- [257] U. Ziemann, K. Ishii, A. Borgheresi, Z. Yaseen, F. Battaglia, M. Hallett, M. Cincotta, and E. M. Wassermann, "Dissociation of the pathways mediating ipsilateral and contralateral motor-evoked potentials in human hand and arm muscles," *J. Physiol. (Lond.)*, vol. 518 (Pt 3), pp. 895–906, Aug 1999.
- [258] G. A. Ghacibeh, R. Mirpuri, V. Drago, Y. Jeong, K. M. Heilman, and W. J. Triggs, "Ipsilateral motor activation during unimanual and bimanual motor tasks," *Clin. Neurophysiol.*, vol. 118, pp. 325–332, Feb 2007.
- [259] M. J. Hayashi, D. N. Saito, Y. Aramaki, T. Asai, Y. Fujibayashi, and N. Sadato, "Hemispheric asymmetry of frequency-dependent suppression in the ipsilateral primary motor cortex during finger movement: a functional magnetic resonance imaging study," *Cereb. Cortex*, vol. 18, pp. 2932–2940, Dec 2008.
- [260] D. L. Harrington, S. M. Rao, K. Y. Haaland, J. A. Bobholz, A. R. Mayer, J. R. Binder, and R. W. Cox, "Specialized neural systems underlying representations of sequential movements," *J. Cogn. Neurosci.*, vol. 12, pp. 56–77, Jan 2000.
- [261] P. A. Gelnar, B. R. Krauss, P. R. Sheehe, N. M. Szeverenyi, and A. V. Apkarian, "A comparative fMRI study of cortical representations for thermal painful, vibrotactile, and motor performance tasks," *NeuroImage*, vol. 10, no. 4, pp. 460–82, 1999.
- [262] K. D. Davis, "The neural circuitry of pain as explored with functional MRI," *Neurol. Res.*, vol. 22, no. 3, pp. 313–7, 2000.

BIBLIOGRAPHY

- [263] I. Tracey, L. Becerra, I. Chang, H. Breiter, L. Jenkins, D. Borsook, and R. G. Gonzalez, "Noxious hot and cold stimulation produce common patterns of brain activation in humans: a functional magnetic resonance imaging study," *Neurosci. Lett.*, vol. 288, no. 2, pp. 159–62, 2000.
- [264] K. D. Davis, C. L. Kwan, A. P. Crawley, and D. J. Mikulis, "Functional MRI study of thalamic and cortical activations evoked by cutaneous heat, cold, and tactile stimuli," *J. Neurophysiol.*, vol. 80, no. 3, pp. 1533–46, 1998.
- [265] J. Kong, M. L. Loggia, C. Zyloney, P. Tu, P. Laviolette, and R. L. Gollub, "Exploring the brain in pain: activations, deactivations and their relation," *Pain*, vol. 148, pp. 257–267, Feb 2010.
- [266] R. C. Coghill, I. Gilron, and M. J. Iadarola, "Hemispheric lateralization of somatosensory processing," *J. Neurophysiol.*, vol. 85, pp. 2602–2612, Jun 2001.
- [267] L. L. Symonds, N. S. Gordon, J. C. Bixby, and M. M. Mande, "Right-lateralized pain processing in the human cortex: an fMRI study," *J. Neurophysiol.*, vol. 95, pp. 3823–3830, Jun 2006.
- [268] J. H. Kaas and C. E. Collins, "The organization of somatosensory cortex in anthropoid primates," *Adv. Neurol.*, vol. 93, pp. 57–67, 2003.
- [269] J. H. Kaas, "Evolution of somatosensory and motor cortex in primates," *Anat. Rec. A. Discov. Mol. Cell Evol. Biol.*, vol. 281, pp. 1148–1156, Nov 2004.
- [270] L. Krubitzer, "The organization of neocortex in mammals: are species differences really so different?," *Trends Neurosci.*, vol. 18, pp. 408–417, Sep 1995.
- [271] S. J. Karlen and L. Krubitzer, "The evolution of the neocortex in mammals: intrinsic and extrinsic contributions to the cortical phenotype," *Novartis Found. Symp.*, vol. 270, pp. 146–159, 2006.
- [272] S. B. Eickhoff, C. Grefkes, G. R. Fink, and K. Zilles, "Functional lateralization of face, hand, and trunk representation in anatomically defined human somatosensory areas," *Cereb. Cortex*, vol. 18, pp. 2820–2830, Dec 2008.
- [273] Y. Hlushchuk and R. Hari, "Transient suppression of ipsilateral primary somatosensory cortex during tactile finger stimulation," *J. Neurosci.*, vol. 26, pp. 5819–5824, May 2006.
- [274] E. Disbrow, T. Roberts, and L. Krubitzer, "Somatotopic organization of cortical fields in the lateral sulcus of *Homo sapiens*: evidence for SII and PV," *J. Comp. Neurol.*, vol. 418, pp. 1–21, Feb 2000.
- [275] J. Ruben, J. Schwiemann, M. Deuchert, R. Meyer, T. Krause, G. Curio, K. Villringer, R. Kurth, and A. Villringer, "Somatotopic organization of human secondary somatosensory cortex," *Cereb. Cortex*, vol. 11, pp. 463–473, May 2001.
- [276] A. Ferretti, C. Babiloni, C. D. Gratta, M. Caulo, A. Tartaro, L. Bonomo, P. M. Rossini, and G. L. Romani, "Functional topography of the secondary somatosensory cortex for nonpainful and painful stimuli: an fMRI study," *NeuroImage*, vol. 20, pp. 1625–1638, Nov 2003.

- [277] J. P. Young, P. Herath, S. Eickhoff, J. Choi, C. Grefkes, K. Zilles, and P. E. Roland, "Somatotopy and attentional modulation of the human parietal and opercular regions," *J. Neurosci.*, vol. 24, pp. 5391–5399, Jun 2004.
- [278] E. Naito, P. E. Roland, C. Grefkes, H. J. Choi, S. Eickhoff, S. Geyer, K. Zilles, and H. H. Ehrsson, "Dominance of the right hemisphere and role of area 2 in human kinesthesia," *J. Neurophysiol.*, vol. 93, pp. 1020–1034, Feb 2005.
- [279] M. Blatow, E. Nennig, A. Durst, K. Sartor, and C. Stippich, "fMRI reflects functional connectivity of human somatosensory cortex," *NeuroImage*, vol. 37, pp. 927–936, Sep 2007.
- [280] J. A. Maldjian, A. Gottschalk, R. S. Patel, D. Pincus, J. A. Detre, and D. C. Alsop, "Mapping of secondary somatosensory cortex activation induced by vibrational stimulation: an fMRI study," *Brain Res.*, vol. 824, pp. 291–295, Apr 1999.
- [281] W. H. Backes, W. H. Mess, V. van Kranen-Mastenbroek, and J. P. Reulen, "Somatosensory cortex responses to median nerve stimulation: fMRI effects of current amplitude and selective attention," *Clin. Neurophysiol.*, vol. 111, pp. 1738–1744, Oct 2000.
- [282] C. Del Gratta, S. Della Penna, A. Ferretti, R. Franciotti, V. Pizzella, A. Tartaro, K. Torquati, L. Bonomo, G. L. Romani, and P. M. Rossini, "Topographic organization of the human primary and secondary somatosensory cortices: comparison of fMRI and MEG findings," *NeuroImage*, vol. 17, pp. 1373–1383, Nov 2002.
- [283] G. D. Iannetti, C. A. Porro, P. Pantano, P. L. Romanelli, F. Galeotti, and G. Cruccu, "Representation of different trigeminal divisions within the primary and secondary human somatosensory cortex," *NeuroImage*, vol. 19, pp. 906–912, Jul 2003.
- [284] C. Stippich, A. Romanowski, E. Nennig, B. Kress, and K. Sartor, "Time-efficient localization of the human secondary somatosensory cortex by functional magnetic resonance imaging," *Neurosci. Lett.*, vol. 381, pp. 264–268, Jun 2005.
- [285] A. Korvenoja, J. Huttunen, E. Salli, H. Pohjonen, S. Martinkauppi, J. M. Palva, L. Lauronen, J. Virtanen, R. Ilmoniemi, and H. J. Aronen, "Activation of multiple cortical areas in response to somatosensory stimulation: combined magnetoencephalographic and functional magnetic resonance imaging," *Hum. Brain Mapp.*, vol. 8, pp. 13–27, 1999.
- [286] T. Nishishi, S. Naganawa, C. Sato, H. Kawai, T. Nakamura, H. Fukatsu, T. Ishigaki, and I. Aoki, "Contralateral and ipsilateral responses in primary somatosensory cortex following electrical median nerve stimulation—an fMRI study," *Clin. Neurophysiol.*, vol. 116, pp. 842–848, Apr 2005.
- [287] H. H. Jantsch, P. Kemppainen, R. Ringler, H. O. Handwerker, and C. Forster, "Cortical representation of experimental tooth pain in humans," *Pain*, vol. 118, pp. 390–399, Dec 2005.

BIBLIOGRAPHY

- [288] M. T. Sutherland and A. C. Tang, "Reliable detection of bilateral activation in human primary somatosensory cortex by unilateral median nerve stimulation," *NeuroImage*, vol. 33, pp. 1042–1054, Dec 2006.
- [289] M. Duquette, P. Rainville, F. Alary, M. Lassonde, and F. Lepore, "Ipsilateral cortical representation of tactile and painful information in acallosal and callosotomized subjects," *Neuropsychologia*, vol. 46, pp. 2274–2279, 2008.
- [290] L. Becerra, W. Harris, M. Grant, E. George, D. Boas, and D. Borsook, "Diffuse optical tomography activation in the somatosensory cortex: specific activation by painful vs. non-painful thermal stimuli," *PLoS ONE*, vol. 4, p. e8016, 2009.
- [291] H. Hadoush, K. Inoue, K. Nakanishi, H. Kurumadani, T. Sunagawa, and M. Ochi, "Ipsilateral primary sensorimotor cortical response to mechanical tactile stimuli," *Neuroreport*, vol. 21, pp. 108–113, Jan 2010.
- [292] A. Kastrup, J. Baudewig, S. Schnaudigel, R. Huonker, L. Becker, J. M. Sohns, P. Dechent, C. Klingner, and O. W. Witte, "Behavioral correlates of negative BOLD signal changes in the primary somatosensory cortex," *NeuroImage*, vol. 41, pp. 1364–1371, Jul 2008.
- [293] C. M. Klingner, R. Huonker, S. Flemming, C. Hasler, S. Brodoehl, C. Preul, H. Burmeister, A. Kastrup, and O. W. Witte, "Functional deactivations: multiple ipsilateral brain areas engaged in the processing of somatosensory information," *Hum. Brain Mapp.*, vol. 32, pp. 127–140, Jan 2011.
- [294] M. C. Bushnell, G. H. Duncan, R. K. Hofbauer, B. Ha, J. I. Chen, and B. Carrier, "Pain perception: is there a role for primary somatosensory cortex?," *Proc. Natl. Acad. Sci. U.S.A.*, vol. 96, pp. 7705–7709, Jul 1999.
- [295] K. S. Taylor and K. D. Davis, "Stability of tactile- and pain-related fMRI brain activations: an examination of threshold-dependent and threshold-independent methods," *Hum. Brain Mapp.*, vol. 30, pp. 1947–1962, Jul 2009.
- [296] P. Pauli, G. Wiedemann, and M. Nickola, "Pain sensitivity, cerebral laterality, and negative affect," *Pain*, vol. 80, pp. 359–364, Mar 1999.
- [297] M. Lugo, G. Isturiz, C. Lara, N. Garcia, and A. Eblen-Zajjur, "Sensory lateralization in pain subjective perception for noxious heat stimulus," *Somatosens. Mot. Res.*, vol. 19, pp. 207–212, 2002.
- [298] E. Sarlani, N. Farooq, and J. D. Greenspan, "Gender and laterality differences in thermosensation throughout the perceptible range," *Pain*, vol. 106, pp. 9–18, Nov 2003.
- [299] J. Sernal, J. C. Krieg, and S. Lautenbacher, "Pain thresholds as a putative functional test for cerebral laterality in major depressive disorder and panic disorder," *Neuropsychobiology*, vol. 48, pp. 146–151, 2003.

- [300] J. C. W. Brooks, T. J. Nurmikko, W. E. Bimson, K. D. Singh, and N. Roberts, "fMRI of thermal pain: effects of stimulus laterality and attention.," *NeuroImage*, vol. 15, no. 2, pp. 293–301, 2002.
- [301] U. Bingel, M. Quante, R. Knab, B. Bromm, C. Weiller, and C. Buchel, "Single trial fMRI reveals significant contralateral bias in responses to laser pain within thalamus and somatosensory cortices," *NeuroImage*, vol. 18, pp. 740–748, Mar 2003.
- [302] P. D. Youell, R. G. Wise, D. E. Bentley, M. R. Dickinson, T. A. King, I. Tracey, and A. K. Jones, "Lateralisation of nociceptive processing in the human brain: a functional magnetic resonance imaging study," *NeuroImage*, vol. 23, pp. 1068–1077, Nov 2004.
- [303] K. L. Casey, "Forebrain mechanisms of nociception and pain: analysis through imaging," *Proc. Natl. Acad. Sci. U.S.A.*, vol. 96, pp. 7668–7674, Jul 1999.
- [304] R. Peyron, B. Laurent, and L. García-Larrea, "Functional imaging of brain responses to pain. A review and meta-analysis," *Neurophysiologie Clinique/Clinical Neurophysiology*, vol. 30, pp. 263–288, Oct 2000.
- [305] M. J. Farrell, A. R. Laird, and G. F. Egan, "Brain activity associated with painfully hot stimuli applied to the upper limb: a meta-analysis," *Hum. Brain Mapp.*, vol. 25, pp. 129–139, May 2005.
- [306] A. V. Apkarian, M. C. Bushnell, R. D. Treede, and J. K. Zubieta, "Human brain mechanisms of pain perception and regulation in health and disease," *Eur. J. Pain*, vol. 9, pp. 463–484, Aug 2005.
- [307] S. W. Derbyshire, M. G. Whalley, V. A. Stenger, and D. A. Oakley, "Cerebral activation during hypnotically induced and imagined pain," *NeuroImage*, vol. 23, pp. 392–401, Sep 2004.
- [308] T. D. Wager, J. K. Rilling, E. E. Smith, A. Sokolik, K. L. Casey, R. J. Davidson, S. M. Kosslyn, R. M. Rose, and J. D. Cohen, "Placebo-induced changes in fMRI in the anticipation and experience of pain," *Science*, vol. 303, pp. 1162–1167, Feb 2004.
- [309] A. Kanno, N. Nakasato, K. Hatanaka, and T. Yoshimoto, "Ipsilateral area 3b responses to median nerve somatosensory stimulation," *NeuroImage*, vol. 18, pp. 169–177, Jan 2003.
- [310] M. T. Sutherland, "The hand and the ipsilateral primary somatosensory cortex," *J. Neurosci.*, vol. 26, pp. 8217–8218, Aug 2006.
- [311] M. Tommerdahl, S. B. Simons, J. S. Chiu, O. Favorov, and B. L. Whitsel, "Ipsilateral input modifies the primary somatosensory cortex response to contralateral skin flutter," *J. Neurosci.*, vol. 26, pp. 5970–5977, May 2006.
- [312] E. G. Jones and S. H. Hendry, "Distribution of callosal fibers around the hand representations in monkey somatic sensory cortex," *Neurosci. Lett.*, vol. 19, pp. 167–172, Sep 1980.
- [313] H. P. Killackey, H. J. Gould, C. G. Cusick, T. P. Pons, and J. H. Kaas, "The relation of corpus callosum connections to architectonic fields and body surface maps in sensorimotor cortex of new and old world monkeys," *J. Comp. Neurol.*, vol. 219, pp. 384–419, Oct 1983.

BIBLIOGRAPHY

- [314] L. A. Krubitzer and J. H. Kaas, "The organization and connections of somatosensory cortex in marmosets," *J. Neurosci.*, vol. 10, pp. 952–974, Mar 1990.
- [315] J. Padberg, E. Disbrow, and L. Krubitzer, "The organization and connections of anterior and posterior parietal cortex in titi monkeys: do New World monkeys have an area 2?," *Cereb. Cortex*, vol. 15, pp. 1938–1963, Dec 2005.
- [316] Y. Iwamura, "Bilateral receptive field neurons and callosal connections in the somatosensory cortex," *Philos. Trans. R. Soc. Lond., B, Biol. Sci.*, vol. 355, pp. 267–273, Feb 2000.
- [317] Y. Iwamura, M. Tanaka, A. Iriki, M. Taoka, and T. Toda, "Processing of tactile and kinesthetic signals from bilateral sides of the body in the postcentral gyrus of awake monkeys," *Behav. Brain Res.*, vol. 135, pp. 185–190, Sep 2002.
- [318] M. Fabri, G. Polonara, A. Quattrini, U. Salvolini, M. Del Pesce, and T. Manzoni, "Role of the corpus callosum in the somatosensory activation of the ipsilateral cerebral cortex: an fMRI study of callosotomized patients," *Eur. J. Neurosci.*, vol. 11, pp. 3983–3994, Nov 1999.
- [319] T. Manzoni, F. Conti, and M. Fabri, "Callosal projections from area SII to SI in monkeys: anatomical organization and comparison with association projections," *J. Comp. Neurol.*, vol. 252, pp. 245–263, Oct 1986.
- [320] E. Disbrow, T. Roberts, D. Poeppel, and L. Krubitzer, "Evidence for interhemispheric processing of inputs from the hands in human S2 and PV," *J. Neurophysiol.*, vol. 85, pp. 2236–2244, May 2001.
- [321] E. Kapreli, S. Athanasopoulos, M. Papathanasiou, P. Van Hecke, N. Strimpakos, A. Gouliamos, R. Peeters, and S. Sunaert, "Lateralization of brain activity during lower limb joints movement. An fMRI study," *NeuroImage*, vol. 32, pp. 1709–1721, Oct 2006.
- [322] D. Pud, Y. Golan, and R. Pesta, "Hand dominancy—a feature affecting sensitivity to pain," *Neurosci. Lett.*, vol. 467, pp. 237–240, Dec 2009.
- [323] H. Merskey and G. D. Watson, "The lateralisation of pain," *Pain*, vol. 7, pp. 271–280, Dec 1979.
- [324] A. Newton, V. Morgan, and J. Gore, "Task demand modulation of steady-state functional connectivity to primary motor cortex," *Hum. Brain Mapp.*, vol. 28, pp. 663–672, Jul 2007.
- [325] M. Amann, J. G. Hirsch, and A. Gass, "A serial functional connectivity MRI study in healthy individuals assessing the variability of connectivity measures: reduced interhemispheric connectivity in the motor network during continuous performance," *Magnetic Resonance Imaging*, vol. 27, pp. 1347–1359, Dec 2009.
- [326] M. van Buuren, T. E. Gladwin, B. B. Zandbelt, M. van den Heuvel, N. F. Ramsey, R. S. Kahn, and M. Vink, "Cardiorespiratory effects on default-mode network activity as measured with fMRI," *Hum. Brain Mapp.*, vol. 30, no. 9, pp. 3031–42, 2009.

- [327] B. Biswal, F. Yetkin, V. Haughton, and J. Hyde, "Functional connectivity in the motor cortex of resting human brain using echo-planar MRI," *Magn. Reson. Med.*, vol. 34, pp. 537–541, Oct 1995.
- [328] B. R. White, A. Z. Snyder, A. L. Cohen, S. E. Petersen, M. E. Raichle, B. L. Schlaggar, and J. P. Culver, "Resting-state functional connectivity in the human brain revealed with diffuse optical tomography.," *NeuroImage*, vol. 47, pp. 148–56, Aug 2009.
- [329] J. Zhang, H. Chen, F. Fang, and W. Liao, "Quantitative analysis of asymmetrical cortical activity based on power spectrum changes," *Brain Topogr.*, vol. 23, pp. 257–268, Sep 2010.
- [330] Y. J. Zhang, C. M. Lu, B. B. Biswal, Y. F. Zang, D. Peng, and C. Z. Zhu, "Detecting resting-state functional connectivity in the language system using functional near-infrared spectroscopy," *J. Biomed. Opt.*, vol. 15, p. 047003, 2010.
- [331] R. C. Mesquita, M. A. Franceschini, and D. A. Boas, "Resting state functional connectivity of the whole head with near-infrared spectroscopy," *Optics Express*, vol. 1, no. 1, pp. 676–682, 2010.
- [332] C.-M. Lu, Y.-J. Zhang, B. B. Biswal, Y.-F. Zang, D.-L. Peng, and C.-Z. Zhu, "Use of fNIRS to assess resting state functional connectivity," *Journal of neuroscience methods*, vol. 186, pp. 242–9, Mar 2010.
- [333] M. Hampson, I. Olson, H. Leung, P. Skudlarski, and J. Gore, "Changes in functional connectivity of human MT/V5 with visual motion input," *Neuroreport*, vol. 15, pp. 1315–1319, Jun 2004.
- [334] M. Hampson, B. Peterson, P. Skudlarski, J. Gatenby, and J. Gore, "Detection of functional connectivity using temporal correlations in MR images," *Hum. Brain Mapp.*, vol. 15, pp. 247–262, Apr 2002.
- [335] M. Fox, M. Corbetta, A. Snyder, J. Vincent, and M. Raichle, "Spontaneous neuronal activity distinguishes human dorsal and ventral attention systems," *Proc. Natl. Acad. Sci. U.S.A.*, vol. 103, pp. 10046–10051, Jun 2006.
- [336] J. Damoiseaux, S. Rombouts, F. Barkhof, P. Scheltens, C. Stam, S. Smith, and C. Beckmann, "Consistent resting-state networks across healthy subjects," *Proc. Natl. Acad. Sci. U.S.A.*, vol. 103, pp. 13848–13853, Sep 2006.
- [337] M. Lowe, M. Phillips, J. Lurito, D. Mattson, M. Dziedzic, and V. Mathews, "Multiple sclerosis: low-frequency temporal blood oxygen level-dependent fluctuations indicate reduced functional connectivity initial results," *Radiology*, vol. 224, pp. 184–192, Jul 2002.
- [338] K. Wang, T. Jiang, M. Liang, L. Wang, L. Tian, X. Zhang, K. Li, and Z. Liu, "Discriminative analysis of early Alzheimer's disease based on two intrinsically anti-correlated networks with resting-state fMRI," *Med. Image Comput. Comput. Assist. Interv. Int. Conf. Med. Image Comput. Comput. Assist. Interv.*, vol. 9, pp. 340–347, 2006.
- [339] L. Wang, Y. Zang, Y. He, M. Liang, X. Zhang, L. Tian, T. Wu, T. Jiang, and K. Li, "Changes in hippocampal connectivity in the early stages of Alzheimer's disease: evidence from resting state fMRI," *NeuroImage*, vol. 31, pp. 496–504, Jun 2006.

BIBLIOGRAPHY

- [340] M. Liang, Y. Zhou, T. Jiang, Z. Liu, L. Tian, H. Liu, and Y. Hao, "Widespread functional disconnection in schizophrenia with resting-state functional magnetic resonance imaging," *Neuroreport*, vol. 17, pp. 209–213, Feb 2006.
- [341] Y. Zhou, M. Liang, T. Jiang, L. Tian, Y. Liu, Z. Liu, H. Liu, and F. Kuang, "Functional dysconnectivity of the dorsolateral prefrontal cortex in first-episode schizophrenia using resting-state fMRI," *Neurosci. Lett.*, vol. 417, pp. 297–302, May 2007.
- [342] Y. Zhou, M. Liang, L. Tian, K. Wang, Y. Hao, H. Liu, Z. Liu, and T. Jiang, "Functional disintegration in paranoid schizophrenia using resting-state fMRI," *Schizophr. Res.*, vol. 97, pp. 194–205, Dec 2007.
- [343] V. Cherkassky, R. Kana, T. Keller, and M. Just, "Functional connectivity in a baseline resting-state network in autism," *Neuroreport*, vol. 17, pp. 1687–1690, Nov 2006.
- [344] A. Anand, Y. Li, Y. Wang, J. Wu, S. Gao, L. Bukhari, V. Mathews, A. Kalnin, and M. Lowe, "Activity and connectivity of brain mood regulating circuit in depression: a functional magnetic resonance study," *Biol. Psychiatry*, vol. 57, pp. 1079–1088, May 2005.
- [345] C. Yu, Y. Liu, J. Li, Y. Zhou, K. Wang, L. Tian, W. Qin, T. Jiang, and K. Li, "Altered functional connectivity of primary visual cortex in early blindness," *Hum. Brain Mapp.*, May 2007.
- [346] L. Uddin, A. Kelly, B. Biswal, D. Margulies, Z. Shehzad, D. Shaw, M. Ghaffari, J. Rotrosen, L. Adler, F. Castellanos, and M. Milham, "Network homogeneity reveals decreased integrity of default-mode network in ADHD," *J. Neurosci. Methods*, Dec 2007.
- [347] D. Margulies, A. Kelly, L. Uddin, B. Biswal, F. Castellanos, and M. Milham, "Mapping the functional connectivity of anterior cingulate cortex," *NeuroImage*, vol. 37, pp. 579–588, Aug 2007.
- [348] P. Fransson, "How default is the default mode of brain function? Further evidence from intrinsic BOLD signal fluctuations," *Neuropsychologia*, vol. 44, pp. 2836–2845, 2006.
- [349] M. Hampson, N. Driesen, P. Skudlarski, J. Gore, and R. Constable, "Brain connectivity related to working memory performance," *J. Neurosci.*, vol. 26, pp. 13338–13343, Dec 2006.
- [350] A. T. Newton, V. L. Morgan, B. P. Rogers, and J. C. Gore, "Modulation of steady state functional connectivity in the default mode and working memory networks by cognitive load," *Hum. Brain Mapp.*, vol. 32, pp. 1649–1659, Oct 2011.
- [351] K. R. Van Dijk, T. Hedden, A. Venkataraman, K. C. Evans, S. W. Lazar, and R. L. Buckner, "Intrinsic functional connectivity as a tool for human connectomics: theory, properties, and optimization," *J. Neurophysiol.*, vol. 103, pp. 297–321, Jan 2010.
- [352] B. J. Harrison, J. Pujol, H. Ortiz, A. Fornito, C. Pantelis, and M. Yucel, "Modulation of brain resting-state networks by sad mood induction," *PLoS ONE*, vol. 3, p. e1794, 2008.

- [353] U. Hasson, H. C. Nusbaum, and S. L. Small, "Task-dependent organization of brain regions active during rest," *Proc. Natl. Acad. Sci. U.S.A.*, vol. 106, pp. 10841–10846, Jun 2009.
- [354] J. Damoiseaux, C. Beckmann, E. Arigita, F. Barkhof, P. Scheltens, C. Stam, S. Smith, and S. Rombouts, "Reduced resting-state brain activity in the "default network" in normal aging," *Cereb. Cortex*, Dec 2007.
- [355] B. Biswal and J. Hyde, "Functional connectivity during continuous task activation," in *Proceedings of the Sixth Annual Meeting of the International Society for Magnetic Resonance in Medicine*, vol. 3, (Berkeley (CA)), ISMRM, 1998.
- [356] M. Lowe, M. Dzemidzic, J. Lurito, V. Mathews, and M. Phillips, "Correlations in low-frequency BOLD fluctuations reflect cortico-cortical connections," *NeuroImage*, vol. 12, pp. 582–587, Nov 2000.
- [357] V. L. Morgan and R. R. Price, "The effect of sensorimotor activation on functional connectivity mapping with MRI," *Magnetic Resonance Imaging*, vol. 22, pp. 1069–1075, Oct 2004.
- [358] F. Sun, L. Miller, and M. D'Esposito, "Measuring interregional functional connectivity using coherence and partial coherence analyses of fMRI data," *NeuroImage*, vol. 21, pp. 647–658, Feb 2004.
- [359] T. Jiang, Y. He, Y. Zang, and X. Weng, "Modulation of functional connectivity during the resting state and the motor task," *Hum. Brain Mapp.*, vol. 22, pp. 63–71, May 2004.
- [360] Y. Nir, U. Hasson, I. Levy, Y. Yeshurun, and R. Malach, "Widespread functional connectivity and fMRI fluctuations in human visual cortex in the absence of visual stimulation," *NeuroImage*, vol. 30, pp. 1313–1324, May 2006.
- [361] B. Biswal, A. Hudetz, F. Yetkin, V. Haughton, and J. Hyde, "Hypercapnia reversibly suppresses low-frequency fluctuations in the human motor cortex during rest using echo-planar MRI," *J. Cereb. Blood Flow Metab.*, vol. 17, pp. 301–308, Mar 1997.
- [362] U. Wolf, V. Toronov, J. H. Choi, R. Gupta, A. Michalos, E. Gratton, and M. Wolf, "Correlation of functional and resting state connectivity of cerebral oxy-, deoxy-, and total hemoglobin concentration changes measured by near-infrared spectrophotometry," *J. Biomed. Opt.*, vol. 16, p. 087013, Aug 2011.
- [363] H. Zhang, Y.-J. Zhang, C.-M. Lu, S.-Y. Ma, Y.-F. Zang, and C.-Z. Zhu, "Functional connectivity as revealed by independent component analysis of resting-state fNIRS measurements.," *NeuroImage*, vol. 51, pp. 1150–61, Jul 2010.
- [364] L. Duan, Y. J. Zhang, and C. Z. Zhu, "Quantitative comparison of resting-state functional connectivity derived from fNIRS and fMRI: a simultaneous recording study," *Neuroimage*, vol. 60, pp. 2008–2018, May 2012.
- [365] U. Chaudhary, M. Hall, J. DeCerce, G. Rey, and A. Godavarty, "Frontal activation and connectivity using near-infrared spectroscopy: verbal fluency language study," *Brain Res. Bull.*, vol. 84, pp. 197–205, Feb 2011.

BIBLIOGRAPHY

- [366] S. Aydore, K. Mihcak, K. Ciftci, and A. Akin, "On Temporal Connectivity of PFC Via Gauss - Markov Modeling of fNIRS Signals," *IEEE Trans. Biomed. Eng.*, vol. 57, no. 3, pp. 761–768, 2010.
- [367] A. V. Medvedev, J. M. Kainerstorfer, S. V. Borisov, and J. VanMeter, "Functional connectivity in the prefrontal cortex measured by near-infrared spectroscopy during ultrarapid object recognition," *J. Biomed. Opt.*, vol. 16, p. 016008, 2011.
- [368] F. Homae, H. Watanabe, T. Otobe, T. Nakano, T. Go, Y. Konishi, and G. Taga, "Development of global cortical networks in early infancy," *The Journal of neuroscience: the official journal of the Society for Neuroscience*, vol. 30, pp. 4877–82, Apr 2010.
- [369] F. Homae, H. Watanabe, T. Nakano, and G. Taga, "Large-scale brain networks underlying language acquisition in early infancy," *Frontiers in Psychology*, vol. 2, no. May, pp. 1–14, 2011.
- [370] R. M. Birn, J. B. Diamond, M. A. Smith, and P. A. Bandettini, "Separating respiratory-variation-related fluctuations from neuronal-activity-related fluctuations in fMRI," *NeuroImage*, vol. 31, pp. 1536–1548, Jul 2006.
- [371] K. Shmueli, P. van Gelderen, J. de Zwart, S. Horowitz, M. Fukunaga, J. Jansma, and J. Duyn, "Low-frequency fluctuations in the cardiac rate as a source of variance in the resting-state fMRI BOLD signal," *NeuroImage*, vol. 38, pp. 306–320, Nov 2007.
- [372] X. W. Song, Z. Y. Dong, X. Y. Long, S. F. Li, X. N. Zuo, C. Z. Zhu, Y. He, C. G. Yan, and Y. F. Zang, "REST: a toolkit for resting-state functional magnetic resonance imaging data processing," *PLoS ONE*, vol. 6, p. e25031, 2011.
- [373] H. Obrig, M. Neufang, R. Wenzel, M. Kohl, J. Steinbrink, K. Einhäupl, and A. Villringer, "Spontaneous low frequency oscillations of cerebral hemodynamics and metabolism in human adults," *NeuroImage*, vol. 12, pp. 623–39, Dec 2000.
- [374] H. Yang, X. Y. Long, Y. Yang, H. Yan, C. Z. Zhu, X. P. Zhou, Y. F. Zang, and Q. Y. Gong, "Amplitude of low frequency fluctuation within visual areas revealed by resting-state functional MRI," *NeuroImage*, vol. 36, pp. 144–152, May 2007.
- [375] A. Weissenbacher, C. Kasess, F. Gerstl, R. Lanzenberger, E. Moser, and C. Windischberger, "Correlations and anticorrelations in resting-state functional connectivity MRI: a quantitative comparison of preprocessing strategies," *NeuroImage*, vol. 47, pp. 1408–1416, Oct 2009.
- [376] M. D. Fox, D. Zhang, A. Z. Snyder, and M. E. Raichle, "The global signal and observed anticorrelated resting state brain networks," *J. Neurophysiol.*, vol. 101, pp. 3270–3283, Jun 2009.
- [377] K. Murphy, R. M. Birn, D. A. Handwerker, T. B. Jones, and P. A. Bandettini, "The impact of global signal regression on resting state correlations: are anti-correlated networks introduced?," *NeuroImage*, vol. 44, pp. 893–905, Feb 2009.

-
- [378] C. Chang and G. H. Glover, "Effects of model-based physiological noise correction on default mode network anti-correlations and correlations," *NeuroImage*, vol. 47, pp. 1448–1459, Oct 2009.
- [379] G. Buzsaki and A. Draguhn, "Neuronal oscillations in cortical networks," *Science*, vol. 304, pp. 1926–1929, Jun 2004.
- [380] T. Katura, N. Tanaka, A. Obata, H. Sato, and A. Maki, "Quantitative evaluation of interrelations between spontaneous low-frequency oscillations in cerebral hemodynamics and systemic cardiovascular dynamics," *NeuroImage*, vol. 31, pp. 1592–1600, Jul 2006.
- [381] Y. Tong and B. D. Frederick, "Time lag dependent multimodal processing of concurrent fMRI and near-infrared spectroscopy (NIRS) data suggests a global circulatory origin for low-frequency oscillation signals in human brain," *NeuroImage*, vol. 53, pp. 553–564, Nov 2010.
- [382] Y. Tong, K. P. Lindsey, and B. D. Frederick, "Partitioning of physiological noise signals in the brain with concurrent near-infrared spectroscopy and fMRI," *J. Cereb. Blood Flow Metab.*, Aug 2011.
- [383] R. J. Cooper, L. Gagnon, D. Goldenholz, D. A. Boas, and D. N. Greve, "The utility of near-infrared spectroscopy in the regression of low-frequency physiological noise from functional magnetic resonance imaging data," *NeuroImage*, vol. 59, pp. 3128–3138, Feb 2011.
- [384] J. Kang, L. Wang, C. Yan, J. Wang, X. Liang, and Y. He, "Characterizing dynamic functional connectivity in the resting brain using variable parameter regression and Kalman filtering approaches," *Neuroimage*, vol. 56, pp. 1222–1234, Jun 2011.
- [385] A.-M. Golestani and B. G. Goodyear, "A resting-state connectivity metric independent of temporal signal-to-noise ratio and signal amplitude," *Brain Connectivity*, vol. 1, Aug 2011.
- [386] H. Zhang, Y. J. Zhang, L. Duan, S. Y. Ma, C. M. Lu, and C. Z. Zhu, "Is resting-state functional connectivity revealed by functional near-infrared spectroscopy test-retest reliable?," *J. Biomed. Opt.*, vol. 16, p. 067008, Jun 2011.
- [387] H. Zhang, L. Duan, Y.-J. Zhang, C.-M. Lu, H. Liu, and C.-Z. Zhu, "Test-retest assessment of independent component analysis-derived resting-state functional connectivity based on functional near-infrared spectroscopy," *NeuroImage*, vol. 55, pp. 607–15, Mar 2011.
- [388] H. Niu, S. Khadka, F. Tian, Z. J. Lin, C. Lu, and H. Zhu, C. and Liu, "Resting-state functional connectivity assessed with two diffuse optical tomographic systems," *J. Biomed. Opt.*, vol. 16, p. 046006, Apr 2011.
- [389] S. Sasai, F. Homae, H. Watanabe, and G. Taga, "Frequency-specific functional connectivity in the brain during resting state revealed by NIRS," *NeuroImage*, vol. 56, pp. 252–7, May 2011.
- [390] E. P. Duff, L. A. Johnston, J. Xiong, P. T. Fox, I. Mareels, and G. F. Egan, "The power of spectral density analysis for mapping endogenous BOLD signal fluctuations," *Hum. Brain Mapp.*, vol. 29, pp. 778–790, Jul 2008.

BIBLIOGRAPHY

- [391] A. Waites, A. Stanislavsky, D. Abbott, and G. Jackson, "Effect of prior cognitive state on resting state networks measured with functional connectivity," *Hum. Brain Mapp.*, vol. 24, pp. 59–68, Jan 2005.
- [392] S. Peltier, S. LaConte, D. Niyazov, J. Liu, V. Sahgal, G. Yue, and X. Hu, "Reductions in interhemispheric motor cortex functional connectivity after muscle fatigue," *Brain Res.*, vol. 1057, pp. 10–16, Sep 2005.
- [393] E. Macaluso, A. Cherubini, and U. Sabatini, "Bimanual passive movement: functional activation and inter-regional coupling," *Front. Integr. Neurosci.*, vol. 1, p. 5, 2007.
- [394] A. E. Cavanna and M. R. Trimble, "The precuneus: a review of its functional anatomy and behavioural correlates," *Brain*, vol. 129, pp. 564–583, Mar 2006.
- [395] D. S. Margulies, J. L. Vincent, C. Kelly, G. Lohmann, L. Q. Uddin, B. B. Biswal, A. Villringer, F. X. Castellanos, M. P. Milham, and M. Petrides, "Precuneus shares intrinsic functional architecture in humans and monkeys," *Proc. Natl. Acad. Sci. U.S.A.*, vol. 106, pp. 20069–20074, Nov 2009.
- [396] M. D. Fox, A. Z. Snyder, J. L. Vincent, and M. E. Raichle, "Intrinsic fluctuations within cortical systems account for intertrial variability in human behavior," *Neuron*, vol. 56, pp. 171–184, Oct 2007.
- [397] N. Wenderoth, F. Debaere, S. Sunaert, and S. P. Swinnen, "The role of anterior cingulate cortex and precuneus in the coordination of motor behaviour," *Eur. J. Neurosci.*, vol. 22, pp. 235–246, Jul 2005.
- [398] G. Albouy, V. Sterpenich, G. Vandewalle, A. Darsaud, S. Gais, G. Rauchs, M. Desseilles, M. Boly, T. Dang-Vu, E. Balteau, C. Degueldre, C. Phillips, A. Luxen, and P. Maquet, "Neural correlates of performance variability during motor sequence acquisition," *NeuroImage*, Dec 2011.
- [399] D. A. Fair, B. L. Schlaggar, A. L. Cohen, N. U. Miezins, F. M. Dosenbach, K. K. Wenger, M. D. Fox, M. E. Snyder, A. Z. Raichle, and S. E. Petersen, "A method for using blocked and event-related fMRI data to study "resting state" functional connectivity," *Neuroimage*, vol. 35, pp. 396–405, Mar 2007.
- [400] A. Barnes, E. T. Bullmore, and J. Suckling, "Endogenous human brain dynamics recover slowly following cognitive effort," *PLoS ONE*, vol. 4, p. e6626, 2009.
- [401] C. Julien, "The enigma of Mayer waves: Facts and models," *Cardiovasc. Res.*, vol. 70, pp. 12–21, Apr 2006.

List of revisions

(Revisions addressing comments from examiner 2 are bulleted, those addressing examiner 3's comments are numbered).

- Changed headings in section 4.1.1 on page 47 to Subjects, NIRS optode setup and Task
- Chapter 5 describes the subjects and tasks used in the remainder of the theses, therefore the Subjects and Tasks subsections in chapter 5 apply to all subsequent chapters. Added subheadings 9.2.1 on page 159 and 9.2.1 on page 159 (Subjects and tasks) to chapters 7 and 9.

Abstract

- Specified that the system used was continuous wave DYNOT
- Replaced “pilot” experiment with “initial” experiment
- Replaced “right-handed” cold stimulus with “right hand” cold stimulus.

Abbreviations

Added RTAP, LTAP, RCOLD, LCOLD, LF, VLF, PMU, CW

Chapter 1

Specified that scanner was 3T Siemens Allegra.

Chapter 2

- Added section “Analysis of fMRI data” 2.3 on page 12
- Added paragraph about MRI scanner requirements in section 2.1 on page 9
- Added references

-
- Added sentence and references about source-detector spacing and path length in section 2.4.2 on page 14
 - Added paragraphs about continuous wave, frequency domain and time domain NIRS in section 2.4.1 on page 14 and justifying selection of DYNOT system in section 2.5.5 on page 17.
 - Changed sentence in section 2.8 on page 20. The intended meaning was that the more common approach was not to consider spatial statistics - have tried to make this clearer.
 - Added bullet list in section 2.8 on page 21

Chapter 3

- Added text to figure 3.1 on page 28 caption explaining that each optode contains both a source and a detector
- Added 3 sentences explaining co-location referring to the figure in section 3.1.2 on page 29
- Modified sentence in section 3.4 on page 44 to specify negligible distance compared to channels that are actually used in the image reconstruction.

Chapter 4

- Changed title.
- Added paragraph discussing depth of DOT in section 4.1.2 on page 54
- Changed smoothing to temporal smoothing

Chapter 5

- Made section 5.3 a new chapter
- Stimulus presentation in both NIRS and fMRI experiments is described in section 5.1.1 on page 72. Modified section 5.1.3.2 on page 74 to avoid repeating stimulus presentation method for NIRS here.
- Modified paragraph in section 5.2.3 on page 89 to make it clearer that the subject could always see the visual stimulus, but was not able to see his own hands, and hence the cold stimulus being applied, during MRI, and that during NIRS it was not possible to fully recline the chair and still have the subject able to see the computer screen with the task cues.
- Added paragraph in section 6.3.3 on page 100 commenting on the possibility to perform NIRS without MRI (now in Chapter 6)

Chapter 6 (now 7)

- Added figures 7.3 on page 115 and 7.4 on page 116 showing NIRS activation images and explanatory paragraph 7.3.3 on page 112
- Added text explaining the notation $LTAP > RTAP$ etc to captions of tables and figures 7.4 on page 114, 7.2 on page 114, 7.5 on page 115, 7.8 on page 121, 7.9 on page 121, 7.10 on page 122, 7.11 on page 123 7.1 on page 111 7.3 on page 113 (also added LTAP and RTAP to list of abbreviations)
- Incorporated examiner's comment about relative deoxyHb into discussion in section 7.4 on page 128.

Chapter 7 (now 8)

- Added text explaining the notation $LCOLD > RCOLD$ etc to captions of tables and figures 8.1 on page 135 8.3 on page 137 8.5 on page 139 8.6 on page 142 8.9 on page 146 8.12 on page 150 (also added LCOLD and RCOLD to list of abbreviations)
- Specified that figures 8.2 on page 138 and 8.1 on page 137 are BOLD
- Add figures 8.3 on page 140 and 8.4 on page 141 and descriptive paragraph 8.3.2 on page 138

Chapter 8 (now 9)

- Did not change steady-state to rest because connectivity is evaluated during continuous performance of a task as well
 - Specified that correlation coefficient is Pearson correlation in section 9.2.4 on page 160. A correlation function was not used, added sentence in section 9.2.4 on page 160 specifying that only zero-latency correlation was considered.
 - In captions 9.3 on page 170 and 9.1 on page 165 changed "connectivity" to "BOLD signal connectivity" for clarity. Added a sentence in section 9.4 on page 177 explaining that using fMRI one is able to look at connectivity to all brain regions, but using NIRS only superficial sensorimotor cortex (surface of the brain) connectivity was considered.
1. Added text in sections 9.2.4 on page 160 and 9.3.1 on page 161 clarifying that resting connectivity is evaluated during the first resting condition
 2. Added text in section 9.2.4 on page 160 explaining selection of band pass filter cutoff
 3. Text in section 9.3.1 on page 161 explains that connectivity is calculated during rest and task (steady-state)
 4. Agree that subject 13 should not have been excluded.

-
5. Modified section 9.4.7 on page 183 adding 3 paragraphs to address questions about task design.
 6. Added a sentence in section 9.2.1 on page 159 explaining that the first 30s of each block was discarded to exclude transient task effects.
 7. Added text in section 9.2.1 on page 159 explaining the selection/use of two different TRs
 8. Corrected colourbar in figure 9.1 on page 165
 9. Presentation of NIRS data in fMRI space has been partially addressed through addition of activation/deactivation images for NIRS in chapters 7 and 8
 10. Added text in sections 9.4.3 and 9.5 to try and explain almost global connectivity observed with NIRS
 11. Changed CNR to SNR
 12. Added section 9.4.4 on page 179 discussing discrepancies between NIRS and fMRI
 13. Added in reference to Duan 2012 in section 9.1.3 on page 158

Chapter 9 (now 10)

- Changed “near infrared optical imaging” to “near infrared imaging”
- First sentence in second paragraph reads fine.
- SNR of deoxyHb discussed in chapter 10 on page 188
- Added a sentence in chapter 10 on page 187 describing results if both oxyHb and deoxyHb results are considered
- Added a sentence in chapter 10 on page 188 describing the influence of systemic processes on functional imaging results
- Added reference/justification for SNR of deoxyHb (see chapter 10 on page 188)
- Added reference for blood pressure oscillations
- Removed the ambiguous sentence
- Added paragraph in chapter 10 on page 189 discussing penetration depth limitations
- Added text in chapter 10 on page 191 suggesting improvements to the fNIRS system
- Added text in chapter 10 on page 188 commenting on the possibility of performing fNIRS without a subject-specific MRI